Title

Numerical Modeling and Uncertainty Analysis of Tunneling- and Deep Excavation-Induced Structural Damage

Permalink

Author

Zhao, Jinyan

Publication Date

2023

Numerical Modeling and Uncertainty Analysis of Tunneling- and Deep Excavation-Induced Structural Damage

By

Jinyan Zhao

A dissertation submitted in partial satisfaction of the

requirements for the degree of

Doctor of Philosophy

in

Engineering-Civil and Environmental Engineering

in the

Graduate Division

of the

University of California, Berkeley

Committee in charge:

Prof. Matthew J. DeJong, Chair
Prof. Kenichi Soga
Prof. Sanjay Govindjee
Prof. James Demmel

Spring 2023

Numerical Modeling and Uncertainty Analysis of Tunneling- and Deep Excavation-Induced Structural Damage

Abstract

Numerical Modeling and Uncertainty Analysis of Tunneling- and Deep Excavation-Induced Structural Damage

by

Jinyan Zhao

Doctor of Philosophy in Engineering-Civil and Environmental Engineering

University of California, Berkeley

Prof. Matthew J. DeJong, Chair

The assessment of tunneling- and deep excavation-induced structural damage is in great demand due to the fast development of underground spaces in major cities. Tunneling and deep excavations may cause substantial ground movements and surface building damage, and the potential damage needs to be assessed. The limited site characterization and building condition surveys and the lack of knowledge in soil-structure modeling may cause significant uncertainty in the building damage assessment. The substantial potential damage and uncertainty have made tunneling- and deep excavation-induced ground movements a human-made hazard in urban environments. To design resilient urban infrastructure, the consequence of this human-made hazard needs to be quantified, and a resilience performance-based engineering approach needs to be developed. This study borrows the performance-based engineering approach in natural hazard engineering, especially in earthquake engineering, and creates a probabilistic performance-based engineering (PPBE) framework for the assessment of building damage in large tunneling and deep excavation projects. This dissertation focuses on hazard analysis, soil-structural analysis, and some damage analysis methods in the proposed PPBE framework because they are significantly different from the existing natural hazard assessment frameworks. The other components of the PPBE, such as building asset inventory development and economic/environmental loss estimation, are briefly discussed and more theories can be referenced from other natural hazard assessment approaches.

A computational tool named Uncertainty Quantification in Tunnel and Excavation Soil-Structure Interaction (`UQ-TESSI`) is developed to implement the proposed hazard analysis, soil-structure analysis, and the associated uncertainty quantification. `UQ-TESSI` incorporates a suite of deterministic soil-structure analysis models named Analysis of Structure Response to Excavation (`ASRE`) with the PPBE framework. Applying the proposed PPBE framework in the assessment of tunneling- and deep excavation-induced building damage faces two major challenges: (1) the large number of buildings needed to be analyzed, (2) the high-dimensional uncertainty associated with material, workmanship, and tunneling- and deep excavation-induced soil-structure interaction (T&DE SSI) modeling processes. These challenges are alleviated by: 1) creating T&DE SSI modeling and computation tools that minimize uncertainty with reasonably small modeling effort, 2) creating probabilistic models to quantify the uncertainty in the assessment approach, and 3) applying high-performance computing and advanced uncertainty propagation and quantification techniques. The application of the proposed PPBE approach and `UQ-TESSI` are demonstrated with multiple case studies enabling building performance assessment in T&DE on a regional or community-level scale.

The case study results enable the following observations. The application of the proposed PPBE and 2D soil-structure models confirmed several widely recognized soil-structure interaction mechanisms. The 2D modeling case studies also revealed the large uncertainty associated with the building stiffness estimation and the inability of 2D models to appropriately simulate the effects of analyzing progressive excavations. For the 3D case studies, soil-structure analysis modeling was found to successfully capture the out-of-plane spatial variability in both tunneling and deep excavations. In addition, the coupling effect among masonry façade walls needs to be considered in tunneling, and the results indicate that neglecting the coupling effect may lead to an overestimation of building strain when the building is skewed compared to the tunnel axes. The case history data collected in the construction of the Elizabeth Line and several deep excavation projects in Norway confirmed the expectation that the ground movements in tunneling and deep excavation have strong spatial variability, and the spatial variability needs to be considered in the probabilistic modeling of ground movements in regional building damage assessment. Overall, it is observed that the uncertainty in ground displacement estimation in the current analysis approach produced the most uncertainty in the large-scale building damage assessment, and quantifying the uncertainty is a high-dimensional uncertainty quantification problem, which is arguably only feasible with high-performance computation and advanced Monte Carlo methods.

Contents

List of Figures

List of Tables

Acknowledgments

I want to express my most sincere gratitude to my advisor, Professor Matthew DeJong, for his guidance and countless support. His vision of understanding the uncertainty in excavation-induced building risk assessment led to my interest and passion in uncertainty quantification and computational analysis of civil engineering infrastructure. The amount of guidance, but also freedom, he offered me to explore this area is tremendous, and I am very grateful for this. I also thank him for all the opportunities he provided me, such as the teaching experiences, the many conferences I attended, the presentations at engineering firms, my research visit to Norway, and many others. Despite my dullness on many occasions, his intelligence, kindness, and dedication to mentoring made my Ph.D. more fruitful and enjoyable than I ever expected.

I am also very grateful to Dr. Stefan Ritter at NGI for the great amount of knowledge he shared with me regarding excavation and soil-structure interactions. With his help, I was generously treated during my visit at NGI and introduced to many brilliant engineers and researchers. Many of them contributed much to this research, and I hope to acknowledge senior engineer Thomas Sandene for his help with understanding case history data and project engineer Dr. Luca Piciullo for his guidance in ground movement models. I also hope to acknowledge the others I met at NGI for their exceptional intelligence and kindness, and they greatly broadened my mind in geohazards, civil engineering, and the world.

Additionally, I am grateful to Professor Kenichi Soga, Dr. Dayu Apoji, and Dr. Zhangwei Ning, from whom I learned a great deal about tunnel engineering and monitoring in geotechnical engineering. I also would like to thank Professor Filip Filippou, Sanjay Govindjee, James Demmel, and Elizabeth Purdom for serving on my qualifying exam committee and educating me in their classes. The classes helped me to establish my perception of structural analysis, mechanics, computation, and statistics and greatly complemented my research. I would also like to acknowledge Prof. Jin-Guang Teng and Prof. Guan Lin from my underground school for shaping my fundamental interest and understanding of civil engineering.

I would also like to acknowledge several individuals at UC Berkeley from whom I learned very much. I thank Prof. Joan Walker for including me in the department DEIB committee and for her leadership and advocacy. I thank Han, Charlie, Shenghan, Nanda, Yuqing, Eduardo, James, Huy, Miguel, Xuan, Yaheng, Sang-ri, Kuanshi, and Aakash for their friendship and many discussions about study and life. Most of all, I thank Huan for her accompany and encouragement at many difficult times during my study. Finally, I want to thank my parents for their unconditional support all the time. I am indebted to them and this would not have been possible without the endless support from my family.

Chapter 1

Introduction

1.1 Background

Underground construction is in great demand globally due to congested cities and dense urban environments. In the planning and during the construction process of underground constructions, it is important to predict the potential ground movements and the associated surface building deformations. Two commonly adopted underground construction methods are tunneling and open-cut deep excavations. The influences of these two types of excavation on surface structures are studied in this project.

In practice, sophisticated numerical models can be used to analyze and predict building damages for some important buildings [19, 47, 53, 78, 77]. However, such detailed numerical analysis is generally not feasible in the early stage of large tunnel projects, where hundreds of buildings are required to be assessed. Further, the value of such detailed numerical analysis is debated because the models may experience significant uncertainty with respect to the calibration of constitutive models, simulation of tunnel/deep excavation systems, etc. To address this challenge, a staged approach proposed by Mair, Taylor, and Burland [120] is commonly adopted, which consists of three stages: a preliminary assessment, a second stage assessment, and a detailed evaluation. In the preliminary assessment stage, a settlement contour is computed, and the buildings with a predicted settlement of less than 10mm and a predicted slope of less than 1:500 are considered to have a negligible risk of damage. Otherwise, buildings are qualified for a second stage assessment, in which some engineering demand parameters (e.g., distortion, deflection ratio, and tensile strain) are calculated. Based on the engineering demand parameter, a potential damage category is assigned to each building, and the buildings with severe damage potential are required to be evaluated in detail in a third assessment stage.

1.2 Motivation and research objectives

The current second-stage assessment methods consist of many simplified models and empirical equations, which often lead to unreliable and overly conservative damage evaluation results. Moreover, because comprehensive surveys are generally not available in the second assessment stage, details of structure layouts and material properties are often unavailable. Consequently, many assumptions and approximations are made in the analyses, which introduce large uncertainty to building damage evaluations. To develop more reliable soil-structure interaction models, the interaction mechanism was studied with geotechnical centrifuge modeling, and a soil-structure interface model was proposed based on the centrifuge modeling tests[160, 65]. Because centrifuge tests are costly and time-consuming, this project takes advantage of and extends the previously developed soil-structure interface model and uses a numerical modeling method to study the behavior of buildings under tunneling and deep excavation (T&DE) with various excavation and building configurations.

More specifically, the research objectives are:

- Identify and understand the uncertainty in the current T&DE-soil-structure interaction analysis.
- Find an optimal modeling fidelity that minimizes the uncertainty in the T&DE-soil-structure interaction with a practical modeling effort for large-scale assessment.
- Create a set of probabilistic modeling methods to formally quantify the variability of T&DE-induced ground movements and the uncertainty in the estimated soil and surface building property.
- Develop a probabilistic performance-based engineering approach to quantify building performance in large T&DE constructions.
- Develop a computational tool that facilitates the T&DE-soil-structure modeling and high-dimensional uncertainty quantification in the probabilistic performance-based assessment of building damage.

1.3 Research outline

The research starts with a 2D deterministic numerical study using simplified surface-building models. Realizing that large uncertainty exists in the simplified modeling method of the tunneling and deep excavation-induced soil-structure interaction (T&DE SSI), an uncertainty quantification approach is adopted to understand the effect of the uncertainty on the analysis results so that suggestions on an optimal trade-off between analysis complexity and prediction accuracy can be proposed. After studying the 2D numerical models and several case studies, it is observed that approximating the 3-dimensional (3D) building and T&DE-induced ground movements with 2D models is too simple, and it may cause unreliable prediction of building responses to T&DE. As a result, a 3D T&DE SSI model is developed. Further, the 3D T&DE SSI model is applied to study the uncertainty effect of soil stiffness, ground movements, and building properties on the T&DE SSI assessment. Because tunnel and deep excavation construction may impact buildings in a large area, the 3D model is designed to be applicable for regional scale T&DE SSI assessments. In regional assessment, models for the spatial correlation/variability of soil stiffness and ground movements are adopted, where the models for ground movements are derived from collected case history data.

Based on the uncertainty study of 2D and 3D T&DE SSI models, a probabilistic performance-based engineering (PPBE) approach is proposed for practical T&DE SSI assessment. The assessment approach borrows the concept of the PPBE approach in seismic performance assessment, and it works in four stages, which are hazard analysis, soil-structural analysis, damage analysis, and loss analysis. First, the hazard analysis describes the possible ground movements with probabilistic models of intensity measures (IMs). A soil-structural analysis is then performed to calculate the response of buildings to ground movements of given IMs, and the building responses are described with engineering demand parameters (EDPs), such as drifts, cracks, and strains. Next, in the damage analysis stage, the EDPs are used with predefined (e.g., FEMA P-58[128]) fragility functions to determine the damage states or damage measures (DMs) of the buildings. Finally, given the DMs, the repair costs, repair duration, repair emission, and other decision variables (DVs) are evaluated in the loss analysis stage. This dissertation covers hazard analysis, soil-structure analysis, and part of the damage analysis methods, while the loss analysis method may again refer to FEMA P-58 volume 1 [128] for general loss and FEMA P-58 volume 4 [130] for environmental impacts. In addition, a computer program named Uncertainty Quantification in Tunneling and Excavation-Induced Soil-Structure Interaction (`UQ-TESSI`) is developed in this dissertation to facilitate the application of the proposed PPBE regional assessment approach.

One limitation of the study is the developed soil-structure analysis model only considers shallow foundation buildings. However, the proposed PPBE approach can be applied to the assessment of deep-foundation buildings and other types of underground structures if soil-structure interaction models and their associated uncertainties are available. Another limitation is that this dissertation focuses on the short-term building response to T&DE primarily constructed in clay, and an elastic behavior under an undrained condition is adopted. It is believed that the probabilistic modeling method and PPBE approach can quantify the effect of the simplified soil constitutive model, and more detailed modeling is only needed for buildings experiencing large potential damage. The consideration of long-term consolidation ground movements and more realistic soil constitutive models may potentially reduce the uncertainty in the proposed PPBE framework and needs further investigation.

1.4 Dissertation structure

This dissertation is structured as follows.

- A review of common practices of T&DE induced structure damage assessments, existing numerical studies in T&DE and building interaction, and existing uncertainty analysis in the area of T&DE are provided in Chapter 2.
- The development and validation of the 2D/3D T&DE soil-structure analysis model are shown in Chapter 3. This chapter forms the basis of the soil-structural model analysis and damage analysis stage in the proposed PPBE assessment approach.
- The uncertainty analysis framework, the quantification of input uncertainties in T&DE SSI, and several advanced Monte Carlo-based uncertainty quantification and sensitivity analysis methods are presented in Chapter 4. In addition, a regional assessment framework is presented. This chapter covers the hazard analysis stage and the uncertainty quantification procedures in the proposed PPBE assessment approach.
- Chapter 5 shows the design and implementation of the computer program Uncertainty Quantification in Tunneling and Excavation-induced Soil-Structure Interaction (`UQ-TESSI`), which can be used for regional probabilistic modeling of T&DE SSI assessment.
- A number of case studies using 2D/3D SSI models in both tunneling and deep excavation are presented in Chapter 6. The case studies cover both single building and regional/community-scale probabilistic T&DE SSI assessment.
- Conclusions and recommendations for further research are given in Chapter 7.

Chapter 2

Literature review

2.1 Current practice of tunneling and deep excavation induced surface building damage

The three-stage assessment approach (Fig. 2.1)outlined by Mair, Taylor, and Burland [120] is the most widely adopted approach when the potential damage of a relatively large number of buildings needs to be evaluated in the planning of both tunnels (e.g., the Jubilee Line Extension [43] and the Elizabeth Line[186]) and deep excavations [173, 10, 76]. In the three-stage approach, increasing details are required at each stage to achieve a conservative assessment result with affordable modeling efforts.

In the first stage, a settlement profile induced by tunneling and deep excavation (T&DE) is estimated with empirical methods, and all structures, buildings, and utilities in the vicinity of the settlement profiles are identified. The methods to estimate ground settlement profiles for T&DE applications are reviewed and discussed in Section 3.1. In the first stage, the effect of building stiffness on the settlement pattern is ignored, and the derived settlement is called the "greenfield settlement". The buildings subject to a greenfield settlement smaller than 10 mm and a maximum settlement slope less than 1/500 are considered safe and eliminated from the assessment. Because building stiffness (the soil-structure interaction effect) is neglected in this assessment stage, the first-stage assessment is often overly conservative.

In the second stage outlined by Mair, Taylor, and Burland [120], the limiting tensile strain method [26, 22] is used to estimate a potential damage category of the buildings. In the limiting strain method, the surface buildings are modeled as elastic beams with a displacement equal to the greenfield ground displacement derived in the first stage. Building bending strain and diagonal strain are calculated, and compared with the limiting tensile strains for different damage categories proposed by Boscardin and Cording [22]. The limiting tensile strains (summarized in Table. 2.1) are derived from a number of case studies and analyses of different building materials, such as bricks and reinforced concrete. Building bending strain and diagonal strain can be calculated from deflection ratios and horizontal strains. The building settlement profiles are divided into sagging and hogging regions as shown in Fig. 2.2, and the deflection ratios are estimated for each region. Assuming a simply supported condition, the bending and diagonal strain can be calculated with Eq. 2.1. If horizontal ground movements are considered, the horizontal building strain can be estimated by taking the derivative of the horizontal displacement profile(see Eq. 3.10). The resultant bending and diagonal strain can be then estimated from Eq. 2.2. Because the maximum strain in a building is usually calculated from deflection ratios and horizontal strain, interaction diagrams (e.g., Fig.2.3) are usually used for fast damage assessment. Because the soil-structure interaction effect is still neglected in this stage, the assessment is again prone to overly conservative. If the damage category is considered moderate or greater, a more detailed third-stage assessment will be performed.

$$\varepsilon_{b(max)} = \frac{\Delta}{L}\frac{12y}{L}\frac{1}{1+\frac{18}{L^2}\frac{I}{H}\frac{E}{G}} \tag{2.1a}$$

$$\varepsilon_{d(max)} = \frac{\Delta}{L}\frac{1}{1+\frac{L^2}{18}\frac{H}{I}\frac{G}{E}} \tag{2.1b}$$

$$\varepsilon_{br(max)} = \varepsilon_{b(max)} + \varepsilon_h \tag{2.2a}$$

$$\varepsilon_{dr(max)} = \frac{\varepsilon_h}{2} + \sqrt{\left(\frac{\varepsilon_h}{2}\right)^2 + \varepsilon_{b(max)}^2} \tag{2.2b}$$

In the third stage, the details of building configuration, tunnel construction techniques and sequence, and soil-structure interaction mechanisms are considered. The design engineers are usually required to consider the sequence and method of tunneling, the three-dimensional layout of the tunnels with respect to the building, structural details, and continuities in this stage. The third-stage assessment usually adopts full-scale numerical models, and it is very time-consuming to survey the structural details, calibrate the large numerical models, and execute the numerical models. If a third-stage assessment results in a damage category of moderate or greater, design engineers are often required to recommend protective measures either to minimize the likelihood of unacceptable levels of settlement or to control the structural response of the affected building.

2.1.1 Relative stiffness methods and modification factors

As demonstrated by field data [44, 54] and centrifuge tests [54, 160], the surface structures may modify the ground response in T&DE significantly and the deformation of buildings are generally smaller than the greenfield settlements. As a result, the second stage assessment discussed above is considered overly conservative and a group of relative stiffness methods were proposed by multiple researchers [158, 66, 81, 173] to consider the soil-structure interaction effect without significantly increasing the analysis effort. The widely adopted methods are summarized here, and some theories behind the methods are reviewed in Section 2.2.

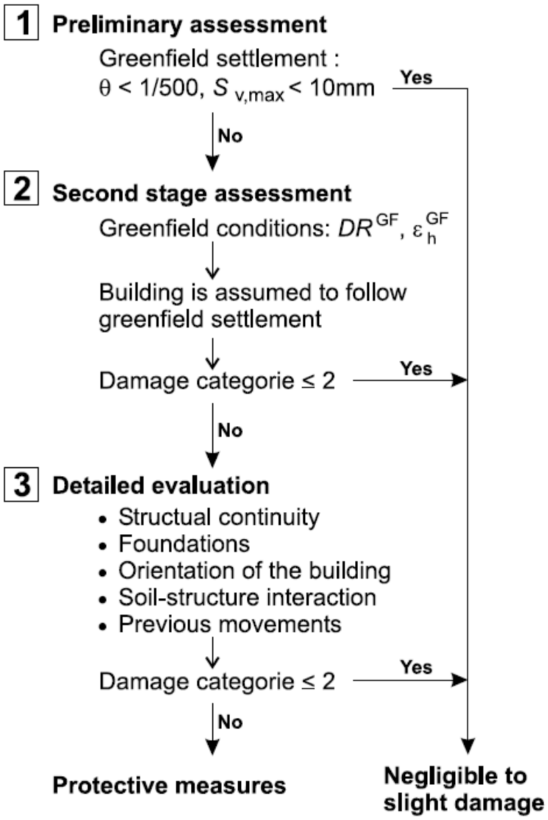

Figure 2.1: Three-stage damage assessment framework outlined by Mair, Taylor, and Burland [120] (after [160]).

Category of damage	Normal degree of severity	Critical tensile strain * (ε_{crit}) (%)
0	Negligible	0 - 0.05
1	Very slight	0.05 - 0.075
2	Slight	0.075 - 0.15 (0.075 - 0.167)
3	Moderate	0.15 - 0.3 (0.167 - 0.333)
4 to 5	Severe to very severe	>0.3 (>0.333)
∗The values in bracket are suggested by Son and Cording [173]		

Table 2.1: Relationship between category of damage and building principal tensile strain (after [22])

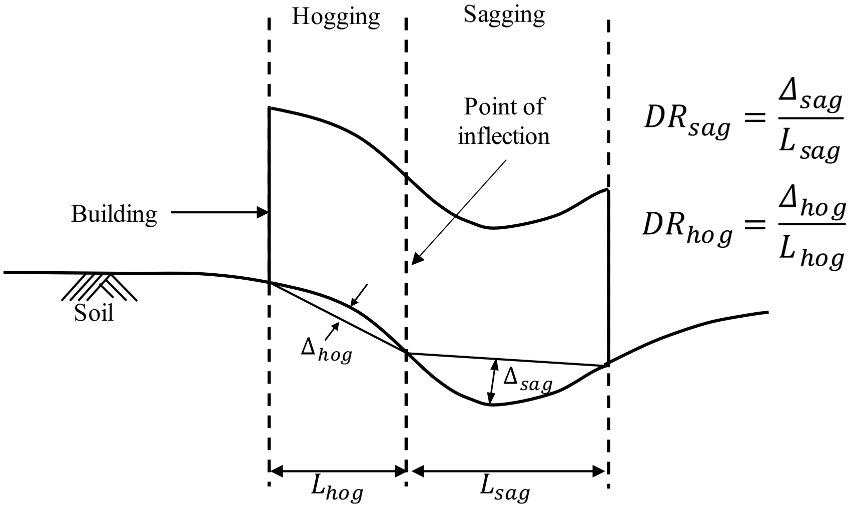

Figure 2.2: Notations in T&DE and structure interaction.

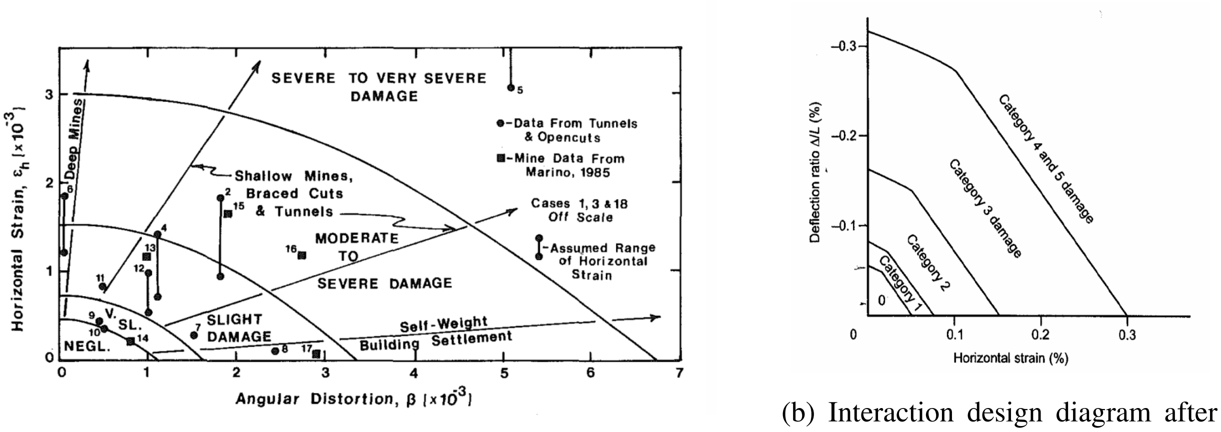

(a) Interaction design diagram after Boscardin and Cording [22]

(b) Interaction design diagram after Burland [25]

Figure 2.3: Interaction design diagrams used in the second stage assessment.

Potts and Addenbrooke [158] investigate the effect of axial and bending structural stiffness on the ground movements due to tunneling. A number of plain-strain parametric studies using the finite element method (FEM) were performed by Potts and Addenbrooke [158], in which the effect of building length (perpendicular to tunnel axis or deep excavation walls and denoted as B in [158]), axial and bending stiffness, tunnel depth, and the distance from building to tunnel axis were investigated. The surface buildings are modeled as weightless Euler-Bernoulli beams, and two relative stiffness parameters (Eq. 2.3a) were defined to describe the relative axial and bending stiffness between buildings and soils. EI and EA are the bending and axial stiffness of the building per meter length parallel to the tunnel axis. The soil stiffness E_s is the secant stiffness at 0.01% of axial strain at half of the tunnel depth. After defining the relative stiffness, Potts and Addenbrooke [158] proposed to use modification factors (Eq. 2.4a and Eq. 2.4b) to describe the difference between building deformations and greenfield deformations, where bld stands for buildings and gf stands for greenfield. Design curves (Fig. 2.4) that relate relative stiffness and modification factors were proposed based on the parametric studies. Some details about the adopted finite element method are reviewed in Section 2.2.

The method developed by Potts and Addenbrooke [158] didn't consider the effect of building weights and building width (parallel to tunnel axis or deep excavation walls). As a result, Franzius, Potts, and Burland [68] extended the study of Potts and Addenbrooke [158] and used 3D finite element models to investigate the effects of building width (L), building weights, different interfaces between the beam and the soil, and different tunnel depths. After considering the additional parameters, a new pair of relative stiffness (Eq. 2.3b) and a set group of design curves (Fig. 2.5 and 2.6) were proposed.

Although the study of Potts and Addenbrooke [158] and Franzius, Potts, and Burland [68] focused on tunneling and building interaction, Mair [117] showed that the relative stiffness could also be applied to deep excavation-induced building damage assessment. The relative bending stiffness was further refined as Eq. 2.3c so that the sagging and hogging regions have different relative stiffness. Further, the representative soil stiffness was defined as the weighted average of the elastic modulus of the soil layers above the tunnel (or excavation level in the case of deep excavations). It was shown in [117] that the modification factors obtained from centrifuge tests and finite element analysis have a stronger correlation with the newly proposed relative stiffness parameters. In other words, Eq. 2.3c can better predict the modification factors.

Son and Cording [173] carried out relatively large-scale (1/4-1/10) physical model tests to study the response of brick-bearing walls to deep excavation-induced ground movements. Further, the distinct element method was adopted in a suit of numerical models to study the behavior of brick-bearing walls that are subject to ground subsidence. It is suggested that the shear deformation mode is an important deformation mechanism of brick-bearing walls, and a relative soil/structure shear stiffness parameter was proposed as Eq. 2.3d. Further, a state of strain theory (Eq. 2.5) was adopted to estimate the principal tensile strain ε of a building unit from its angular distortion β and horizontal strain ε_h. The angular distortion β can be estimated from the design curves derived from field cases, physical models, and numerical tests (Fig. 2.7), and the method proposed by Boscardin and Cording [22] was suggested by Son and Cording [173] to estimate ε_h.

A recent development of the relative stiffness method was by Franza, Ritter, and DeJong [65], in which the differences between the building sagging/hogging length and the greenfield sagging/hogging length were considered. Modification factors describing the length difference were defined as Eq. 2.4c, and $B_{sag,bld}$ and $B_{hog,bld}$ were suggested to replace B_{sag} and B_{hog} in the relative stiffness proposed by Mair [117]. Curves were also provided in [65] to estimate $M_{L,sag}$ and $M_{L,hog}$ from a rigid factor $R = \frac{EI}{E_s i^3}$, and maximum and minimum offsets (D_u and D_l) of the structure edges from the tunnel axis, where i is the distance from the tunnel axis to the reflection point of the Gaussian greenfield settlement profile and E_s is the representative soil stiffness defined in [117].

$$\rho^* = \frac{EI}{E_s(B/2)^4} \qquad \alpha^* = \frac{EA}{E_s(B/2)} \tag{2.3a}$$

$$\rho^* = \frac{EI}{E_s B^2 z_0 L} \qquad \alpha^* = \frac{EA}{E_s BL} \tag{2.3b}$$

$$\rho^*_{sag} = \frac{EI}{E_s B^3_{sag} L} \qquad \rho^*_{hog} = \frac{EI}{E_s B^3_{hog} L} \tag{2.3c}$$

$$\rho^*_{shear} = \frac{E_s}{G_b HB} \qquad \alpha^*_{hog} = \frac{EA}{E_s BL} \tag{2.3d}$$

$$\rho^*_{sag} = \frac{EI}{E_s B^3_{sag,bld} L} \qquad \rho^*_{hog} = \frac{EI}{E_s B^3_{hog,bld} L} \tag{2.3e}$$

$$M^{DR,sag} = \frac{DR_{sag,bld}}{DR_{sag,gf}} \qquad M^{DR,hog} = \frac{DR_{hog,bld}}{DR_{hog,gf}} \tag{2.4a}$$

$$M^{\varepsilon_h,sag} = \frac{\varepsilon_{h,sag,bld}}{\varepsilon_{h,sag,gf}} \qquad M^{\varepsilon_h,hog} = \frac{\varepsilon_{h,hog,bld}}{\varepsilon_{h,hog,fg}} \tag{2.4b}$$

$$M^{L,sag} = \frac{L_{sag,bld}}{L_{sag,gf}} \qquad M^{L,hog} = \frac{L_{hog,bld}}{L_{hog,gf}} \tag{2.4c}$$

$$\varepsilon_p = \varepsilon_h \cos^2\theta_{max} + \beta \sin\theta_{max} \cos\theta_{max} \tag{2.5a}$$

$$\tan(2\theta_{max}) = \frac{\beta}{\varepsilon_h} \tag{2.5b}$$

In practice, the relative stiffness approach can be easily implemented but may experience large uncertainty in the estimation of building stiffness (EA and EI) and soil stiffness. Further, many factors, such as building weights, the soil-structure interface friction, and 3D building configurations, are not considered in the relative stiffness method. Such significant simplification of the T&DE SSI system causes large uncertainty. Overall, the relative stiffness approach can generally provide a satisfactory estimation of building deformation but there can be a considerable discrepancy between field observations and the analysis results using different relative stiffness parameters [74].

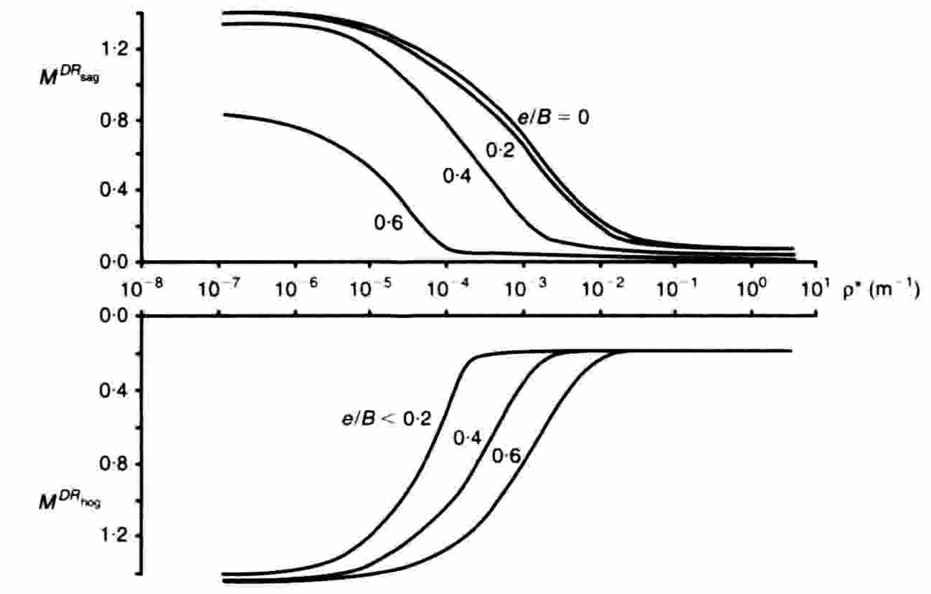

(a) Design curves for the modification factors of deflection ratio.

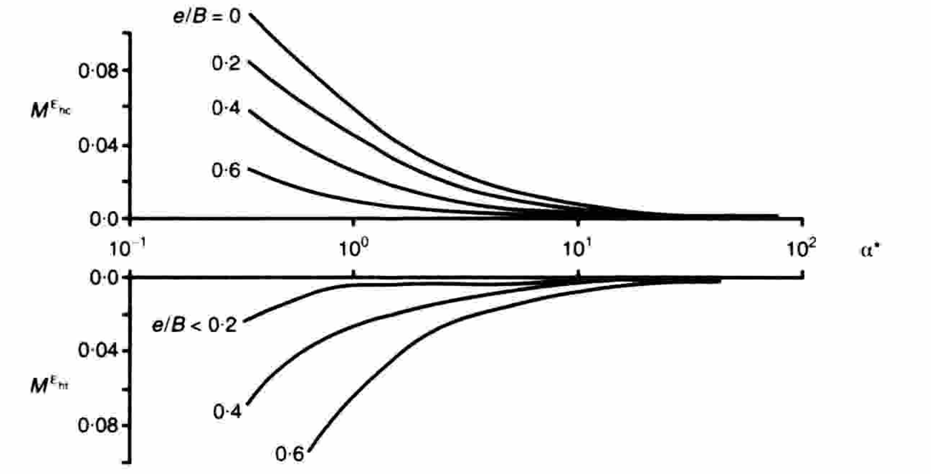

(b) Design curves for the modification factors of horizontal strain.

Figure 2.4: Design curves developed by Potts and Addenbrooke [158].

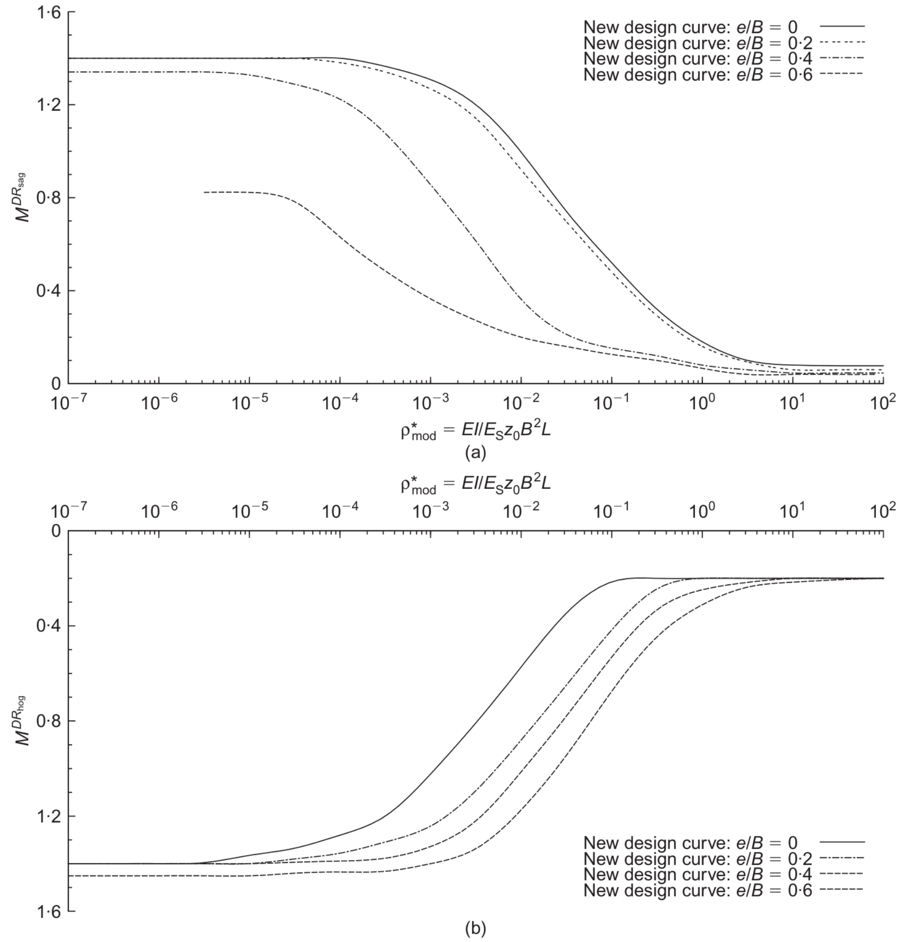

Figure 2.5: Design curves for modification factors of deflection ratio developed by Franzius, Potts, and Burland [68].

2.2 Numerical studies of the interaction between tunneling/deep excavation and shallow foundation buildings

There are a large number of numerical studies on the interaction between tunneling or deep excavation and adjacent buildings. This dissertation focuses on the responses of shallow foundation buildings, and several state-of-the-art numerical studies in each stage along the development of this area are reviewed in this section.

One of the earliest numerical studies of tunneling and surface structure interaction was done by Potts and Addenbrooke [158], in which 100 finite element analyses (FEAs) were performed in

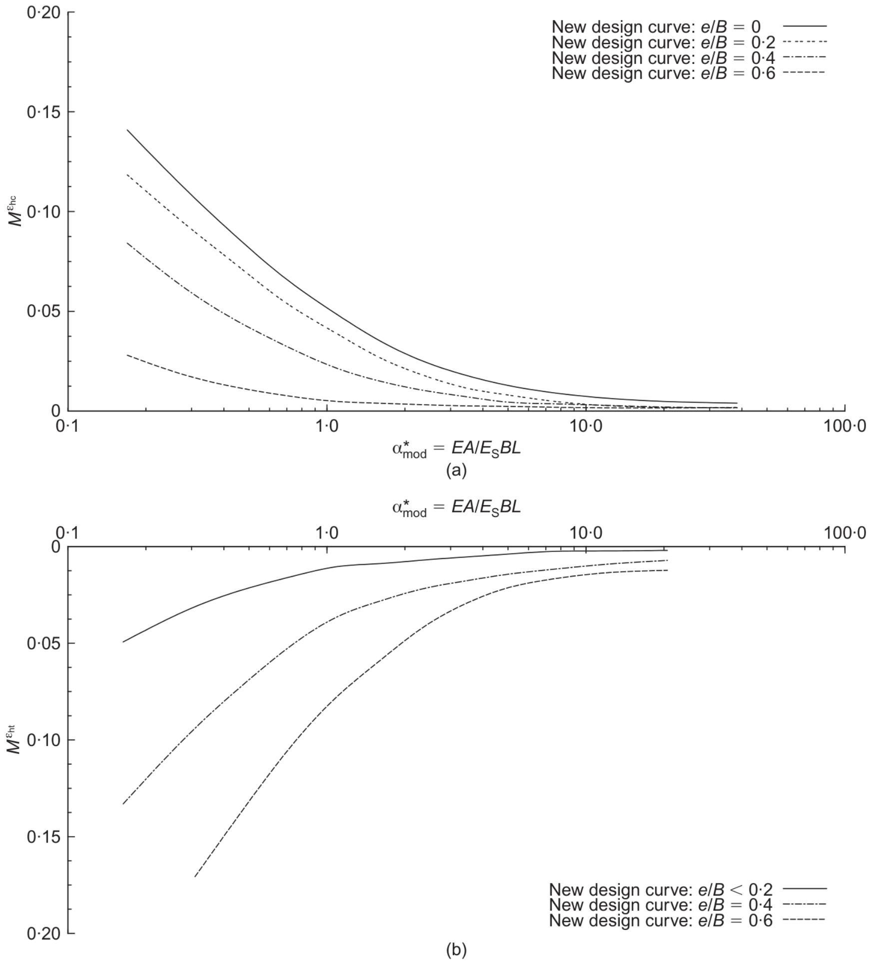

Figure 2.6: Design curves for modification factors of horizontal strain developed by Franzius, Potts, and Burland [68].

a parametric study to derive the design curves between modification factors and relative stiffness discussed in Section 2.1. In the FEAs, surface buildings were modeled as elastic beams that allow both bending and shear deformation, the soil was modeled as London clay represented by a non-linear elastic-plastic constitutive model [99] under an undrained condition, and a "rough" soil-structure interface was modeled, where separation and slippage were not allowed at the interface. The FEAs were performed with the Imperial College Finite Element Program (ICFEP) under a 2D plane strain condition. The tunnel excavation was modeled by the incremental removal of the solid elements within the tunnel boundary. That is, the stresses that the soil within the tunnel applied to the tunnel boundary were evaluated and then applied in the reverse direction over several increments. The movements of the tunnel boundary were monitored, and the stress increment

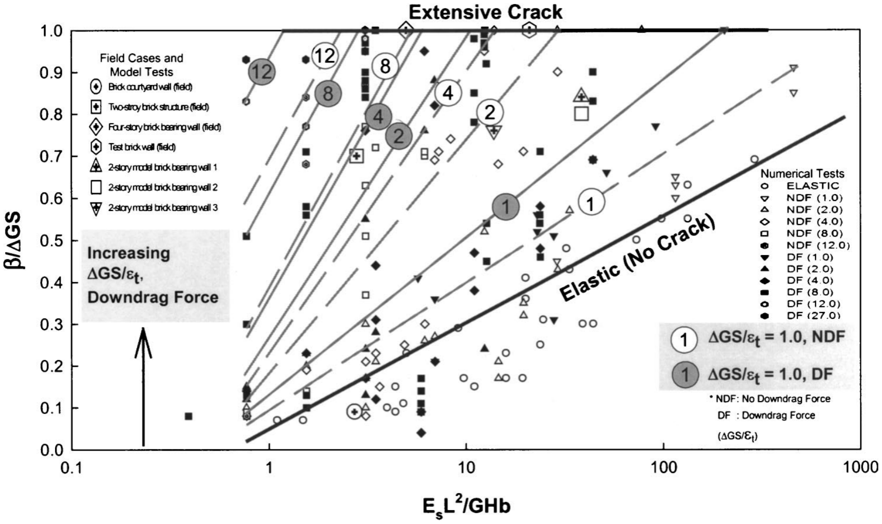

Figure 2.7: Relationship between normalized angular distortion and relative soil-structure shear stiffness, where ΔGS is the ground settlement slope (after Son and Cording [173]).

stopped when a 1.5% volume loss (V_L, defined as the ratio of shrunk tunnel cross-section area over the nominal cross-section area) was achieved. The results showed that both the axial and bending stiffness of the surface structure influence the ground surface movements, and these movements can be very different from greenfield ground movements.

Extending from [158], Franzius, Potts, and Burland [68] performed both 2D plane-strain and 3D FEAs using ICFEP. The soil model was the same as the soil in [158] and was modeled by 8-node elements in 2D and 20-node elements in 3D analyses. In 2D plane-strain analyses, buildings were represented by elastic beams characterized by Young's modulus, Poisson's ratio, and cross-sectional geometry and modeled by 3-node beam elements. In 3D analyses, buildings were represented by elastic shells characterized by Young's modulus and thickness and modeled by 8-node shell elements in ICFEP. The soil-structure interface was modeled by zero thickness interface elements [37] that enable a Mohr-Coulomb failure criterion at the interface. If the normal tensile strength ($c'/tan\phi'$, where c' is the cohesion and ϕ' is the maximum angle of shearing resistance) of the interface elements is exceeded, the interface opens and the residual tensile stress is redistributed. When the interface is open, the normal stress remains equal to $c'/tan\phi'$, and the shear stress remains equal to zero. As a result, opening and slip at the soil-structure interface were modeled. To model the tunneling process, the same procedure in [158] was adopted in 2D analyses. In 3D analyses, the effect of the 3D tunneling sequence on buildings was investigated, and a step-by-step approach was adopted. In the step-by-step approach, the 3D soil mesh was divided in the tunnel axis direction into slices of equal length L_{exc}. In one excavation step, elements within the tunnel boundary were excavated over L_{exc}, and the tunnel lining was subsequently installed over L_{exc}. The tunnel lining was modeled by elastic shell elements that represent a continuous concrete lining. The tunnel modeling method was not V_L controlled, and the resultant V_L at the ground surface depends on the choices of L_{exc}. Franzius and Potts [67] compared the V_L obtained from different L_{exc} values, and observed that this method might overestimate the resultant V_L at the ground surface. Franzius and Potts [67], therefore, recommended to scale down the calculated V_L to a realistic value (1.5% in Franzius, Potts, and Burland [68]), and the associated building deflection was also scaled down by the same factor. It is interesting to notice that the 3D model has 10434 solid elements and 46930 nodes, and it took around 200 hours to evaluate in a Sun SF880 server, which is a high-performance computer in early 2000 with 16 microprocessors running at 600-900 MHz and up to 32 Gb memory shared by the microprocessors. A personal workstation nowadays may have 6 or more microprocessors running at over 3 GHz and 16 to 128 Gb shared memory, which could complete a comparable or larger number of floating point operations with the Sun SF880 server per second (the effect of I/O and memory consumption is neglected). Despite the fast development of computing power, the evaluation of big T&DE SSI models may still be very time-consuming and challenging in personal workstations, and many civil engineering design consultants have explored the usage of cloud computing to accelerate model evaluations.

Besides tunneling and the simplified beam surface building models, Goh [80] studied the response to braced deep excavations, in which buildings were modeled by simplified beams or frames. Two 2D plane strain finite element models were developed in Plaxis and Abaqus, respectively, where the model in Plaxis served as a preliminary study. In the Plaxis model, a total stress analysis was adopted using a linear-elastic perfectly plastic soil model associated with the Mohr-Coulomb failure criterion. This study using a simplified soil constitutive was carried out to simulate the state-of-the-practice in the industry. The soil was modeled by 15-node triangular elements, the retaining wall was modeled using plate elements, and multi-level brace struts were modeled by one-node elastic spring elements. Surface buildings were modeled by plate elements in a 2D plane-strain condition, and 5-node interface elements were used to model a similar soil-structure interface with the model in [68]. A sequential excavation is modeled by de-activating relevant soil clusters and activating the one-node spring models of brace struts. In the Abaqus model, the soft clay was modeled by the Modified Cam Clay model, and a linear elastic-perfectly plastic model was used to model the stiff soil layers. Plane strain solid continuum elements were used to model the retaining walls and brace struts, and surface buildings were modeled by 1D Timoshenko beam elements. The master-slave contact surface in Abaqus was adopted to model the soil-wall, soil-building, and strut-wall interfaces. The strut-wall interfaces were defined to resist penetration and relative sliding, while a non-penetration Coulomb friction model with a shear stress limit was adopted at soil-building and soil-wall interfaces. The sequential excavation was modeled by removing soil elements and corresponding soil-wall contact pairs, and then activating struts elements and corresponding strut-wall contact pairs. The time step for the excavation process was set to be very small so that an undrained condition could be simulated. It was shown that both the Plaxis model and Abaqus model produced reasonable predictions of greenfield displacements and building deflections, although the Plaxis model produced an unrealistic wall deflection shape in the first excavation stage. The linear-elastic perfectly plastic soil models in Plaxis caused wider surface displacement troughs than the Abaqus model, but the magnitude of maximum wall deflection and surface displacements were comparable.Frame buildings on continuous footings and individual footings modeled as rigid elastic beam-column frames were then studied. It was observed that frames might have a similar deflection ratio with an equivalent elastic beam, but the horizontal strain in framed buildings may be significantly different from the simplified beam models.

Another suite of numerical studies using the finite element modeling method was carried out by Burd et al. [23] and colleagues[153, 202]. One of their latest study [202] is reviewed here and later used to validate the 3D T&DE soil-structure analysis model developed in this dissertation (see Section 3.4). Instead of the simplified beam models in previously reviewed studies, masonry buildings founded on strip footings were modeled exactly by 3D walls and openings, and the six-node shell elements with five Gauss points (STRI65) in Abaqus were used. The foundation and the soil were modeled by ten-node tetrahedral solid elements (C3D10). The modeled soil was an 8 m layer of Terrace Gravel over London Clay. The extended Mohr-Coulomb model [46] was selected as the constitutive model for Terrace Gravel, and the multiple yield surface kinematic hardening model of Houlsby [92] was used to represent the undrained behavior of the London Clay. A concrete damaged plasticity model [109] built-in Abaqus was adopted to model the constitutive of masonry buildings. The soil-foundation interface was modeled to allow slip and opening by Coulomb's friction model with a friction coefficient of 0.3. The tunneling process was modeled by applying a prescribed displacement, which consisted of radial shrinkage combined with a rigid vertical movement at the tunnel perimeter. The surface buildings were modeled with fully coupled facade walls or independent walls, and the building response with a range of eccentricity and oblique angles were studied. It was observed that when the tunnel and building are perpendicular to each other, the fully coupled facade walls provide comparable analysis results with independent walls. However, the performance of skewed buildings needs further investigation. Moreover, the entire tunnel is simulated simultaneously and the progressive excavation effect was not studied.

The studies reviewed above are considered fully coupled analyses where the tunnel/deep excavation process and soil-structure systems are analyzed in one numerical model. Some other similar studies can be found in [76, 121, 131, 114, 4, 19]. It can be observed that a prescribed volume loss or displacement field is often needed to produce a realistic T&DE ground movement. The prescribed displacement field is usually derived from empirical analysis and this may undermine the complex models of tunneling/deep excavation. As an alternative, a two-stage approach can be adopted, in which the greenfield ground displacements are first estimated from experiments, empirical methods, or numerical analysis. The greenfield ground displacements are then applied on a soil-structure system and a new equilibrium state is solved. Several numerical studies using the two-stage analysis approach are reviewed here.

Son and Cording [173] applied the distinct element model using the software UDEC (Itasca Consulting Group Inc. 2000) to simulate the response of brick-bearing structures to deep excavations. In the distinct element method, the brick-bearing structure is represented as an assembly of distinct bodies. The brick/mortar contacts are viewed as interfaces between distinct bodies (i.e., the discontinuity is treated as a boundary condition). The contact forces and displacements at the interfaces of a stressed assembly of distinct bodies are found through a series of calculations that trace the movements of the distinct bodies. Movements of each brick block are determined from the propagation through the block system of disturbances caused by applied loads or body forces. The soil was modeled elastically with a stiffness selected to provide the same pressure/displacement relation with a physical test. Sliding friction of the foundations was considered by adjusting the properties of the interface between the building element and the soil mass element. The lateral and vertical displacement profile observed in a free-field physical model test was applied to the elastic soil mass beneath the model. The numerical analysis results were compared with physical test results, and it was shown that the numerical model produced very similar overall structure deformations, crack patterns, and crack width with the physical test.

In contrast to Son and Cording [173], Giardina et al. [78] used the continuum finite element method to model a masonry façade building. The brick units and mortar joints were represented as a single material with homogenized properties. Eight-node plane stress elements were used to model the masonry façade, and the coaxial rotating crack model and fixed crack model were adopted to model the constitutive of masonry. The façade behaves as a homogeneous isotropic linear elastic continuum before cracking, and it behaves as a non-linear orthotropic continuum with linear tension softening after cracking. Due to the softening behavior of quasi-brittle materials and the sudden release of elastic energy at cracks, convergence problems may arise if a conventional incremental-iterative scheme is used to solve the nonlinear equations. As a result, the sequentially linear analysis (SLA) method [39] was adopted to produce a robust numerical scheme. The soil-building interface, which was characterized by no-tension, as- signed stiffness in compression and negligible stiffness in shear was modeled with 6-node line interface elements. The greenfield ground displacement obtained in a physical model test [79] is applied at the soil-structure interface, and a physical model test is used to validate the numerical model. It was shown that the SLA method produces a robust algorithm for the simulation of brittle material, but both the conventional incremental-iterative scheme and SLA applied in the continuum FE approach can capture the crack pattern development in masonry reasonably well.

Another suite of numerical studies using the two-stage analysis approach was done by Andrea Franza, Matthew DeJong, and collaborators [63, 65, 62, 20], and much of this dissertation builds upon this suite of studies. The surface buildings were modeled with 1D simplified beams (mostly for low-rise bearing wall structures) or elastic beam-column frames (mostly for bare frame structures). Soils were modeled by a homogeneous half-space continuum represented with coupled springs. The soil-structure interaction effect was modeled as constraining surface structures to a homogeneous elastic continuum (the soil) through sliders that were rigid-perfectly plastic elements with upper and lower limit forces. The homogeneous elastic continuum was modeled by coupled vertical and horizontal springs that interact with each other. Slippage and gap formation were modeled by decoupled sliders in the horizontal and vertical directions, respectively. As a two-stage approach, the greenfield displacement fields due to tunneling/deep excavation were first evaluated with empirical methods or other numerical methods. The greenfield displacements were then applied to the soil springs and an elastoplastic equation was solved to find the structure deflection. This method was validated by a comparison with centrifuge tests [162, 200] and proved to be capable of predicting structure response to tunnel excavations.

Although a large volume of numerical study methods is proposed to predict building responses to T&DE, the numerical models may be subject to significant uncertainty in the estimation of building stiffness, soil stiffness, and other modeling parameters. More details of the uncertainties in the T&DE SSI process are discussed in Chapter 4, and one important part of this dissertation is to quantify the effect of these uncertainties in the assessment of building damage. In the next section, some common uncertainty quantification methods in civil engineering are reviewed.

2.3 A review of common uncertainty quantification methods

In structural engineering, especially earthquake engineering, loading is usually stochastic, and the modeling of material properties and boundary conditions usually experiences considerable uncertainty. In geotechnical engineering, significant uncertainties exist in limited site characterizations and the inherent random underground conditions. As a result, some recent regulatory and legal pressures force engineers to adopt uncertainty quantification methods to provide answers about the reliability of their designs and to facilitate the decision-making on whether to proceed with a project, how to finance it, and when to schedule it. To formally quantify the effect of the uncertainties and facilitate engineering decision-making, two groups of methods, i.e., reliability analysis methods and direct simulation methods, have emerged.

The common procedure of reliability analysis is: 1) establish an analytical model; 2) estimate statistical descriptions of the input parameters ($\mathbf{x}$); 3) calculate statistical moments of performance functions ($g(\mathbf{x})$); 4) calculate the reliability index; 5) estimate the probability of failure. The third step is considered to be the most difficult because engineering models in civil engineering are usually high-dimensional and nonlinear, which makes it hard to estimate the statistical properties of $g(\mathbf{x})$ from $\mathbf{x}$. The fourth step may also be controversial because reliability indices are usually problem-dependent and can not provide an absolute measure of failure probabilities. As a result, the direct simulation methods bypass steps 3 and 4 with Monte-Carlo methods, which are usually combined with surrogate modeling or reduced-order models to estimate the failure probabilities, and are considered more straightforward to use. Baecher and Christian [12] and Choi, Grandhi, and Canfield [33] summarized the most common reliability and simulation methods in geotechnical and structural engineering, respectively. A recent book published by Der Kiureghian [40] provided a more comprehensive discussion of reliability and direct simulation methods in structural and system engineering and presented many open-ended questions and opportunities to stimulate further research and development. The common reliability analysis techniques include First Order Second Moment methods (FOSM), the Hasofer-Lind approach (FORM), and the Second Order Reliability Method (SORM). The direct simulation methods are mostly based on Monte-Carlo methods combined with surrogate models, such as Polynomial Chaos Expansion (PCE) and Gaussian Process. A method that lies in between reliability and direct simulation methods is the Point Estimate Method (PEM) which may only provide a rough estimation of the failure probabilities. This section briefly reviews these common reliability analysis and direct simulation methods and summarizes their major advantages and disadvantages.

The first-order second-moment method (FOSM) starts from representing the performance function $g(\mathbf{x})$ by its Taylor series:

$$\begin{aligned} g(x_1, x_2, ..., x_n) = g(\mu_{x_1}, \mu_{x_2}, ..., \mu_{x_n}) &+ \frac{1}{1!}\sum_{i=1}^{n}(x_i - \mu_{x_i})\frac{\partial g}{\partial x_i} \\ &+ \frac{1}{2!}\sum_{i=1}^{n}\sum_{j=1}^{n}(x_i - \mu_{x_i})(x_j - \mu_{x_j})\frac{\partial^2 g}{\partial x_i \partial x_j} \\ &+ \frac{1}{3!}\sum_{i=1}^{n}\sum_{j=1}^{n}\sum_{k=1}^{n}(x_i - \mu_{x_i})(x_j - \mu_{x_j})(x_k - \mu_{x_k})\frac{\partial^3 g}{\partial x_i \partial x_j \partial x_k} \\ &+ ... \end{aligned} \tag{2.6}$$

where the partial derivatives $\frac{\partial g}{\partial x_i}$ are evaluated at the means μ_{X_1}, μ_{X_2}, ..., μ_{X_n}. Then, considering only the first order term gives:

$$g(x_1, x_2, ..., x_n) \approx g(\mu_{x_1}, \mu_{x_2}, ..., \mu_{x_n}) + \sum_{i=1}^{n}(x_i - \mu_{x_i})\frac{\partial g}{\partial x_i} \tag{2.7}$$

And the expectation and variance of $g(\mathbf{x})$ (μ_g and σ_g^2) can be approximated by:

$$\begin{aligned} \mu_g &\approx g(\mu_{x_1}, \mu_{x_2}, ..., \mu_{x_n}) + \sum_{i=1}^{n}\frac{\partial g}{\partial x_i}\int_{-\infty}^{+\infty}(x_i - \mu_{x_i})f_{x_i}(x_i)dx_i \\ &= g(\mu_{x_1}, \mu_{x_2}, ..., \mu_{x_n}) \end{aligned} \tag{2.8}$$

$$\begin{aligned} \sigma_g^2 &\approx E\left[\left(\sum_{i=1}^{n}(x_i - \mu_{x_i})\frac{\partial g}{\partial x_i}\right)^2\right] \\ &= \sum_{i=1}^{n}\sum_{j=1}^{n}\rho_{x_i x_j}\sigma_{x_i}\sigma_{x_j}\frac{\partial g}{\partial x_i}\frac{\partial g}{\partial x_j} \end{aligned} \tag{2.9}$$

$$\frac{\partial g}{\partial x_i} \approx \frac{1}{2\epsilon_i}g(\mu_{x_1}, \mu_{x_2}, ..., \mu_{x_i} + \epsilon_i, ..., \mu_{x_n}) - g(\mu_{x_1}, \mu_{x_2}, ..., \mu_{x_i} - \epsilon_i, ..., \mu_{x_n}) \tag{2.10}$$

where $f_{x_i}(x_i)$ is the probability density function of the i^{th} variable, and $\rho_{x_i x_j} = \frac{E[(x_i - \mu_{x_i})(x_j - \mu_{x_j})]}{\sigma_{x_i}\sigma_{x_j}}$, which is the Pearson correlation coefficient between x_i and x_j. All the partial derivatives are evaluated at the means of the individual variables, so each of the terms after the summation sign in Eq. 2.8 is identically zero.

In practice, the partial derivatives are usually found numerically by central differences as shown in Eq.2.10. And a reliability index, defined as $\beta = \frac{\mu_g}{\sigma_g}$ or $\beta = \frac{\mu_g - 1}{\sigma_g}$, can be calculated for margin of safety (e.g., $Resistance - Disturbance$) or factor of safety (e.g., $\frac{Resistance}{Disturbance}$), respectively. $\beta = \frac{\mu_g}{\sigma_g}$ describes the distance of margin of safety from zero and $\beta = \frac{\mu_g - 1}{\sigma_g}$ describes the distance of factor of safety from 1. A larger reliability index implies a smaller failure probability. However, different formulations of the factor of safety usually generate different values of β for the same problem. This inconsistency and the error caused by the first order approximation of the performance function are the major limitations of the FOSM. The numerical differentiation method in Eq. 2.10 has an error proportional to ϵ_i^2 (i.e., a second order accuracy) and may be numerically unstable. Higher order finite difference approximations for $\frac{\partial g}{\partial x_i}$ can be found in the first chapter of LeVeque [112], but more model ($g(\mathbf{x})$) evaluations are also needed for better accuracy. Additionally, a probability distribution function has to be assumed for $g(\mathbf{x})$ to estimate the probability of failure, while the FOSM does not provide any insight on what assumption should be made.

The Hasofer-Lind formulation (FORM) doesn't seek to find the statistical properties of the performance functions $g(\mathbf{x})$. It rather studies the probability of failure in the input variables domain. The first step in the FORM is to reformulate the problem with dimensionless variables. The Rosenblatt transformation [164] can be used to transform multivariate random variables $\mathbf{X} = (X_1, ...X_n)$ with CDF $F_{\mathbf{X}}(\mathbf{X})$ and PDF $f_{\mathbf{X}}(\mathbf{X})$ to a standard multivariate normal vectors $\mathbf{U}$ by Eq. 2.11. The probability of failure can be then estimated from the shaded area of Fig. 2.8. The design point $\mathbf{x}^*$ and $\mathbf{u}^*$ can be determined from the gradient descent or the iHL-RF algorithm [207], by minimizing the constraint minimization problem formulated in Eq. 2.12. In FORM, a first order Taylor's series approximation of the limit-state function is made at $\mathbf{u}^*$ as Eq. 2.13, and the probability of failure can be estimated from Eq. 2.14. When the second order of Taylor's series is adopted to approximate the limit-state function, the method is called Second Order Reliability Method (SORM), and the details can be found in [41] and [42]. The disadvantage of FORM and SORM is that the algorithm to find design points requires the estimation of the gradient of $g(\mathbf{x})$, which is generally infeasible when $g(\mathbf{x})$ is in a numerical form. Additionally, the approximation of the limit-state function as first-or second-order function may also introduce biases. Quasi-Monte Carlo method could be adopted to obtain an unbiased estimation of the probability of failure, although the computational cost could be much higher, and a direct simulation method may be preferred.

$$\begin{aligned}
U_1 &= \Phi^{-1}[F_1(X_1)] & X_1 &= F^{-1}[\Phi_1(X_1)] \\
U_2 &= \Phi^{-1}[F_{2|1}(X_2|X_1)] & X_2 &= F^{-1}[\Phi_{2|1}(X_2|X_1)] \\
&\vdots & &\vdots \\
U_n &= \Phi^{-1}[F_{n|1,\ldots,n-1}(X_n|X_1,\ldots,X_{n-1})] & X_n &= F^{-1}[\Phi_{n|1,\ldots,n-1}(X_n|X_1,\ldots,X_{n-1})]
\end{aligned} \tag{2.11}$$

$$\mathbf{u}^* = argmin\{||u|| \mid G(\mathbf{u}) = 0\} \tag{2.12}$$

$$\begin{aligned}
g(\mathbf{u}) &\approx G(\mathbf{u}^*) + \nabla G(\mathbf{u}^*)(\mathbf{u} - \mathbf{u}^*) \\
&= ||\nabla G(\mathbf{u}^*)||(\beta - \alpha \mathbf{u}) \\
&= \hat{\beta} - \hat{\alpha}\mathbf{u}
\end{aligned} \tag{2.13}$$

$$\begin{aligned}
P_F &\approx \int_{\hat{\beta}-\hat{\alpha}\mathbf{u}\le 0} \phi_n(\mathbf{u}) d\mathbf{u} \\
&= \Phi(-\hat{\beta})
\end{aligned} \tag{2.14}$$

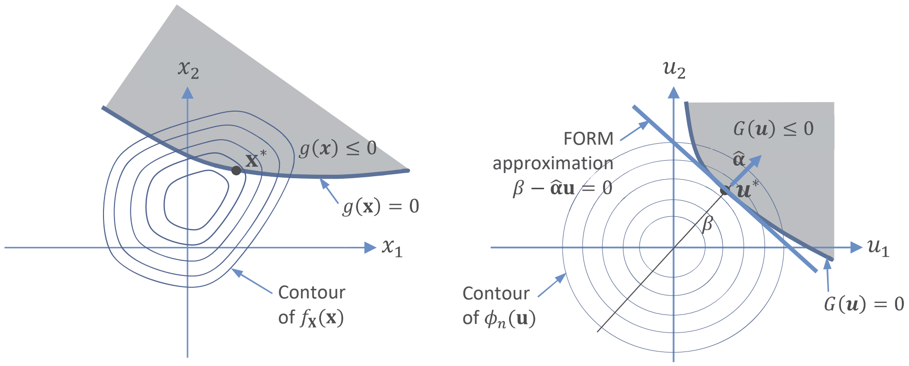

Figure 2.8: Probability of failure in original (left) and standard normal space (right) (after the class notes of Prof. Der Kiureghian).

The point estimate method (PEM) is considered a semi-simulation-based method and was first proposed by Rosenblueth [165], who approximates the continuous random variable $g(\mathbf{x})$ with its lower moments. Three cases are discussed by Rosenblueth [165], and the most common case is when $g(\mathbf{x})$ is a function of n variables whose skewness is zero but which may be correlated with each other. The procedure chooses 2^n points at the value of one standard deviation above or below the mean of each variable. The m_{th} moment of $g(\mathbf{x})$ can be approximated with Eq. 2.15, where s_i is +1 when the value of the i_{th} variable is one standard deviation above the mean and -1 if the variable is one standard deviation lower than the mean. The i in Eq. 2.3 is a combination of + and $-$, and x_i is the combination of variables with a value of one standard deviation above or lower than the mean. x_i is also called point coordinates. In this formulation, the number of point coordinates (2^n) may still be too large. Two relatively simpler methods [85][91][90] have been proposed to reduce the number of points in the general case to $2n$ or $2n+1$. Hong [90] also dealt with the problem of uncorrelated variables with significant skewness. The PEM bypasses the estimation of partial derivatives in the FOSM and provides an accurate estimate of the moment of $g(\mathbf{x})$ for low-dimension small skewness variables. However, two points may not be adequate to obtain accurate estimates of the moments of $g(\mathbf{x})$, and Harr [85] observed that only the estimation of the first two moments of $g(\mathbf{x})$ can be considered reliable.

$$P_{s_1 s_2 \ldots s_n} = \frac{1}{2^n}\left[1 + \sum_{i=1}^{n-1}\sum_{j=i+1}^{n}(s_i)(s_j)\rho_{ij}\right] \tag{2.15}$$

$$E[g(\mathbf{x})^m] = \sum P_i(g(\mathbf{x_i}))^m \tag{2.16}$$

When there are many input random variables in $\mathbf{x}$ (often called high-dimensional uncertainty quantification) or the performance function $g(\mathbf{x})$ is strongly non-linear, direct simulation using Monte-Carlo (MC) methods may be considered the most accurate method to estimate the failure probability, especially when no explicit form of $g(\mathbf{x})$ is available. The advantage of MC methods is that their convergence rates are generally independent with the dimension of $\mathbf{x}$. That is, increasing the number of stochastic input variables does not increase the number of runs for the same level of accuracy. However, the computation cost is still expensive and hundreds or thousands of simulation runs are usually required to achieve reasonable accuracy. When an approximation of the PDF of $g(\mathbf{x})$ can be made, the importance sampling method can be adopted to accelerate the convergence of the MC method, especially when a small failure probability is being estimated. The stratified sampling or Latin Hypercube Sampling method (one type of quasi-Monte Carlo method) can also be adopted to increase the efficiency of the Monte Carlo methods. More discussion of MC methods can be found in Section 4.4.

Monte Carlo methods are often infeasible when large numerical models are used in the analysis and the model evaluation time is long. Surrogate models can be adopted to alleviate this problem. One of the common surrogate models is Polynomial Chaos Expansion (PCE) based surrogate model, where the performance function $g(\mathbf{x})$ is approximated as Eq. 2.17, in which Ψ_j are orthogonal polynomials and $\boldsymbol{\xi}$ are the random variables used to represent the multivariate distribution of $\mathbf{x}$ trough a transformation $\mathbf{x} = \mathbf{T}(\boldsymbol{\xi})$. For example, it is usually convenient to select $\boldsymbol{\xi}$ as multivariate normal variables, such that $\boldsymbol{\xi} = \mathbf{U}$ in Eq. 2.11 and $\mathbf{T}$ stands for the Rosenblatt transformation from X_i to U_i. The selection of the type of polynomials depends on the type of random variables

$\boldsymbol{\xi}$, and a comprehensive survey is done in [199]. The coefficients b_j can be determined from the projection method or regression method. For the projection method, the orthogonal property of Ψ is utilized and b_j can be estimated by $b_j = \frac{E[g(\mathbf{x})\Psi_j]}{E[\Psi_j^2]}$. The numerator and denominator can be estimated with the Gaussian quadrature scheme, as discussed by Le Maitre et al. [108], Matthies and Keese [124] and Berveiller, Sudret, and Lemaire [17]. For the regression method, the numerical model being analyzed is evaluated at experimental design points. The coefficients b_j are estimated by minimizing the mean squared error between the value predicted by Eq.2.17 and deterministic evaluated by the numerical model. Sudret [182] introduced an optimal experimental design, in which the number of model evaluations required to obtain accurate b_j is significantly reduced.

$$g(\mathbf{x}) \approx \sum_{j=0}^{P-1} b_j \Psi_j(\boldsymbol{\xi}), \qquad \boldsymbol{\xi} = \{\xi_1, \xi_2, ..., \xi_M\} \tag{2.17}$$

Another common type of surrogate model is Gaussian Process, which is also referred to as Kriging in some geostatistics literature. In this method, the performance function $g(\mathbf{x})$ is approximated with a surrogate model $\hat{g}(\mathbf{x})$ that is a realization of a Gaussian Process, as denoted in Eq. 2.18. In Eq. 2.18, $\mu(\mathbf{x})$ is a trend function, which is often taken as polynomials, $\kappa(\mathbf{x}, \mathbf{x}')$ is a positive definitive covariance function ($\mathbf{x}'$ stands for the transpose of $\mathbf{x}$), which is usually chosen from linear, cubic, spline, and Matérn covariance functions, and θ is a set of parameters describing $\mu(\mathbf{x})$ and $\kappa(\mathbf{x}, \mathbf{x}')$. Similar to the regression method in PCE-based surrogate modeling, the parameters θ are estimated by generalized least squares [135] on a training set $\{(\mathbf{x_i}, g(\mathbf{x_i})), i = 1, 2, ..., d\}$. To use $\hat{g}(\mathbf{x})$ to predict $\mathbf{y}^* = g(\mathbf{x}^*)$, the definition of Gaussian Process gives the joint distribution of $\mathbf{y}$ and $\mathbf{y}^*$ as Eq. 2.19,and the conditional distribution of $f_{\mathbf{y}^*}(\mathbf{y}^*|\mathbf{y})$ can be calculated with Eq. 2.20. The mean value of $f_{\mathbf{y}^*}(\mathbf{y}^*|\mathbf{y})$ is usually taken as the point estimator for $\mathbf{y}^*$. It can be observed that the Gaussian Process surrogate models provide not only point estimators but also a confidence measure because the prediction y^* follows a multinormal distribution (see Eq. 2.20a). As a result, experiment points (training data set) can be selected adaptively according to the confidence interval of y^*, and this adaptive experiment design is often called an active learning strategy [49, 195].

$$\hat{g}(\mathbf{x}) \sim GP(\mu(\mathbf{x}), \kappa(\mathbf{x}, \mathbf{x}')|\theta), \text{where} \tag{2.18a}$$

$$\mu(\mathbf{x}) = \mathbf{E}[\hat{g}(\mathbf{x})] \tag{2.18b}$$

$$\kappa(\mathbf{x}, \mathbf{x}') = \mathbf{E}[(\hat{g}(\mathbf{x}) - \mu(\mathbf{x}))(\hat{g}(\mathbf{x}') - \mu(\mathbf{x}'))] \tag{2.18c}$$

$$\begin{pmatrix} \mathbf{y} \\ \mathbf{y}^* \end{pmatrix} \sim \mathbf{N}\left[\begin{pmatrix} \mu(\mathbf{y}) \\ \mu(\mathbf{y}^*) \end{pmatrix}, \begin{pmatrix} \kappa(\mathbf{x}, \mathbf{x}') & \kappa(\mathbf{x}, \mathbf{x}^{*\prime}) \\ \kappa(\mathbf{x}, \mathbf{x}^{*\prime})^T & \kappa(\mathbf{x}^*, \mathbf{x}^{*\prime}) \end{pmatrix}\right] \tag{2.19}$$

$$f_{\mathbf{y}^*}(\mathbf{y}^*|\mathbf{y}) = \mathbf{N}(y^*|\mu_{y^*}, K_{y^*}) \tag{2.20a}$$

$$\mu_{y^*} = \mu(\mathbf{x}^*) + \kappa(\mathbf{x}, \mathbf{x}^{*\prime})^T \kappa(\mathbf{x}, \mathbf{x}^{*\prime})^{-1}(\mathbf{y} - \mu(\mathbf{x})) \tag{2.20b}$$

$$K_{y^*} = \kappa(\mathbf{x}^*, \mathbf{x}^{*\prime}) - \kappa(\mathbf{x}, \mathbf{x}^{*\prime})^T \kappa(\mathbf{x}, \mathbf{x}^{*\prime})^{-1} \kappa(\mathbf{x}, \mathbf{x}^{*\prime}) \tag{2.20c}$$

There are many other types of surrogate models, especially data-driven and machine learning-based methods, such as Support Vector Machine [178], Artificial Neural Network [141], etc. A comprehensive survey can be found in [150]. The above-mentioned methods consider the structure/geotechnical analysis models as black boxes and evaluate the models repetitively to estimate quantities of interest. As a result, they are often referred to as non-intrusive methods. Another group of methods may change the formulation of the numerical models and are often referred to as intrusive methods. Some intrusive surrogate modeling methods are spectral stochastic finite element methods (SFEM) [72] and some reduced-order modeling methods [13, 115, 15].

2.4 Uncertainty analyses and probabilistic modeling in tunneling and deep excavation

Despite the fast development of uncertainty quantification methods and the widely recognized fact that building damage assessment in T&DE using either empirical or numerical methods may experience significant uncertainty, the number of studies that formally quantified the uncertainty in T&DE is very limited. Some existing studies in this area are reviewed.

Boone [21] reported the probability distribution of tunnel V_L, face pressures, and injected grout volume recorded in tunnels driven in Singapore and Toronto. It was argued that current building damage assessments are significantly based on discrete assumptions on ground behavior and workmanship. However, quantitatively evaluating risks, being the probability that a building damage event will occur, through stochastic modeling may be the most "technically sound" approach to project decision-making. A case study of tunneling in urban areas was presented to demonstrate the stochastic modeling approach. Uncertainties in ground loss and soil proprieties were modeled with random variables, and the crude Monte Carlo method was used to estimate building damage probabilities, where building damage in each MC realization was estimated with a strain superposition method (similar to the method in the second stage assessment described in Section 2.1 but with a more detailed ground displacement analysis). Although the uncertainty models and the soil-structure interaction models were relatively simple, a comparison between deterministic and stochastic modeling showed that stochastic analyses allowed the use of realistic tunneling performance estimates, based on measured data, to determine the probability of structures suffering different categories of damage. The stochastic modeling approach also avoided either overemphasizing potential damage if lower-bound (or conservative) soil parameters were used or the possibility that, if average or upper-bound soil parameters were used, significant risks of damage might be overlooked. This research shows a promising application of uncertainty quantification in the building damage assessment in urban T&DE.

Hsiao et al. [93] applied the FORM method to assess building serviceability under excavation-induced ground settlements. The maximum ground surface settlement δ_{vm} was selected as an indicator to assess the excavation-induce building damage potential (load or impact), and the tolerable limit of δ_{vm} was considered as the resistance. Both the load and resistance were modeled as random variables, where the statistics of the load were estimated from a semiempirical model KJHH[105] using random input variables, and the probabilistic limiting tolerable settlement proposed by Zhang and Ng [205] was adopted to measure the resistance. In this study, a comprehensive uncertainty modeling of input parameters, e.g., mean and coefficients of variation for soil shear strength and stiffness, was performed, but the soil-structure interaction effect was not considered. Moreover, an accurate estimation of building damage probability was not available due to the limitation of the FORM method.

Castaldo, Calvello, and Palazzo [32] studied the damage probability of a historic building adjacent to an open-pit excavation in Naples (Italy) with the point estimation method. A 2D finite element model in Plaxis was used to estimate the ground deformation. The soil-structure interaction effect was not considered and the surface building was modeled as a uniform distributed load on the ground. The heterogeneous soil layers were modeled and the hardening-soil H-S model in Plaxis was adopted to model the non-linear soil constitutive relationship. Three variables, which describe the permeability, secant stiffness, and friction angle of soils, are considered uncertain and quantified with their mean values and standard deviations. Due to the large computation cost, the point estimation method was selected for uncertainty forward propagation, and eight model evaluations were carried out. Bivariate lognormal distribution of horizontal strain and deflection ratio was estimated from the eight data points using the maximum likelihood method. Probabilities of each damage state were then calculated according to the interactive design diagrams (Fig. 2.3). Although the point estimation method may be biased and the soil-structure interaction effect was neglected, this research is one of the earliest to quantify building damage probability using a simulation-based method. Similar to Castaldo, Calvello, and Palazzo [32], Franco, Gitirana, and Assis [60] adopted a hybrid point estimation method and fully coupled finite element to quantify the damage probability of a frame building under the impact of an adjacent tunnel. The soil-structure interaction effect was considered in a 3D FE model, which is more accurate than Castaldo, Calvello, and Palazzo [32]. However, the possible error associated with the point estimation method in uncertainty propagation might undermine the effort of the 3D FE model.

El Kahi et al. [50] and Obel, Ahrens, and Mark [141] adopted the crude Monte Carlo method and surrogate models for the uncertainty quantification. Both researches studied the soil-structure interaction using 2D FE models. Based on the 2D FE analysis, a simplified analytical model is proposed in [50] to relate relative soil-structure stiffness with deflection ratio. The simplified model was used as a surrogate in later probabilistic analysis. In [141], an Artificial Neuron Network (ANN) surrogate model was developed based on a training set of 500 evaluations of a 2D FE tunnel-soil-structure interaction model. However, the ANN introduces additional model uncertainty, which is hard to be quantified, and the generation of training and testing data sets was also very time-consuming.

Camós et al. [31] proposed the probabilistic model of building damage due to tunneling considering a 3D ground movement profile. The ground movements were estimated with a set of empirical equations. The surface building was modeled by a 1D equivalent beam, and the soil-structure interaction mechanism was neglected. The principal strain in the building was calculated by imposing the ground displacement on the equivalent beam, which requires the evaluation of a set of analytical and empirical equations. As a result, the computational cost was very small, and the crude Monte Carlo method was adopted to estimate the probability of the principal strain exceeding the damage state limiting strains. The uncertainty in tunnel trough width, tunnel volume loss, building stiffness, and modeling errors was studied. Despite the model's simplicity, the progressive tunnel construction was considered by the 3D ground movement model. Moreover, methods were proposed to update the estimated building damage probability using the settlement measured from early tunnel excavation stages.

Through the review of current uncertainty quantification (UQ) and probabilistic modeling of T&DE SSI, it is found that the current studies can not fit in the early stage and large scale assessment of the staged assessment approach discussed in Section 2.1 because the adopted model fidelity is either too low (e.g., in [21, 93, 31]) such that the soil-structure interaction mechanisms are not captured, or too "high" (e.g., in [32, 50, 141]) such that the UQ can not be completed within a reasonable modeling and computation effort. The research in [32, 50, 141] provides a method to quantify the assessment uncertainty for individual buildings in later stages (e.g., the third stage in Section 2.1). Another limitation of the current probabilistic T&DE SSI modeling is that spatial variability, which is one of the most important uncertainties in underground engineering [57, 206], is not considered. As a result, this dissertation aims to 1) propose T&DE soil-structure interaction analysis methods that minimize assessment uncertainty without significantly increasing modeling effort, and 2) improve the quantification of the uncertainty in the assessment to facilitate engineering decision-making.

Chapter 3

Modeling surface structure response to tunneling and deep excavations

A two-stage approach is adopted to study the behavior of surface structures in tunneling and deep excavations. Because the presence of surface structures usually has a slight effect on the behavior of tunnel lining and deep excavation support systems, the first stage analyzes tunnels and deep excavations without considering the surrounding structures. Ground movement fields can be evaluated from the first stage analysis, and then applied as a displacement boundary condition on surface structures. The two-stage approach is simple and has been proven accurate in many soil-structure interaction studies. [103, 111, 63, 65]. The two-stage approach consists of modeling the tunneling or deep excavation-induced ground movements, modeling surface structures, and modeling the soil-structure interaction effects. The three components of the two-stage approach and a damage analysis method to quantify building damage are described in this chapter. The two-stage approach is initially implemented in a computer program named Analysis of Structure Response to Excavations (ASRE) by Franza and DeJong [63] and Franza, Ritter, and DeJong [65], and the extensions of the program to more versatile soil-structure systems and a 3-dimensional version (ASRE 3D) are presented in this chapter. Specifically, `ASRE` is extended from tunnel-structure analysis to deep excavation-structure analysis by implementing a deep excavation-induced ground movement model (see Section 3.1.2) in `ASRE`. The 2D beam-column structure model is extended to simulate buildings with a larger variety of structure and footing configurations. Most of all, a 3D version `ASRE3D` is developed, which consists of the implementation of a 3D ground displacement model (Section 3.1.1), a 3D solid model for bearing wall structures (Section 3.2), and a 3D soil-structure interface (Section 3.3).The deterministic models `ASRE` and `ASRE3D` form the soil-structure analysis part of the proposed probabilistic assessment framework (Chapter 4) and the uncertainty quantification soil-structure interaction program `UQ-TESSI` (Chapter 5).

3.1 Modeling tunneling- and deep excavation-induced ground movements

Two types of ground movements are studied: (1) ground movements induced by tunnel boring machines (TBM tunnels), and (2) ground movements induced by braced deep excavations. The methods to model 2D and 3D settlement profiles are discussed in this chapter. The ground movements discussed in this chapter are "greenfield" ground movements, which correspond to the ground movements when no structures are present on top of the interested areas. It is widely recognized that the presence of structure may modify the surface ground movements through the soil-structure interaction effect, which will be discussed in Section 3.3.

3.1.1 Tunneling-induced ground movements

In current tunnel engineering, as reviewed in Section 2.1, greenfield ground movements are used as the starting point of the assessment. The ground movements for the greenfield condition, i.e., assuming no structures are present, can be estimated by empirical methods (e.g.,[64, 119, 140, 192]), analytical methods (e.g.,[144, 113, 190]), and numerical methods (e.g., [101, 132, 133, 184]). O'Reilly and New [140] summarized a large number of site monitoring data and proposed that the vertical ground settlement profile can be approximated by a Gaussian curve defined by the maximum settlement S_{max} and a width parameter i (see Eq.3.1). i describes the distance from the tunnel axis to the inflection point of the Gaussian settlement profile and is approximated as a linear function of the tunnel depth (see Eq. 3.2). Mair et al. [119] modified the formulation of the Gaussian curve and proposed to use volume loss (V_L) and width parameter (K) to define the settlement profile (Eq. 3.3). Fig. 3.1 is a plot of the Gaussian curve and the definition of terms used to describe the coordinate systems in Eq. 3.1 - Eq. 3.12. Volume loss is defined by the ratio of the ground subsidence volume to the excavation volume as shown by Eq. 3.5, and the relationship between S_{max} and V_L is also derived (Eq. 3.6). Mair et al. [119] also studied data both in the UK and worldwide and argued that K could be taken as 0.5 for practical purposes of tunnels primarily excavated in clay. While Vorster et al. [192] observed the settlement profile of sandy soils may be considerably different from that in clay and proposed a modified Gaussian curve (Eq. 3.8), where a is an additional fitting parameter with respect to the standard Gaussian curve. The relationship between V_L and K has been studied extensively with centrifuge experiments, [192, 122, 54, 83]. It was found that in dry sand, the trough width K decreases as the tunnel volume loss increases, while in clay, the trough width is independent of the magnitude of tunnel volume loss. Grant and Taylor [83] reported the shape and width of the settlement trough over a range of volume losses between 2% to 20% in clay, and the tunnel width and trough shape didn't change with an increasing volume loss. For clays, O'Reilly and New [140] also provided a relationship (Eq. 3.10) to calculate the horizontal displacements from V_L and K. This relationship is proposed based on the assumption that the soil displacement vectors point directly toward the center of the tunnel axis and the trough width parameter K is a constant along the depth as suggested in [83]. Based on these assumptions, the vertical and horizontal displacement at the subsurface level (z meters below ground surface) can be calculated in Eq. 3.9 and Eq. 3.10. Fig. 3.2depicts the assumptions of the orientation of soil displacement vectors and the settlement trough at and below the ground surface.

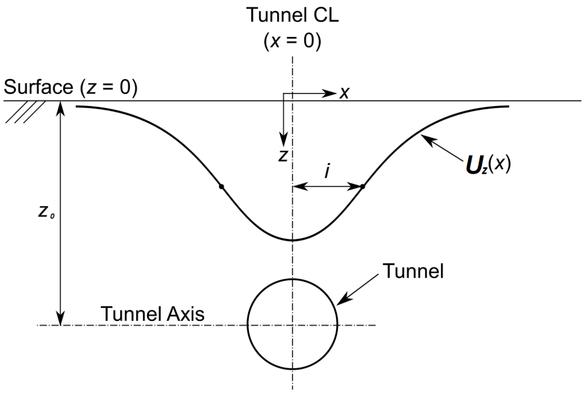

Figure 3.1: Vertical greenfield surface displacements described by a Gaussian curve, after [160]

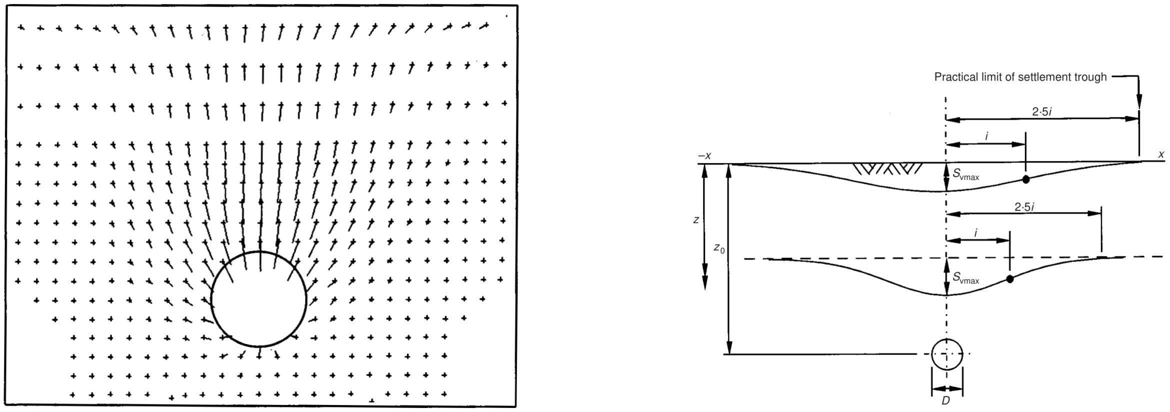

(a) Vectors of ground movement in a centrifuge test of a tunnel in clay, after [83]

(b) Tunnel settlement trough at the ground surface and below ground surface, after [83]

Figure 3.2: Tunneling induced ground movements

Analytical solutions assuming shallow tunnel and elastic soil constitutive relationships are widely researched, which can mainly be classified into two categories: superposition of singularities [166, 190, 144, 154] and exact solutions of movement using complex variable method [69, 189, 179, 191, 208]. It is observed that elastic solutions can adequately estimate greenfield ground movement for tunnels in clay, while it sometimes overestimates the ground movement and trough width [113]. Gonzalez and Sagaseta [82] took the compressibility of soil into account and developed an elastoplastic solution for shallow tunnels. To simplify the analytical solutions, some semi-empirical or semi-analytical solutions were also developed. Loganathan and Poulos [113] modified the Gaussian curve proposed by Mair, Taylor, and Bracegirdle [119] by adding terms to calibrate the ground movements caused by the ovalization of the excavation shape. Franza and Marshall [64] used centrifuge test results to calibrate the elastic solution of Verruijt and Booker [190] by two corrective parameters corresponding to vertical and horizontal ground movement, respectively.

Finite element methods [132, 101, 184] and finite volume methods [134, 133] are the two most commonly adopted numerical methods to estimate tunneling-induced ground movements. Although analytic and numerical solutions are validated with experimental and field observations, they are generally not applied in engineering practice, especially in regional analyses, due to 1) the complexity of the model is usually not affordable for large-scale simulations, and 2) the large uncertainty in the calibration of modeling parameters, such as tunnel face pressures and small strain soil stiffness, may undermine the complex model. Moreover, as reviewed in Section 2.2, an empirically estimated artificial displacement field needs to be applied at the tunnel-soil interface to simulate the displacement around the TBM lining in many numerical analysis approaches (e.g., [45, 134, 209]), which again undermines the efficiency of large-scale numerical models. As a result, the empirical method [120], in which the settlement trough is approximated by a Gaussian curve, is the most commonly adopted in the industry to estimate the ground movements induced by tunneling in soft clays. This method, as shown by Eq. 3.9 - Eq. 3.12, has been proven to be simple yet accurate in multiple existing soil-structure interaction research using the two-stage elastoplastic analysis method adopted in this research [65, 62, 63]. In Eq. 3.9 - Eq. 3.12, u_z is the vertical displacement, u_x is the horizontal displacement in the direction transverse to the tunnel axis, x is the horizontal distance of a point on the trough to the tunnel axis, $u_{z,max}$ is the maximum settlement, z_t is the depth of tunnel axis, K is the surface width parameter, R is the tunnel radius, V_L is the tunnel volume loss and i is the horizontal distance of the trough inflection point to the tunnel center line.

$$u_z = S_{max}\exp(-x^2/2i^2) \tag{3.1}$$

$$i = 0.43z_0 + 1.1 \tag{3.2}$$

$$u_z(x,z) = \frac{0.313V_LD}{Kz_0}\exp(-x^2/2(Kz_0)^2) \tag{3.3}$$

$$i = K(z_0 - z) \tag{3.4}$$

$$V_L = \frac{4V_s}{\pi D^2} \tag{3.5}$$

$$\frac{\pi D^2 V_L}{4} = \sqrt{2\pi} i S_{max} \tag{3.6}$$

$$u_z = u_{z,max}\frac{n}{n-1+\exp[a(x/i)^2]} \tag{3.7}$$

$$n = e^a\frac{2a-1}{2a+1}+1 \tag{3.8}$$

$$u_z(x,z) = -u_{z,max}\exp(-\frac{x^2}{2i^2}) \tag{3.9}$$

$$u_x(x,z) = \frac{u_z x}{z_0 - z} \tag{3.10}$$

$$i = K(z_0 - z) \tag{3.11}$$

$$u_{z,max} = 1.25R^2V_L/(100i) \tag{3.12}$$

When the 3-dimensional ground movements need to be considered, the model proposed by Attewell [9] and O'Reilly and New [140], and later summarized by Camós and Mollin [29] can be adopted. The coordinate of a typical tunnel and building position is defined in Fig. 3.3, where the z-axis is defined to be vertically upward. The Gaussian profile [148, 9, 140] is used to model the vertical ground displacement (u_z) at each cross section perpendicular to the tunnel axis, and u_z at any position with coordinates x, y, z can be calculated with Eq. 3.13

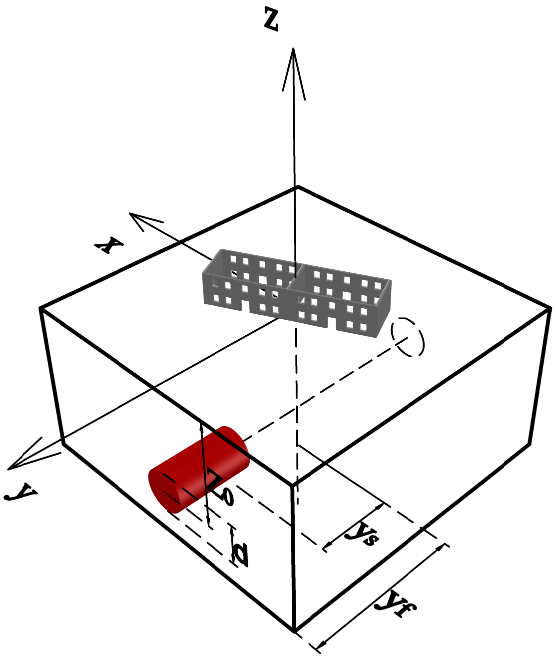

Figure 3.3: 3 dimensional tunnel and building coordinate system.

$$\begin{aligned} u_z(x,y,z) = & -u_{z,max} \cdot \exp\left[-\frac{x^2}{2K_x^2(z_0-z)^2}\right] \\ & \cdot \left[\Phi\left(\frac{y-(y_s+y_0)}{K_y(z_0-z)}\right) - \Phi\left(\frac{y-y_f}{K_y(z_0-z)}\right)\right] \end{aligned} \tag{3.13a}$$

$$u_{z,max} = \frac{\pi V_L d^2}{4\sqrt{2\pi}K_x(z_0-z)} \tag{3.13b}$$

$$y_0 = -\Phi^{-1}(\delta)Kz_0 \tag{3.13c}$$

Where $u_{z,max}$ is the magnitude of maximum settlement, d is the tunnel diameter, z_0 is the depth of the tunnel axis, y_f and y_s are the distances from the origin to the tunnel portal and tunnel face. $\Phi(\cdot)$ stands for the standard normal cumulative distribution function. V_L is the ground volume loss given in percentage, K_x and K_y are non-dimensional trough width parameters in x and y directions. V_L is the ratio of the area enclosed by the settlement profile and tunnel cross-section area when $y_s \to -\infty$, and K_x and K_y are defined as the ratio of distances from trough inflection points to the origin in the x and y directions over tunnel axis depth. In this study, $K_x = K_y = K$ is assumed, as suggested by Attewell [9]. y_0 is the distance from tunnel face to the point that $0.5u_{z,max}$ occurs, and can be calculated with Eq. 3.13c [29], where δ is the ratio between the surface settlement above the tunnel face and $u_{z,max}$. δ is taken as 0.3 in this dissertation, following the suggestion in [31]. The 3D ground movement model is implemented in ASRE3D.

The horizontal ground displacement model created in [140] (Eq. 3.14) is adopted to estimate u_x and u_y. If other greenfield ground displacement models, for example, the model proposed for twin tunnels[148, 119], are needed, they can be readily applied in the two-stage model in this study.

$$u_x = \frac{x}{z_0-z}u_z \tag{3.14a}$$

$$u_y = \frac{V_L d^2}{8(z_0-z)} \cdot \left[\exp\left(\frac{-(y-(y_s+y_0))^2-x^2}{2K_y^2(z_0-z)^2}\right) - \exp\left(\frac{-(y-y_f)^2-x^2}{2K_y^2(z_0-z)^2}\right)\right] \tag{3.14b}$$

In both 2D and 3D ground movement models, Volume loss (V_L) is an important parameter that describes the ground settlement curve and is defined by the ratio of soil subsidence volume and tunnel excavation volume. When Eq. 3.9 is used to estimate ground movement, V_L is equal to the ratio of the area enclosed by the Gaussian curve and the area of the tunnel cross-section. The value of V_L in clay mainly depends on construction techniques, workmanship, and underground conditions of the tunnel, and is commonly in the range of 0.5 to 1.5%. Despite that V_L is a vital parameter, it shows a large uncertainty in existing tunnel projects, e.g., [27, 74, 116]. K defines the tunnel trough width and mainly depends on soil type and underground condition. In clay, K can be approximated as 0.5 [119], although significant scatter and uncertainty are also observed in several case studies [118]. Therefore, in the analysis of SSI of TBM tunnels, the uncertainty associated with V_L and K are the major sources of uncertainty in greenfield ground movements prediction and the probabilistic modeling methods will be discussed later in Section 4.2 to quantify the uncertainty.

3.1.2 Deep excavation-induced ground movement

The ground movement prediction in deep excavation is generally more complicated than that in tunneling cases due to variance supporting and construction techniques adopted in deep excavations. Finite-element-method is often used to model complex deep excavation systems, especially brace-supported or soil-anchor tied diaphragm wall or sheet pile wall systems. However, existing studies [197, 196, 95, 88, 175] indicate the prediction of ground settlement using FEM may be biased due to the difficulty of modeling the soil behavior at small strain correctly. This is mainly because the soil behind the walls in braced excavation systems is often difficult to be surveyed [105], and the stress-strain relationship at a small strain of geomaterials is hard to be simulated in FEM analysis. Although FEM may be inaccurate in predicting ground settlement profile, it is proven reliable in the prediction of the deflection of the braced walls [196, 95]. Therefore, in engineering practice, the following 4 steps incorporating FEM and empirical methods are commonly used in the analysis of excavation-induced ground movements:

1. Estimate the maximum lateral wall deflection δ_{lm}.
2. Estimate the vertical deformation ratio R_v ($=\delta_{vm}/\delta_{lm}$).
3. Estimate the horizontal deformation ratio R_h ($=\delta_{hm}/\delta_{lm}$).
4. Calculate the maximum surface settlement δ_{vm} and δ_{hm}.
5. Estimate the surface settlement profile.

where the terms are defined in Fig. 3.4.

For braced excavations, a concave-shaped ground displacement profile is usually adopted. Hsieh and Ou [94] proposed a method to estimate the vertical ground settlement profile Eq. 3.15. Hsieh and Ou [94]'s ground profile is derived based on a regression analysis of 10 case studies and might be biased due to a small sample size. Kung et al. [105] therefore extended the regression analysis by including more case studies and a suite of artificial scenarios analyzed with the finite element method. The vertical ground displacement profile revised by Kung et al. [105] is shown in Eq. 3.16. Based on regression analysis, Kung et al. [105] also proposed empirical equations to estimate the maximum horizontal wall deflection (δ_{hm}) and the deformation ratio (R_v) between δ_{vm} and δ_{hm} (i.e., $R_v = \frac{\delta_{vm}}{\delta_{hm}}$). The empirical equations (also referred to as the KJHH model) estimate δ_{hm} and δ_{vm} based on the dimensions of the excavation system, the soil shear strength, the soil elastic modulus, the soil effective stress, the support system stiffness and the depth to hard stratum. A comparison of Hsieh and Ou [94] and Kung et al. [105]'s settlement profile is shown in Fig. 3.5a.

Schuster et al. [171] studied the lateral displacement induced by deep excavation using the same finite element model as developed by Kung et al. [105]. A horizontal ground displacement (δ_l) profile (Eq. 3.17) and empirical equations to estimate the lateral deformation ratio ($R_l = \frac{\delta_{lm}}{\delta_{hm}}$) are proposed. The parameters used to estimate R_l are identical to the parameters used in the KJHH model, and the empirical equation is referred to as KSJH model.

$$\delta_v(d) = (\frac{d}{H_e} + 0.5)\delta_{vm} \qquad 0.0 < \frac{d}{H_e} \leq 0.5 \tag{3.15a}$$

$$\delta_v(d) = (-0.6\frac{d}{H_e} + 1.3)\delta_{vm} \qquad 0.5 < \frac{d}{H_e} \leq 2.0 \tag{3.15b}$$

$$\delta_v(d) = (-0.05\frac{d}{H_e} + 0.2)\delta_{vm} \qquad 2.0 < \frac{d}{H_e} \leq 4.0 \tag{3.15c}$$

$$\delta_v(d) = (1.6\frac{d}{H_e} + 0.2)\delta_{vm} \qquad 0.0 < \frac{d}{H_e} \leq 0.5 \tag{3.16a}$$

$$\delta_v(d) = (-0.6\frac{d}{H_e} + 1.3)\delta_{vm} \qquad 0.5 < \frac{d}{H_e} \leq 2.0 \tag{3.16b}$$

$$\delta_v(d) = (-0.05\frac{d}{H_e} + 0.2)\delta_{vm} \qquad 2.0 < \frac{d}{H_e} \leq 4.0 \tag{3.16c}$$

$$\delta_l(d) = (1.6\frac{d}{H_e} + 0.2)\delta_{vm} \qquad 0.0 < \frac{d}{H_e} \leq 0.5 \tag{3.17a}$$

$$\delta_l(d) = (-0.6\frac{d}{H_e} + 1.3)\delta_{vm} \qquad 0.5 < \frac{d}{H_e} \leq 2.0 \tag{3.17b}$$

$$\delta_l(d) = (-0.05\frac{d}{H_e} + 0.2)\delta_{vm} \qquad 2.0 < \frac{d}{H_e} \leq 4.0 \tag{3.17c}$$

The KJHH and KSJH models are considered an appropriate method to estimate ground displacement profiles for the early assessment stage in deep excavations because δ_{hm}, δ_v and δ_l can be approximated without much complex modeling of the excavation system. This leads to a simple analysis procedure, although some uncertainty is introduced due to the variance and possible bias of the regression analyses. The implementation of the KJHH and KSJH models to assess SSI mechanisms and associated uncertainties are discussed in Section 4.2.1. Empirical equations to estimate R_v and R_l from soil condition, excavation geometry, and support stiffness are studied in the KJHH model [105] and the KSJH model [171]. They consist of a complete estimation procedure that links horizontal wall deflection to vertical and lateral ground movement profiles. Moreover, the model uncertainty of the KJHH and KSJH are well documented, so the influence of their uncertainty on building damage is ready to be analyzed. However, the ground displacement profiles in both models are described discretely with 4 pivot points (A-D as shown in Fig. 3.5), and

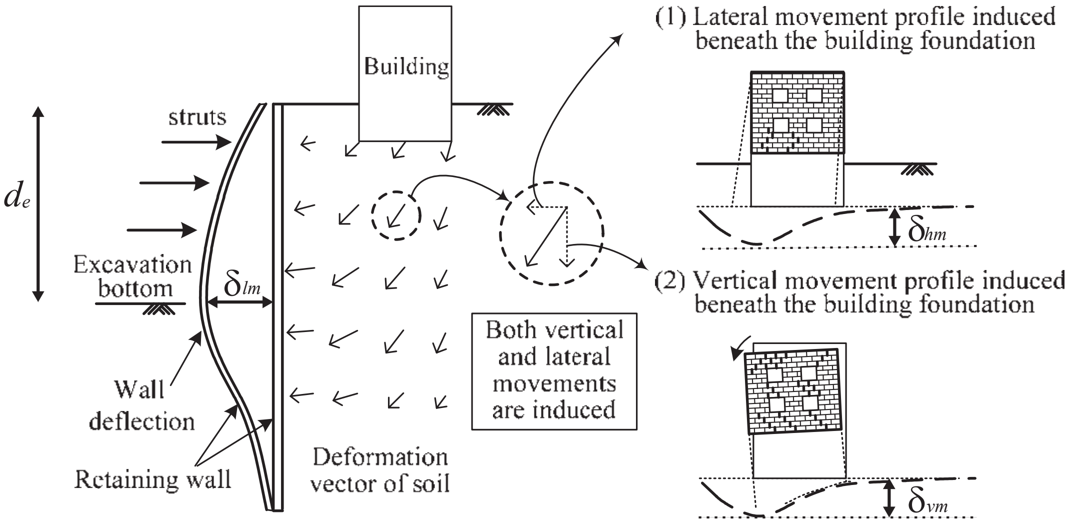

Figure 3.4: Notations in deep excavation induced ground movements after Kung et al. [105].

can not be applied to the elastoplastic two-stage analysis directly, in which a continuous ground displacement profiles are required. Therefore, a pair of shifted log-normal curves are fitted to the KJHH and KSJH ground displacement profiles in Fig. 3.5. The log-normal curves pass through pivot points A, B and C in the KJHH and KSJH models exactly and smoothen the sharp corners. The fitted curves also coincide well with the displacements observed in case histories reported by Kung et al. [105] and Schuster et al. [171]. The coefficient of determination (R^2) for the proposed vertical and lateral displacement profiles are 0.95 and 0.93, respectively, while the R^2 values for the original discrete KJHH and KSJH profiles are 0.92 and 0.88. Eq. 3.18 describes the formulation of the greenfield ground displacement profile proposed in this dissertation, where d is the distance from excavation, H_e is the depth of excavation, δ_{vm} and δ_{lm} are respectively the maximum vertical and lateral ground displacement.

There are many other methods to estimate the ground movements induced by deep excavations, e.g., [163, 86, 203, 47, 136]. If desired, these methods can be readily applied as the ground movement input to the two-stage analysis approach adopted in this study.

$$\frac{\delta_v(d/H_e)}{\delta_{vm}} = \frac{1.14}{d/H_e+0.39}\frac{1}{0.46\sqrt{2\pi}}\exp(-\frac{(ln(d/H_e+0.39)-0.095)^2}{0.423}) \tag{3.18a}$$

$$\frac{\delta_l(d/H_e)}{\delta_{lm}} = \frac{2.14}{d/H_e+0.82}\frac{1}{0.44\sqrt{2\pi}}\exp(-\frac{(ln(d/H_e+0.82)-0.80)^2}{0.387}) \tag{3.18b}$$

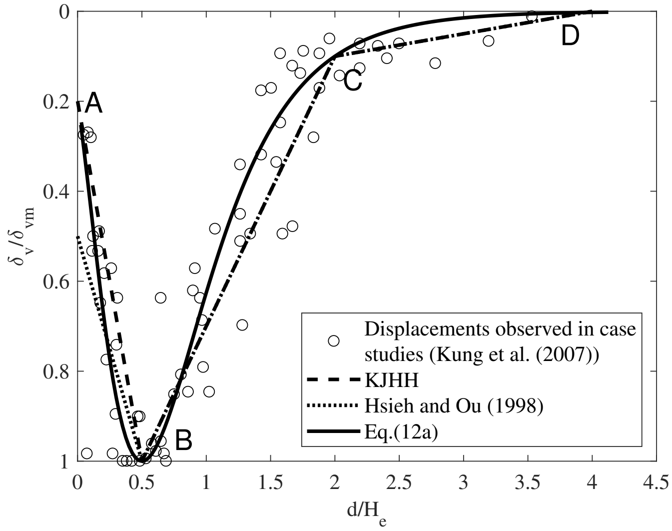

(a) Vertical ground displacement profile

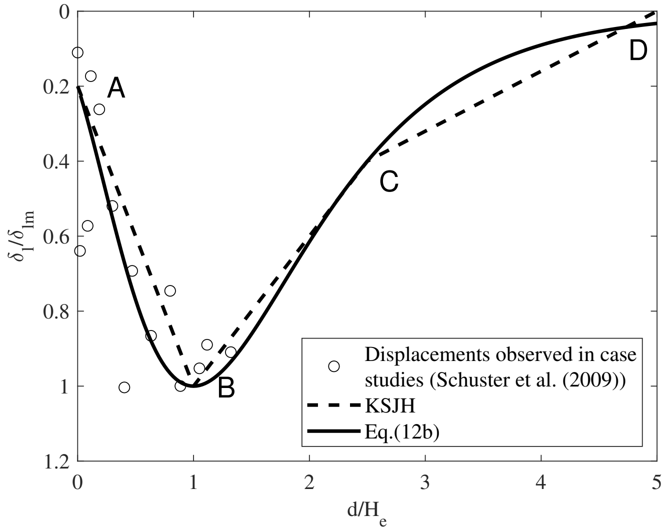

(b) Lateral ground displacement profile

Figure 3.5: The proposed deep excavation induced surface ground movement profiles.

3.1.3 Opportunities in data-driven predictions of ground movements

Under the rapid growth of ground monitoring data, data-driven methods are becoming popular in tunnel and deep-excavation engineering. One of the earliest applications was done by Suwansawat and Einstein in 2006 [183], where an artificial neural network is trained with the data collected after the completion of the first part of a tunnel in Bangkok. The neural network is then applied to predict the maximum ground settlement in the later tunnel segments. Since then, research and literature in this area developed fast and Zhang et al. [206] provided a state-of-the-art review of data-driven methods in underground excavation. In one recent development [6], state-of-the-art ground movement sensing and TBM operation data are gathered, and 3D ground movement fields (Fig. 3.6) at each chainage point can be estimated with a random forest algorithm. However, the application of data-driven methods suffers from two challenges. The first is the data collected from each TBM project is strongly associated with the local geology and specific tunnel design, which makes it difficult to apply case history data to new tunnel projects. A transfer-learning style data-driven method may be needed for the practical use of data-driven methods in new tunnel projects. The second challenge is that despite the ground monitoring and TBM data growing rapidly, the amount of data is still small compared to the data used in other successful applications of artificial intelligence, such as self-driving cars and large natural language models. The inadequate data may result in large uncertainty in the behavior of the tunnel boring machine predicted by existing data-driven methods.

Similar to the empirical or numerical-based methods, the data-driven prediction of ground movements can also be readily applied in the two-stage analysis approach. Moreover, data-driven methods usually provide estimations of variances and biases in addition to ground movements. The probabilistic analysis approach developed in this study can quantify the effect of the uncertainty in data-driven methods on the assessment of surface buildings, which could help mitigate the second challenge mentioned above.

3.2 Modeling surface structures

In most existing early-stage or regional assessments of the impact of tunnels and deep excavation on buildings, the surface structures are modeled as equivalent beams. Equivalent bending stiffness [75, 68, 84] or equivalent shear stiffness [173] is used as the dominant parameters to characterize the equivalent beam. A Timoshenko beam model [62] was also introduced to combine the effect of bending and shear stiffness.

Three types of structural analysis models are studied in this dissertation: an equivalent Timoshenko beam model, a 2D elastic frame model, and a 3D finite element model. The first two models were originally implemented in ASRE by Franza, Acikgoz, and DeJong [62] and Franza and DeJong [63] but revised, extended, and computationally optimized in this dissertation. In the Timoshenko beam model, the target building is modeled as an equivalent isotropic Timonshenko beam defined by its dimensions, elastic modulus (E_b), and elastic over shear modulus ratio (E_b/G_b).

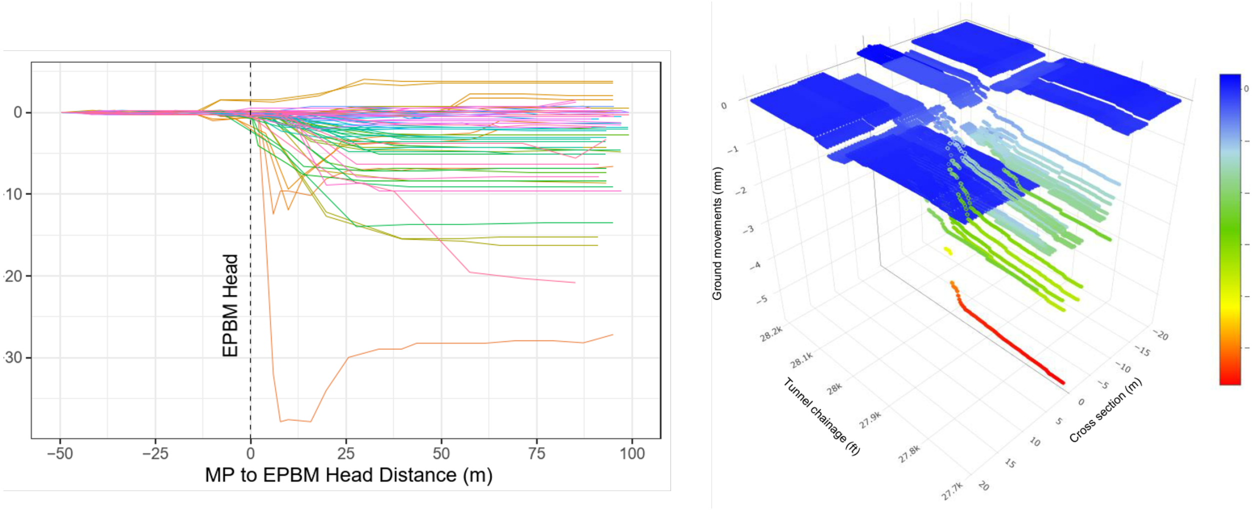

Figure 3.6: Ground movement profile predicted by Dayu et al. (2022).

The equivalent beam is discretized, and a stiffness matrix ($\mathbf{S}$) is formulated and applied to Eq. 3.20. Burland, Broms, and De Mello [26] investigated many case histories and suggested that the value of E_b/G_b should be taken as 2.6 for bear-wall structures and 12.5 for frame structures. The solution of ASRE consists of the displacement at each discretization node and the moment and axial forces in each element. The Timoshenko beam model was validated by comparing with field and centrifuge test results and resulted in reliable predictions for bearing wall structures on continuous foundations when the building geometry is simple and the skew angle between tunnel axes and structure is small [62].

The elastic 2D frame model considers each frame member as an isotropic elastic beam element and formulates the frame stiffness matrix with the displacement method. However, the elastic 2D frame model originally implemented in [63] is considered too simple because it only supports the modeling of structures with identical footings, one column on each footing, equal floor elevations, equal beam span widths, and identical beam and column dimensions. Moreover, infill walls, which can significantly affect the structure stiffness, were not previously considered. Therefore, the structural analysis model for frame structures in ASRE is updated in this research to include irregular frames and infill walls.

Fig. 3.7a schematizes the frame structure model developed in this research. The beams and columns are discretized at each junction node and each foundation element is discretized with a small element size. A fine grid is adopted for foundations because the foundations are connected to soil-structure interface elements, and a small element size can capture the ground movements more accurately. Because all frame members deform elastically in this model and building self-weight loads are applied at beam and column junctions, a coarse discretization of the frame is considered sufficient. In the updated frame structure model, footings with varying dimensions and footings connected to multiple columns can be modeled. The floor elevations and bay spans can be distinct at each frame panel, and each beam and column can have different dimensions and material properties. The infill walls are modeled as equivalent diagonal compression struts to simulate the stiffness of the walls. Eq. 3.19 is used to estimate the stiffness of the struts, as recommended by FEMA 306 [56], where t is the thickness of the infill panel, h and l are respectively the height and length of the infill panel, E_c and E_m denote the elastic moduli of column and masonry infill respectively, θ is the inclination angle of the strut, I_c is the moment of inertia of the adjacent columns and H_w is the height of the infill wall, as shown in Fig. 3.7b. Diagonal struts are only placed when the diagonal strain is compressive. In other words, The tensile strength of the diagonal struts is assumed to be zero.

The surface structures usually have an irregular out-of-plane layout and geometry, which makes them difficult to be modeled with the equivalent Timoshenko beam or 2D beam-column frame model. As a result, a 3D surface structure model using the finite element method (FEM) is developed. The 3D surface building model is implemented in a newer version of ASRE, ASRE3D, which implements the 3D ground movement models and 3D surface buildings. A typical mesh for a 3D building is shown in Fig. 3.8. Eight node isoparametric trilinear hexahedral elements [97] with 8 Gauss points are used to model the facade, partition walls, and foundations. The strain level in the building is assumed to remain in the elastic range, so an isotropic elastic constitutive model is assumed for surface structures. Although this elastic assumption is not necessarily correct, particularly for masonry structures due to the discontinuity caused by brick-mortar connections, it is consistent with the assumption that Boscardin and Cording [22] made to introduce the widely applied damage classification method (see Section 3.5), which is also adopted in this study. Yiu et al. [202] also suggested that employing simple constitutive models for most practical assessments is feasible. Alternatively, higher fidelity constitutive models that capture the structures' nonlinear structural behavior could be implemented in this two-stage assessment model, as discussed in Section 7.3. Although, it should be noted that even if higher fidelity constitutive models were adopted, the information needed to calibrate such models, and the detailed geometry and construction details needed to make them beneficial, are often not available in practical assessments. The adopted simplified constitutive model will unavoidably produce some uncertainty, but similar to many probabilistic analysis practices (e.g., [138]), such uncertainty can be quantified with the probabilistic assessment approach described in Chapter 4. The stiffness matrix and external force vectors of surface structure can be calculated through finite element theories (e.g., [97]). The displacements at each node can be solved by a set of equilibrium equations discussed in Section 3.3.

$$A_e = W_e t \tag{3.19a}$$

$$W_e = 0.175(\lambda h)^{-0.4}\sqrt{h^2 + l^2} \tag{3.19b}$$

$$\lambda = 4\sqrt{\frac{E_m t sin(2\theta)}{4E_c I_c H_w}} \tag{3.19c}$$

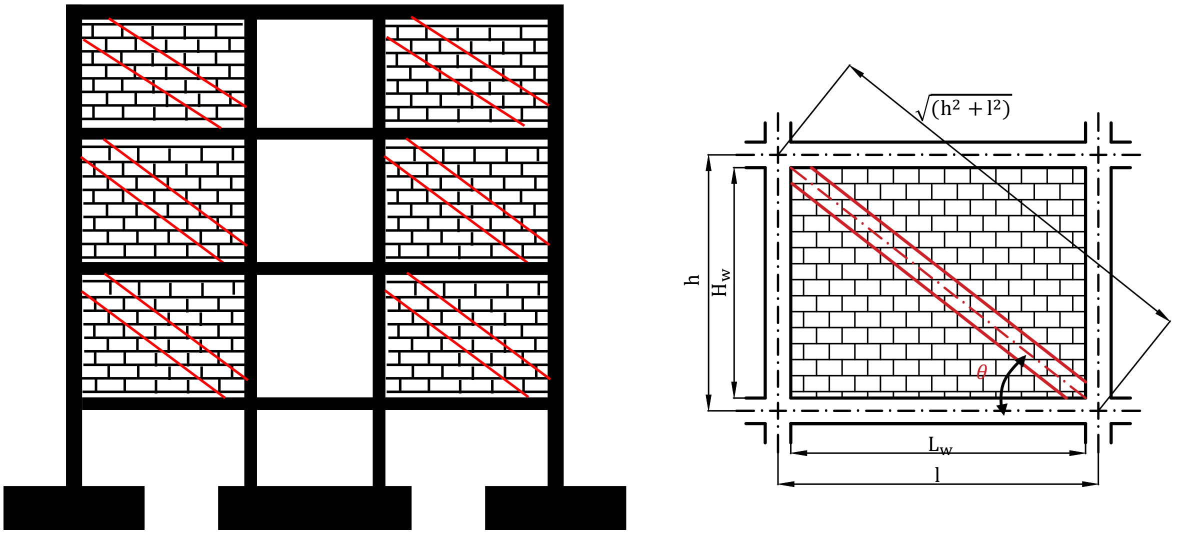

(a) Schematic frame model (b) Equivalent diagonal strut of masonry infill walls

Figure 3.7: The proposed 2D elastic frame model.

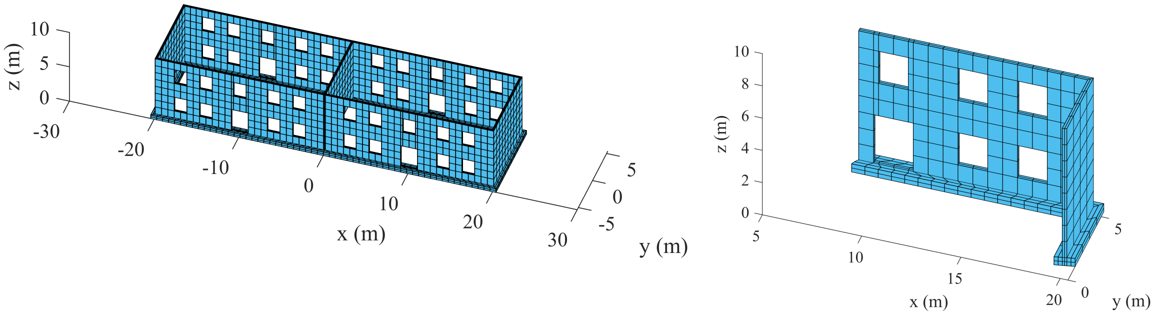

(a) Whole building. (b) Facade and foundation details.

Figure 3.8: An example of mesh employed in ASRE 3D.

3.3 Modeling the soil-structure interaction effect

As discussed in Chapter 2, previous studies showed that the displaced shape of the soil at the base of a surface structure is usually different from measured greenfield ground displacements. This difference can be roughly related to the relative stiffness between soil and building using a suite of relative stiffness methods. To improve the quantification of the effect of structural stiffness in the soil-structure interaction, an elastoplastic soil-structure interface model is adopted in this study.

The adopted soil-structure interface model is initially proposed by Franza and DeJong [63] borrowing a soil-structure interaction model in the analysis of underground pipes and tunnels [103]. The interface between soil and structure is modeled as rigid-perfectly plastic elements (also called plastic sliders) with lower and upper limit forces (see Fig. 3.9) connected to fully coupled linear elastic springs, which model the soils. The soil structure interface is discretized, and sliders (see Fig. 3.10) are applied both vertically and horizontally at the nodes. The soil is modeled as a homogeneous half-space continuum represented by coupled interactive springs. Gaps and Coulomb's friction model between soil and structure can be simulated with the plastic sliders by setting a zero upper limit force and a horizontal limit force proportional to the vertical stress in the sliders. This elastoplastic interface is a common simplified method to simulate the contact mechanics of non-penetration bodies under small relative displacements. The building displacement ($\mathbf{u}$) at each node can be solved with an equilibrium equation (Eq. 3.20), where $\mathbf{S}$ is building stiffness, $\mathbf{K}^*$ is the stiffness matrix of soil, $\mathbf{P}$ is the external loading applied at the foundation, $\mathbf{u}^{ip}$ is the plastic displacement of the sliders, $\mathbf{\Lambda}^*$ is the soil flexibility matrix without the main diagonal and $\mathbf{u}^{cat}$ is the greenfield ground displacement induced by excavation. The plastic property of sliders are governed by Eq. 3.20b and Eq. 3.20c, where $f_{i,low}$ and $f_{i,up}$ are lower and upper limits of the vertical force in sliders, μ is the friction coefficient at the interface of soil and structure and i and j are respectively the vertical and horizontal degree of freedom. The soil stiffness matrices $\mathbf{K}^*$ and $\mathbf{\Lambda}^*$ can be derived from the Mindlin's solution given by Vaziri et al. [188]. The structure stiffness $\mathbf{S}$ can be determined with analytical solutions (in the Timoshenko Beam model) or finite element formulations (in ASRE 3D). Because Eq. 3.20 is nonlinear without closed-form solutions, it is solved with the iterative algorithm proposed by Klar et al. [103]. The analysis result of Eq. 3.20 has been compared with centrifuge tests and confirmed to be reliable by Franza and DeJong [63] and Franza, Ritter, and DeJong [65]. Elkayam and Klar [51] also validated this elastoplastic formulation with a finite difference model of the soil continuum. Besides this elastoplastic solution, there are other SSI analysis methods involving full-scale finite element interface modeling and more rigorous soil constitutive models, as reviewed in Section 2.2 (e.g., [78, 77, 4, 53, 19, 202]). However, such complex models are generally not practicable in the regional assessment of large urban infrastructure projects and, therefore, not selected in this study.

$$(\mathbf{S} + \mathbf{K}^*)\mathbf{u} = \mathbf{P} + \mathbf{K}^*\mathbf{u}^{cat} + \mathbf{K}^*\mathbf{\Lambda}^*(\mathbf{P} - \mathbf{S}\mathbf{u}) + \mathbf{K}^*\mathbf{u}^{ip} \tag{3.20a}$$

subject to:

$$f_{i,low} \leq (\mathbf{P} - \mathbf{S}\mathbf{u})_i \leq f_{i,up} \tag{3.20b}$$

$$|(\mathbf{P} - \mathbf{S}\mathbf{u})_j| \leq \mu(\mathbf{P} - \mathbf{S}\mathbf{u})_i \tag{3.20c}$$

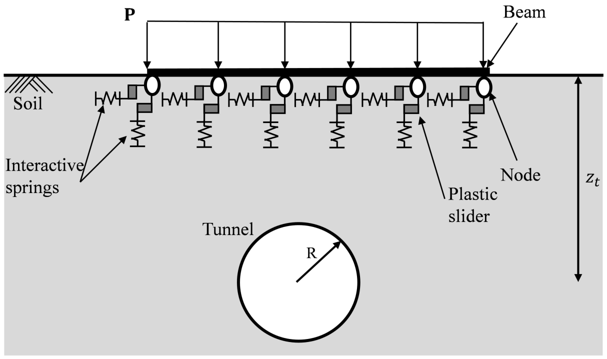

(a) Sketch of the elastoplastic soil structure interaction model in tunneling.

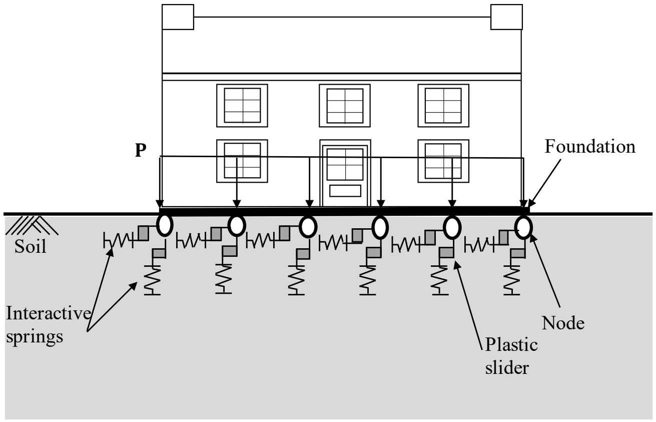

(b) Sketch of the elastoplastic soil structure interaction model in deep excavation.

Figure 3.9: Soil-structure-interaction model after [63]

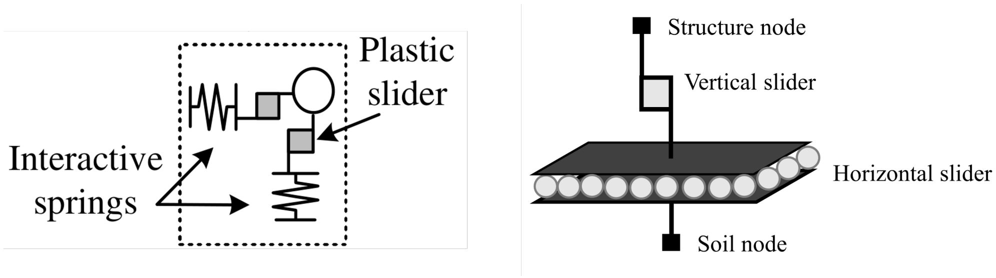

Figure 3.10: 2D and 3D soil-structure interface slider model.

3.4 Model validation

The two-stage approach using the 2D Timoshenko beam and beam-column frame models implemented in ASRE are validated by experimental measurement by Franza, Ritter, and DeJong [65] and Franza and DeJong [63]. The models are used to predict the deformation of a 3D-printed model building under the settlement induced by a tunnel, which is simulated with a centrifuge test in a plane-strain test setup. The model analysis shows a close comparison with the experimental results. To validate ASRE3D, the analysis results are compared with the finite element analysis results reported in [24], where the response of a two-story masonry facade building with 8 m height, 40 m length, and 10 m width is calculated with a 3D fully coupled tunnel-soil-structure finite element (FE) model implemented in the software Abaqus (Dassault Systemes Simulia Corp., Providence, RI, USA) and a simplified 1D soil to masonry (S2M) model respectively. The thickness of the masonry facades and partition walls in the analyzed building is 0.215 m. A strip footing with 1 m width, 0.5 m height, and 1 m embedded depth is also modeled. The geometric details of the analyzed building can be found in [24] and Fig. 3.11. A single tunnel with an 11 m diameter is excavated 23 m below the ground surface, which leads to a surface volume loss (V_L) of 1.65% and a width parameter (K) of 0.57. An isotropic elastic constitutive model with a Young's modulus of 3 GPa and a Poisson's ratio of 0.2 is specified for the masonry. The extended Mohr-Coulomb model and the multiple yield surface kinematic hardening model are adopted for the soils in the fully coupled FE model, and a calibrated soil-foundation interaction model is adopted in the S2M model. In the analysis using ASRE3D, the soil Young's modulus is taken as 14.5 MPa, which is the weighted average stiffness [157, 117] of the terrace gravel and London Clay modeled in [24]. All the other dimensions and parameters are the same as in the 3D FE model specified in [24]. Fig. 3.12 shows the comparison of the tunnel-induced vertical displacements at the foundation base level under three eccentricities (horizontal distances from tunnel axis to building center line). Overall, ASRE3D shows a close match with the 3D fully coupled analysis computed with the finite element program Abaqus.

Fig. 3.13 shows a comparison of the principal tensile strains computed with ASRE3D, the 3D fully coupled FEM method, and the S2M method employed by Burd et al. [24]. Burd et al. [24] reported the 99% quantile of the principal tensile strain (ε^t_{99}) of all building elements to eliminate the strain concentration effect at mesh corners and connections. Therefore, the ε^t_{99} are computed with ASRE3D and then plotted for eccentricities of 0, 5, 10, 15, 20, and 25 m. ASRE3D shows a reasonable match with the prediction of the 3D fully coupled FEM. The comparison of the vertical displacement profiles (Fig. 3.12) and ε^t_{99} (Fig. 3.13) indicates that ASRE3D can provide a similar result as the fully coupled 3D FE model, while ASRE3D is simpler and computationally cheaper. The simple and computationally cheap nature makes it feasible to apply ASRE3D in the proposed probabilistic PPBE assessment approach in this dissertation. Although ASRE3D is subject to some loss of fidelity (especially for larger eccentricities) compared with the fully coupled 3D finite element analysis due to the two-stage modeling approach and the coarse mesh adopted for surface buildings, the possible modeling errors of ASRE3D are considered to be acceptable and much less critical than the uncertainty discussed in Section 4.

3.5 Structure damage quantification

After the building deformation is estimated, a measure of potential damage in the building is needed. Burland, Broms, and De Mello [26] proposed to evaluate building cracking potential by simplifying buildings as deep isotropic simply supported beams. Both bending and shear deformation are considered, and equations to calculate the maximum bending strain ($\varepsilon_{b(max)}$) and maximum diagonal tensile strain ($\varepsilon_{d(max)}$) from deflection ratio ($\frac{\Delta}{L}$) are provided (Eq. 3.21 and 3.22). Eq. 3.21 and 3.22 are derived based on the deflection at the middle of a center loaded simply supported Timoshenko beam, where E and G are elastic and shear modulus of the beam, I is the moment of inertia, L is the length of the sagging or hogging beam segment and y is the distance from the extreme fiber to the neutral axis. In sagging deformation, it is assumed that the beam neutral axis is at the mid-height of the beam (i.e., $y = \frac{H}{2}$). In hogging deformation, Burland, Broms, and De Mello [26] assumed that foundations and soil provide significant restraint to the buildings and the neutral axis should be considered at the bottom of the beam (i.e., the extreme fiber is at the beam top and $y = H$). The larger of $\varepsilon_{b(max)}$ and $\varepsilon_{d(max)}$ is considered the maximum principal tensile strain ($\varepsilon_{p,max}$), and Burland, Broms, and De Mello [26] suggested that the average $\varepsilon_{p,max}$ that will result in the initiation of cracks in brickwork is around 0.05%. Consequently, 0.05% is named the critical tensile strain in bricks.

$$\varepsilon_{b(max)} = \frac{\Delta}{L}\frac{12y}{L}\frac{1}{1+\frac{18}{L^2}\frac{I}{H}\frac{E}{G}} \tag{3.21}$$

$$\varepsilon_{d(max)} = \frac{\Delta}{L}\frac{1}{1+\frac{L^2}{18}\frac{H}{I}\frac{G}{E}} \tag{3.22}$$

Burland, Broms, and De Mello [26]'s method is widely adopted for analysis of bearing wall structures on continuous footings, though there are several deficiencies with this method. First, assuming a bottom neutral axis in hogging deformation mode leads to a large shear stress at the beam bottom, which can not be balanced with the friction between soil and structure [36]. This implies the importance of modeling the slippage between the soil and the foundation. Second, although this method works well with buildings on continuous footings, it may not be reasonable to model a frame structure on separate footings as a continuous, simply supported beam. Finally, Burland, Broms, and De Mello [26]'s method does not consider horizontal strain, which is argued by Boscardin and Cording [22] to be a significant component of $\varepsilon_{p,max}$.

Boscardin and Cording [22] therefore modified Burland, Broms, and De Mello [26]'s definition of $\varepsilon_{p,max}$ and as Eq. 3.23 and 3.24, where ε_h is defined as the change of building length divided by the original building length. $\varepsilon_{b(max)}$ and $\varepsilon_{d(max)}$ can be determined with Eq. 3.21 and Eq. 3.22. To quantify the level of building damage, Boscardin and Cording [22] suggested classifying building damage into 5 categories according to the magnitude of $\varepsilon_{p,max}$, as summarized in Table 2.1. The

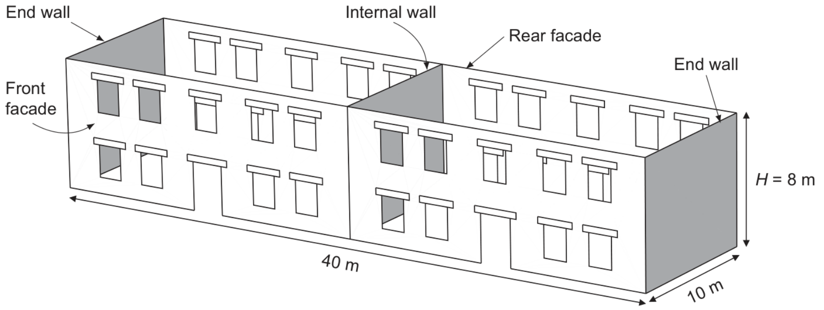

(a) Building layout and dimensions.

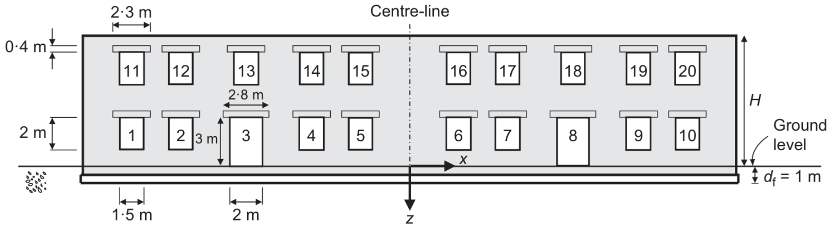

(b) Dimensions of facade openings.

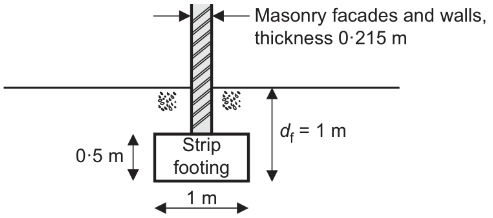

(c) Details of masonry and foundation.

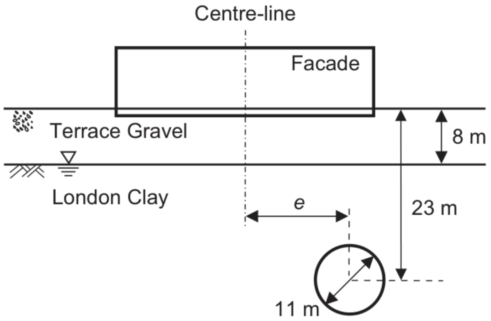

(d) Tunnel configuration and definition of eccentricity e.

Figure 3.11: The configuration of tunnel-soil-structure used to validate ASRE3D, after Yiu, Burd, and Martin [202].

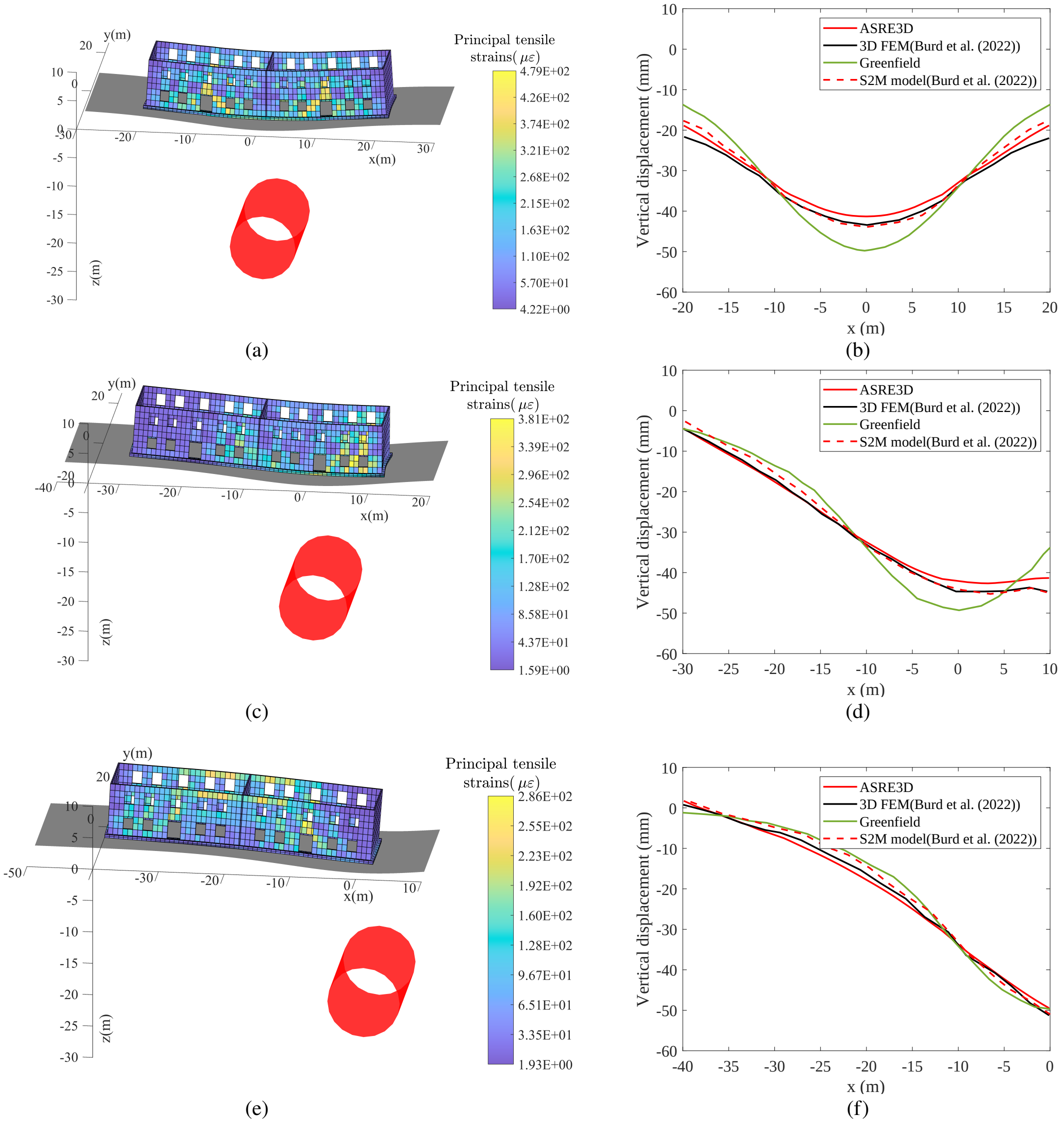

(a) (b)

(c) (d)

(e) (f)

Figure 3.12: Principal tensile strains calculated with ASRE3D and vertical displacements at the foundation base level induced by tunneling: (a,b) eccentricity = 0 m; (c,d) eccentricity = 10 m, (e,f) eccentricity = 20 m.

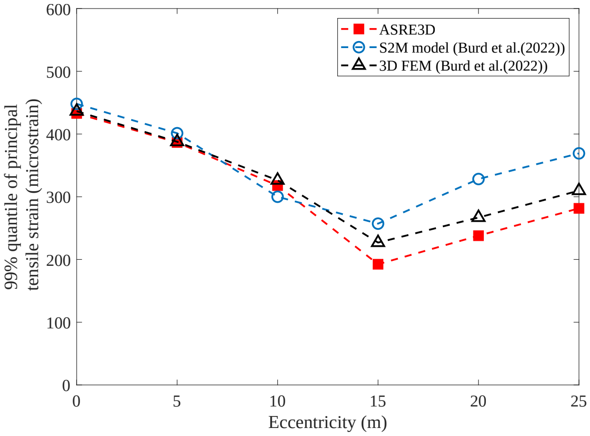

Figure 3.13: Variation of the 99% quantile principal tensile strains (ε^t_{99}) with eccentricity.

limits between different damage levels are named limiting tensile strains, and this method is called the limiting tensile strain method.

Although ε_h is taken into account, Boscardin and Cording [22] still modeled the entire building as a deep beam and does not consider separate footings. To evaluate the damage of a building that consists of individual units governing its structural response, Son and Cording [173] updated Boscardin and Cording's method[22] based on the state of strain at each building unit. A building unit, as defined by Son and Cording [173], can be characterized as a section between two columns, two different building geometries or stiffness characteristics, and two different ground displacement gradients. Son and Cording [173] suggested using angular distortion β to compute $\varepsilon_{p,max}$ instead of using deflection ratio $\frac{\Delta}{L}$ in Burland, Broms, and De Mello's method[26]. In Son and Cording[173], the $\varepsilon_{p,max}$ determined from angular distortion (β) and the horizontal strain (ε_h) determined with Eq. 3.26 and 3.27 are used to classify building damage, where β is defined as settlement difference (slope) minus rigid rotation (tilt) of a building unit (see Fig. 3.14). Due to a different definition of $\varepsilon_{p,max}$, the limiting strains of building damage categories are also updated and shown in the brackets in Table 2.1.

$$\varepsilon_{bend,max} = \varepsilon_{b(max)} + \varepsilon_h \tag{3.23}$$

$$\varepsilon_{diag,max} = \max_{\theta}\{\varepsilon_h \cos^2\theta + 2\varepsilon_{b(max)}\cos\theta\sin\theta\} \tag{3.24}$$

$$\varepsilon_{p,max} = \max\{\varepsilon_{bend,max}, \varepsilon_{diag,max}\} \tag{3.25}$$

$$\varepsilon_{p,max} = \varepsilon_h \cos^2\theta_{max} + \beta\sin\theta_{max}\cos\theta_{max} \tag{3.26}$$

$$\tan(2\theta_{max}) = \frac{\beta}{\varepsilon_h} \tag{3.27}$$

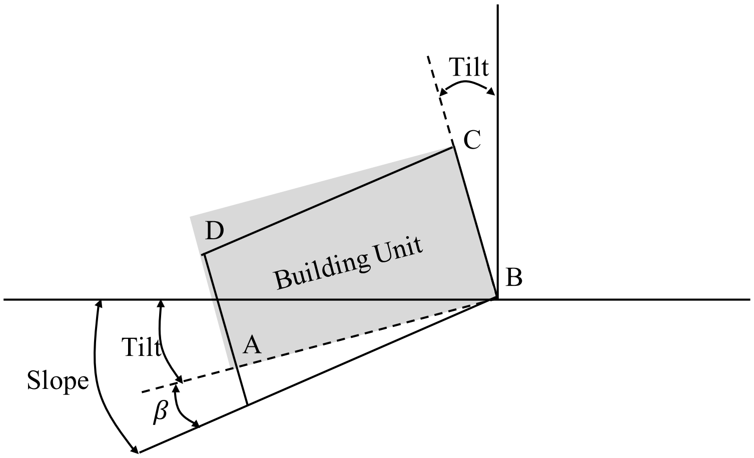

Figure 3.14: Slope, tilt and angular distortion (β) of a building unit.

The methods proposed by Burland, Broms, and De Mello [26], Boscardin and Cording [22] and Son and Cording [173] are semi-empirical methods because no detailed analysis of each building element is done, and only the deformation mode, construction type, and potentially building materials are taken into consideration. When prediction methods can provide more specific information, e.g., building internal forces or strains, more detailed damage assessment approaches can be adopted. Franza, Acikgoz, and DeJong [62] proposed a direct strain-based approach where no assumptions of deflection ratio or angular distortion are used. The building strains are directly calculated from measured deformations of the building or internal forces of the equivalent beam using Eq. 3.28, where χ_m is the beam curvature, γ_m is the beam engineering shear strain, $\varepsilon_{axis,m}$ is the beam axis strain, and N_m, V_m, M_m are the internal axial force, shear force and bending moment computed from numerical analysis; k and c are the shear correction factor and the average shear stress corrective factor, which depend on the geometry of building cross section, t is the distance between the neutral axis and extreme fiber and s is the vertical distance between the neutral axis and the fiber where ε_{dt} is calculated. The larger of ε_{bt} and ε_{dt} is taken as $\varepsilon_{p,max}$ and compared with the limiting strains in Table 2.1. This direct strain-based approach also uses an isotropic equivalent beam to model an entire building, therefore only the damage level of the entire building can be estimated. If the damage condition of some building elements or the locations of damages is desired, more detailed models have to be adopted. The detailed models should contain both structural and non-structural elements (e.g., infill walls). One such detailed damage assessment method for frame structures is proposed later.

$$\varepsilon_b = \chi_m t = \frac{M_m t}{EI} \quad \varepsilon'_b = \chi_m s = \frac{M_m s}{EI} \quad \varepsilon_d = \frac{c\gamma_m}{2} = \frac{cV_m}{s\kappa AG} \quad \varepsilon_h = \varepsilon_{axis,m} = \frac{N_m}{EA} \tag{3.28a}$$

$$\varepsilon_{bt} = \varepsilon_b + \varepsilon_h \qquad \varepsilon_{dt} = (\varepsilon'_b + \varepsilon_h)(\frac{1-\nu}{2}) + \sqrt{(\varepsilon'_b + \varepsilon_h)^2(\frac{1+\nu}{2})^2 + \varepsilon_d^2} \tag{3.28b}$$

As discussed in Section 3.3, three types of structural analysis model are studied, and the structural damage model for each of them are described here. For the 2D Timoshenko beam model, the direct strain-based approach by Franza, Acikgoz, and DeJong [62] is adopted in this dissertation because it overcomes possible errors due to the simplification in the calculation of $\frac{\Delta}{L}$ and β in the methods by Burland, Broms, and De Mello [26] and Son and Cording [173]. In other words, the maximum principle tensile strain in the Timoshenko beam is selected as the engineering demand parameters, instead of the deflection ratio ($\frac{\Delta}{L}$) and tilting angle (β) used in [26, 173]. In the direct strain-based approach, the maximum internal forces N_m, M_m and V_m among all cross sections of the beam are first computed with ASRE and $\varepsilon_{b(max)}$, $\varepsilon_{d(max)}$, and ε_h are calculated with Eq. 3.28. For a rectangular cross-section, κ and c are taken as $\kappa = \frac{10(1+\nu)}{12+11*\nu}$ and $c = 3/2$, where ν is the Poisson's ratio of the beam. The engineering demand parameter $\varepsilon_{p,max}$ is taken as the larger value of ε_b and ε_{dt}, and compared with the limiting tensile strains by Son and Cording [173] (Table 2.1) to obtain a damage category of the building. Son and Cording's limiting strains [173] were derived from the state of strain theory, which is appropriate to be compared with the maximum principal strain directly calculated from a numerical model.

For the 2D elastic frame model proposed in this dissertation, damage to infill walls and the structural frame are evaluated separately. To evaluate the damage of infill walls, Son and Cording's method [173] is adopted. The vertical displacements (A_v, B_v, C_v, D_v) and lateral displacements (A_l, B_l, C_l, D_l) at the corners (A, B, C, D) of each infill panel are determined (Fig. 3.14). The slope, rigid body rotation (tilt), angular distortion (β), and lateral strain at the top and bottom are calculated with Eq. 3.29. The maximum strain of each infill wall can be estimated with Eq. 3.26 and 3.27, and the damage category of each infill wall is classified according to Son and Cording's criterion [173] in Table 2.1.

To evaluate the damage in the structural frames, the method of Ghobarah [73] is adopted. Ghobarah's method [73] was originally used to evaluate building damage after an earthquake, and inter-story drift ratio is considered as the engineering demand parameter to classify building damage. Ghobarah [73] defined inter-story drift ratio by the difference of horizontal displacement of the top and base floor divided by the floor elevation. In this definition, each floor is assumed to remain horizontal. However, in the case of excavation-induced building deformation, each frame panel experiences both vertical and horizontal drifts (see Fig. 3.14). Therefore, the inter-story drift ratio is equivalent to the horizontal displacement difference after rotating the frame panel by the slope angle (i.e., drift ratio = tanβ, where β is the angular distortion defined by Son and Cording [173]). When β is small, it is reasonable to assume tan$\beta \approx \beta$. Therefore, assuming the drift-ratio is equivalent to angular distortion, the criterion of Ghobarah [73] can be used to classify potential damage of each frame panel using Table. 3.1.

State of damage	Ductile frame	Nonductile frame
No damage	0 - 0.2	0- 0.1
Repairable damage		
a) Light (aesthetic) damage	0.2 – 0.4	0.1 – 0.2
b) Moderate (serviceability) damage	0.4 – 1.0	0.2 – 0.5
Irreparable damage (structural damage)	1.0 – 1.8	0.5 – 0.8
Severe damage (collapse)	1.8 – 3.0	0.8 – 1.0

Table 3.1: Relationship between damage category and angular distortion (After [73]).

This proposed damage assessment method which considers both the structural frame and infill walls can provide an overall estimate of the building, but it also identifies locations of potential damage in the form of the $\varepsilon_{p,max}$ and β values that are calculated for each panel. The application of this method is demonstrated by a case study in Section 6.1.2.

$$\text{Slope} = \frac{A_v - B_v}{L_w} \tag{3.29a}$$

$$\text{Tilt} = \frac{(C_l - B_l) + (D_l - A_l)}{2H_w} \tag{3.29b}$$

$$\beta = \text{Slope} - \text{Tile} \tag{3.29c}$$

$$\varepsilon_{h,\text{top}} = \frac{D_l - C_l}{L_w} \tag{3.29d}$$

$$\varepsilon_{h,\text{bottom}} = \frac{A_l - B_l}{L_w} \tag{3.29e}$$

To quantify the damage level with the 3D finite element model, the characteristic strain defined by Yiu, Burd, and Martin [202] is adopted to describe the maximum tensile strain in the surface building and used as the engineering demand parameter. It is often observed that the computed strains at corners and connections by finite element models are subjected to stress singularities (e.g., [89, 202]), and the maximum strain computed from finite element models are liable to overestimate the damage in structures. To avoid overestimation, the principal tensile strain in all finite elements are sorted, and the 99% percentile is defined as the characteristic strain (ε_c) and compared with the $\varepsilon_{lim,lower}$ and $\varepsilon_{lim,up}$ given in Table 2.1. This is conceptually similar to taking ε^t_{99} as the characteristic strain in [24, 202].

3.6 Summary

This chapter presented the methods and theories of modeling the ground displacements, surface buildings, and soil-structure interaction mechanisms in the two-stage T&DE SSI modeling approach adopted in this research. The adopted ground displacement model can simulate both 2D and 3D ground displacement fields for tunneling. For deep excavations, only a 2D ground displacement model was discussed. However, the 3D ground displacements effect can be studied when the spatial variability of ground displacements is considered (see Section 4.2.1 and case study 8 in Chapter 6). Three types of surface structure models (i.e., Timoshenko beam, 2D frame, 3D finite element) were discussed. A modeling method to simulate the soil-structure interaction mechanism was also introduced. The suite of T&DE SSI models is named ASRE or ASRE3D, depending on if the 3D effect is considered. By validating ASRE and ASRE3D against geotechnical centrifuge tests or models created in proprietary software, it was concluded that the presented models are reasonably accurate. Meanwhile, the modeling processes of ASRE and ASRE3D are relatively simple and can be considered natural extensions of the second-stage assessment in the widely applied three-stage assessment approach reviewed in Section 2.1. Therefore, ASRE and ASRE3D showed a potential to be applied in the probabilistic performance-based engineering assessment approach this dissertation seeks to create. Further, as discussed in Section 1.2, this dissertation aims to identify the uncertainty and create a set of probabilistic modeling methods to formally quantify the uncertainty in the T&DE SSI modeling process. As a result, the uncertainty quantification and probabilistic assessment approach based on ASRE and ASRE3D are studied in the next chapter.

Chapter 4

Uncertainty quantification and a regional probabilistic assessment approach

4.1 The framework of uncertainty analysis with deterministic numerical models

As discussed in Section 2.3, First and Second Order Reliability Methods (FORM and SORM) can be used to estimate the statistical properties of engineering demand parameters (EDPs), however, errors may be induced by biased estimation of the design point and failure surface shape. The point estimation method (PEM) can estimate statistical properties of EDPs with low computational cost but it may introduce bias because only two integration points are used in each dimension and the appropriate type of statistical distribution for each EDP is assumed based on experience. To achieve an accurate and complete probabilistic description of tunneling or excavation-induced structural damage, Monte-Carlo (MC) methods are adopted together with the uncertainty analysis with deterministic numerical models approach initially proposed by Schweiger, Thurner, and Pöttler [172]. A modified version of the approach of probabilistic analysis with deterministic numerical models [172] is adopted here. The PEM used by Schweiger, Thurner, and Pöttler [172] is substituted with Monte-Carlo methods to achieve an accurate and unbiased uncertainty propagation. In addition to the substitution of PEM with MC methods, a variance-based global sensitivity analysis (Sobol's method) and factor mapping analysis are supplemented to Schweiger, Thurner and Pöttle's [172] procedure and the modified probabilistic analysis procedure is shown in Fig. 4.1. The details of uncertainty input quantification, sensitivity analysis (SA), and factor mapping analysis are discussed later in this chapter.

The MC methods adopted in this study are simple in concept and provide unbiased and complete probabilistic information about system outputs. Most importantly, MC methods are (arguably) free from the curse of dimensionality and they can be used in high-dimension uncertainty quantification, such as the large-scale assessment of tunnels and deep excavations. However, a large number of model evaluations is usually required in MC methods, and the ASRE implementation originally developed by Franza and DeJong [63], which creates limitations for uncertainty quantification due to higher computational costs, is not feasible. To increase computation efficiency, some optimization procedures are adopted and described in Section 4.4 and 5, and the computation time for the entire uncertainty analysis and sensitivity analysis can be considered to be reasonably cheap for engineering practice. Due to the heavy computation cost required in the MC method, surrogate models have to be employed in most current studies involving MC simulation and complex numerical models (e.g. [48, 201]). However, due to the high-dimensional uncertainty considered in this study, especially when spatial variabilities are considered with random field models, surrogate models are difficult to develop, and this dissertation presents the first study (as far as the author knows) in the area of T&DE SSI that uses a nonlinear numerical model in MC methods without surrogate modeling.

The analysis framework starts with modeling the input uncertainties, which depend on the fidelity and scale of the analysis. When a single building is analyzed and spatial variabilities are neglected, random variable models describing the ground movements, soil stiffness, and surface building properties need to be proposed. When a regional/community-scale analysis is conducted, a spatially variable ground movement random field, a spatially variable soil-stiffness field, random building dead load factors, and random building stiffness reduction factors are used to model the input uncertainty. Modeling the input uncertainties is called "Uncertainty input quantification", and is the first step (see Fig. 4.1) in the proposed uncertainty analysis framework. The uncertainty input quantification method is discussed in Section 4.2. The input uncertainties are propagated to EDPs with MC methods, and realizations (samples) of the input uncertainties need to be generated. The method to generate samples and the adopted MC methods are discussed in Section 4.3. Three MC methods, which are the crude MC method, a multi-fidelity MC method, and a randomized quasi-MC method, are studied and their performances are compared in Section 4.4. Factor mapping analysis and variance-based sensitivity analysis are presented in Section 4.5 to study the effect of each input uncertainty on EDPs. In the end, an extension of the proposed framework in the regional T& ESSI assessment is discussed in Section 4.6.

4.2 Uncertainty input quantification

Schweiger, Thurner, and Pöttler [172] suggested that site investigation and laboratory testing are typically restricted due to financial and time constraints in geoengineering practice, and therefore the site and lab data are usually not sufficient for the statistical description of uncertainty input variables. Baecher and Christian [12] suggested that engineering judgment based on information from in-situ tests and similar engineering applications could be made to quantify uncertainty input. The uncertainty input quantification for tunneling cases and deep excavation cases are discussed in this section. The uncertainty input quantification will start with a simplified approach where the spatial variabilities are ignored. As a result, the input uncertainties are modeled with random

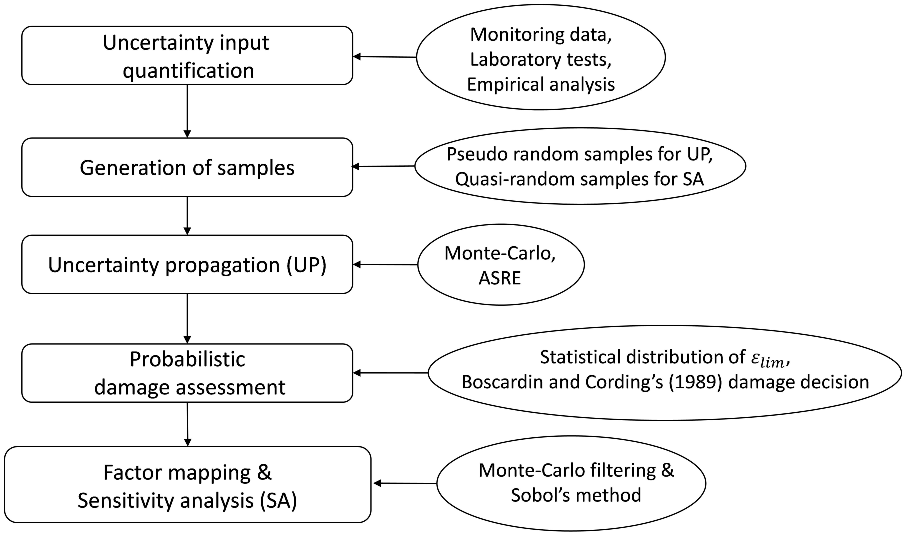

Figure 4.1: Probabilistic modeling approach of tunneling and excavation induced structural damage

variables. The spatial variabilities in ground movements and soil stiffnesses are then considered with random field models.

4.2.1 Uncertainty in ground movements

When spatial variabilities are not considered in tunneling cases, two parameters, which are volume loss (V_L) and trough width parameter (K), are considered as random variables to model the uncertainty in the ground movements predicted by the models described in Section 3.1.1. The uncertainty of V_L and K are quantified according to previous numerical analysis and field monitoring data. Camós et al. [31] assumed that V_L and K are statistically independent, and each of them can be described by a lognormal distribution. These assumptions are followed in this dissertation and the monitoring data collected from Channel Tunnel Rail Link Contract 220 [198] and Crossrail [8] were used to estimate the coefficient of variance (CV_{V_L}, and CV_K) for V_L and K. The V_L and K at 53 transects are monitored and the values of CV_{V_L}, and CV_K are calculated and reported in Table 4.1. The spatial correlation along the length of the tunnel, for both V_L and K, is assumed to be zero because the monitored transects are far from each other. The collected data also revealed that V_L and K roughly follow a lognormal distribution with a very small covariance. Although the amount of data is small, the data complies with the lognormal and independent assumptions made by Camós et al. [31].

When spatial variabilities are not considered in deep excavation cases, four parameters, which are the maximum horizontal wall deflection (δ_{hm}), vertical deformation ratio ($R_v = \frac{\delta_{vm}}{\delta_{hm}}$), lateral deformation ratio ($R_l = \frac{\delta_{lm}}{\delta_{hm}}$), and ground displacement profile width parameter (η) are used to model the uncertainty in the ground movements predicted with the KJHH & KSJH models described in Section 3.1.2, where the definition of δ_{hm}, δ_{vm}, and δ_{lm} can be found in Section 3.1.2. The uncertainty of δ_{hm}, R_v and R_l are quantified by Kung et al. [105] and Schuster et al. [171] as Eq.4.1, where $\bar{\delta}_{hm}$, $\bar{R}_v$ and $\bar{R}_l$ are the mean values of δ_{hm}, R_v and R_l. The mean values and variances were estimated by adopting the regression equations in the KJHH & KSJH models. The uncertainty of δ_{hm}, R_v and R_l are described with corresponding bias factors (BF_{hm}, BF_v and BF_l defined in Eq. 4.1), which are statistically independent random variables. Consequently, δ_{hm}, R_v, and R_l are also random variables because they are a product of random variables and constants. It is important to notice that δ_{hm}, R_v, and R_l are highly correlated, but they are conditionally independent to each other when they are conditioned on the input parameters of the regression equations in the KJHH & KSJH models. In other words, when the underground conditions and excavation system are defined, the model errors in the estimation of δ_{hm}, R_v, and R_l are statistically independent from each other. The mean and standard deviations for BF_{hm}, BF_v and BF_l are reported by Kung et al. [105] and Schuster et al. [171], as shown in Table. 4.2. Because BF_{hm}, BF_v and BF_l are error correction factors of regression analysis, their distributions are modeled as the normal distribution, which is a common practice in statistical studies of geotechnical engineering [12].

Kung et al. [105] and Schuster et al. [171] also indicated that uncertainty exists in the estimation of the shape of ground displacement profiles. By observing case histories used to derive Eq. 3.18, it is concluded that the pivot point A does not vary among the case histories while the distances of points B, C, and D to the excavation wall show large fluctuations (see definition of points A-D in Fig. 3.5). To quantify the uncertainty of the ground displacement profile shape, a scale factor η is added to Eq. 4.2 to shrink or elongate the ground displacement profile width. In the case histories reported in [105, 171], the distance of pivot point B to the excavation wall varies in the range $0.3H_e$ to $0.7H_e$ and $0.6H_e$ to $1.4H_e$ for vertical and lateral displacements, respectively. These variance ranges correspond to a η with a range from 0.6 to 1.4. If a normal distribution centered at 1 is assumed for η, the standard deviation can be estimated as 0.16 to ensure a 99% likelihood that η is in the interval $(0.6, 1.4)$. Considering η describes the ratio between the true trough width and the estimated trough width, a ratio distribution model (e.g., Cauchy distribution) might be more realistic. However, the normal distribution is selected for convenience, similar to many probabilistic studies in civil engineering [12, 31, 33], and a sensitivity study about the probabilistic models is needed in the future. The case histories reported in [105, 171] are in Singapore. For deep excavation projects in other areas (e.g., in Norway, as discussed later in Chapter 6), local case history data should be used to estimate the uncertainty in δ_{hm}, R_v, R_l, and η.

$$\delta_{hm} = BF_{hm}\bar{\delta}_{hm} \tag{4.1a}$$

$$R_v = BF_v\bar{R}_v \tag{4.1b}$$

$$R_l = BF_l\bar{R}_l \tag{4.1c}$$

$$\delta_v(x) = \delta_{vm}\frac{1.14}{\frac{x}{\eta}+0.39}\frac{1}{0.46\sqrt{2\pi}}\exp(-\frac{(ln(\frac{x}{\eta}+0.39)-0.095)^2}{0.423}) \tag{4.2a}$$

$$\delta_l(x) = \delta_{lm}\frac{2.14}{\frac{x}{\eta}+0.82}\frac{1}{0.44\sqrt{2\pi}}\exp(-\frac{(ln(\frac{x}{\eta}+0.82)-0.80)^2}{0.387}) \tag{4.2b}$$

When the spatial variability of ground movements needs to be considered in tunneling cases, random field models can be developed from the ground movement data collected from tunneling with similar construction techniques, tunnel dimensions, and geology layers. The data collected from the Crossrail (Elizabeth Line) tunnel excavation in London is used as an example to describe the procedure to model the spatial variability. Fig. 4.2 reports the variation of V_L and K against chainage. Assuming stationary 1D random fields for V_L and K along chainage, empirical semi-variance ($1/2$ of variance) can be estimated from the collected data. The ordinary least squares algorithm [35] implemented in the R package gstat [146] is used to fit a Gaussian and a Whittle-Matern variogram model for V_L and K, respectively. The Gaussian variogram model for V_L is defined as Eq. 4.3a, where $c_e = 0.0343$, $\alpha = 247.460$, and nugget = 0.0268. The Whittle-Matern variogram model for K is defined as Eq. 4.3b, where $\sigma^2 = 0.00347$, $\nu = 0.300$, $\alpha = 228.169$, $K_\nu()$ is the modified Bessel function of the second kind with an order ν, and $\Gamma()$ is the Gamma function. V_L and K are modeled as normal random fields, which are completely determined by their variogram models. If the positive definite property is desired for V_L and K, new empirical variograms can be estimated after taking the logarithm of V_L and K. Consequently, Lognormal random field models can be developed to describe the spatial variabilities of V_L and K.

$$\gamma(h) = c_e\left\{1-\exp\left(-\left(\frac{h}{\alpha}\right)^2\right)\right\} + nugget \tag{4.3a}$$

$$\gamma(h) = \sigma^2\left\{1-\frac{2^{1-\nu}}{\Gamma(\nu)}\left(\frac{h}{\alpha}\right)^\nu K_\nu\left(\frac{h}{\alpha}\right)\right\} + nugget \tag{4.3b}$$

When the spatial variability of ground movements in deep excavation cases needs to be considered, random field models can be developed from the ground movement data collected from deep excavation case histories with similar geology layers and support systems. The deep excavations investigated in this study are primarily braced excavations, and ground movement data are collected from two case histories in Norway. Norway was selected because the author was funded by the Peder Sather Advanced Study Center to conduct an investigation on the deep excavation-induced building damage assessment in Norway. Accordingly, the case study demonstration (see Chapter 6) of the regional probabilistic assessment proposed in this study is in Norway. Civil engineers can select corresponding case history data if they apply the proposed assessment method to specific projects. Fig.4.4 is the plan view of the deep excavation and ground monitoring points, and Fig.

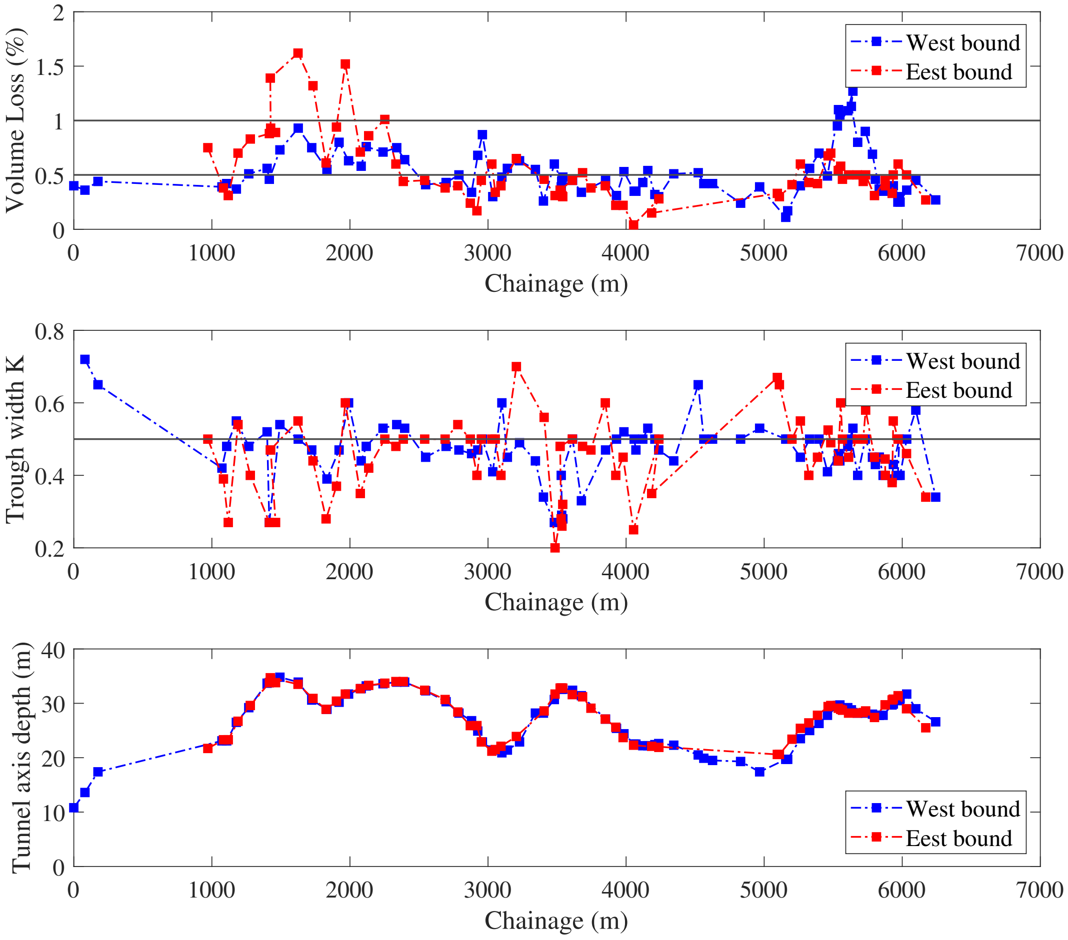

Figure 4.2: Ground movement records collected from the Crossrail. Top: Volume Loss. Middle: Trough Width (K). Bottom: Tunnel axis depth.

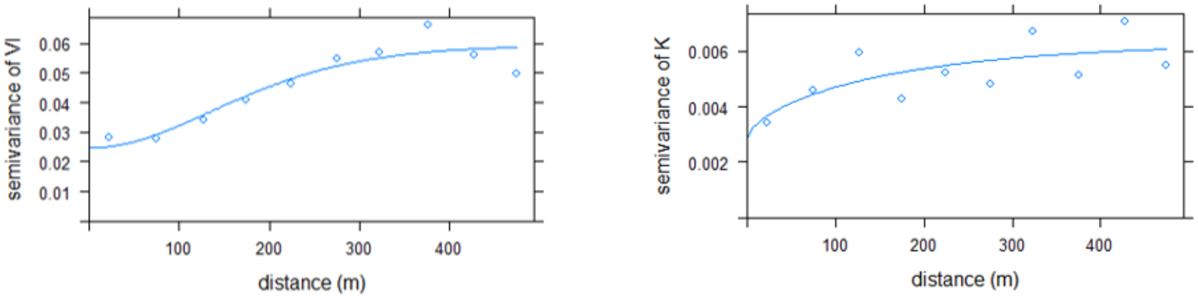

(a) Empirical semivariance and semi-variogram model for V_L.

(b) Empirical semivariance and semi-variogram model for K.

Figure 4.3: Spatial variability models for V_L and K.

4.5-4.6 are the ground movement records along 16 cross-sections perpendicular to the deep excavation walls. The values of δ_{vm}/H_e and η (see Eq. 4.2) are estimated from the ground movement records. To ensure δ_{vm}/H_e and η are positive-definite in the uncertainty models, their empirical variograms are estimated in the logarithmic space (i.e., $\log(\delta_{vm}/H_e)$ and $\log(\eta)$). Fig. 4.7 shows the empirical semivariance and Gaussian variogram modes created for $\log(\delta_{vm}/H_e)$ and $\log(\eta)$. Further assuming normal marginal distributions for $\log(\delta_{vm}/H_e)$ and $\log(\eta)$, lognormal random field models that capture the ground spatial variable behavior are obtained for δ_{vm}/H_e and η. It is noteworthy that the empirical semivariance with long lags (i.e., points to the right of Fig. 4.7) are estimated with a small amount of data and may experience large biases. One may also argue that other marginal distributions might be selected over lognormal distributions. However, given the very limited data (especially after considering the spatial correlation), the first two moments are the most important to capture the variability of δ_{vm}/H_e and η in this application and the shape of the distribution is considered to be of secondary importance. If more data in a similar geology is available, the empirical semivariance and corresponding semi-variogram models can be refined with the proposed framework. The goodness of fit or hypothesis tests should also be employed to justify the marginal distribution of the random fields.

4.2.2 Uncertainty in soil and structure properties

The soil properties used in ASRE and ASRE3D that may experience large uncertainty are E_s and ϕ, which are assumed equal to the critical state values. Because a linear elastic model of the ground is adopted, representative values should be selected to account for the T&DE SSI.

When the spatial variability in soil properties is not considered, Phoon and Kulhawy [152] reported that the CV of ϕ (CV_ϕ) varies between 7% and 21% and the CV of E_s (CV_{E_s}) ranges from 16% to 95% depending on the test methods. In general, median values of CV_ϕ and CV_{E_s}, i.e., 13.4% and 43% can be adopted. E_s and ϕ are assumed to be statistically independent. The

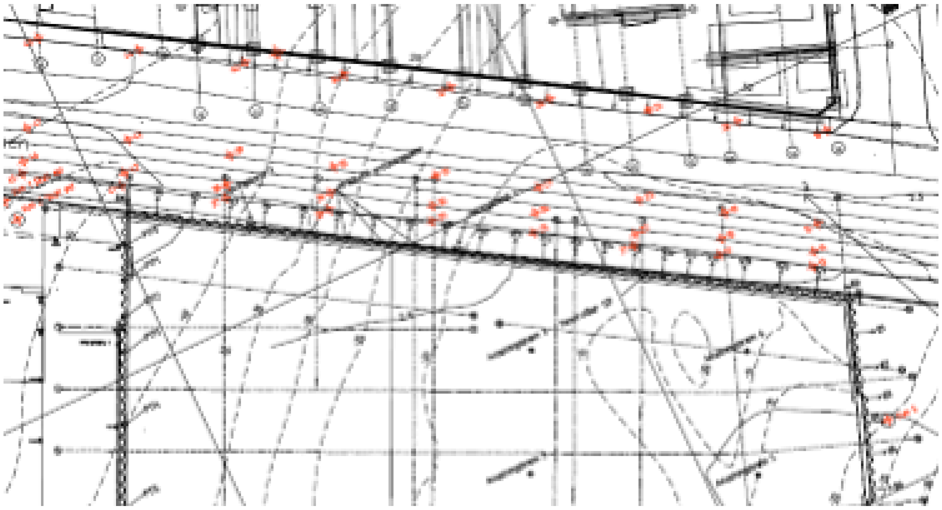

(a) Plan view and ground monitoring points in deep excavation 1.

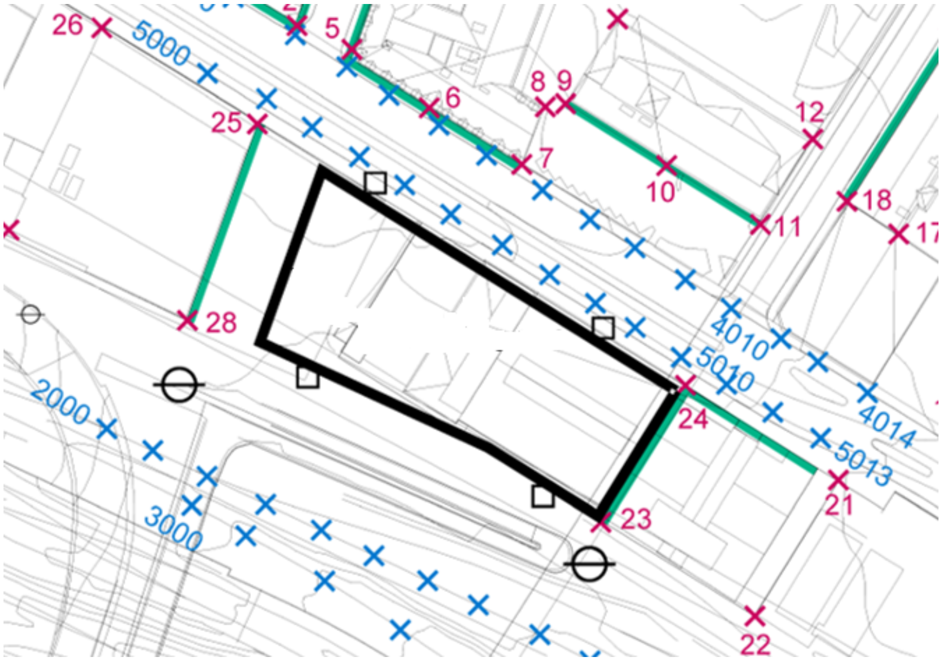

(b) Plan view and ground monitoring points in deep excavation 2.

Figure 4.4: Deep excavation cases used to estimate ground movement variability.

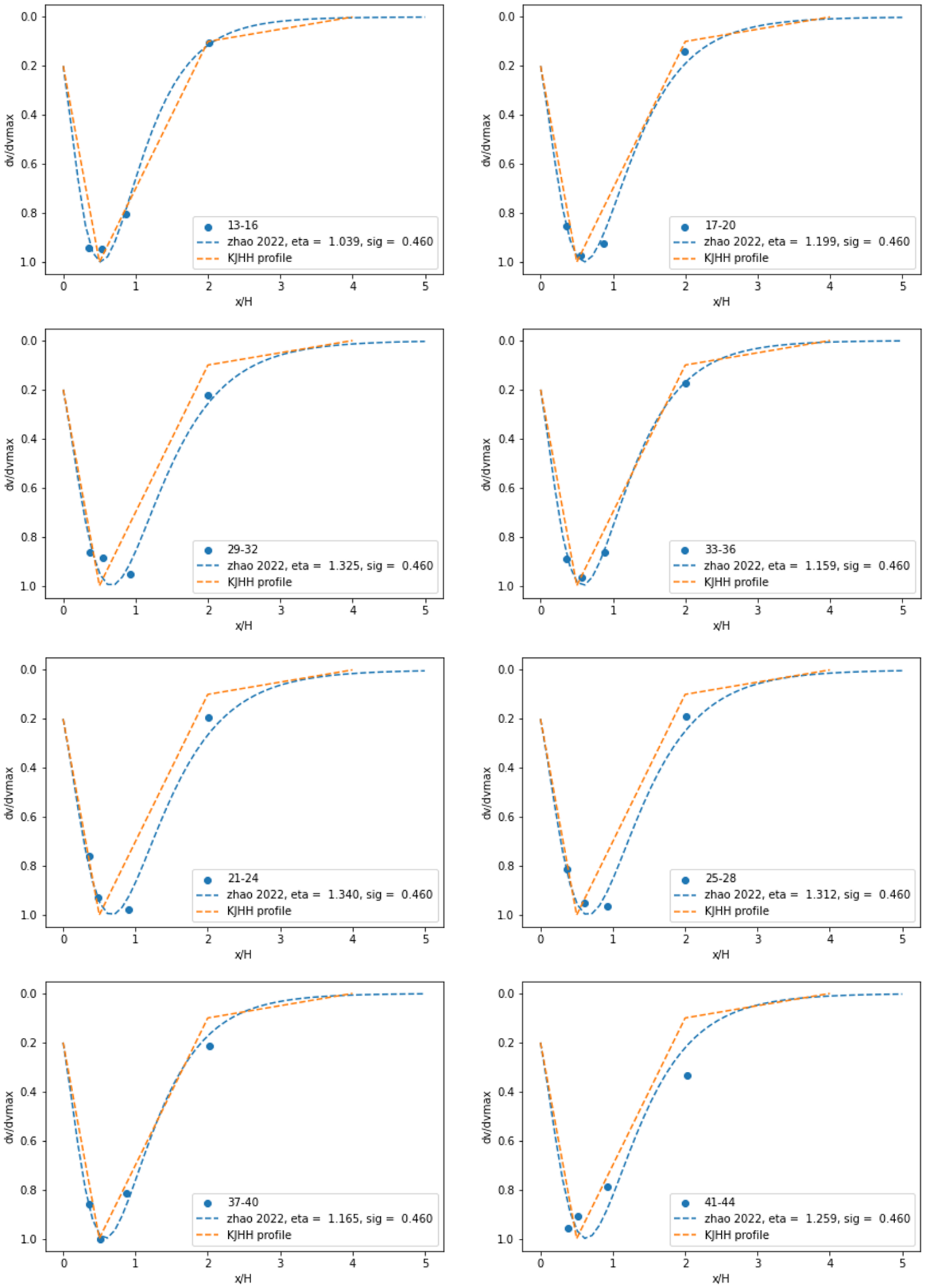

Figure 4.5: Ground movement records collected from deep excavation 1.

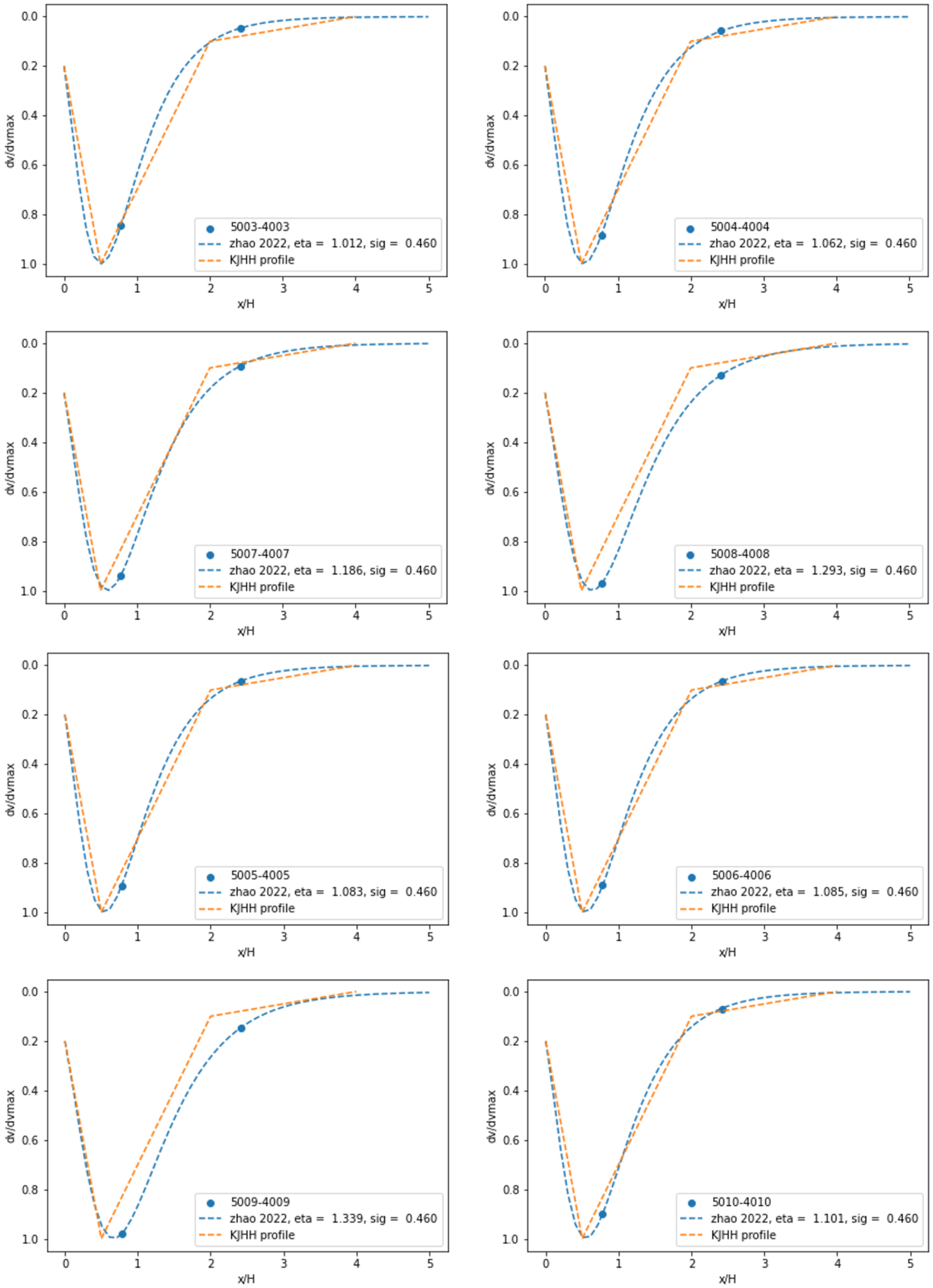

Figure 4.6: Ground movement records collected from deep excavation 2.

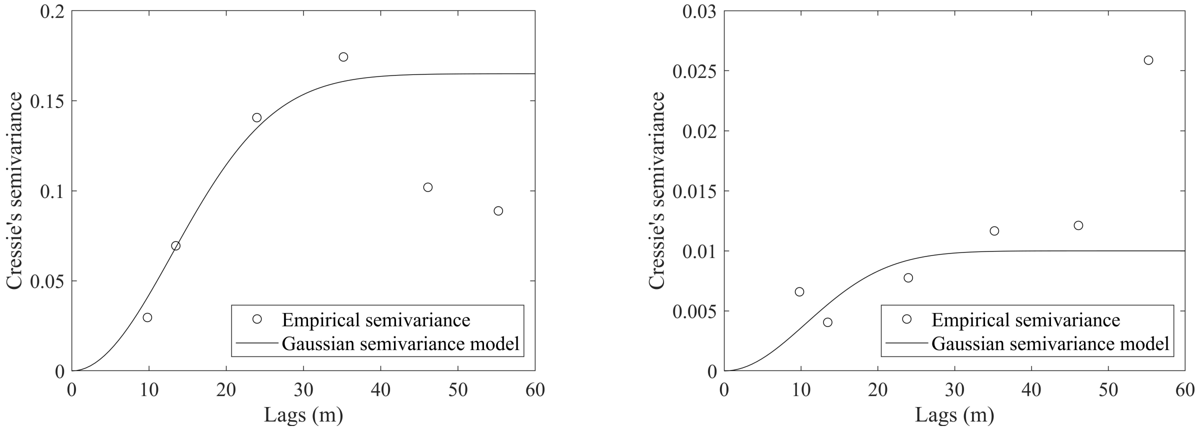

(a) Empirical semivariance and semi-variogram for δ_{vm}/H_e.

(b) Empirical semivariance and semi-variogram for η.

Figure 4.7: Spatial variability models for δ_{vm}/H_e and η.

normal distribution is assumed for E_s and ϕ in Zhao, Franza, and DeJong [213], as suggested by Mollon, Dias, and Soubra [133] and Franco, Gitirana, and Assis [60]. However, normal distribution may result in negative samples of E_s and ϕ when their mean values are small. As a result, in the subsequent study, E_s are assumed to follow a lognormal distribution in [214], and a beta distribution in [212]. A sensitivity study and parametric study presented in Section 6.5 and published in [213] suggested that the uncertainty in ϕ contributes negligibly to the uncertainty of the critical strain in the buildings. As a result, the uncertainty of ϕ is only considered in [213] and a few case studies presented in Section 6, and may be neglected in future T&DE SSI analysis.

When the spatial variability in soil properties needs to be considered, random field models can be estimated from case history data with a similar approach adopted for the ground displacement models. Alternatively, many researchers (e.g. Kok-Kwang Phoon's, Vaughan Griffiths's, and Gregory Baecher's research groups) proposed random field models for soil properties based on geology conditions. For example, Cami et al. [28] summarized the most commonly adopted variogram models in geotechnical engineering for a variety of soil properties. Methods to estimate the scale of fluctuation and typical values for different geotechnical applications are also reviewed in [28]. Besides estimating soil spatial variability models from site characterization data, many researchers (e.g., [98, 180]) have studied the worst-case scenarios of soil spatial variability that will lead to most adverse results (such as maximum foundation tilting). The worst-case scale of fluctuation may be selected if site characterization data is not available to achieve a conservative analysis. In T&DE SSI analyses, larger differential settlement may induce more significant surface building damage. Ahmed and Soubra [1] and Stuedlein and Bong [180] studied the differential settlement under uniform ground movement and liquefaction. Both Ahmed and Soubra [1] and

Stuedlein and Bong [180] suggested a scale of fluctuation approximately equal to footing spacing may lead to worst-case building differential settlements. As a result, a scale of fluctuation equal to footing spacing or strip footing span was selected in T&DE SSI analyses.

When 2D equivalent beam models are used to model surface buildings, two parameters, which are the elastic modulus of the equivalent beam (E_b) and elastic over shear moduli ratio (E_b/G_b), are considered random variables to model the uncertainty in structural properties. As suggested by Dimmock and Mair [44], when an equivalent beam is used to model surface buildings, E_b for masonry structures is approximately 3 GPa, with an E_b/G_b ratio of 2.6 for bearing wall structures with no openings and approximately 12.5 for frame structures. Both E_b and E_b/G_b may be associated with large uncertainty due to ignorance of material properties and the great simplification of modeling the whole building as an equivalent beam. Son and Cording [174] studied the effect of building stiffness to T&DE SSI and suggested E_b/G_b is harder to estimate than E_b. Therefore, a large CV (40%) is assumed for E_b and an even larger CV (70%) is assumed for E_b/G_b. E_b is assumed to follow a lognormal distribution, which is a common practice for positive definite random variables [172]. Because 2.6 is a theoretical lower limit of E_b/G_b [44], a truncated normal distribution with a lower limit of 2.6 is assumed for E_b/G_b. For the 2D elastic frame model, the concrete compressive strength (f_c'), masonry elastic modulus (E_m), and 2D frame beam width (b_b) are also considered random variables. The uncertainty input quantification process of 2D column-frame model is based on the case studies described in Section 6.1.3 and 6.2.1. For example, the compression strength of concrete is estimated as 30 MPa, and the corresponding elastic modulus is $E_c = 4700\sqrt{f_c'} = 26$ GPa, as suggested by ACI 318. If a 5% reinforcement ratio is assumed, the elastic modulus for beams and columns is estimated as 36 GPa with the equivalent area method. In reality, the compressive strength of normal-strength concrete is in the range of 20 MPa to 40 Mpa. Assuming in the early-assessment stage with no further information to better estimate the most likely concrete strength in a building, a uniform distribution between 20 MPa and 40 MPa can be used to model f_c'. Consequently, the elastic modulus of concrete is a random variable depending on f_c'.

When ASRE3D is adopted for the T&DE SSI analysis, the building stiffness (E_b) and building dead load L may experience large uncertainty. Probabilistic characterization for stiffness, strength, and load can be found in probabilistic design regulations for different types of structures (e.g., [34, 52, 7]). In ASRE3D, unreinforced masonry structures are primarily considered, and the suggestion of the US Brick Industry Association [18] is adopted to quantify the uncertainty associated with E_b. To quantify the uncertainty of L, the method suggested by Ellingwood [52] is followed, where the mean of L should be taken as 1.05 times the nominal design load and the CV should be taken as 10%. A comprehensive discussion of probabilistic characterization of structure properties can be found in [125].

It should be noted that the correlation between ground movements (e.g., V_L, K) and soil properties (e.g., E_s, ϕ) are ignored in this dissertation. This is because: (1) the proposed uncertainty analysis approach focuses on early-stage assessment, and the correlation effect is hard to determine with a reasonable effort; (2) the correlation between input variables generally reduces the variability

Parameter	Description	Distribution	CV
V_L	Volume loss	Lognormal	73.11%
K	Trough width parameter	Lognormal	14.44%
E_s	Soil elastic modulus	Normal	43%
ϕ	Soil-foundation interface friction angel	Normal	13.5%
E_b	Building elastic modulus	Lognormal	40%
E_b/G_b	Building elastic over shear moduli ratio	Truncated normal *	70%
$*$ Truncated with a lower limit of 2.6			

Table 4.1: Coefficient of variance and distribution type of uncertainty input variables in tunneling cases

Random Variable	Statistical model
BF of Maximum wall deflection (BF_{hm})	Normal(1, 0.25^2)
BF of Vertical deformation ratio (BF_v)	Normal(1, 0.13^2)
BF of Lateral deformation ratio (BF_l)	Normal(1, 0.11^2)
Ground displacement profile width parameter (η)	Normal(1, 0.16^2)
Elastic modulus of equivalent beam model (E_b (GPa))	Lognormal(1.57, 0.086)
Elastic over shear modulus ratio of equivalent beam model(E_b/G_b)	Lognormal(1.54, 0.15)
Concrete compressive strength(f_c' (MPa))	Uniform(20, 40)
Masonry elastic modulus(E_m (GPa))	Uniform(6, 21)
2D frame beam width (b_b (m))	Normal(5.76, 0.58^2)

Table 4.2: Coefficient of variance and distribution type of uncertainty input variables in deep excavation cases

of system output [12] and ignoring correlation provides a conservative estimation of the damage assessment uncertainty.

4.3 Sample generation and Monte Carlo-based uncertainty forward propagation

The input uncertainties are propagated to engineering demand parameters (EDPs) with MC methods, and realizations (samples) of the input uncertainties need to be generated. Random variable samples are generated by the inversing cumulative density function method, and random field samples are generated with the discrete Karhunen-Loève expansion approach [169]. The variograms of the lognormal random field models in this dissertation are defined in the underlying Gaussian distribution space, and the Gaussian fields are first generated. The random fields are discretized at soil-structure interaction nodes in the structural analysis models (SAMs), and a covariance matrix is calculated for each random field. The covariance matrices are eigen decomposed, and the first 99% eigen modes are selected to reduce the number of input uncertainty dimensions while preserving the major uncertainty. By multiplying a diagonal matrix of the square root of eigenvalues and a matrix whose columns are the corresponding eigenvectors with a vector of independent normal variables, a realization of the discretized Gaussian field is generated. The Gaussian fields are then transformed into lognormal fields by applying the exponential operator. The independent normal random variables are generated with MC or quasi-MC sampling method discussed later. If variograms of the lognormal field need to be specified, realizations can be generated with the nonlinear Gaussian spectrum method [71].

In this dissertation, uncertainty propagation is used to estimate the probabilistic distribution of building damage (P_I) under the influence of the uncertainty input parameters through a transformation of the deterministic model ASRE/ASRE3D. Because ASRE/ASRE3D is nonlinear with a relatively high input dimension, many conventional uncertainty propagation and reliability analysis methods (e.g., point estimation method, first-order second-moment (FOSM) method) may introduce large biases, as discussed previously in Section 2.3. In contrast, Monte Carlo (MC) methods are generally simple in concept and provide an unbiased estimation of quantities of interest. Therefore, MC methods are employed herein to estimate the cumulative distribution ($F(\text{EDP})$) of EDP, such as characteristic strain or floor drift ratio, with an empirical distribution $\hat{F}_n(\text{EDP})$. The crude MC method (See Eq. 4.4, where n is the number of simulations, $\mathbb{1}$ stands for the indicator operator, and $\varepsilon_{c,i}$ is the characteristic strain determined from the i^{th} model evaluation of ASRE/ASRE3D) is first applied in this study. For a given building, using the crude MC method, an empirical probability distribution ($\hat{F}_n(\text{EDP})$) of EDP can be obtained, and the probability ($\hat{P}_I$) of the damage category I can be estimated with Eq. 4.5a. If failure is defined as damage category I or above, the failure probability is denoted with $\hat{P}_{I+}$ and can be calculated with Eq. 4.5b. To achieve sufficient accuracy, a convergence analysis should be conducted to determine the proper number of simulations (n). For example, the number of simulations was increased consecutively and $\hat{P}_{1+}$ for one of the case studies using ASRE3D in a tunneling scenario was calculated and plotted in Fig. 4.8. It is observed that $\hat{P}_{1+}$ converged to a constant when the sample size reaches 1000 and the 95% confidence interval obtained with the bootstrap sampling method is small. To ensure satisfactory accuracy, 1200 samples are used for the following crude MC simulations in tunneling scenarios using ASRE3D.

The convergence of the crude MC method is often considered too slow, and advanced MC methods can be applied to reduce the number of model evaluations. The convergence rate and the concept of **efficiency** are first reviewed to analyze the performance of the MC methods. Let $\varepsilon = g(\mathbf{X})$ stand for ASRE/ASRE3D, where $\mathbf{X}$ is the vector of random variables used to generate the realizations of the input uncertainties and ε is the EDP. The quantity of interest (QoI) of the MC methods, such as failure probability (P_{1+}), can be written as $p_f = \mathbb{P}(\varepsilon > \varepsilon_{lim}) = \mathbf{E}[\mathbb{I}(\varepsilon > \varepsilon_{lim}) = \mathbf{E}[f(\mathbf{X})]$. A crude MC estimator of p_f is defined as $Q_n = \frac{1}{n}\sum_{i=1}^{n} f(\mathbf{X}_i)$, which is also a random variable. The expectation of Q_n is $\mathbf{E}[Q_n] = \frac{1}{n}\sum_{i=1}^{n} \mathbf{E}[f(\mathbf{X}_i)] = p_f$, i.e., the crude MC estimator is unbiased. According to the central limit theorem, $\frac{Q_n - \mathbf{E}[Q_n]}{\sigma/\sqrt{n}}$ converges to the standard normal distribution (i.e., $\frac{Q_n - \mathbf{E}[Q_n]}{\sigma/\sqrt{n}} \Rightarrow \mathbf{N}(0,1)$), where $\sigma = \left(\int_{\Omega_{\mathbf{X}}} (f(\mathbf{X}) - \mathbf{E}[f(\mathbf{X})]) d\mathbf{X}\right)^{1/2}$. As a result, a confidence interval of Q_n in the form of $\left(Q_n \pm \frac{\sigma}{\sqrt{n}} z_{\alpha/2}\right)$ when n is sufficiently large, where $z_{\alpha/2}$ is the 100(1-α/2)th percentile of the standard normal distribution, and σ can be estimated with the sample standard deviation $\hat{\sigma} = \left(\sum_{i=1}^{n} \frac{(f(\mathbf{X}_i) - Q_n)^2}{n-1}\right)^{1/2}$. It can be observed that the confidence interval shrinks at a rate of $\frac{\sigma}{\sqrt{n}}$, and the convergence rate of Q_n is usually considered in the order of $\mathbf{O}(1/\sqrt{n})$ [142]. It can also be observed that the convergence rate is independent of the dimension of $\mathbf{X}$, which confirms that Q_n is preferred for high-dimension uncertainty quantification over surrogate modeling methods.

To improve the convergence performance compared with the crude MC method, two groups of advanced MC methods are available. The first group method (e.g., Antithetic Variates, Control Variates, Importance Sampling, Conditional Sampling, etc.) seeks to reduce the magnitude of σ, which is discussed extensively in Chapter 4 of [110] and often referred to as variance reduction techniques, and the second group method is referred to as quasi-MC methods, which uses a deterministic sequence of numbers (often called quasi-random or low-discrepancy samples) to replace the pseudorandom numbers in the crude MC. The low discrepancy samples are designed to be more uniform than pseudorandom samples used in the crude MC, especially when the sample size is small, and the convergence rate of the quasi-MC estimators for sufficiently smooth integrands can be as high as $\mathrm{O}(n^{-3/2}\log_{s/2} n)$, where s is the dimension of $\mathbf{X}$ [142]. Low-discrepancy samples, such as lattice sequences, Halton sequences, and Sobol's sequences, are hard to design when the dimension of $\mathbf{X}$ is large. However, recent research [100] constructed Sobol's sequences with dimensions up to 21201. In this dissertation, the application of a variance reduction technique using the Multi-fidelity MC (MFMC) method and a randomized quasi-MC (RQMC) method using Sobol's quasi-random sampling are studied.

To describe and compare the performance of the MC methods, the concept of efficiency

[110] is adopted. The efficiency of an estimator $\hat{\mu}$ for a quantity μ is given by Eq. 4.6, Where $\mathrm{MSE}(\hat{\mu}) = \mathrm{Var}(\hat{\mu}) + \mathrm{Bias}(\hat{\mu})$ is the mean-square error of $\hat{\mu}$ and $\mathrm{C}(\hat{\mu})$ is the expected computation time for $\hat{\mu}$. For a crude MC estimator Q_n, $\mathrm{Bias}(\hat{\mu})$ is zero, $\mathrm{Var}(\hat{\mu}) = \sigma^2/n$, and $\mathrm{C}(Q_n) = cn$, where c is the cost for single integrand evaluation and n is the number of samples. As a result, $\mathrm{Eff}(Q_n) = \left[\frac{\sigma^2}{n} \times cn\right]^{-1} = [\sigma^2 c]^{-1}$, which is independent of the sample size, i.e., increasing sample size does not increase efficiency for the crude MC method. To achieve better efficiency, a faster reduction of $\mathrm{MSE}(\hat{\mu})$ than the increase of $\mathrm{C}(\hat{\mu})$ is needed. Because efficiency considers both MSE and computation expense, it is used to compare the performance of the MC methods in this dissertation.

$$F(\varepsilon_c) = \mathbb{P}(\boldsymbol{\varepsilon_c} \leq \varepsilon_c) = \mathbf{E}(\mathbb{1}_{\boldsymbol{\varepsilon_c} < \varepsilon_c}) \approx \hat{F}_n(\varepsilon_c) = \frac{1}{n}\sum_{i=1}^{n} \mathbb{1}_{\varepsilon_{c,i} < \varepsilon_c} \tag{4.4}$$

$$\hat{P}_I = \hat{F}_n(\varepsilon_{lim,up}) - \hat{F}_n(\varepsilon_{lim,low}) \tag{4.5a}$$

$$\hat{P}_{I+} = 1 - \hat{F}_n(\varepsilon_{lim,low}) \tag{4.5b}$$

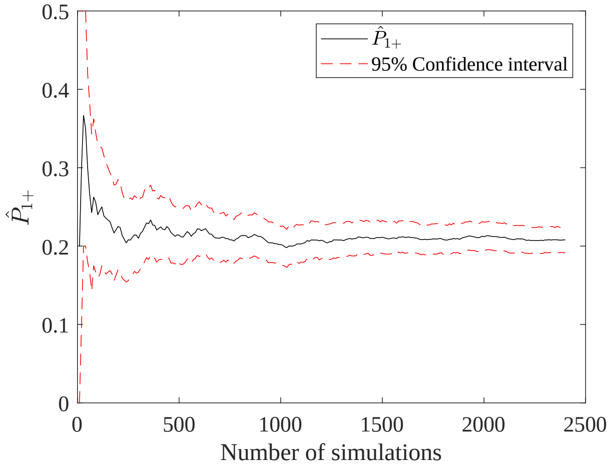

Figure 4.8: Evolution of failure probability $\hat{P}_{1+}$.

$$\mathrm{Eff}(\hat{\mu}) = [\mathrm{MSE}(\hat{\mu}) \times \mathrm{C}(\hat{\mu})]^{-1} \tag{4.6}$$

4.4 Application and a numerical experiment of advanced MC methods: Multi-fidelity MC and Randomized quasi-MC

A multi-fidelity MC method, a randomized quasi-MC method, and their performance in the application of T&DE SSI analysis are discussed in this section. This part of the study is published as a conference paper [211] at the 5th International Conference on Uncertainty Quantification in Computational Science and Engineering.

The MFMC method studied in this dissertation is based on the control variate framework. Given a crude MC estimator $Q_n = \sum_{i=1}^{n} f(\mathbf{X}_i)$, the control variate method calibrates Q_n by the error of another MC estimator $Q_{c,n} = \sum_{i=1}^{n} h(\mathbf{X}_i)$, where $h(\mathbf{X})$ is positively correlated to $f(\mathbf{X})$ and $\mathbf{E}[h(\mathbf{X})]$ is known or cheaper to compute. Because $h(\mathbf{X})$ and $f(\mathbf{X})$ are positively correlated, Q_n is likely to be overestimating $\mathbf{E}[f(\mathbf{X})]$ if $Q_{c,n}$ is larger than $\mathbf{E}[h(\mathbf{X})]$. Since $\mathbf{E}[h(\mathbf{X})]$ is known or cheap to estimate, the error of $Q_{c,n}$, can be estimated cheaply, and Q_n can be calibrated to reduce the variance/MSE of Q_n with a low computation cost. More specifically, a control variate estimator $Q_{cv,n}$, is defined as:

$$Q_{cv,n} = \frac{1}{n}\sum_{i=1}^{n} \left(f(\mathbf{X}_i) + \beta(\mathbf{E}[h(\mathbf{X})] - h(\mathbf{X}_i))\right) \tag{4.7}$$

where β is a constant to be determined. It can be proved that $Q_{cv,n}$, is unbiased because $\mathbf{E}[f(\mathbf{X}_i) + \beta(\mathbf{E}[h(\mathbf{X})] - h(\mathbf{X}_i))] = \mathbf{E}[f(\mathbf{X}_i)] + \beta(\mathbf{E}[h(\mathbf{X}_i)] - \mathbf{E}[h(\mathbf{X}_i)]) = \mathbf{E}[f(\mathbf{X})]$. In addition, it can also be proved that $\mathrm{Var}(Q_{cv,n})$ is minimized when $\beta = \beta^* = \frac{\mathrm{COV}(f(\mathbf{x}),h(\mathbf{x}))}{\mathrm{Var}(h(\mathbf{X}))}$, and $\mathrm{Var}(Q_{cv,n}) = \frac{1}{n(n-1)}\sum_{i=1}^{n}\left(f(\mathbf{X}_i) + \beta^*\left(\mathbf{E}[h(\mathbf{X}_i)] - h(\mathbf{X_i})\right) - Q_{cv,n}\right)^2$. In practice, the covariance $\mathrm{COV}(f(\mathbf{x}), h(\mathbf{x}))$ is usually unknown. Therefore, a small number r of pilot simulations can be used to estimate the β^* with:

$$\hat{\beta} = \frac{\sum_{i=1}^{n} f(\mathbf{X}_i) \cdot h(\mathbf{X}_i) - r(Q_r \cdot Q_{c,r})}{(r-1)\mathrm{Var}(h(\mathbf{X}_i))} \tag{4.8}$$

In the T&DE SSI application, the nonlinear ASRE/ASRE3D can be selected as $f(\mathbf{X})$. If a rigid connection is assumed at the soil-structure interface and the nonlinear sliders (see Fig. 3.10) are deactivated, a linear model can be easily obtained. The linear model can be considered a lower-fidelity model of the nonlinear ASRE/ASRE3D and is much cheaper to evaluate. The linear (lower fidelity) and nonlinear (higher fidelity) models are strongly correlated, and the linear model is used as $h(\mathbf{X})$ in this study. Because multiple fidelity models are used in the MC method, this method is called the multi-fidelity MC method in many engineering communities (e.g., [149, 150, 145]). $h(\mathbf{X})$ can be estimated with a much smaller computation expense (e.g., 40 seconds in ASRE3D using 1 process on the HPC Savio at UC Berkeley `https://research-it.berkeley.edu/services-projects/high-performance-computing-savio`, and 5000 crude MC simulations are completed first to estimate $\mathbf{E}[h(\mathbf{X})]$. Afterward, 200 pilot simulations ($r = 200$) are adopted to estimate $\hat{\beta}$, and another 4800 MC simulations are conducted to calculate an MFMC estimator with Eq. 4.7. The convergence and efficiency of the MFMC estimator are discussed later.

Quasi-MC methods use low-discrepancy point sets that behave more similarly to multi-variate uniform distributions than pseudorandom samples when the dimension is high and the sample size is relatively small. In fact, discrepancy (e.g., the star discrepancy defined in [137]) is a group of measures that describe the distinction between the empirical distribution of a point set and multivariate uniform distribution. It is widely recognized that in numerical integration, the trapezoidal and quadrature rules provide faster convergence than random samples when the integral dimension is low. This is because the design of experiment (DOE) points in trapezoidal/quadrature rules are more uniformly distributed (i.e., have lower discrepancy) than random sample points. However, as the integral dimension increases, trapezoidal/quadrature rules construct DOE points with a complete combination or product rule, and the number of DOE points increases exponentially with dimension. As a result, the number of integrand evaluations in trapezoidal/quadrature rules is not affordable in high-dimensional integral, and this phenomenon is called the "curse of dimensionality" [14]. Fig. 4.9a shows a plot of 64 DOE points for the trapezoidal rule in two dimensions, and it can be observed that the points in the same column/row have the same first/second coordinate. In contrast, points in crude MC samples or low-discrepancy point sets have distinct coordinates when they are projected on each dimension, as illustrated in Fig. 4.9b-4.9d, so that the integrand $f(\mathbf{X})$ is evaluated at more locations with a small sample size under high dimensionality. Moreover, low-discrepancy point sets (e.g., Fig. 4.9c and Fig. 4.9d) are designed such that the projection of the points on each coordinate distributes more evenly than crude MC sample points. As a result, low-discrepancy sample points take advantage of both trapezoidal/quadrature rules and crude MC method to achieve fast numerical integration. An estimator $Q_{qmc} = \frac{1}{n}\sum_{i=1}^{n} f(\tilde{\mathbf{X}}_i)$, where $\tilde{\mathbf{X}}_i$ are points in a low-discrepancy point set (P_n), is called a quasi-MC estimator. The lattices method and digit sequence/digit net are two groups of methods to construct low-discrepancy samples. A digit sequence, Sobol's sequence, is adopted in this dissertation.

It needs to be noted that points ($\tilde{\mathbf{X}}_i$) in low-discrepancy samples are not independent of each other. Therefore, the central limit theorem does not hold for Q_{qmc} , and the confidence interval $\left(Q_n \pm \frac{\sigma}{\sqrt{n}} z_{\alpha/2}\right)$ cannot be used. Instead, a randomized quasi-MC method can be applied to estimate the error of Q_{qmc}. The idea of RQMC is to create m random samples of Q_{qmc}, based on m randomized low-discrepancy point sets of size n. The randomized low-discrepancy point sets can be obtained from Sobol's sequences by scrambling and permutation [110], and the m Q_{qmc} can be considered m i.i.d. samples drawn from the population distribution of Q_{qmc} . As a result, an RQMC estimator Q_{rqmc} can be defined as the mean of the m quasi-random estimators (i.e., $Q_{rqmc} = \frac{1}{m}\sum_{i=1}^{m} Q_{qmc,l}$), and the central limit theory can be applied to Q_{rqmc}. The variance of Q_{rqmc} can be estimated with $\hat{\sigma}^2_{m,rqmc} = \frac{1}{m}\hat{\sigma}^2_{rqmc}$, where $\hat{\sigma}^2_{rqmc} = \frac{1}{m-1}\left(Q_{qmc,l} - Q_{rqmc}\right)^2$. The total number of model evaluations in RQMC is $m \times n$, and m and n are taken as 10 and 512 in this study. In theory, n should be taken as large as possible to reduce the variance of the quasi-random estimators, and m needs to be sufficiently large ($m \geq 10$) to achieve a reliable estimation of $\hat{\sigma}^2_{m,rqmc}$ [110].

The performance of the MFMC and RQMC methods is studied with a numerical experiment.

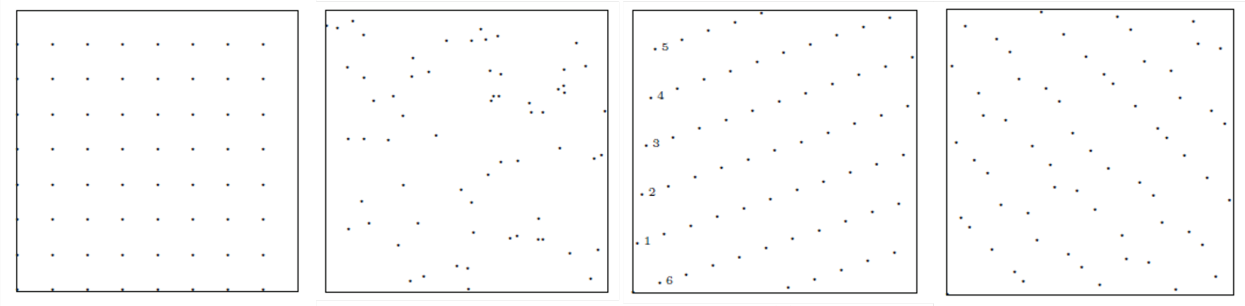

(a) (b) (c) (d)

Figure 4.9: Four different design of experiment point sets with 64 samples (a) trapezoidal rule; (b) crude MC; (c) A low discrepancy point set constructed with Korobov lattices; (d) A low discrepancy point set constructed with Sobol's sequence (after [110])

A community-level probabilistic building damage assessment (part of the 8th case study discussed in Chapter 6) in a deep excavation project is selected as the experimental problem. ASRE3D is adopted to model the excavation-soil-structure system (see Fig. 4.10). The uncertainty inputs are an RF model of the excavation-induced ground displacement, an RF model of soil stiffnesses, and four random variables describing building stiffnesses and building weights. The ground displacement profile perpendicular to the wall is described with the profiles proposed in Section 3.1.2, which is determined by three parameters δ_{vm}/H_e, η, and δ_{lm}/H_e, as shown in Eq. 4.2. The spatial variabilities of δ_{vm}/H_e, and η along the excavation wall are investigated in Section 4.2.1 and described with two 1D lognormal RFs with Gaussian semivariogram functions. δ_{lm}/H_e is modeled as δ_{vm}/H_e multiplying a random variable as suggested in [171]. The soil stiffness (E_s) in the area is described by another lognormal RF model, with a scale of fluctuation (SOF) equal to 10 m, which corresponds to the worst-case SOF scenario of building differential settlement as discussed in Section 4.2.1.

To generate the uncertainty input samples, the discrete Karhunen-Loève Expansion method is adopted. The number of independent random variables needed to realize δ_{vm}/H_e, η and E_s are 4, 10, and 510. With another 6 independent variables describing the uncertainty in the estimated δ_{lm}/δ_{vm}, building stiffnesses, and building dead loads, the total uncertainty dimension in the experiment problem is 550. The independent random variables are generated with the PCG64 pseudorandom number generator implemented in the python package NumpPy. The period of PCG64 is 2^{128}, which is greater than the square of the total number of random numbers needed in the experiment. As suggested by Lemieux [110], a pseudorandom generator with a period greater than the square of the total random numbers is suggested to ensure the random behavior of the samples. The MT19937 (default in Matlab) pseudorandom number generator with a long period of $2^{19937} - 1$ can be adopted if a larger number of random numbers is needed in the study. The engineering demand parameters (output from ASRE3D) are the characteristic strains in the two buildings (ε_A and ε_B). The quantities of interests are the probabilities ($p_{f,A}$ and $p_{f,B}$) that ε_A and ε_B exceed the limit state strains (ε_{lim}, see Section 3.5).

The crude MC, MFMC, and RQMC methods are applied to the experiment problem, and their performance is compared. In the crude MC methods, 5000 simulations are conducted. To enable fast simulation, ASRE 3D is computationally optimized by C++ optimizing compiler, sparse storage scheme, and high-performance linear solver (see Section 5.2). The time required for one model evaluation is around 108 seconds using one process on the HPC Savio at UC Berkeley. Using the same HPC, 5000 MC simulations take 2 hours, 6 minutes, and 35 seconds.

Fig. 4.11 compares the evolution of $p_{f,A}$ and $p_{f,B}$ with the number of model evaluations between the crude MC and MFMC methods. It can be observed that $p_{f,A}$ and $p_{f,B}$ estimated with the MFMC method are very close to the values estimated with the crude MC method, but the 95% confidence interval (CI) half-width bandwidths of the MFMC estimators are much smaller than the crude MC estimators. The values of $p_{f,A}$ and $p_{f,B}$ estimated with the MFMC method at a small sample size are also closer to the final estimations than the crude MC method. This shows that the MFMC method needs fewer model evaluations to achieve the same level of accuracy as the crude MC method. The computation times and efficiencies are reported in Table 4.3 and Table 4.4. ε_A and ε_B are two outputs from the structural analysis model, so the computation time for each method is the same in Table 4.3 and Table 4.4. The computation time in the MFMC method is longer than the crude MC method because of the additional evaluations of the lower fidelity model. Building A in ASRE3D shows weak nonlinearity, and the correlation coefficient between the linear and nonlinear models is around 0.7. In contrast, building B shows stronger nonlinearity, and the correlation coefficient between linear and nonlinear models is around 0.5. Since a strong correlation between multi-fidelity models is preferred in the MFMC method, the efficiency of building A increased more from the MFMC method.

Fig. 4.12 compares the convergence of the crude MC method and the RQMC method. The $p_{f,A}$ and $p_{f,B}$ estimated with RQMC also show smaller confidence intervals than the crude MC method. The computation time and efficiency are also reported in Table 4.3 and Table 4.4. The computation time is slightly larger than the crude MC method because around 100 more model evaluations are required in the RQMC method. However, the efficiency for estimating both $p_{f,A}$ and $p_{f,B}$ improved significantly, and the efficiency improvement of $p_{f,A}$ is larger than $p_{f,B}$. To better study the convergence rate of $p_{f,A}$ and $p_{f,B}$, another 5120 quasi-random samples are generated (i.e., $m = 20$) and evaluated with ASRE3D for a better estimation of $\hat{\sigma}^2_{rqmc}$. A log2-log2 plot is then produced for the 95% confidence half-width bandwidths of the crude MC and $Q_{qmc,l}$ in Fig. 4.13. As suggested in [107, 106], RQMC can also reduce the estimator variance because:

$$\mathrm{Var}[Q_{qmc,l}] = \frac{\mathrm{Var}[f(\tilde{\mathbf{X}}_i)]}{n} + \frac{2}{n^2}\sum_{i<j}\mathrm{COV}[f(\tilde{\mathbf{X}}_i), f(\tilde{\mathbf{X}}_j)] \tag{4.9}$$

and $\mathrm{COV}[f(\tilde{\mathbf{X}}_i), f(\tilde{\mathbf{X}}_j)]$ is generally pairwise negative in the RQMC method. Fig. 4.13 shows that the variance reduction effect for estimating $p_{f,A}$ is more significant than $p_{f,B}$. This may again because the nonlinearity in building A is weaker than building B, and $\tilde{\mathbf{X}}_i$ and $\tilde{\mathbf{X}}_j$ are better separated after being transformed by f (i.e., ASRE3D). $p_{f,B}$ shows a larger convergence rate than $p_{f,A}$, and this may be because the SAM of building B is "smoother" than building A. Quasi-MC methods can usually achieve faster convergence when the integrand is "smoother." However, the "smoothness" is defined based on the derivative of $f(\mathbf{X})$ and is hard to be examined for ASRE3D.

From the numerical experiment, it was found that the MFMC method improved the numerical integration efficiency by 30-70%, and the RQMC method improved the efficiency by 70-140%. The performance of the MFMC method depends on the correlation between the lower- and higher-fidelity models. A more considerable efficiency improvement can be achieved if a lower-fidelity model strongly correlated to the higher-fidelity model can be constructed. On the other hand, the performance of the RQMC method may depend on the integrand (the structural analysis model) in the numerical integration. A "smoother" SAM with weaker nonlinearity may benefit more from the RQMC method. In practice, a lower-fidelity model needs to be developed for the MFMC method, while the RQMC method is easier to implement. Quasi-random number generators can be found in many scientific computing platforms, such as Python, R, Matlab, and C++. Simply replacing pseudo-random generators with quasi-random generators may significantly increase the efficiency of uncertainty propagation. However, the number of samples in RQMC needs to be carefully selected (e.g., Sobol's sequence requires the sample size to be a power of 2), and the estimation of variance is not as easy as the crude MC method. Nevertheless, both MFMC and RQMC methods show promising potential in T&DE engineering and broader civil infrastructure engineering applications.

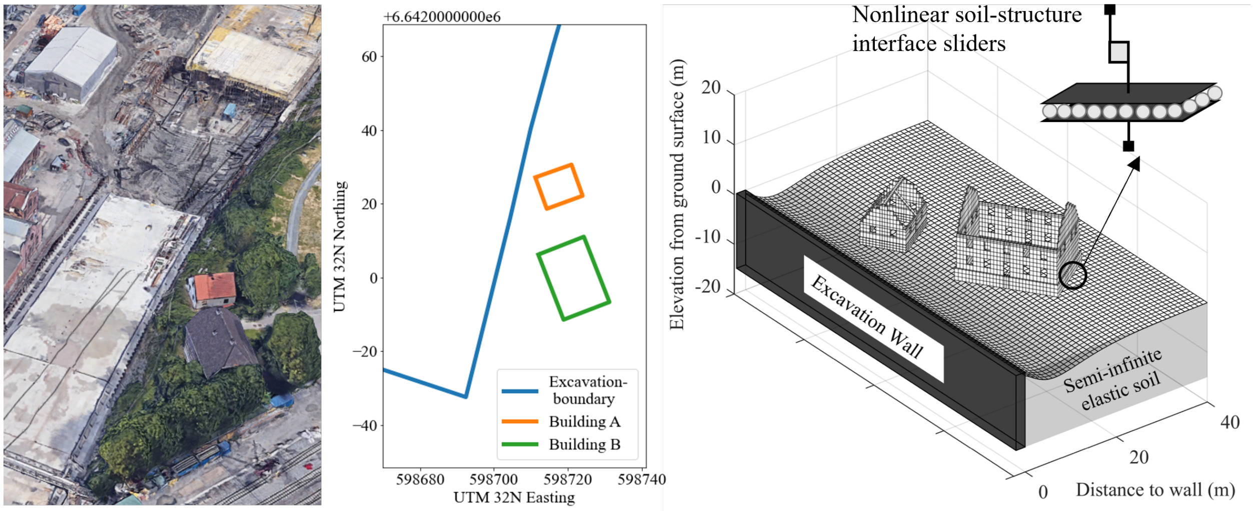

Figure 4.10: Numerical experiment problem: (a) bird's eye view of the studied area; (b) location of the excavation wall and studied buildings; (c) ASRE3D model

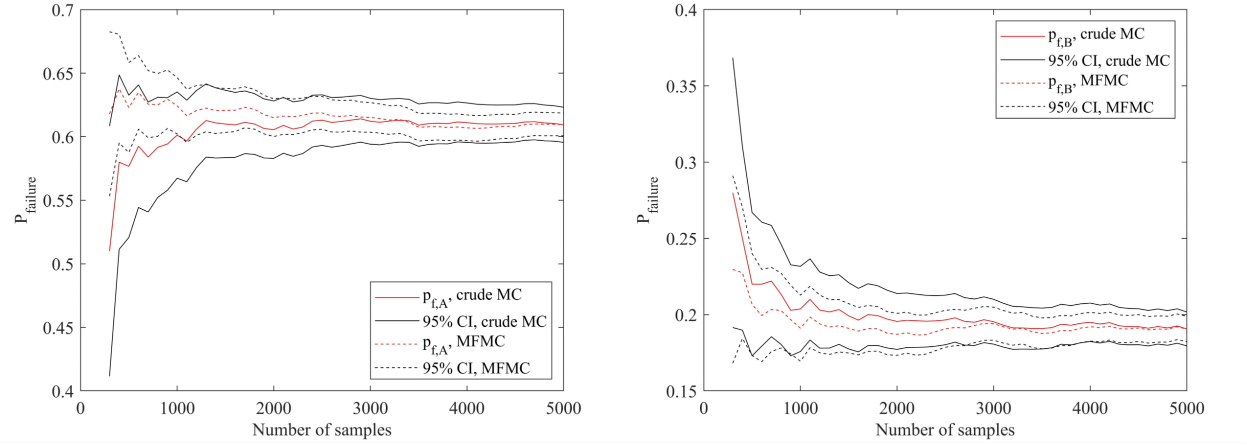

(a) (b)

Figure 4.11: Convergence of crude MC vs MFMC: (a) evolution of $p_{f,A}$; (b) evolution of $p_{f,B}$.

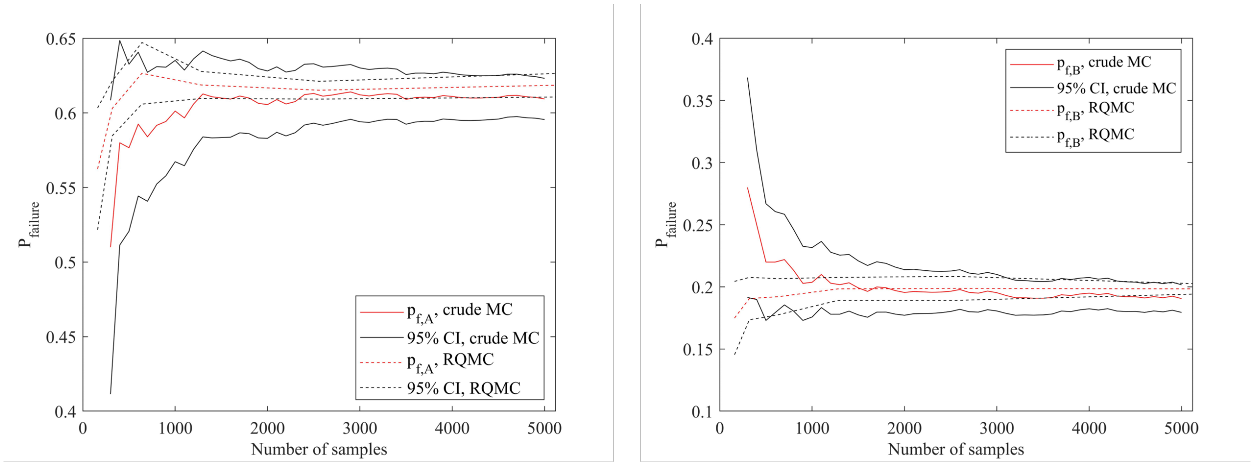

(a) (b)

Figure 4.12: Convergence of crude MC vs RQMC: (a) evolution of $p_{f,A}$; (b) evolution of $p_{f,B}$.

Method	$p_{f,A}$	HW	Time (min)	Efficiency	Efficiency improvement
Crude MC	61.12%	1.35%	126.6	166.19	0%
MFMC	60.97%	0.9%	169.8	281.13	69.16%
RQMC	61.86%	0.79%	151.2	408.26	145.66%

Table 4.3: Comparison of MC estimators for $p_{f,A}$, where HW is the half-width of the 95% confidence interval.

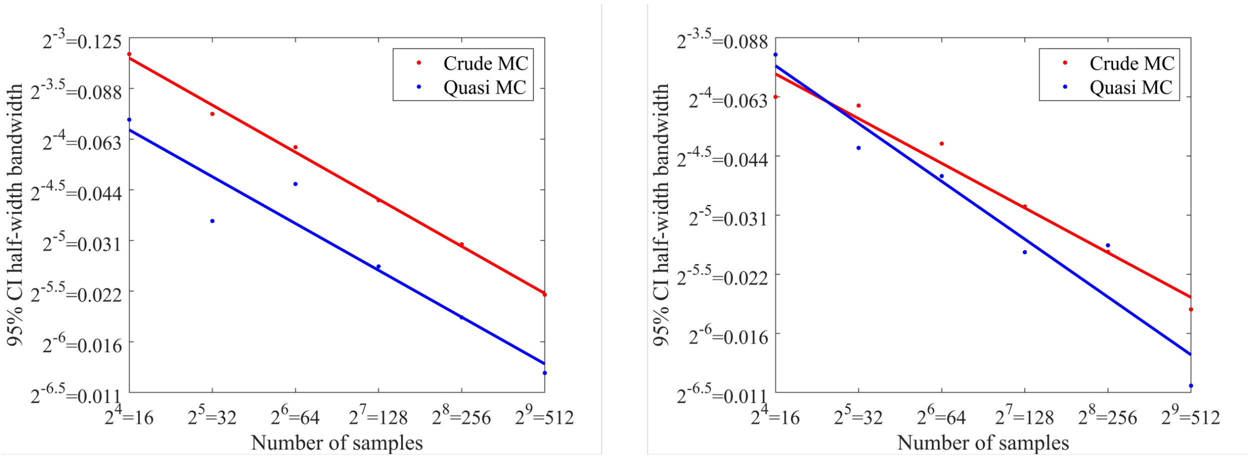

(a) (b)

Figure 4.13: Convergence rate of crude MC and QMC. (a) building A; (b) building B.

Method	$p_{f,B}$	HW	Time (min)	Efficiency	Efficiency improvement
Crude MC	19.04%	1.09%	126.6	256.19	0%
MFMC	19.06%	0.83%	169.8	329.40	28.58%
RQMC	19.84%	0.64%	151.2	438.68	71.23%

Table 4.4: Comparison of MC estimators for $p_{f,B}$, where HW is the half-width of the 95% confidence interval.

4.5 Factor mapping analysis and variance-based sensitivity analysis

After an empirical probability distribution of the engineering demand parameters (e.g., ε_{lim} in equivalent beam model) is obtained from the MC simulation, it is helpful to research which input parameters are the most responsible for building damage. Burland, Mair, and Standing [27] suggested that the causes of surface building damage are useful but difficult to determine. A factor mapping analysis [167] can be implemented to research the association between the input random variables and the damage level of buildings. In factor mapping analysis, the model realizations from the previous MC simulations are partitioned into "behavioral" (B) and "nonbehavioral" ($\bar{B}$) groups. The input samples are therefore divided into two subgroups ($X_i|B$ and $X_i|\bar{B}$), where X_i stands for the i^{th} input random variable. The cumulative density functions (CDF) of the two subgroups ($F(X_i|B)$ and $F(X_i|\bar{B})$) are compared with each other and the difference between them is used to measure the strength of correlation between the i^{th} input variable and "behavioral" damage. The Smirnov two-sample test [177], as shown in Eq. 4.10, is used in this study to quantify the difference between

$F(X_i|B)$ and $F(X_i|\bar{B})$. A larger Smirnov two-sample test index for X_i indicates that there is larger difference between $F(X_i|B)$ and $F(X_i|\bar{B})$, and X_i has a larger contribution for a behavioral result. This technique is also called Monte-Carlo Filtering or Regional Sensitivity Analysis, which was first introduced by Young, Hornberger, and Spear [204].

$$d_{B,\bar{B}}(X_i) = sup||F(X_i|B) - F(X_i|\bar{B})|| \tag{4.10}$$

To investigate how the uncertainty in the EDP can be apportioned to different sources of uncertainty in the input variables, a global sensitivity analysis can be conducted. Variance based sensitivity analysis (Sobol's method) is a robust and widely accepted global sensitivity analysis which requires a large number of deterministic model evaluations [167, 168]. Sobol's method is commonly not feasible in research without surrogate models, but it is adopted in this dissertation directly because of the fast nature of ASRE/ASRE3D. The procedures of Sobol's method can be found in [167, 168], and briefly described here:

- Generate two (N, k) sample matrices A and B, where N is the base sample size and k corresponds to the number of input uncertainty parameters. Each row of A and B corresponds to a group of independent samples of the k parameters, and A and B each consist of N groups of independent samples.

- Create k matrices C_i with all columns identical to B except for the i^{th} column which is identical to A, where i ranges from 1 to k.

- Compute the model output by evaluating ASRE/ASRE3D with input from A,B and C_i and denote the results as y_A, y_B and $y_{(C_i)}$ respectively. There are $N(k+2)$ model evaluations in total.

- Calculate the first order Sobol's indices (main effect) and the total effect indices, S_i and $S_{(T_i)}$, using Eq. 4.11.

$$S_i = \frac{V[E(Y|X_i)]}{V(Y)} = \frac{y_A y_{C_i} - f_0^2}{y_A y_A - f_0^2} = \frac{\frac{1}{N}\sum_{j=1}^{N} {y_A}^{(j)} {y_{C_i}}^{(j)} - f_0^2}{\frac{1}{N}\sum_{j=1}^{N} {y_A}^{(j)} {y_A}^{(j)} - f_0^2} \tag{4.11a}$$

$$S_{T_i} = \frac{V[E(Y|X_{\sim i})]}{V(Y)} = 1 - \frac{y_B y_{C_i} - f_0^2}{y_A y_A - f_0^2} = 1 - \frac{\frac{1}{N}\sum_{j=1}^{N} {y_B}^{(j)} {y_{C_i}}^{(j)} - f_0^2}{\frac{1}{N}\sum_{j=1}^{N} {y_A}^{(j)} {y_A}^{(j)} - f_0^2} \tag{4.11b}$$

$$f_0^2 = \left(\frac{1}{N}\sum_{j=1}^{N} {y_A}^{(j)}\right)^2 \tag{4.11c}$$

The first order Sobol's index (S_i) equals to the variance of the conditional mean of the system output when the i^{th} parameter is fixed. It represents the main effect contribution of each input random variable to the variance of the output, without interaction with other random variables.

The total effect index (S_{T_i}) accounts for the total contribution of the i^{th} parameter to the output variation, i.e., the first-order effect plus all higher-order effects due to interaction. A small total effect index indicates that if the corresponding input parameter was fixed at any value within its range of variability, there would only be a slight effect on the output. Similar to other Monte Carlo methods, a convergence test, as suggested by Nossent, Elsen, and Bauwens [139], is needed to determine the base sample size required for the sensitivity analysis. As an example, the base sample size in the sensitivity analysis of the case study in Section 6.1.1 is increased consecutively, and the variation of S_i and S_{T_i} versus base sample size are plotted in Fig. 4.14, together with the corresponding 90% confidence intervals. For clarity, only the indices for V_L are plotted, while the indices for all 6 uncertain parameters converge when the base sample size is 3072. To ensure satisfactory convergence, the base sample size is conservatively taken as 4096 for the sensitivity analysis in this case study. The probability model-based framework consists of two main elements. The first is data extraction, in which the variables of interest (VoI) and quantity of interest (QoI) from an input-output data matrix are extracted. The second element is probability model training, in which a probability model, such as Gaussian copula model or Gaussian mixture model, is built to approximate the joint probability density function between the VoI and QoI. The learned probability model is then used to compute various Sobol's indices. The probability model-based sensitivity analysis can estimate Sobol's indices without additional model evaluation from the MC-based uncertainty propagation. However, assumptions of probability models have to be made, which may increase model uncertainty in the analysis.

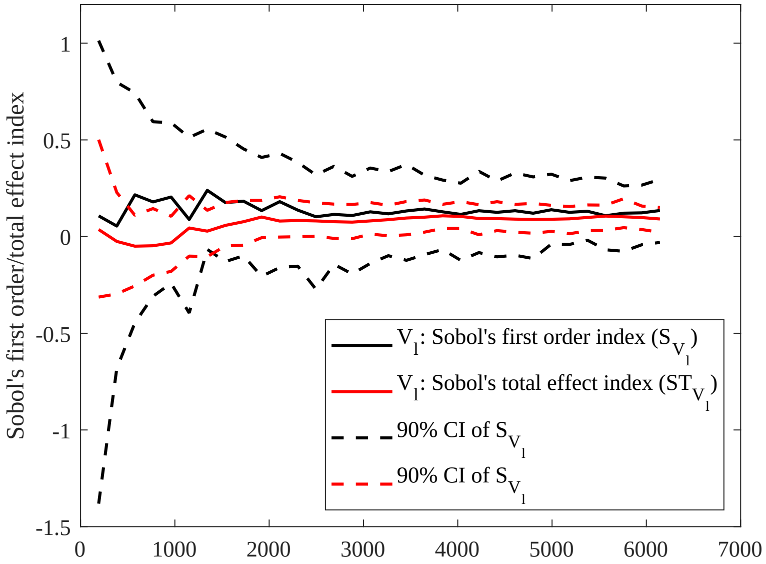

Figure 4.14: Evolution of Sobol's first and total effect index of V_L

The procedures of Sobol's method described above are not applicable when the spatial variability in T&DE SSI is considered and random field models are adopted to simulate the input uncertainty. As a result, the input uncertainty can be divided into groups, e.g., all the random variables used in the discrete Karhunen-Loève expansion to simulate the random field of V_L are classified in one group, all the random variables used to simulate E_s are classified in one, etc. When constructing the C_i metrics in the second step described above, all the columns corresponding to each input parameter group are substituted from the A matrix by the columns in the B matrix. The rest procedure is the same as above. If the Monte Carlo-based sensitivity analysis is considered too computationally costly, a probability model-based approach [96] can be adopted.

4.6 A regional probabilistic assessment approach

In large tunneling or deep excavation projects, the building performance analysis has to be conducted on a regional scale so that holistic performance-based engineering can be accomplished. Owing to the complexity of the large-scale problems, soil-structure interaction analysis may experience significant uncertainty induced by limited site characterization and building characterization. As a result, the probabilistic analysis and sensitivity analysis framework proposed in this dissertation is very helpful in quantifying the uncertainty on the regional scale, making decisions under high-dimensional uncertainty, and allocating limited modeling and investigating resources. Moreover, thanks to the fast nature of the soil-structure models described in Chapter 3 and the advanced uncertainty quantification approaches described in Section 4.4, a practical computation tool has been developed (see Chapter 5). In concept, the regional assessment in this context is just to loop through all buildings in the region, however, four challenges need to be taken care of. The first is to simulate the spatial correlation/variability structure of the uncertainty. This challenge is discussed extensively in Section 4.2. The second challenge is generating a building and geotechnical asset inventory and structural analysis model generation. The third is the large computational cost in regional scale simulations, and the fourth challenge is the visualization of the analysis results. The last three challenges are discussed in this section.

In large tunnel projects, desktop studies and pre-construction surveys are usually conducted, which provide data resources to create regional building inventory. For example, in the Alaskan Way Viaduct replacement program in Seattle, WA, a two-mile tunnel wad built underneath the city of Seattle. The Washington State Department of Transportation (WSDOT) conducted a pre-construction survey of 110 buildings. For each building, a report consisting of "building information", "project background", "introduction", "observation and types of issues", and "survey limitations" is prepared and is openly accessible from the WSDOT database. The "building information" consists of basic building geographic information, building height, and footprint area. The "project background and introduction" describes the information about the tunnel adjacent to the building. "Observation and type of issues" describes the types and locations of existing damages, such as concrete cracks, spalling, and surface deterioration. "Survey limitations" describes the part of the buildings that are not accessible. Furthermore, in the appendix, floor plans are attached if available. In addition to pre-construction surveys, open-source geographic databases and open-accessible public census records can be used to supplement the building inventory. Fig. 4.15 is an example of the floor plan reported in a pre-construction survey published by the WSDOT, and Fig. 4.16 is the building information published by the King's County GIS center. Despite the large volume of information, there are a few challenges in building inventory development. The first challenge is that the available data, e.g., the floor plan in Fig. 4.15 may show a low resolution, and much information about the foundation system is missing. There are many current research projects on extracting building information from imagery remote sensing data. For example, the NHERI Natural Hazards Reconnaissance (RAPID) facility has done tremendous research on UAV and Lidar-based 3D point cloud scanning of urban buildings. Another research project is the artificial intelligence-enabled building recognition tool BRAILS [193], in which building information is extracted from street images and similar buildings, developed by the NHERI SimCenter at UC Berkeley. However, most of the street images only contain information about the superstructure, and the recognition of foundation systems remains challenging. The second challenge in building inventory development is the automated structure analysis model developed according to the metadata in building inventory. There is research (e.g., [143, 155]) in detecting beam-column location and dimensions from floor plan drawings, but a complete workflow from building inventory to soil-structure analysis model (e.g., ASRE3D or OpenSees model) is still missing. In the regional assessment presented in this dissertation (i.e., the 8th case study in Chapter 6), the building and foundation information is surveyed on-site by the author, and ASRE3D models are created manually. Future research is needed to automate this process, and the application of AI techniques is important to analyze and transform the big building inventory data into structural analysis models.

Another challenge in regional simulation and assessment is the high computation cost. A full-scale nonlinear structural analysis model evaluation for a single building may take hours to days in a workstation. The computation cost is dramatic when hundreds of buildings need to be analyzed on a regional scale. Furthermore, uncertainty quantification, especially when high-dimensional uncertainty is considered and MC methods are adopted, can increase the computation time by hundreds/thousands of times. Besides optimizing the computational performance of the structural analysis model (e.g., developing reduced order models and optimized computer programs such as ASRE/ASRE3D) and utilizing advanced uncertainty quantification algorithms, the research for this dissertation uses the staged assessment approach and high-performance computers to achieve regional assessment in a reasonable time. In the staged building damage assessment, the first stage assessment only considers the impact level (greenfield ground movements), and buildings subject to significant impact are identified. Significantly impacted buildings are then sent to a second stage assessment, where ASRE/ASRE3D models are developed, and MC simulations are conducted in high-performance computers to estimate the damage probabilities of the buildings. This demonstrates that the combination of a staged or multilevel assessment approach and high-performance computers/cloud computer provides one solution to the challenge of high computation cost in regional assessment.

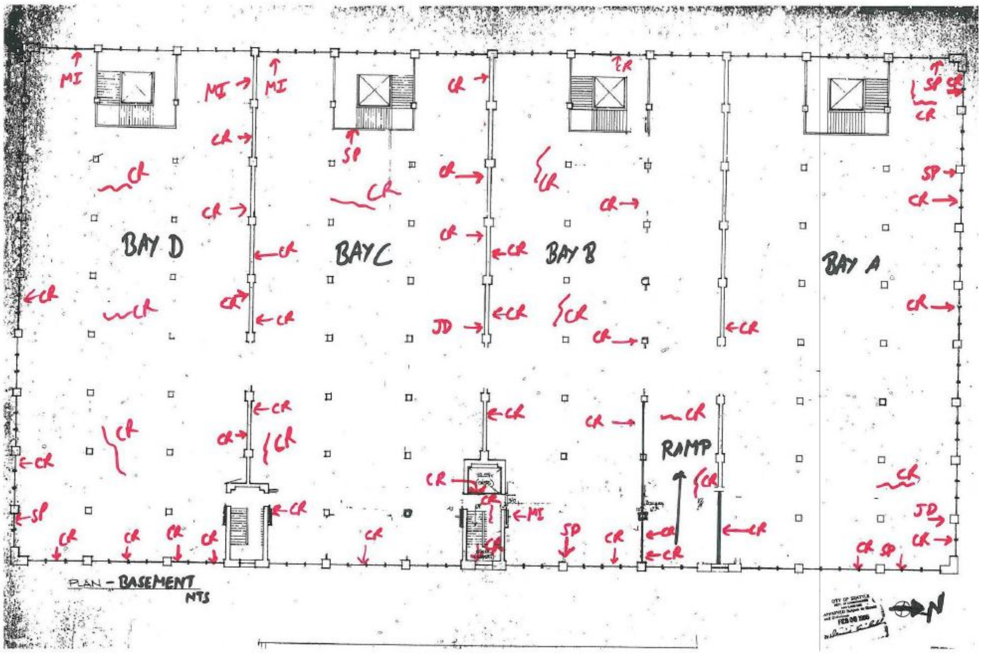

Figure 4.15: Floor plan of a building published by the WSDOT's pre-construction survey

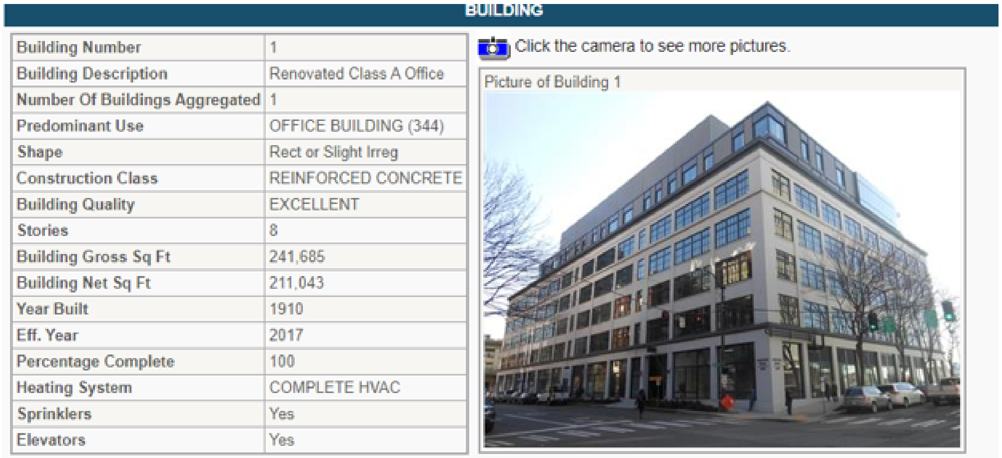

Building Number	1
Building Description	Renovated Class A Office
Number Of Buildings Aggregated	1
Predominant Use	OFFICE BUILDING (344)
Shape	Rect or Slight Irreg
Construction Class	REINFORCED CONCRETE
Building Quality	EXCELLENT
Stories	8
Building Gross Sq Ft	241,685
Building Net Sq Ft	211,043
Year Built	1910
Eff. Year	2017
Percentage Complete	100
Heating System	COMPLETE HVAC
Sprinklers	Yes
Elevators	Yes

Figure 4.16: Information of a building published by King's County GIS center

The final challenge is to analyze and visualize the spatially distributed simulation result. A geographic information system (GIS) is adopted in this dissertation. The open-source package Geopanda is used to manage the geographic information of surface buildings in tunneling and deep excavation projects and produce interactive maps and visualization of assessment results on the regional scale. Some interactive maps can be found at the link: `git@github.com:jinyan1214/interactivePlots.git`. Besides GIS, researchers at Ruhr University Bochum have developed a tunnel information modeling framework to support the management, simulations, and visualizations of spatially distributed tunnel projects [104, 126]. The tunnel information model may provide a great tool for the management and visualization of building inventory and assessment results. However, more development is needed for the connection between model management and scientific computation.

4.7 Summary

The uncertainty in T&DE SSI modeling using ASRE and ASRE3D was discussed in this chapter. First, probabilistic models describing the variance and spatial variability of ground displacements were proposed based on case history data. In addition, commonly adopted probabilistic models describing the uncertainty of soil and building stiffness were reviewed and summarized. It was found that the 2D T&DE SSI models may not capture the 3D soil-structure interaction mechanisms, even if probabilistic models are adopted to describe the uncertainty of the building stiffness in the 2D models. As a result, it was concluded that the 3D model is a more appropriate modeling fidelity when the T&DE and building configuration can not be approximated with a plane strain condition. Moreover, a framework of probabilistic performance-based engineering (PPBE) was proposed. The proposed PPBE framework involves high-dimension uncertainty quantification and advanced Monte Carlo-based uncertainty propagation methods. Through a numerical experiment, the advanced Monte Carlo methods were shown to increase the efficiency of the uncertainty propagation process significantly. However, the computational cost of the proposed PPBE approach may still be significant. To enable applying the proposed PPBE approach on a regional scale, a high-performance computational tool is developed and presented in the next Chapter.

Chapter 5

The computer program UQ-TESSI

5.1 General design

As part of the research for this dissertaion, a computer program was developed by the author to implement the T&DE SSI analysis with the uncertainty and sensitivity analysis described in Chapter 4. The program is named `UQ-TESSI` and is developed on the basis of the Matlab-based computer program `ASRE`, which was originally created by Franza and DeJong [63]. However, it is rewritten and extended in C++ to achieve the high computational performance required by the uncertainty analysis approach.

`UQ-TESSI` has three modules, namely `Drivers`, `Samplers`, and `ASRE`, as shown in Fig. 5.1. The object-oriented programing paradigm is adopted to enable polymorphism and a flexible connection between modules. The program is driven by four types of `Drivers`, of which three are used for MC-based uncertainty propagation and the other is a variance-based global sensitivity analysis driver using Sobol's method. Users choose a `Driver` and the corresponding `Sampler`. If spatial variability is not considered and only independent random variable samples are needed, a `Sampler` written in C++ can be invoked by the `Drivers`. If spatial variability is considered, `Samplers` in Jupyter Notebook is developed to achieve a convenient input of uncertainty models and visualization of the generated samples. A JSON file containing the samples is created by `Samplers` and passed to `Drivers`. The `Drivers` then invoke `ASRE` and evaluate the user-selected T&DE SSI model in `ASRE` at the sample points. The `Drivers` and `ASRE` are written in C++ to achieve fast computational performance. After completing the uncertainty quantification routine, `Drivers` write the sample of EDPs in a .txt file. A post-processing python code is developed to estimate the QoIs and the associated error and visualize the QoIs on a regional/community scale using open-source Geographic Information Systems packages.

The program is designed to be object-oriented, and the four `Drivers` are both child classes of a parent class `driverbase`. Similarly, all the models in `ASRE` are child classes of a parent `SAM`, which stands for structural analysis models. The object-oriented paradigm is selected because: 1) in the regional analysis approach, each building can be treated as one object with its associated `SAM` and building properties, and as a result, it is easier to manage regional-scale modeling and simulation; 2) each building may have multiple `SAM`s, so that the multi-fidelity uncertainty quantification approach is easier to be realized; 3) polymorphism is achieved and other `Drivers` (e.g., surrogate modeling driver) or other types of `SAM` can be easily added to `UQ-TESSI`.

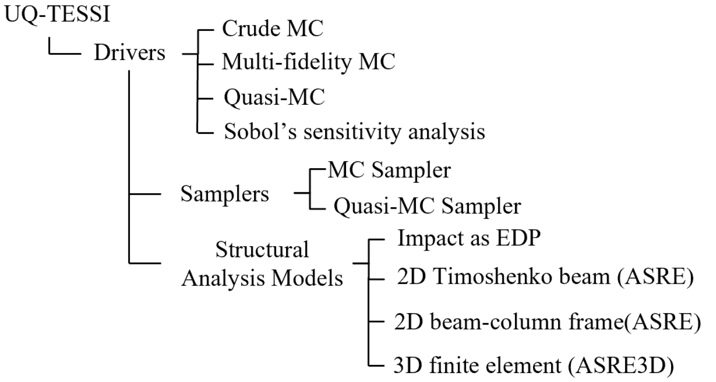

Figure 5.1: Design of UQ-TESSI

The structural analysis models included in `UQ-TESSI` are the impact as EDP model, 2D equivalent Timoshenko beam model, 2D beam-column frame model, and 3D finite element model (ASRE3D). An `IO` class is created to read the input sample and model parameters from the file system and write the uncertainty quantification results in the file system. The input model parameters of the Timoshenko beam model are the dimensions, relative location to tunnel or deep excavation, material properties, and discretization size, as noted in Chapter 3. The elastic 2D frame model in `ASRE` initially developed by Franza and DeJong [63] considers each frame member as an isotropic elastic beam element and formulates the frame stiffness matrix with the displacement method. However, the initial elastic 2D frame model implementation is considered to be too simple because it only supports the modeling of structures with identical footings, one column on each footing, equal floor elevations, equal beam span widths, and the same beam and column dimensions. Moreover, infill walls, which may significantly affect the structure stiffness, were not previously considered. The structural analysis model for frame structures in the initial `ASRE` is extended in this study to include irregular frames and infill walls. The 2D elastic frame structure model in `UQ-TESSI` takes the dimensions and locations of each frame panel and the material properties of each structure element, and runs structure analysis as described in Section 3.3. `ASRE3D` take the mesh of 3D finite element models, the representative soil stiffnesses at each discretization point at the soil-structure interface, the building stiffness and weight, and greenfield ground movements as input and run soil-structure interaction analysis as discussed in Section 3.2. `ImpactAsEDP` model is designed for fast first-stage assessment where the soil-structure interaction effect is neglected, and the building damage stage is estimated directly from the impact level (i.e., the magnitude of the greenfield ground displacement). All the `SAM` contains the member function `setRV` and `run` to set the random parameters as samples generated by `Samplers` and run analysis.

To facilitate the usage of `ASRE3D`, a Matlab package `MasonMesh` [210] is also developed to generate 3D structured FEM meshes for shallow foundation masonry buildings. Users input building geometry, foundation geometry, location of openings, and size of elements. The package will generate the coordinates of nodes and the connectivity of 8-node finite elements. The package is developed so that structured meshes (the elements in the mesh are more similar to squares or cubes than an unstructured mesh). Despite structured meshes not being applicable to arbitrary geometries, they can be applied to most masonry buildings since the facade in most buildings are polygons with similar wall thickness. Meshes generated with other meshing packages, such as Gmsh [70] or Grasshopper Plugins, can also be used in `ASRE3D`.

An `IO` is designed to take the input files of multiple buildings with different types of `SAM`, and uncertainty or Sobol's sensitivity analysis can be done for all the buildings. The external libraries used in `UQ-TESSI` are `openMP`, `OpenMPI`, `Boost`, and `Eigen`, which are adopted for parallel computation, random number handling, linear algebra calculation, and linear equation solving. When `ImpactAsEDP` or 2D `ASRE` are adopted, `UQ-TESSI` can run uncertainty quantification on a single workstation in a reasonable time (within tens of minutes for each building as shown in Chapter 6). When `ASRE3D` is adopted, the computation cost increases significantly, and `UQ-TESSI` runs on high-performance computers. The HPC SAVIO at UC Berkeley `https://research-it.berkeley.edu/services-projects/high-performance-computing-savio` is used in this dissertation and the uncertainty quantification of one building takes around 1-2 hours using round 100-200 processes. The computation time may depend on the size of the analyzed building and the number of computation nodes employed.

5.2 Computational performance optimization

As discussed in Chapter 4, Monte Carlo methods are adopted as the uncertainty propagation method in this dissertation. Despite two advanced MC methods being adopted, the MC methods require a large number of model evaluations to ensure an accurate estimation of the quantities of interest. Therefore, it is crucial to optimize the computational performance of `UQ-TESSI`. Four considerations are made to ensure relatively high performance of `UQ-TESSI`. Firstly, the programming language is chosen to be C++ because it is both a compiled language and an object-oriented language. The programs written in compiled languages are generally faster than those written in interpreted languages, such as Python and Matlab. The object-oriented nature makes it easier to add new features to `UQ-TESSI`. The second high-performance consideration is sparse matrix storage schemes. When `ASRE3D` is adopted, the matrices can be large, and the compressed column storage scheme implemented in `Eigen` is used to store the stiffness matrices. While a sparse storage scheme saves memory consumption, it slows down element access and many linear algebra operations. As a result, the dense storage scheme is used in the 2D models in `ASRE` since memory consumption is not a bottleneck for the 2D models. The third high-performance consideration is the adoption of fast linear equation solvers. When spatial variability of soil is not considered, the soil flexibility matrix is symmetric positive-definite and `LDLT` or `SimplicialLDLT` in the library `Eigen` are adopted in `SAM` classes.When the spatial variability of soil is considered, the soil flexibility matrix may be asymmetric and `PartialPivLU` or `SparseLU` solvers in `Eigen` are adopted. Eq. 3.20 is solved by a modified Newton-Raphson, and the matrix to be solved is kept constant. As a result, the matrix is decomposed at the beginning of the modified Newton-Raphson and a forward substitution is conducted in each iteration. Theoretically, the standard Cholesky decomposition `LLT` is faster than `LDLT` when it is used to solve symmetric positive-definite matrices, and `LDLT` is preferable for symmetric semi-definite matrices. However, several numerical tests showed that the speed difference of `LLT` and `LDLT` is negligible in this dissertation's application. Additionally, `LDLT` might be more stable and accurate if the soil is much softer than the building and the matrix to be inverted may have eigenvalues close to zero due to nearly rigid body motions of part of the soil-structure system. As a result, the `LDLT` solver is selected to solve Eq. 3.20 when spatial variability of soil is neglected and the matrices to be inverted are symmetric positive-definite.

The final high-performance consideration to optimize `UQ-TESSI` is the parallel computation strategy. Because the evaluation of each Monte-Carlo sample is independent of other evaluations, an "embarrassingly parallel" computation strategy can be adopted. 2D `ASRE` in `UQ-TESSI` is primitively designed for local civil engineers to carry out uncertainty analysis and facilitate decision-making in tunneling and deep-excavation projects. Therefore, 2D `ASRE` in `UQ-TESSI` is designed to run on shared memory and multi-core personal computers, and the corresponding multi-thread computation strategy is adopted. With the four optimization considerations, the uncertainty analysis and sensitivity analysis for each 2D `ASRE` model can be completed in around 10 min for a typical tunnel- or deep excavation-soil-structure-interaction case. The computation time is tested on a computer with an Intel 6 core i7-8700 CPU and Ubuntu 18.04.4 LTS operation system. When higher analysis fidelity is desired and `ASRE3D` is selected, HPC clusters have to be adopted to complete the MC-based uncertainty quantification in a reasonable time, and the uncertainty quantification for a typical building may take around 1-2 hours using round 100-200 processes. The time can be further reduced if more HPC nodes are employed. Because a deterministic 3D building model analysis may easily take hours in current civil engineering practice, `ASRE3D` and `UQ-TESSI` are considered a fast solution for the uncertainty quantification for T&DE SSI problems. Moreover, the civil engineering industry has been seeing a fast increase in the usage of cloud computing. As a result, it is believed `ASRE3D` and `UQ-TESSI` are a good addition to practical tunnel and excavation planning and design. In the future, the author is also interested in exploring some *model reduction* (e.g., [15]) techniques to further reduce the computation time of `ASRE3D` and `UQ-TESSI`.

5.3 Usage example

The `UQ-TESSI` takes an overall input file in `json` format, which is designed as Fig. 5.2, in which `"BuildingFileFolder"` is a path to the directory that contains all the individual input files and `"OutputFolder"` is the directory to store simulation results. The individual input file for each building is also a `json` file as shown in Fig. 5.3 and Fig. 5.4, for Timoshenko beam model and 2D elastic frame model, respectively. The fields of the input files are almost self-explanatory. Fig. 5.5 is an example of the input file for `ASRE3D`, where `elem2nInter` and `interNodesXYZ` are 2D mesh at the soil-structure interface used for calculating Mindlin's soil flexibility solution. `wholeElem2n` defines the connectivity of nodes , and `wholeNodesXYZ` defines the coordinates of the nodes in the mesh. If spatial variability is not considered and the `Sampler` in `UQ-TESSI` is employed, the random variables are defined in the field `"RV"`, and all the variables listed above `"RV"` can be included as random variables. Each random variable is defined with corresponding statistical descriptions, which are typically its distribution type, mean, and coefficient of variance. If spatial variability is considered, the `Samplers` in Jupyter Notebook needs to be employed. The path to the `json` file containing samples generated by the `Samplers` needs to be provided in the input file. The analysis results are saved to local file systems (e.g., 5.6), and the post-processing procedures of the data are done in Matlab and Python. Some typical post-processed results are shown in Chapter 6.

```
{
    "BuildingFileType": "json",
    "BuildingFileFolder": "/UQTSI/buildingInfoFrameDE",
    "OutputFolder": "/UQTSI/results/",
    "NumberofBuildings": "5"
    "SampleFileFolder":"/UQTSI/samples"
}
```

Figure 5.2: An example of the overall input file

```
{
    "ID": 1,
    "Building_Type": "Timoshenko_Tunnel",
    "Analysis": {
        "Type": "UQ",
        "ModelType": "Timoshenko",
        "ExcavationType": "Tunnel"
    },
    "Es": 25000000,
    "nis": 0.3,
    "phi_int": 30,
```

```
    "Foot_properties":{
        "d_na": 1.5,
        "B_X_foot": 30,
        "h_el_foot": 2,
        "Efoot": 3000000000,
        "ni_foot": 0.3,
        "EGratio": 12.5,
        "H_target": 6,
        "c_shear": 1.5,
        "s_shear": 0,
        "dfoot": 6,
        "bfoot": 1
    },
    "Footing_dimNloading":{
        "X_foot_centr": 0,
        "Y_foot_centr": 0,
        "Z_foot_centr": 0,
        "Fx_foot_centr": 0,
        "Fz_foot_centr": 0,
        "My_foot_centr": 0,
        "qx_foot": 0,
        "qz_foot": 100000
    },
    "Tunnel_properties":{
        "ht": 11.25,
        "Rt": 6.15,
        "Vltp": 0.589,
        "coeffux": 1,
        "coeffuz": 1,
        "width_para": 0.458
    },
    "RV": {
        "Es": {
            "Type": "normal",
            "Mean": 25000000,
            "CV": 0.05
        },
        "Efoot": {
            "Type": "lognormal",
            "Mean": 3000000000,
```

```json
            "CV": 0.05
        },
        "EGratio": {
            "Type": "lognormal",
            "Mean": 12.5,
            "CV": 0.05
        },
        "phi_int": {
            "Type": "normal",
            "Mean": 30,
            "CV": 0.05
        },
        "Vltp": {
            "Type": "lognormal",
            "Mean": 0.589,
            "CV": 0.05
        },
        "width_para": {
            "Type": "lognormal",
            "Mean": 0.458,
            "CV": 0.05
        },
        "Seed": 200,
        "nSample": 1
    }
}
```

Figure 5.3: An example of the input file for Timoshenko beam model in tunneling scenario

```json
{
    "ID": 4,
    "Building_Type": "FrameOnFoot_DeepExcavation",
    "Analysis": {
        "Type": "SA",
        "SampleSize": "6"
    },
    "Es": 20000000,
    "nis": 0.49,
    "phi_int": 30,
    "Foot_properties":{
```

```
        "d_na": 0,
        "B_X_foot": 4,
        "h_el_foot": 1,
        "Efoot": 3000000000,
        "ni_foot": 0.3,
        "EGratio": 2.6,
        "H_target": 1,
        "c_shear": 1.5,
        "s_shear": 0
    },
    "Footing_dimNloading":{
        "num_of_footing": 3,
        "X_foot_centr": [2.5, 11.93, 28.37],
        "Y_foot_centr": [0, 0, 0],
        "Z_foot_centr": [0, 0, 0],
        "Fx_foot_centr": [0, 0, 0],
        "Fz_foot_centr": [0, 0, 0],
        "My_foot_centr": [0, 0, 0],
        "footing_length": [2, 10, 15],
        "qx_foot": 0,
        "qz_foot": 100000
    },
    "Tunnel_properties":{
        "dwhm": 0.0363,
        "Rv": 0.688,
        "Rl": 0.576,
        "He": 12.5,
        "xScaleFactor": 1,
        "coeffux": 1,
        "coeffuz": 1
    },
    "Superstructure":{
        "foundn": 1,
        "Eframe": 25000000000,
        "num_storey": 4,
        "spanx_frame": 7.5,
        "spanz_frame": 3,
        "f_c": 30000000,
        "Em": 12500000000,
        "bc": 1,
```

```
        "dc": 0.5,
        "bb": 5.76,
        "db": 0.0526,
        "bf": 2.16,
        "df": 0.13,
        "bfoot": 1.3,
        "dfoot": 3,
        "qz_beam": 0,
        "pz_col": 0,
        "floor_elevation": [0, 2.79, 6.75, 10.71, 14.67],
        "column_coordinates": [2.5, 10.08, 13.82, 21.3, 26, 30.6, 34.8],
        "col_b": [0.508, 0.508, 0.546, 0.576, 0.576, 0.576, 0.576],
        "col_d": [0.508, 0.508, 0.546, 1, 0.8, 1.64, 1.47],
        "col_E": [24800000000, 24800000000, 24800000000, 12400000000, 12400000000, 12400000000, 12400000000]
    },
    "Pile":{
        "pipe_switch": 0,
        "d_pipe": 0,
        "zt_pipe": 0
    },
    "RV": {
        "Rv": {
            "Type": "normal",
            "Mean": 0.688,
            "Cv": 0.13
        },
        "Rl": {
            "Type": "normal",
            "Mean": 0.576,
            "CV": 0.11
        },
        "dwhm":{
            "Type": "normal",
            "Mean": 0.0363,
            "CV": 0.25
        },
        "xScaleFactor":{
            "Type": "normal",
            "Mean": 1,
```

```
            "CV": 0.05
        },
        "bb": {
            "Type":"normal",
            "Mean": 5.76,
            "CV": 0.1
        },
        "Em": {
            "Type": "uniform",
            "low": 6000000000,
            "up": 21000000000
        },
        "f_c": {
            "Type": "uniform",
            "low": 20000000,
            "up": 40000000
        },
        "Seed": 200,
        "nSample": 4096
    }
}
```

Figure 5.4: An example of the input file for 2D elastic frame model in deep excavation scenario

```
{
    "ID": 1,
    "Building_Type": "3DSolid_Excavation",
    "Building_properties":{
        "masonry_E":1.7E+9,
        "masonry_nu":0.2,
        "masonry_rho":32511.111111111109,
        "timber_E":1.5E+9,
        "timber_nu":0.2,
        "timber_rho":17658,
        "sampleDim":1284,
        "timberEleIndStr":1,
        "timberEleIndEnd":1007
    },
    "Soil_properties":{
        "Gs":3.6764705882352944E+6,
```

```
        "nus":0.36,
        "mu_int":0.3,
        "lim_t_int":0,
        "lim_c_int":-347.8261
    },
    "elem2nInter":[[0,1,65,64],[1,2,66,65],[2,3,67,66],[3,4,68,67],...],
    "interNodesXYZ":[[598714.71739655279,6.6420189647915671E+6,0],[598715.29887128633,6.6420191701325327E+6,0],[598715.88034602,6.6420193754734974E+6,0],[598716.44610522024,6.6420195752647063E+6,0],...],
     "wholeElem2n":[[0,1,65,64,192,193,257,256],        [1,2,66,65,193,194,258,257],[2,3,67,66,194,195,259,258],[3,4,68,67,195,196,260,259],...],
     "wholeNodesXYZ":[[598714.74696015124,6.642019081283791E+6,1.5],[598715.29700381821,6.642019275525244E+6,1.5],[598715.84704748506,6.6420194697666978E+6,1.5],[598716.41280668543,6.6420196695579067E+6,1.5],...]
}
```

Figure 5.5: An example of the building input file for ASRE3D

5.4 Incorporation with the NHERI SimCenter cyberinfrastructure and future development

The author is working closely with the NHERI SimCenter on two aspects. The first is to incorporate the soil-structure interface model into one of the SimCenter's research cyberinfrastructure applications `R2D` [61, 38], so that the building response under broader types of ground movements, e.g., soil consolidation, can be studied on a large scale. The software `R2D` offers an opportunity to manage and visualize the building asset information (see Fig. 5.7) on a regional scale. `R2D` also provides an opportunity to run Monte Carlo simulation on high-performance computers at the Texas Advanced Computing Center (TACC) for each building listed in the building asset data set. The building response model in the Monte Carlo simulation supported by `R2D` needs to be a Python code. As a result, `ASRE3D` is compiled as a dynamic link library and interfaced with `R2D` through a wrapper code written in Python. The Python library `ctypes` is adopted in the Python wrapper to load the dynamic link library, convert data structure, and call the functions in the dynamic link library. The Python wrapper is completed and the author aims to work on supplementing a ground settlement hazard analysis function to `R2D` to realize regional T&DE SSI assessment.

The second aspect to incorporate `ASRE` and `ASRE3D` with the NHERI SimCenter cyberinfrastructure is to take advantage of the damage and loss estimation functions. The damage and loss functions on a story-level basis using Pelicun [215] and HAZUS [87] were implemented in `R2D` to support loss assessment for all the buildings under earthquake hazards. The HAZUS damage and loss functions consist of tabular data to describe the fragility or expected losses as a function of hazard intensity or response engineering demand parameters. The author aims to calibrate the response engineering demand parameters to correlate the earthquake engineering demand parameters with T&DE engineering demand parameters so that the damage and financial loss can be estimated.

```
Results_2020_11_25_1_22_52
│
├─ UQ_BID_1
│  │
│  ├─ UQresults.txt
│  │
│  └─ UQsamples.txt
│
├─ SobolSA_BID_1
│  │
│  ├─ SobolSAresults.txt
│  │
│  └─ SobolSAsamples.txt
│
└─ SobolSA_BID_4
   │
   ├─ SobolSAresults.txt
   │
   └─ SobolSAsamples.txt
```

Figure 5.6: An example of the directory tree of the UQ-TESSI output

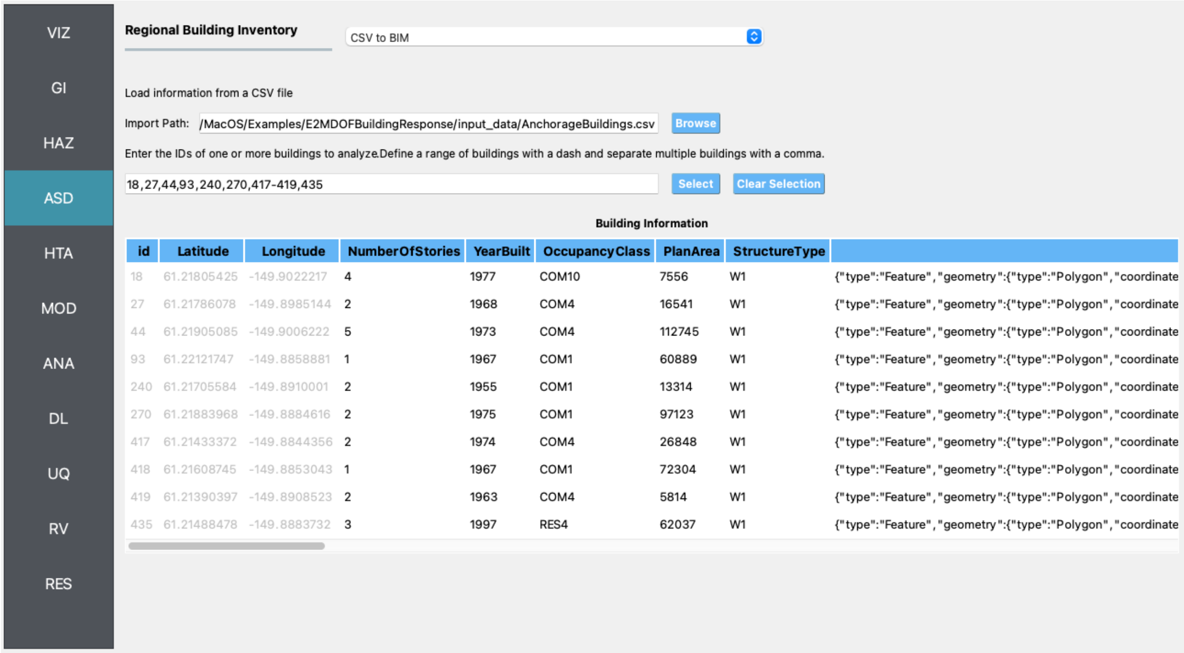

Regional Building Inventory CSV to BIM

Load information from a CSV file

Import Path: /MacOS/Examples/E2MDOFBuildingResponse/input_data/AnchorageBuildings.csv

Enter the IDs of one or more buildings to analyze.Define a range of buildings with a dash and separate multiple buildings with a comma.

18,27,44,93,240,270,417-419,435

Building Information

id	Latitude	Longitude	NumberOfStories	YearBuilt	OccupancyClass	PlanArea	StructureType	
18	61.21805425	-149.9022217	4	1977	COM10	7556	W1	{"type":"Feature","geometry":{"type":"Polygon","coordinate
27	61.21786078	-149.8985144	2	1968	COM4	16541	W1	{"type":"Feature","geometry":{"type":"Polygon","coordinate
44	61.21905085	-149.9006222	5	1973	COM4	112745	W1	{"type":"Feature","geometry":{"type":"Polygon","coordinate
93	61.22121747	-149.8858881	1	1967	COM1	60889	W1	{"type":"Feature","geometry":{"type":"Polygon","coordinate
240	61.21705584	-149.8910001	2	1955	COM1	13314	W1	{"type":"Feature","geometry":{"type":"Polygon","coordinate
270	61.21883968	-149.8884616	2	1975	COM1	97123	W1	{"type":"Feature","geometry":{"type":"Polygon","coordinate
417	61.21433372	-149.8844356	2	1974	COM4	26848	W1	{"type":"Feature","geometry":{"type":"Polygon","coordinate
418	61.21608745	-149.8853043	1	1967	COM1	72304	W1	{"type":"Feature","geometry":{"type":"Polygon","coordinate
419	61.21390397	-149.8908523	2	1963	COM4	5814	W1	{"type":"Feature","geometry":{"type":"Polygon","coordinate
435	61.21488478	-149.8883732	3	1997	RES4	62037	W1	{"type":"Feature","geometry":{"type":"Polygon","coordinate

(a) Assets management in R2D [61]

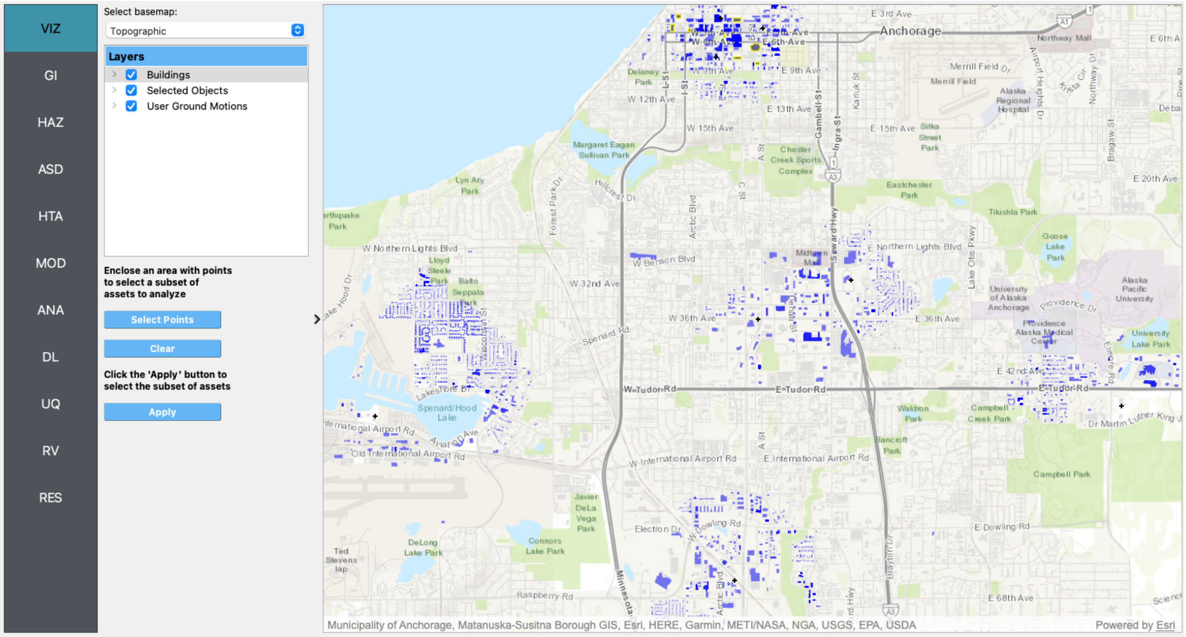

Select basemap: Topographic

Layers

- ☑ Buildings
- ☑ Selected Objects
- ☑ User Ground Motions

Enclose an area with points to select a subset of assets to analyze

Click the 'Apply' button to select the subset of assets

Municipality of Anchorage, Matanuska-Susitna Borough GIS, Esri, HERE, Garmin, METI/NASA, NGA, USGS, EPA, USDA

(b) Regional visualization in R2D [61]

Figure 5.7: User interface of the software R2D [61]

Chapter 6

Case studies and a parametric study

The proposed probabilistic assessment method was applied to multiple published case studies to demonstrate and validate its usage. The calculations in the case studies were conducted with `UQ-TESSI`, which consists of sampling, soil-structural analysis models, uncertainty quantification, and sensitivity analysis drives (see Fig. 5.1 and Chapter 5). The deterministic soil-structural analysis models adopted in `UQ-TESSI` are the models in `ASRE` or `ASRE3D`, and the utility of the probabilistic performance-based assessment approach using various `ASRE` or `ASRE3D` models is demonstrated in this chapter. The soil-structural analysis model applied in the first three case studies is the 2D Timoshenko beam model. The third case study employed the 2D beam-column frame model, and the fifth and sixth case studies analyzed the 3D soil-structure interaction effect with ASRE3D. The first six case studies don't consider spatial variability, while the seventh and eighth case studies are analyses on a regional/community scale with spatial variability of ground movements and/or soil stiffnesses considered. In the end, a parametric analysis using the 2D Timoshenko beam model is presented to find the most important uncertainty sources in various tunnel-soil-structure configurations.

6.1 Case studies using 2D Timoshenko beam model

6.1.1 Case study 1: Building 106 in Bologna, Italy

Building 106 is a two-story masonry building located above a tunnel with a 12 m diameter and 17.3 m depth in Bologna, Italy [55]. The building lies transverse to the tunnel axis and the distance between the midpoint of the building and the tunnel center line is 8.7 m. The soil beneath the building is 15 m silty clay above 25 m sandy silt. The V_L resulting from the excavation was estimated as 5%, and K was estimated as 0.55. The V_L in this case study is larger than typical tunnels in stiff clay (0.5-2.0%). This is caused by the consolidation associated with the horizontal jet grouting adopted after the tunnel excavation for tunnel stability. The damage level is reported to be category 1.

Two methods were used to simplify the building to an equivalent Timoshenko beam, resulting in Models 1 and 2. In Model 1, the stiffness of the building is assumed to be concentrated on two bearing walls which are connected by slabs. Because the slabs are thin and flexible, the two bearing walls are assumed to be isolated and equivalent beams with 38 m length, 10.5 m height, and 0.5 m width are used to model each of the bearing walls independently. The mean value of E_b is taken as 3 GPa, which corresponds to a composite material of masonry and reinforced concrete. Considering the openings in the wall, the mean value of E_b/G_b is assumed to be 4. In Model 2, the stiffness of the whole building is calculated, and an equivalent beam with $E_b = 1.03$GPa, 4.77 m height, and 15 m width is used to model the entire building. For both models, a uniformly distributed load of 200 kN/m is applied to the equivalent beam to model the building weight, and the Timoshenko beam axis is assumed at the mid-height of the beam. The mean of E_s is taken as 90 MPa, which corresponds to the secant stiffness of the soil at 0.01% axial strain at mid-depth to the tunnel axis. The friction angle of the soil-structure interface is assumed to be 30^o to represent clay. To simulate the damage assessment procedure before tunnel excavation, the mean values of V_L and K are assumed as 2% and 0.5, respectively. $V_L = 2\%$ is a large value in typical tunnel projects and is assumed to account for the additional grouting operations. $K = 0.5$ is a typical value used in the design of tunnels excavated in clay [119]. MC simulations are conducted with mean values described here and the CV values listed in Table 4.1.

Fig. 6.1 shows the results of the probabilistic assessment of building damage. The CDFs in Fig. 6.1a are the empirical distribution of ε_{lim} in the building assuming mean values of $V_L = 2\%$ and $K = 0.5$. The dashed vertical lines correspond to the result of deterministic analyses with all random variables equal to their mean value. The CDFs in Fig. 6.1b are the empirical distribution of ε_{lim} when V_L and K are fixed at their monitored values ($V_L = 5\%$, $K = 0.55$) and the dashed lines correspond to deterministic analysis results when $V_L = 5\%$, $K = 0.55$ and all other parameters are assumed equal to their mean value.

In practice, Fig. 6.1a is a prediction of the damage risk level, while Fig. 6.1b can only be plotted after excavation is completed and monitoring data are available. In Fig. 6.1a, it is observed that the probabilistic assessment result of the two modeling methods are close to each other, and the probability of any non-negligible damage level is around 50%. There is approximately a 30% probability that the building will suffer Category 1 damage, a 20% probability of Category 2 damage, and a negligible probability that the damage level in the structure is Category 3 or above. This result indicates that the risk of potential damage should not be neglected even if V_L is significantly underestimated. In Fig. 6.1b, it is observed that the probability of non-negligible damage raises from 50% to 80%, i.e., the uncertainty of damage decreased by a very accurate estimation of V_L and K. This provides insight into how the uncertainty in damage assessment changes when a better estimation of the input uncertainty parameters is achieved.

Fig. 6.2 shows the sensitivity analysis results. Both first-order effects and total effects of E_b, E_b/G_b, and V_L are significantly larger than those of E_s, ϕ, and K. This result indicates that the uncertainty in the damage category of Building 106 is mainly caused by E_b, E_b/G_b and V_L, while E_s, ϕ and K only contribute a minor effect to the uncertainty of damage assessment. Next, Fig. 6.3

displays the factor mapping results. If category 2 or above damage is assumed unacceptable, the marginal CDFs of Behavioral (Category 2 or above damage) and Nonbehavioral (Category 0 or 1 damage) subsamples of each random variable are plotted in Fig. 6.3. The plots of E_b and E_b/G_b imply that unacceptable damage is prone to happen in cases with smaller E_b and larger E_b/G_b, which are associated with larger building flexibility. Larger V_L and E_s showed weak relationships with unacceptable damage, while ϕ and K are almost irrelevant to distinguish damage as category 2 or above. Therefore, factor mapping results indicate, for this considered case study, that increasing the building stiffness by reinforcing the building (e.g., increasing E_b) would mitigate the damage more significantly than controlling the volume loss in tunnel excavation.

6.1.2 Case study 2: Residential building in Barcelona, Spain

The second case study is a one-story residential building located above a tunnel with a 12m diameter and 15m depth in Barcelona, Spain. It lies roughly transverse to the tunnel axis, and the distance between the building midpoint and tunnel center line is 24 m. The soil beneath the building is alluvium clay. According to the monitoring data, the V_L induced by the tunnel was estimated as 1% and the K as 0.46. Category 2 damage was observed in the building. This damage is confirmed by a finite element model, which provided a maximum strain in the building of 0.106% [30].

As for the first case study, two models are used to simplify the building as an equivalent Timoshenko beam. In Model 1, two identical equivalent beams are formed to model two bearing walls. The height of each of the beams is 3 m, the length is 48 m and the width is about 0.3 m. E_b is taken as 3 GPa [30]. In Model 2, an equivalent beam with E_b=1.34 GPa, 3 m height, and 1 m width is used to model the entire building. In both methods, the area of the openings in the bearing wall is small ($\sim$ 15%) and an E_b/G_b of 2.6 is adopted. A uniformly distributed load of 50 kN/m is applied to model the building weight. E_s is assumed to be 27 MPa for the alluvium clay, as suggested by Camós, Molins, and Arnau [30]. As discussed in [62], the neutral axis of structures with stiff foundations are generally lower than the mid-height of the structure. Based on an assumed foundation geometry, the axis of the Timoshenko beam in this case is approximated to be 1 m above the ground. To simulate the design damage assessment process before excavation, the mean design value for V_L is assumed as 0.75%, as suggested by Camós, Molins, and Arnau [30], and the mean design value for K is assumed as 0.5 according to the soil type. The mean values of the other uncertainty parameters are described above and the CV values are listed in Table 4.1.

Fig. 6.4 shows the probabilistic assessment results of the building damage. Fig. 6.4a shows the analysis results when V_L and K are taken as random variables with mean values equal to corresponding design assumptions, while Fig. 6.4b shows the analysis results when V_L and K are fixed at their monitored values. When V_L and K are taken as monitored values in Fig. 6.4b, the deterministic result of method 1 corresponds to a category 2 damage level, which is the same as the damage observed on-site [30]. The deterministic value of ε_{lim} in method 2 is smaller than the actual value, and this may be explained by biased estimation of structure stiffness due to the lack of building details reported by Camós, Molins, and Arnau [30]. When V_L and K are taken as design

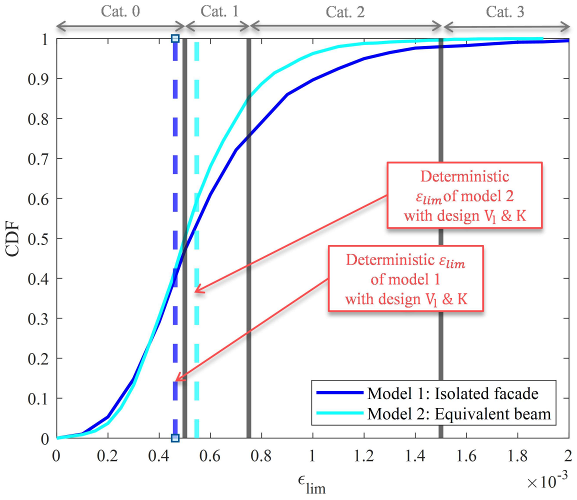

(a) CDFs with all 6 random variables (i.e., the design scenario)

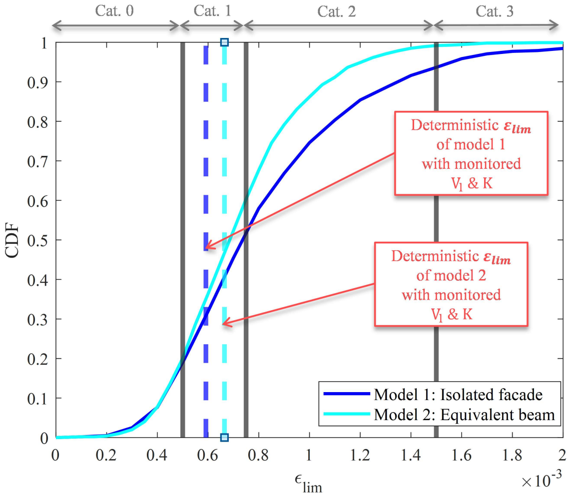

(b) CDFs with 4 random variables and with V_L and K fixed at monitored values

Figure 6.1: Case study 1: cumulative distribution functions (CDFs) of ε_{lim} for Building 106 in Bologna

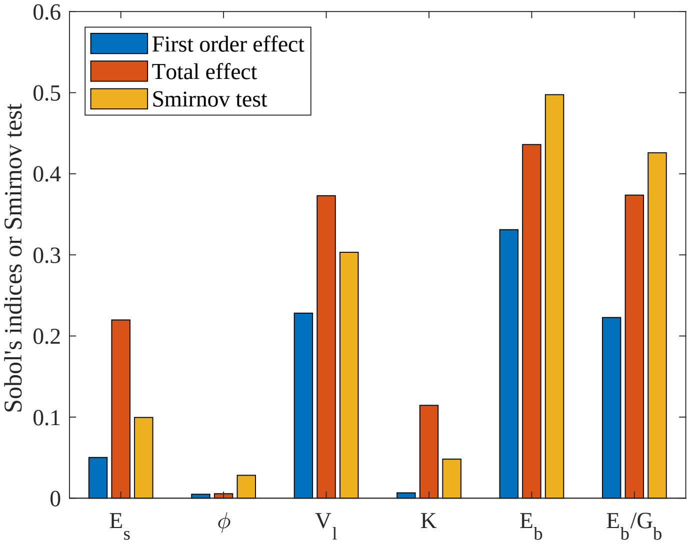

Figure 6.2: Case study 1: Sobol's indices and Smirnov tests for Building 106 in Bologna

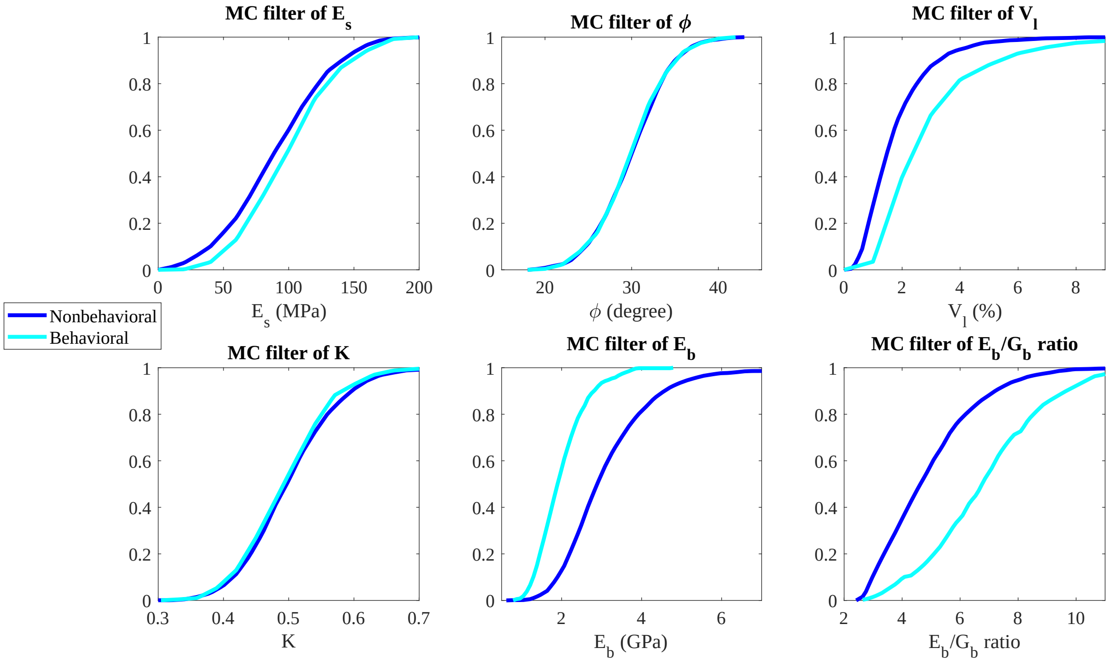

Figure 6.3: Case study 1: Behavioral (acceptable damage) vs Nonbehavioral (unacceptable damage) CDFs by factor mapping analysis for Building 106 in Bologna

values in Fig. 6.4a, the deterministic results underestimate the building damage as the result of the underestimation of V_L. However, the probabilistic analysis also shows that the probability of damage category 2 or above (i.e., slight or moderate damage) is around 20-30%. In other words, if only deterministic analysis is conducted for this case study, only Category 1 damage would be considered during design, while the proposed probabilistic assessment framework quantifies the probable risk of each damage category.

Fig. 6.5 and 6.6 show the sensitivity analysis and factor mapping results. Both first-order effects and total effects of V_L and K are significantly larger than those of E_s, ϕ, E_b, and E_b/G_b. This indicates that the uncertainty in the assessment of the damage category is mainly caused by V_L and K. E_b and E_S contribute relatively little to the uncertainty of damage assessment, while the effect of ϕ and E_b/G_b is negligible. The marginal Behavioral (category 2 or above damage) and Nonbehavioral (category 0 or 1 damage) CDFs for each uncertain parameter are plotted in Fig. 6.6. The plots of K and V_L indicate that damage is most likely associated with smaller K and larger V_L. Smaller E_b and larger E_s show a weak relationship with damage, while ϕ and E_b/G_b are practically irrelevant. The factor mapping result is noticeably different from that in case study 1, where E_b and E_b/G_b contribute most to behavioral damage. This is because the building in case study 2 is vertically short and transversely long and has a relatively small bending stiffness across the entire parameter distribution space, so the building stiffness and soil stiffness don't significantly affect TSSI. Therefore, the behavioral damage of the building is mainly determined by V_L and K. Comparing Fig. 6.1b and Fig. 6.4b, it is observed that the CDFs in Fig. 6.4b are much steeper, which implies that when the uncertainty of V_L and K are eliminated, the uncertainty of ε_{lim} is reduced by a larger amount in case study 2 than case study 1. This agrees with the sensitivity analysis, which indicates that the uncertainty of ε_{lim} mainly results from V_L and K in case study 2, while E_b and E_b/G_b also contribute significantly in case study 1.

6.1.3 Case study 3: Singapore Art Museum

The third case study explored in this dissertation was originally published by Goh and Mair [81]. The east and west wings of the Singapore Art Museum (SAM), which were impacted by the construction of the Bras Basah subway station, are analyzed. The excavation was 35 m deep and approximately 6 m away from the wings of the SAM. The excavation support system consists of a diaphragm wall and 5 layers of bracing. The soil beneath the SAM consists of four layers of clay with intermittent fluvial sand layers. The representative soil stiffness was reported to be 47 MPa. The structural behavior of the SAM is dominated by four masonry walls with an average thickness of about 500 mm. The settlement of four walls (SAM-1, SAM-2, SAM-4, SAM-5, see Fig. 6.7) and the non-suspended, tiled pavement (BBS-1, BBS-2, BBS-4, BBS-5) just outside the walls are monitored by precise leveling. The monitored settlement at BBS-1, 2, 4, 5 are considered as an approximation of corresponding greenfield ground settlements at SAM-1, 2, 4, 5. The height of the walls is around 9.7 m and the Young's modulus of the walls is reported to be 5 GPa. The foundation is shallow and consists of timber layers. Consequently, the contribution of the foundation to the

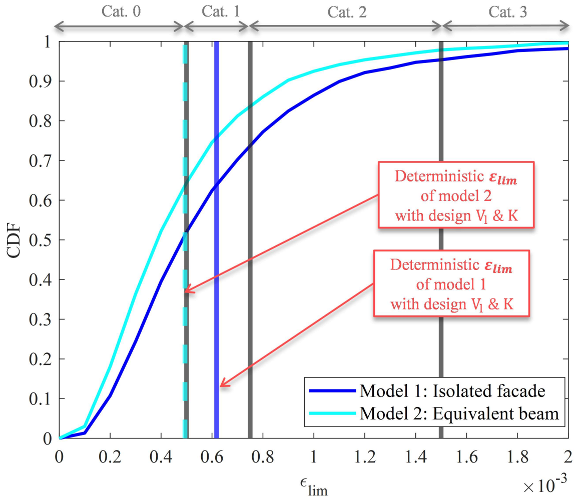

(a) CDFs with all 6 random variables (i.e., the design scenario)

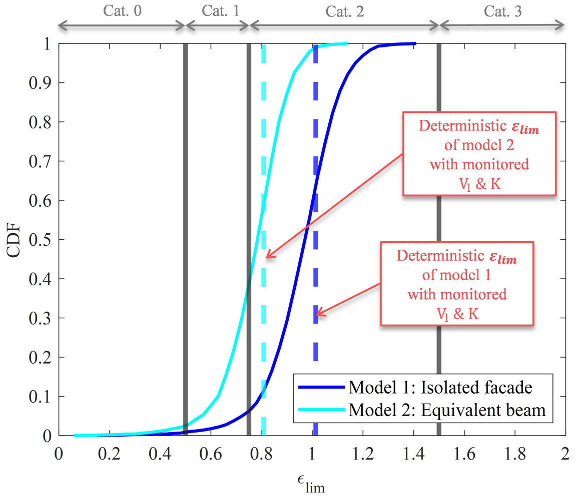

(b) CDFs with 4 random variables and with V_L and K fixed at monitored values

Figure 6.4: Case study 2: cumulative distribution functions (CDFs) of ε_{lim} for the residential building in Barcelona

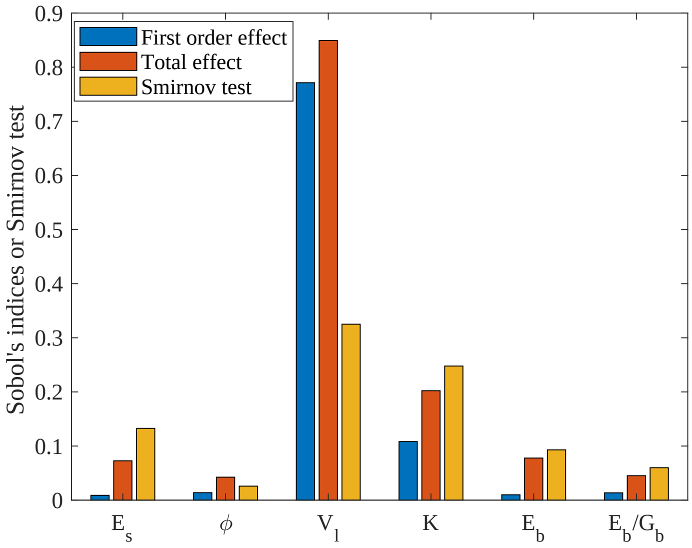

Figure 6.5: Case study 2: Sobol's indices and Smirnov tests for the residential building in Barcelona

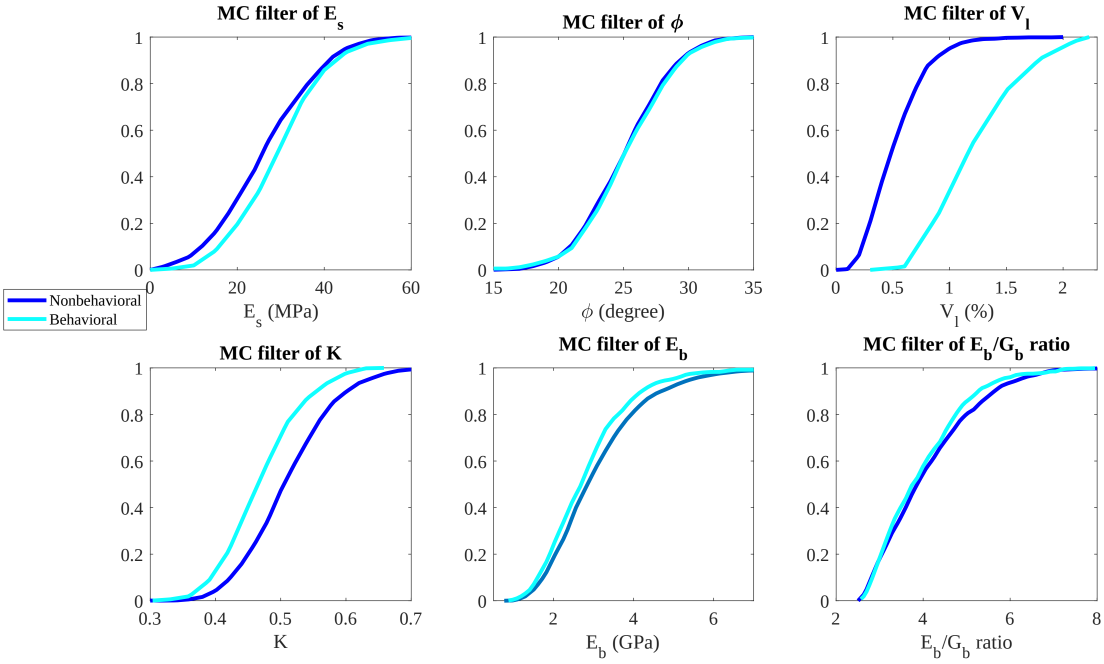

Figure 6.6: Case study 2: Behavioral (acceptable damage) vs Nonbehavioral (unacceptable damage) CDFs by factor mapping analysis for the residential building in Barcelona

overall building stiffness is ignored. The stiffness of the structure is mostly due to the masonry walls as the floor slabs are thin and much more flexible in comparison, as suggested by Goh and Mair [81].

Since the structure section perpendicular to the deep excavation consists of continuous walls, the Timoshenko beam model described above is used to analyze the walls. SAM-1 and SAM-5 are modeled as beams with lengths of 28 m, and SAM-2 and SAM-4 are modeled as beams with lengths of 15 m. All four beams are 9.5 m high and 0.5 m thick. Since the building material is identical for these building sections, a constant elastic modulus of 5 GPa, as suggested by Goh and Mair [81], is adopted. A value of 6 is taken for $\frac{E_b}{G_b}$ to account for the openings in the walls. The maximum horizontal deflection (δ_{hm}) of the diaphragm wall, vertical deformation ratio (R_v), and lateral deformation ratio (R_l) are first calculated according to the KJHH and KSJH models. Vertical and lateral ground movement profiles are then estimated with Eq. 3.18. In other words, these were prediction values and prediction ground settlement curves, assuming no knowledge of the actual settlement. Fig. 6.8a shows the analysis and monitoring results for SAM-1 and SAM-5. Fig. 6.8b shows the analysis and monitoring results for SAM-2 and SAM-4. The support system and underground conditions are assumed to be equal for the four walls, which results in identical ground movement profiles for the four analyzed sections (Fig. 6.8). Note that since walls SAM-1 and SAM-5 are identical, the analysis results are also identical. The analysis results for SAM-2 and SAM-4 are also identical for the same reason.

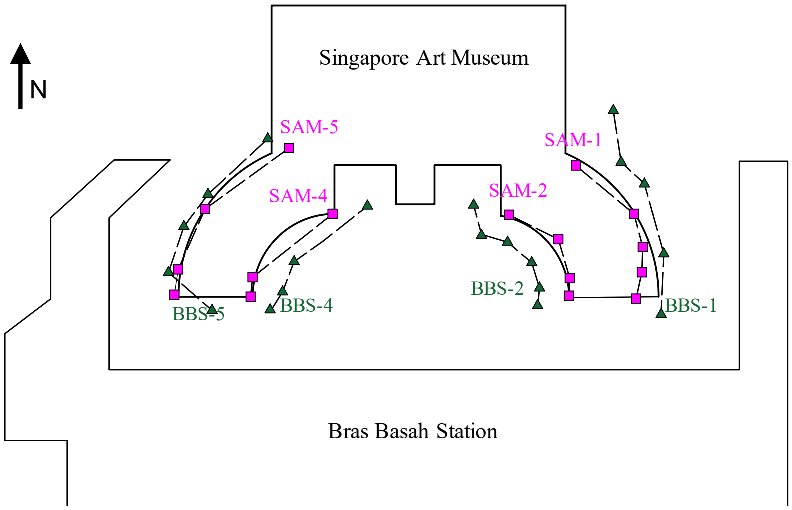

Figure 6.7: Case study 3: plan view showing the locations of building settlement (in squares) and ground settlement (in triangles) monitoring points at the Singapore Art Museum (SAM) (after [81]).

It is observed that the measured ground displacement of BBS-1 and BBS-5 are significantly different, despite that these two scenarios are identical from a prediction perspective. This indicates

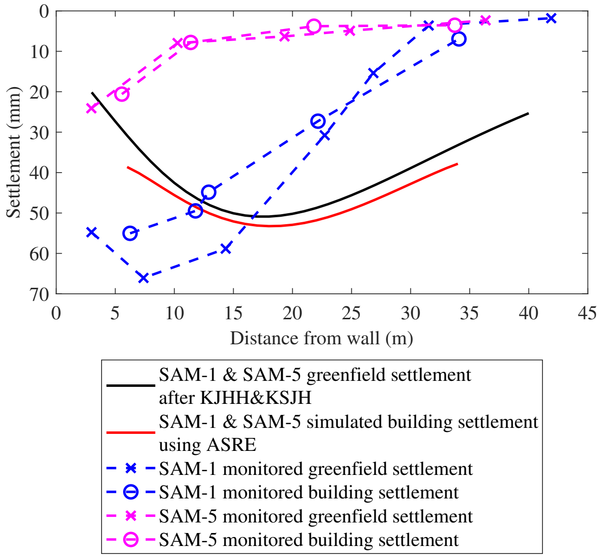

(a) SAM-1 & SAM-5

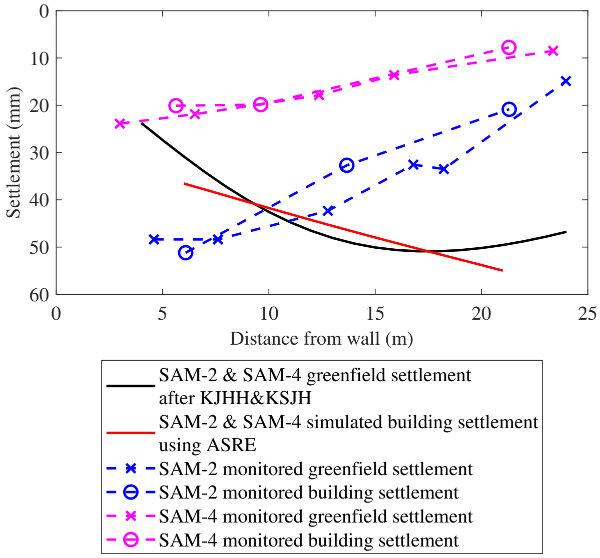

(b) SAM-2 & SAM-4

Figure 6.8: Case study 3: Singapore Art Museum (SAM) case study: Predicted greenfield settlement profiles using the KJHH & KJSH models, predicted building settlement profiles using ASRE, and monitored settlement profiles.

that a single deterministic ground settlement profile prediction, using the KJHH model or otherwise, will not be able to predict both scenarios. The same observation holds for BBS-2 and BBS-4. Goh and Mair [81] explained the difference in the monitoring results by a different order of the construction activities at the east wing and west wing of SAM. This discrepancy between monitored ground displacements implies that notable uncertainty exists. Moreover, Goh and Mair [81] reported that SAM-5 behaved in a more flexible manner compared to SAM-1 even though their structures are similar. This might be explained by some existing structural damage in SAM-5 and it implies that modeling of existing buildings, especially historical buildings, could be associated with large uncertainty. The uncertainty observed in this case study exists in the estimation of δ_{vm}, width of the settlement profile, and building stiffness. Because horizontal ground displacement was not monitored, the accuracy or uncertainty associated with the KSJH model can not be evaluated.

A back-analysis was then undertaken to study the uncertainty in the above modeling method. In the back-analysis, δ_{vm} is taken as the interpolated maximum value of the measured settlement profile. The width of the settlement profile is adjusted by introducing a scaling term (η) to Eq. 3.18, as shown in Eq.4.2. The value of η for each wall is determined by minimizing the mean squared error $\frac{1}{n}\sum_i^n(\delta_v(x) - \hat{\delta}_v(x))^2$, where n is the number of monitoring points, $\delta_v(x)$ are the monitored displacements and $\hat{\delta}_v(x)$ are the values predicted by Eq. 4.2. The elastic stiffness of SAM-5 was reduced to 1 GPa by a trial and error method to recover the monitored building settlements. The back-analysis results are shown in Fig. 6.9. The analysis results for SAM-1, SAM-2, and SAM-4 imply that if the ground settlement profile is estimated accurately, the two-stage elastoplastic solution can predict building response reasonably well, even with a nominal value of structural stiffness. However, the analysis results of SAM-5 indicate that the uncertainty in the modeling of structure (i.e., the reduction in building stiffness due to potential existing damage) should also be considered in the analysis of excavation-induced structure damage. The uncertainty in the estimated structural stiffness is then studied.

For the equivalent Timoshenko beam model used to analyze the SAM, uncertainty exists in the estimation of the equivalent elastic modulus (E_b) and elastic over shear modulus ratio (E_b/G_b). As suggested by Dimmock and Mair [44], E_b can be taken according to the building material, and E_b/G_b can be taken as 2.6 for bearing wall structures with no openings. However, these values are roughly estimated with ignorance of the natural material variability, existing damage, and structure details such as openings and different building layouts. Son and Cording [174] concluded that the value of E_b/G_b has a larger variance range and is harder to estimate compared to E_b. In this study, the coefficient of variance (CV) of E_b for SAM is selected to be 30% and the c.o.v of E_b/G_b for SAM is selected to be 45%. These CV are selected by trial and error so that the 99% coverage intervals of E_b and E_b/G_b are reasonable according to the information provided by Goh and Mair [81]. The mean value for E_b and E_b/G_b is taken as 5 GPa and 6, respectively, which are the same as the values adopted in the deterministic study previously. The type of probability distribution for E_b and E_b/G_b are modeled as log-normal distribution, as commonly adopted for positive definite random variables ([11]). The 99% probability coverage intervals of E_b and E_b/G_b are $(3.84, 5.98)$ and $(3.40, 8.80)$.

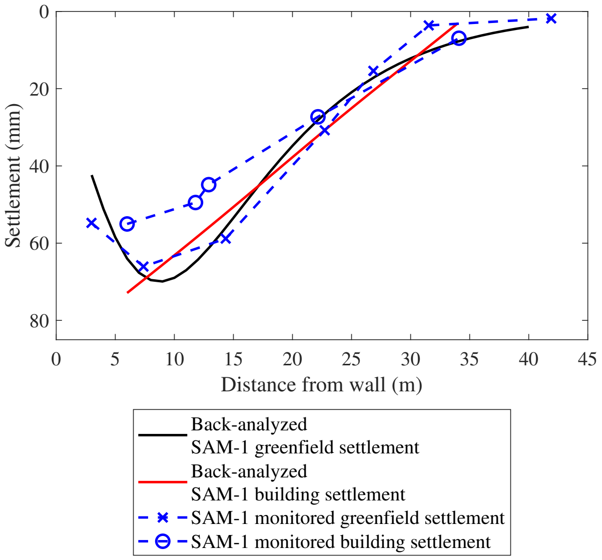

(a) Back-analyzed and monitored settlement of SAM-1

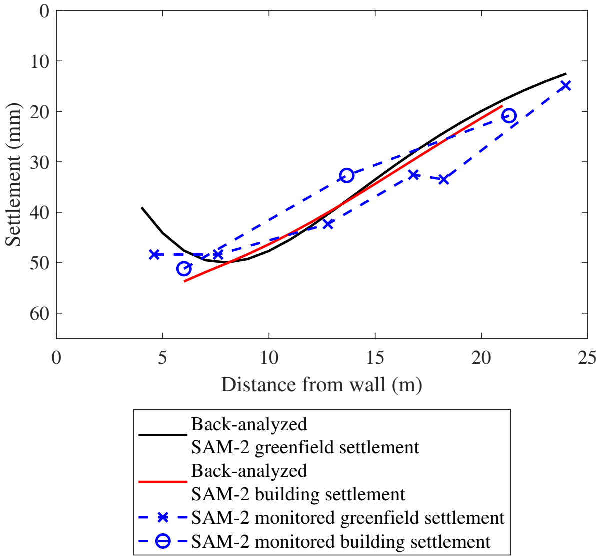

(b) Back-analyzed and monitored settlement of SAM-2

Figure 6.9: Case study 3: settlement of the Singapore Art Museum (SAM) after applying back-analyzed δ_{vm} and δ_{hm}

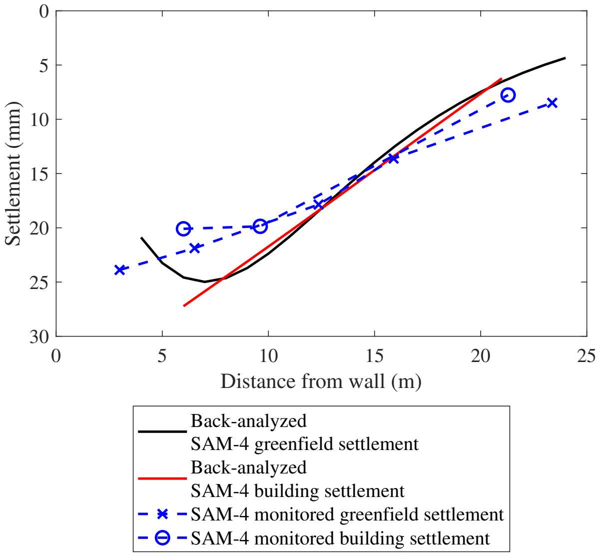

(c) Back-analyzed and monitored settlement of SAM-4

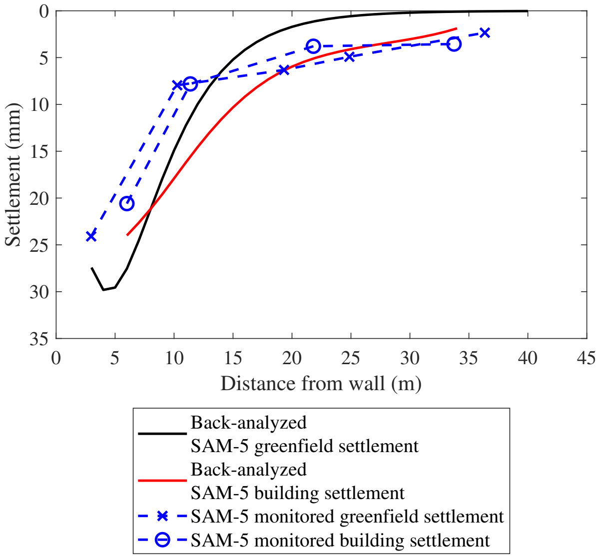

(d) Back-analyzed and monitored settlement of SAM-5

Figure 6.9: Case study 3: settlement of the Singapore Art Museum (SAM) after applying back-analyzed δ_{vm} and δ_{hm} (cont.)

Fig. 6.10 shows the analysis results of SAM with the proposed probabilistic analysis approach, using the uncertainty inputs described in Table 4.2. For SAM-1 and SAM-5, there is about a 30% probability that the deterministic analysis results underestimate the potential damage. The probability of underestimating damage for SAM-2 and SAM-4 is about 50%. As expected, the deterministic analysis results do not provide an upper bound of potential damage. For SAM-1/5 and SAM-2/4, the damage categories predicted based on the probabilistic and deterministic analysis results are the same (i.e., there is approximately 100% probability that the structure will experience the damage category predicted with the deterministic analysis). This provides great confidence in the predicted damage category despite the uncertainty in ground settlement estimation and structural modeling of SAM. This level of confidence is of great benefit because it demonstrates that no further field investigation or model refinement is needed to be confident in the level of damage predicted. In contrast, the previous case studies on tunneling-induced settlement damage demonstrated that in other scenarios, the range of predicted damage could be much larger, and can span several damage category thresholds. This contrast demonstrates the benefit of quantifying the uncertainty. Specifically, deterministic results: 1) may lead to improper classification of potential damage when the deterministic results are close to the damage thresholds, and 2) provide relatively little information on the level of confidence in the predicted result.

The left column of Fig. 6.11 shows the results of the first stage sensitivity analysis. It is observed that among δ_{hm}, R_v, R_l and η, δ_{hm} caused most uncertainty in the estimation of ε_{crit}. For the case of SAM-1 and SAM-5, almost all the uncertainty comes from the uncertainty associated with δ_{hm}, while for SAM-2 and SAM-4, the trough width parameter η also contributes a considerable amount of uncertainty. This may imply that an accurate estimation of η may reduce the uncertainty in damage prediction of structures with short spans, while the uncertainty of long-span structures has a weaker correlation with η. The right column of Fig.6.11 shows the results of the second stage sensitivity analysis. It is observed that the indices of ground settlement input are reduced because the uncertainty from the structure models is also included. In the analysis of SAM-1 and SAM-5, the total amount of uncertainty caused by E_b and E_b/G_b is almost identical to the uncertainty caused by the ground settlement model. In the analysis of SAM-2 and SAM-4, E_b/G_b showed a stronger contribution compared to the analysis of SAM-1 and SAM-5. This implies that the modeling of short-span structures by an equivalent Timoshenko beam may introduce more uncertainty to the system, and both E_b and E_b/G_b are important sources of uncertainty in this circumstance. Future studies and field investigations to more accurately quantify E_b and E_b/G_b could be valuable to further reduce the uncertainty in building damage assessments.

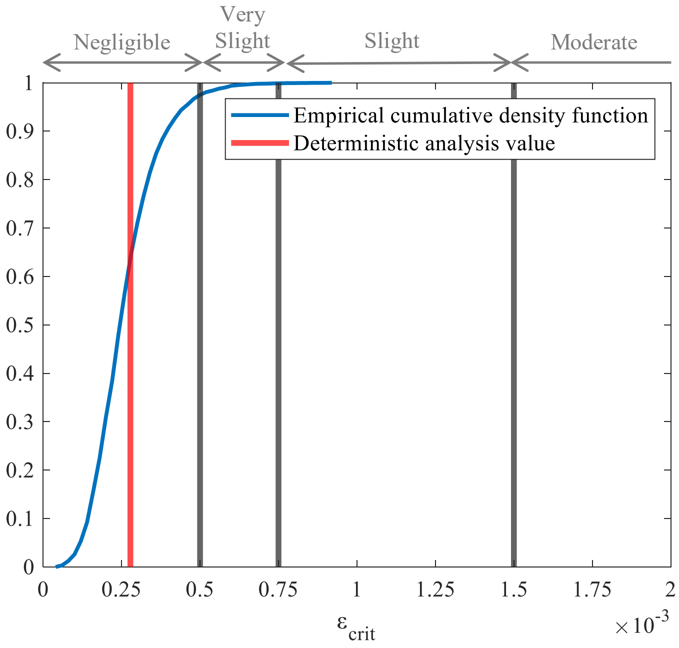

(a) Probabilistic assessment results of ε_{crit} in SAM-1 and SAM-5

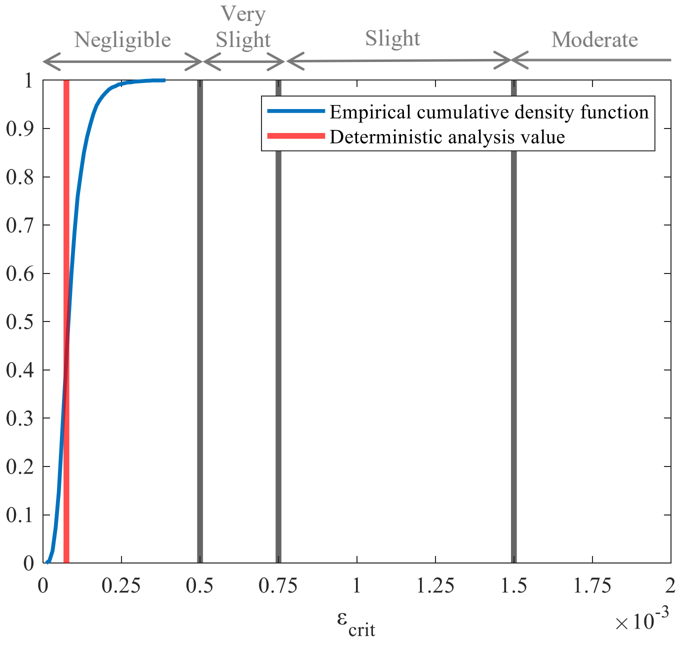

(b) Probabilistic assessment results of ε_{crit} in SAM-2 and SAM-4

Figure 6.10: Case study 3: cumulative distribution functions (CDFs) of ε_{lim} for the Singapore Art Museum (SAM)

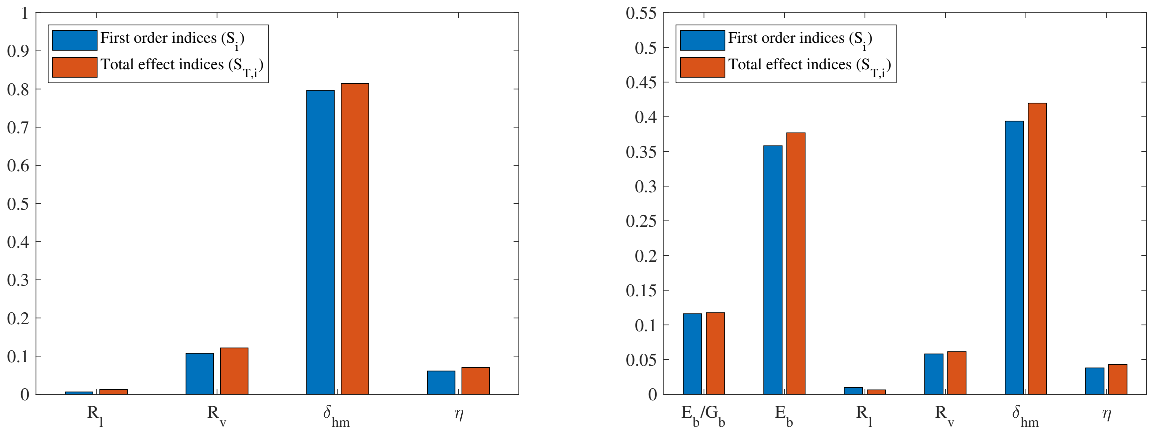

(a) Sobol's sensitivity indices of SAM-1 & SAM-5 (Stage 1)

(b) Sobol's sensitivity indices of SAM-1 & SAM-5 (Stage 2)

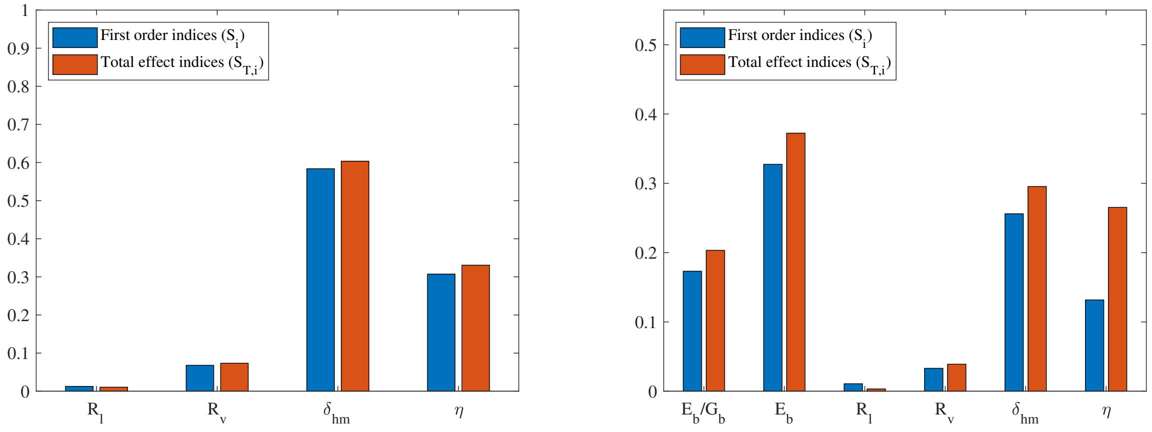

(c) Sobol's sensitivity indices of SAM-2 & SAM-4 (Stage 1)

(d) Sobol's sensitivity indices of SAM-2 & SAM-4 (Stage 2)

Figure 6.11: Case study 3: Sobol's indices for the Singapore Art Museum(SAM)

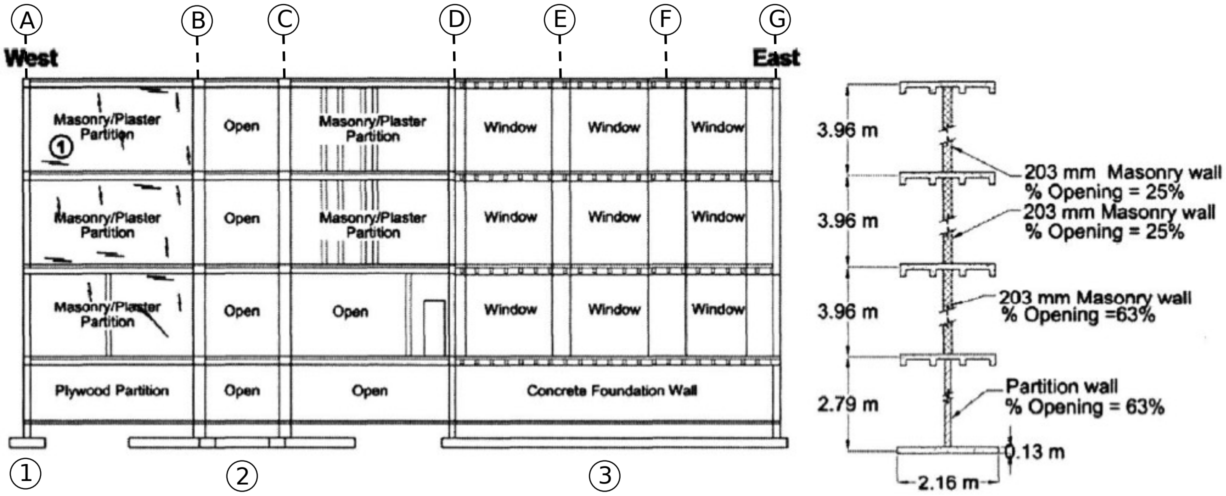

Figure 6.12: Case study 4: elevation view of the analyzed cross-section of Chicago Frances Xavier Warde School (ChiFXWS) (after [59]).

6.2 Case studies using 2D frame models

6.2.1 Case study 4: Chicago Frances Xavier Warde School

The fourth case study explored in this research was originally published by Finno and Bryson [58] and Finno et al. [59]. The analyzed structure is a cross-section of Chicago Frances Xavier Warde School (ChiFXWS), which was impacted by the construction of the subway renovation project on State Street and Chicago Avenue. The cross-section, as shown in Fig. 6.12, is a three-story concrete frame structure with brick partition walls and a basement. The floor system at each level consists of a reinforced concrete pan-joist and supported by interior concrete columns and beams, and masonry-bearing walls around the perimeter. The interior columns and perimeter walls rest on three separate footings. The excavation is 1.2 m to the west of the frame and is almost perpendicular to the frame. The excavation depth is 12.2 m and the excavated soil is soft to medium clay. The excavation support system consists of a secant pile wall with three levels of support. The building settlement is monitored at 5 points along the cross section at the basement level or 1 m above grade with optical survey points. The cross-section is modeled with the 2D elastic frame proposed in Section 3.2. The partition walls are modeled as diagonal compression struts with Eq. 3.19, where the elastic modulus of masonry is taken as 12.5 GPa and the elastic modulus of concrete elements is taken as 36 GPa. The concrete foundation wall at the east part of the frame is also modeled using diagonal compression struts but the value of E_m is taken as 36 GPa. Because the exact values of the material properties are not reported by Finno and Bryson [58] and Finno et al. [59], typical values are adopted. The analysis of this structure here is not aimed to recover the response of the structure exactly, but to simulate the typical situation in design practice, in which the material properties are unknown, and to demonstrate the uncertainty associated with current design procedures.

The settlement of this 2D elastic frame is calculated with the two-stage elastoplastic methods and ASRE. The greenfield input to the two-stage analysis is first estimated with the KJHH and KSJH models. The estimated value of δ_{vm} and δ_{lm} are 25 mm and 20.9 mm, respectively, and a ground movement profile is determined with Eq. 3.18. The monitored building settlement and computed building settlement are plotted in Fig. 6.13a. It is observed that the settlement determined from the two-stage analysis is close to the monitored values for footing 2 and footing 3, while the analyzed settlement of footing 1 is two times smaller than the monitored value. Because there is not any concentrated load applied at footing 1, it is not reasonable to observe a building settlement four times larger than the greenfield settlement. Therefore, it can be argued that the predicted greenfield settlement profile is not accurate, and this uncertainty is an important reason for the discrepancy between predicted and monitored building settlements. A back-analysis is then conducted by adjusting the greenfield settlement with Eq. 4.2. The back-analysis result is shown in Fig. 6.13b. The purpose of the back-analysis is to show that when the uncertainty of δ_{vm} and trough width is taken into account, the monitored building settlement can be recovered in one realization of the probabilistic analysis framework, as will be discussed later.

After the building displacement is computed, the damage level of the frame is analyzed with the method proposed for the 2D elastic frame model. In the prediction analysis, i.e., the direct application of the KJHH and KSJH models to obtain the predicted greenfield settlement, the frame panels between span C-D (see Fig. 6.12) experienced slight to moderate levels of damage at the first floor and the frame panels between span B-C experienced negligible to slight damage at each floor. The angular distortion of the panels between span C-D is around 0.26% and the angular distortion between span B-C increased from 0.10% on the first floor to 0.11% on the third floor. The maximum partition wall strain is 0.13%, which occurs at the partition walls between span C-D on the second and the third floor. The strain levels in other partition walls are small and negligible. The distribution of damage coincides with the cracks observed after the construction works. Finno and Bryson [58] reported that damage mainly occurred in the west part of the building, and cracks were observed at the infill walls on the second and third floors. The back-analysis results suggest a similar distribution of damage with slightly larger strain in each frame panel and infill wall.

Fig. 6.14 shows the analysis results of ChiFXWS with the proposed probabilistic analysis approach. The probability of underestimating potential damage quantified by $\varepsilon_{crit(infill)}$ and β are 40% and 53%, respectively. Similar to cases of SAM, the deterministic analysis results do not provide an upper bound of potential damage. Additionally, the damage categories predicted based on the probabilistic and deterministic analysis results are the same, which provides great confidence in the predicted damage category despite the large uncertainty in ground settlement estimation and structural modeling of ChiFXWS. Finally, it should be noted that the input uncertainty in the analysis of ChiFXWS is small because it is a valuable building, and its underground conditions and building layouts were well surveyed. In practice, even larger uncertainty may exist, which will lead to a wider empirical CDF.

In the analysis of ChiFSWS, the maximum frame panel distortion (β_{crit}) and maximum infill

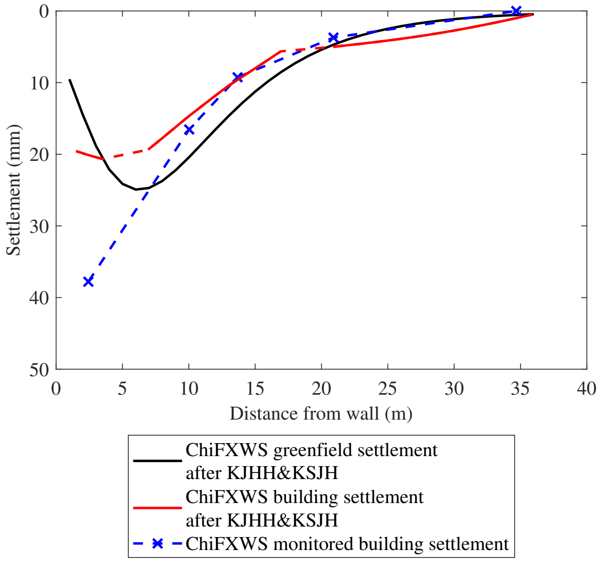

(a) Analyzed and monitored settlement of ChiFXWS after direct KJHH&KSJH

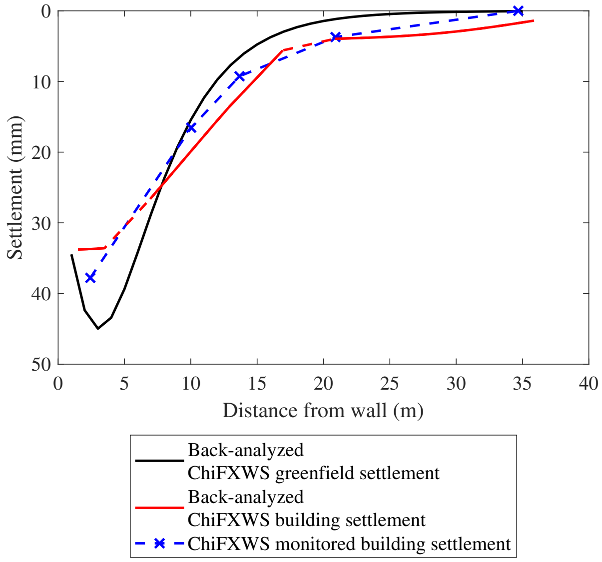

(b) Back-analyzed and monitored settlement of ChiFXWS

Figure 6.13: Case study 4: Chicago Frances Xavier Ward School (ChiFXWS) case study: Predicted greenfield settlement profiles using the KJHH & KJSH models, predicted building settlement profiles using ASRE, and monitored settlement profiles.

wall strain $\varepsilon_{crit(infill)}$ are used as engineering demand parameters, and their Sobol's indices are computed. The sensitivity analysis is done in two stages. Same as in case study 3, only uncertainty of ground movements (i.e., BF_{hm}, BF_l, BF_v, and η) are considered in the first stage. This stage aims to study which part of the KJHH & KSJH models induced the most uncertainty in damage prediction. In the second stage, all the parameters in Table 4.2 are considered. The purpose of the second stage is to study whether the ground movement or the structure models are more responsible for the uncertainty of the building damage assessment.

The left column of Fig. 6.15 shows the results of the first stage sensitivity analysis. It is observed that among δ_{hm}, R_v, R_l and η, δ_{hm} caused most uncertainty in the estimation of $\varepsilon_{crit(infill)}$ and β. The, Sobol's indices computed based on β_{crit} and $\varepsilon_{crit(infill)}$ are almost the same. It can be concluded that the value of β_{crit} and $\varepsilon_{crit(infill)}$ are highly related to each other. About 80% of the uncertainty in the estimation of β_{crit} and $\varepsilon_{crit(infill)}$ comes from δhm and 20% of the uncertainty comes from R_v. The uncertainty of R_l and η have nearly zero effect on the prediction of damage in ChiFXWS.

The right column of Fig. 6.15 shows the results of the second stage sensitivity analysis. It is observed that the uncertainty of f_c and b_b caused almost zero uncertainty in the prediction of both β_{crit} and $\varepsilon_{crit(infill)}$. The uncertainty of infill wall stiffness did show an effect on the analysis result, which implies that proper modeling of infill walls may be important to achieve accurate damage predictions. However, Sobol's indices which correspond to E_m are about $1/7$ of the indices corresponding to δ_{hm}. Therefore, a better estimation of δ_{hm} is the most efficient way to reduce the uncertainty in this system. Comparing the analysis of the Timoshenko beam model and the 2D elastic frame model, it is observed that the Timoshenko beam model introduces more uncertainty in building damage predictions because there are more simplifications when the whole structure is modeled as an equivalent beam. The 2D elastic frame model is more complex and consists of more input parameters. Since many input parameters of the 2D elastic frame model can be evaluated accurately (e.g., floor elevation, beam span, and column dimensions), they are considered with zero uncertainty and treated as constants in the analysis. Therefore, the uncertainty of the structural analysis model in a system using a 2D elastic frame model is less critical, and a better estimation of the ground settlement will reduce the uncertainty of building damage prediction more significantly.

6.3 Case studies using ASRE3D

6.3.1 Case study 5: Residential building in Barcelona, Spain

The first 3D case study (published in [212] and named CS-1) is a one-story masonry residential building located above the L9 metro line in Barcelona [30, 31]. The rectangular building is 46x16 m in plan dimensions. The thickness of the exterior masonry facade and internal partition walls are 0.2 m and 0.04 m, respectively. The walls are 3 m high with multiple windows of dimension 1x1

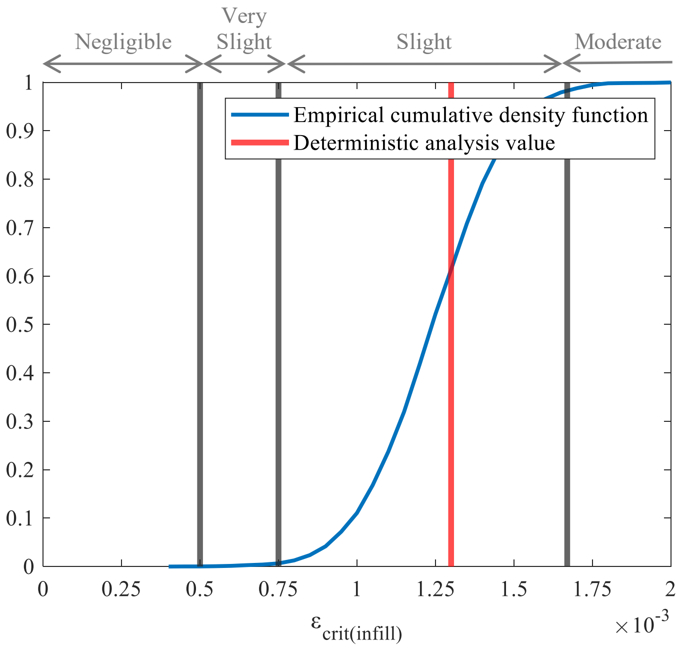

(a) Probabilistic assessment results of $\varepsilon_{crit(infill)}$ in ChiFXWS

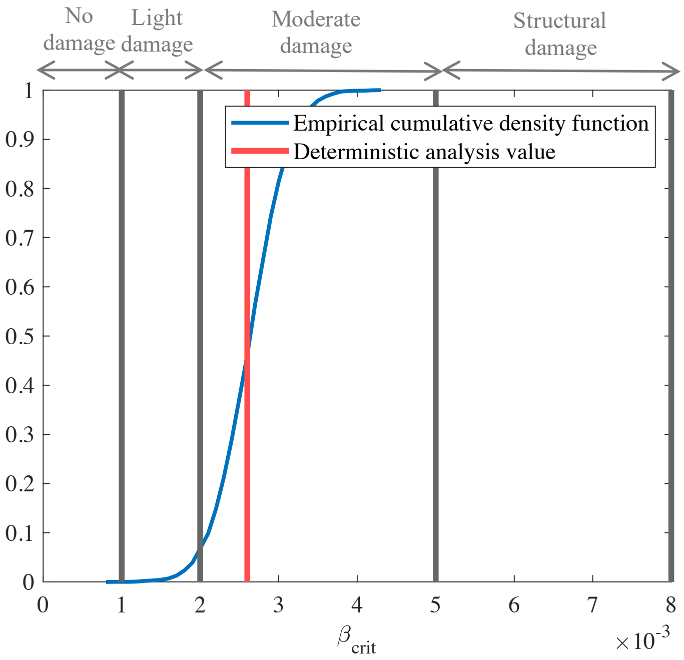

(b) Probabilistic assessment results of β_{crit} in ChiFXWS.

Figure 6.14: Case study 4: probabilistic analysis results of the Chicago Frances Xavier Ward School (ChiFXWS)

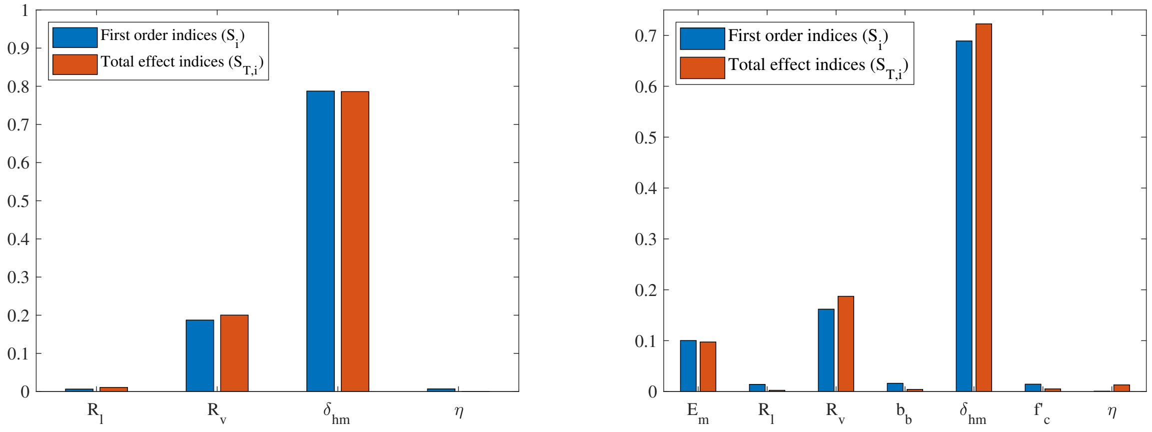

(a) Sobol's sensitivity indices for β_{crit} of ChiFXWS (Stage 1)

(b) Sobol's sensitivity indices for β_{crit} of ChiFXWS (Stage 2)

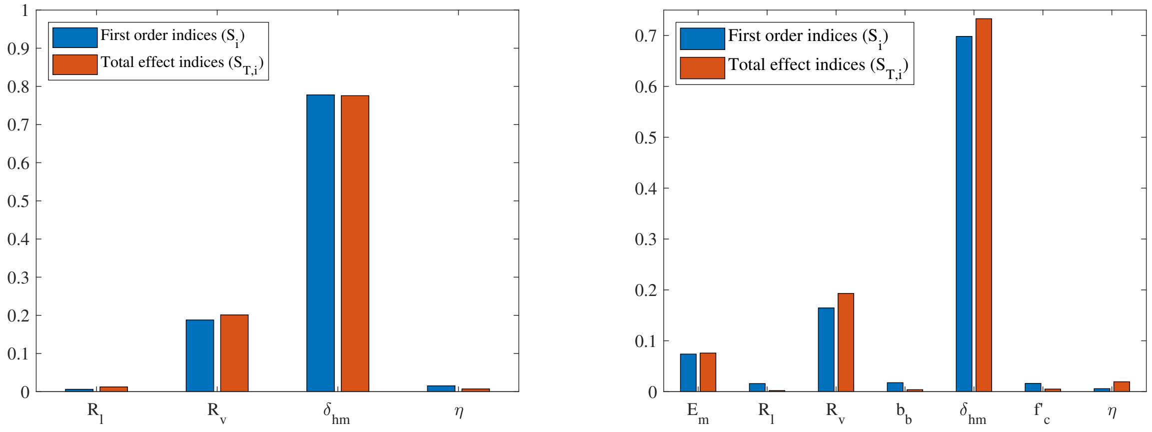

(c) Sobol's sensitivity indices for $\varepsilon_{crit(infill)}$ of ChiFXWS (Stage 1)

(d) Sobol's sensitivity indices for $\varepsilon_{crit(infill)}$ of ChiFXWS (Stage 2)

Figure 6.15: Case study 4: Sobol's indices for the Chicago Frances Xavier Ward School (ChiFXWS)

m and doors of 2x0.8 m on the long facade. The geometry of the building can be found in Fig. 3 of [30]. The tunnel diameter is 12 m, the tunnel depth is 23 m, and the angle between the tunnel axis and the building's long facade is 26^o. Fig. 6.16 shows the relative positions of the building and tunnel. The nominal value for the dead load (L) of the building is taken as the masonry self-weight of 1,800 Kg/m^3 plus a uniform roof load of 1.25 KN/m^2, as suggested by the Spanish regulation. As discussed in [52] and Section 4.2, the mean value of L is taken as 1.05 times the nominal value, and the coefficient of variance (CV) is taken as 10%. The mean values of E_b and E_s are taken as 3,015 MPa and 90 MPa, which are consistent with the FEM model developed by Camós, Molins, and Arnau [30]. The CV of E_s is taken as 30%, which represents a medium level of uncertainty as suggested by Phoon and Kulhawy [152], and the CV of E_b is taken as 35.6%, which is an average value for solid bricks [18]. Camós et al. [31] conducted probabilistic prediction of this case study by modeling the structure as a 2D equivalent beam and assumed that the mean values of V_L and K are 0.4% and 0.3 with CV equal to 40% and 20% in [31]. The same values for V_L and K are adopted in this case study so that the difference in the probabilistic assessment results between ASRE3D and an equivalent beam method that ignores SSI effects can be evaluated.

In CS-1, the proposed probabilistic assessment approach is repeated seven times, each time with the position of tunnel face y_s = +10, +5, 0, -5, -10, -20, -50 m. The empirical distributions for the maximum characteristic strain for each tunnel face position are plotted in Fig. 6.17. The results of deterministic analyses, in which L is taken as the nominal value and the other uncertain input variables taken as their mean value, are indicated with cross markers. The building deformation shape and the distribution of principal tensile strains calculated from the deterministic analyses at each y_s are plotted in Fig. 6.18.

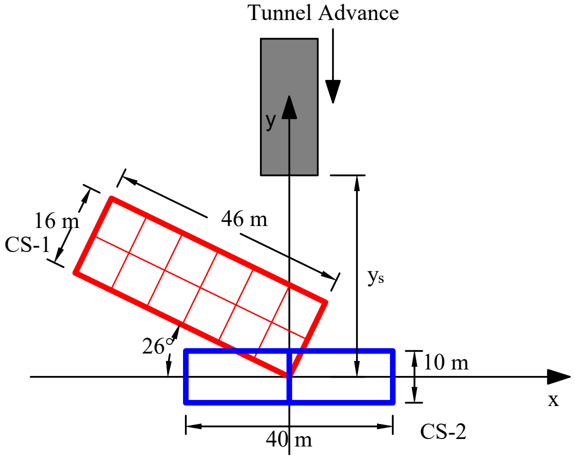

Figure 6.16: Case study 5 & 6: positions of case study 5 (CS-1) and case study 6 (CS-2).

$\hat{P}_{1+}$ for each y_s are calculated with Eq. 4.5b, and shown in Table 6.1. The values predicted by Camós et al. [31] are also presented in Table 6.1. Camós et al. [31] assumed the structure

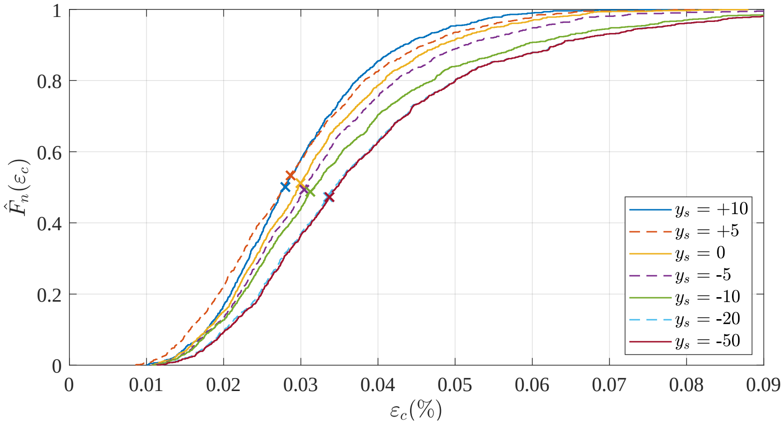

Figure 6.17: Case study 5: probabilistic assessment results of CS-1.

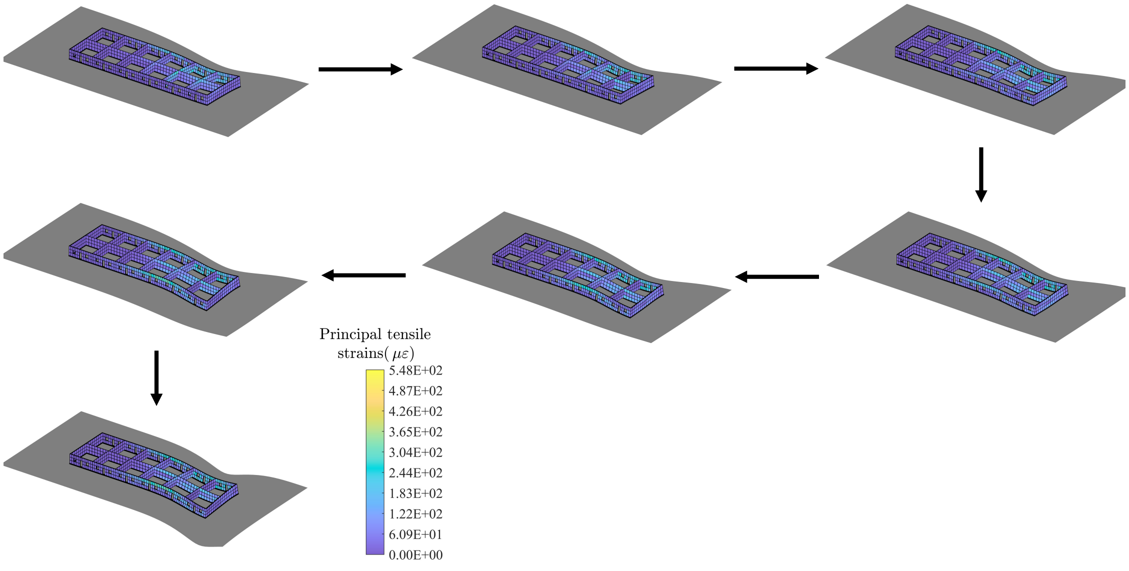

Figure 6.18: Case study 5: building deformation shapes and principal tensile strain distributions at y_s = 10, 5, 0, −5, −10, −20, −50 m in CS-1 (Tunnel approaches from inside of page).

displacements at the foundation are exactly the same as the empirical greenfield ground displacements, and only the rear wall (closer to the origin) was analyzed. For all y_s, the failure probability of the rear wall computed in this case study is smaller than the probabilities computed by Camós et al. [31]. This is because the structure deflection is reduced when the structure stiffness is considered. Camós, Molins, and Arnau [30] observed that $\hat{P}_{1+}$ is slightly higher when $y_s = -10$ m than $y_s = -20$ m. This difference occurs because, given the alignment of the rear wall (26^o with respect to the tunnel axis), the combined ground deflection from the x and y directions is more critical when $y_s = -10$ m. However, when SSI is considered, the rear wall is more vulnerable when the tunnel face has completely passed ($y_s < -20$ m). This could be because the tunnel face has passed the front wall by 16m, and the front wall has reached a state with smaller deformation than the rear wall, so the damage probability of the rear wall is reduced by the support from the front wall. This behavior indicates the significance of the building geometry, and it can only be captured with a 3D analysis. When the tunnel face is far from the structure (e.g, $y_s > -5$ m), the damage probability is higher when the whole structure is considered in addition to the rear wall. This is again because the front wall and partition walls are closer to the tunnel portal, and the potential damage to these walls increased the damage probability of the whole structure.

Because the deterministic analysis results in an ε_c that is smaller than 0.05 % for all y_s, the building will be diagnosed with negligible damage in conventional assessment. However, the probabilistic assessment results indicate that the probability of non-negligible damage is actually around 20%.

Position of tunnel face	y_s = +10 m	y_s = +5 m	y_s = 0 m	y_s = -5 m	y_s = -10 m	y_s = -20 m	y_s = -50 m
Whole structure (this case study)	4.60%	6.42%	8.50%	11.08%	16.00%	19.83%	20.79%
Only rear wall (this case study)	0.00%	0.00%	0.00%	7.76%	15.50%	19.75%	20.50%
Only rear wall [31]	0.00%	0.01%	8.00%	23.00%	28.00%	25.00%	-

Table 6.1: Probability of category 1 or higher damage for different tunnel face positions in Case study 5 (CS-1).

6.3.2 Case study 6: Archetype masonry building defined by Yiu, Burd, and Martin [202]

The second 3D case study (published in [212] and named CS-2) is an archetype scenario first developed by Yiu, Burd, and Martin [202] to represent a masonry building on strip footings influenced by tunnel excavated in a typical London soil profile. CS-2 is used as a validation benchmark in [24] and this dissertation (Section 3.4). The model geometry can be found in Section 3.4, and Fig.3 of [202]. Only the case with zero eccentricity is studied here, and the position is shown in Fig. 6.16. Mean values of the uncertainty input parameters are taken as the values used in

Parameter	Description	Distribution	Typical mean	CV	References
V_L	Volume loss	Lognormal	0.5-1.5%	73.11%	[27], [198], [8]
K	Trough width parameter	Lognormal	0.2-0.7	14.44%	[140], [198], [8]
E_s	Soil elastic modulus	Beta(2, 2)	Sand: 10-320MPa	18-68%	[102], [152, 151]
			Clay: 0.5-80MPa	14-68%	[12, 187, 194]
E_b	Building elastic modulus	Lognormal	700-1200 times masonry prism compressive strength	31-55%	[156, 18, 181]*
L	Dead load	Lognormal	1.05 times nominal load	6-15%	[2, 52]*

$*$ The references are for masonry structures. References for other types of structures can be found in: [34, 7, 18, 125].

Table 6.2: Uncertainty quantification of input variables for Case study 5 and 6.

the aforementioned deterministic analysis, and the CV values are the same as used for CS-1. The input uncertainty is summarized in Table 6.2.

In CS-2, the empirical distributions obtained from probabilistic assessment for y_s = -50, -20, -10, 0, 10 m are plotted in Fig. 6.19, with the results of deterministic analyses marked with crosses. The building deformation shape and the distribution of principal tensile strains calculated from the deterministic analyses at each y_s are plotted in Fig. 6.20. Similar to CS-1, the ε_c determined from deterministic assessment indicates negligible damage, but there is an approximately 34% probability that non-negligible damage will occur. The higher damage probability in CS-2 is most likely due to the larger V_L (1.65%) than the V_L (0.4%) in CS-1.

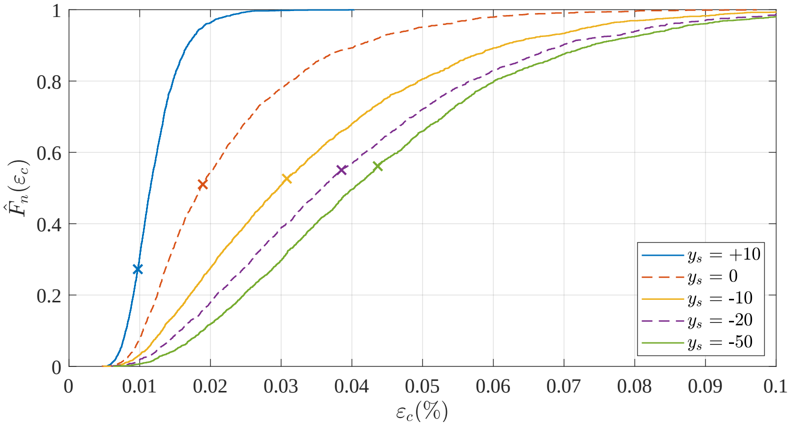

Figure 6.19: Case study 6: probabilistic assessment results of CS-2.

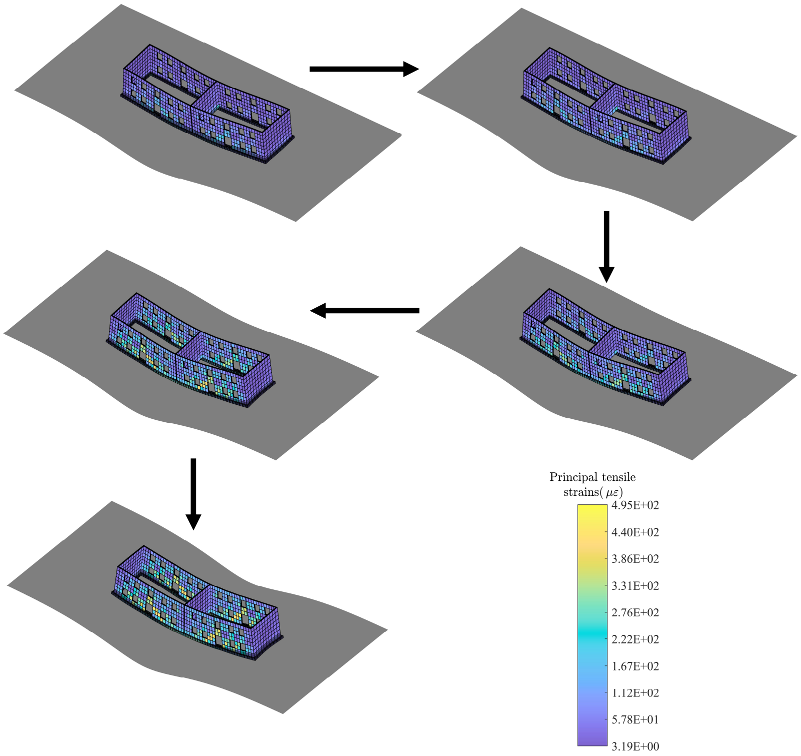

Figure 6.20: Case study 6: building deformation shapes and principal tensile strain distributions at $y_s = 10, 0, -10, -20, -50$ m in CS-2 (tunnel approaches from outside of page).

6.3.3 Discussion of Case study 5 and 6

The sensitivity analysis result of Case study 5 (CS-1) and Case study 6 (CS-2) are presented in Fig. 6.21, together with 95% confidence intervals. The confidence intervals for first-order indices are larger than those for total effect indices. This is because the method [168] adopted in this dissertation is primarily developed for the calculation of total effect indices, and the first-order indices can be obtained by a relatively small amount of additional computation. If only first-order indices are needed, computationally cheaper algorithms [185] can be employed to achieve faster convergence and smaller confidence intervals using the same sample size.

It is observed that in both CS-1 and CS-2, the majority of damage prediction uncertainty is caused by K and V_L. This suggests that, if higher precision is desired in the damage assessment, the most efficient method is to reduce the uncertainty of the predicted K and V_L. The epistemic uncertainty associated with K and V_L can be reduced by employing ground movement prediction models with higher fidelity, and the aleatoric uncertainty can be reduced by better workmanship quality control. Under the same input uncertainty, Sobol's indices for E_b and E_s in CS-1 are significantly smaller than those in CS-2. This is because the building in CS-1 has a low elevation and thin facade, so the building stiffness across the entire parameter distribution space is small. Therefore, the building stiffness and soil stiffness do not significantly affect the SSI in CS-1. In contrast, the building in CS-2 is taller with thicker facade walls, so the E_b and E_s are more important in the SSI, i.e., the difference between building displacements and greenfield ground displacements. It should be kept in mind that the presented Sobol's analysis results are properties of the SSI models for the case studies. They also strongly depend on the input probabilistic models (e.g., CV of the input parameters). As discussed in Section 4.2, the input probabilistic models adopted here are carefully selected according to case history data and widely accepted research literature on risk and uncertainty analyses, and the results can suggest the sensitivity properties of SSI for similar case studies. A parametric study (e.g., [213] and Section 6.5) may be needed to find the sensitivity properties for different SSI scenarios.

From Case studies 5 and 6, some observations on the tunnel-soil-structure interaction mechanism are made:

- In both case studies, the probability of non-negligible damage is on the order of 20-25%, which is usually considered "unlikely" or "fairly unlikely" [5, 12] in typical risk analysis of construction projects. However, this does not undermine the significance of the probabilistic assessment for two reasons: (1) as reported by Alpert and Raiffa [3], engineers, even experts, tend to be over-confident in their assessment, but the proposed probabilistic assessment approach provides a quantitative tool to specify how reliable an assessment result is; (2) the variance of V_L and K adopted in the case studies are smaller than the variance observed in previous tunnel constructions (see Table 6.2). The probability of non-negligible damage may be much higher when practitioners have a more pessimistic uncertainty quantification of the input variables.

- Ignoring the SSI effect usually causes over-conservative assessment results in tunnel and structure interactions. For example, the probability of non-negligible damage computed in case study 6 is smaller than those computed by Camós et al. [31], in which the SSI effect is ignored. For this case study, the approach proposed in this dissertation demonstrates the importance of the SSI effect in damage assessment.

- Yiu, Burd, and Martin [202] studied tunnel-soil-structure interaction and the difference that results from analyzing each facade wall individually and analyzing the complete building altogether. It is reported that for orthogonal tunnel-building scenarios, analyzing individual walls or complete structures provide similar values of characteristic tensile strain, but 3D complete building analysis with a skewed tunnel predicts less damage than the equivalent orthogonal tunnel case. Yiu, Burd, and Martin [202] also suggested that further study is needed for building performance during incremental tunnel construction. The difference between individual and complete analysis for skewed tunnels is revealed by case study 5: Camós et al. [31] reported that the damage probability of the building in CS-1 is at its maximum when $y_s = -10$ when the rear facade is analyzed individually, while the probability reaches the maximum at $y_s = -50$ when the complete building is analyzed in this dissertation. When the tunnel face approaches the front wall, the rear wall is disturbed by very small ground displacements, so the rear wall provides additional support to the front wall. When the tunnel face approaches the rear wall, the front wall has stabilized, and additional supports are provided to the rear wall. This coupling mechanism between the front and rear walls illustrates the importance of a 3D modeling method in skewed tunnel-soil-structure interaction.

- It is observed that $\hat{F}_n(\varepsilon_c)$ changes more significantly with the tunnel face position (y_s) in CS-2 than CS-1. This may be explained by the following three observations. First, the volume loss in CS-2 is much larger than in CS-1 and the change of ground movements with y_s is, therefore, more significant than in CS-1. Second, when a tunnel approaches an orthogonal wall in CS-2, the whole wall experiences ground movements at the same time. However, when the tunnel face approaches a wall from a skewed direction, as in CS-1, the front part of the wall experiences the ground movements first, followed by the rear part. Therefore, the differential ground movements are smoothed between the front and rear part of the wall, and the building deformation of a skewed wall changes slower than for an orthogonal wall when a tunnel approaches. Third, as discussed above and in [202], the coupling effects between the front wall and rear wall are stronger in skewed buildings than in orthogonal buildings. The coupling between the front and rear walls can also smooth differential ground movements through the same mechanism described above.

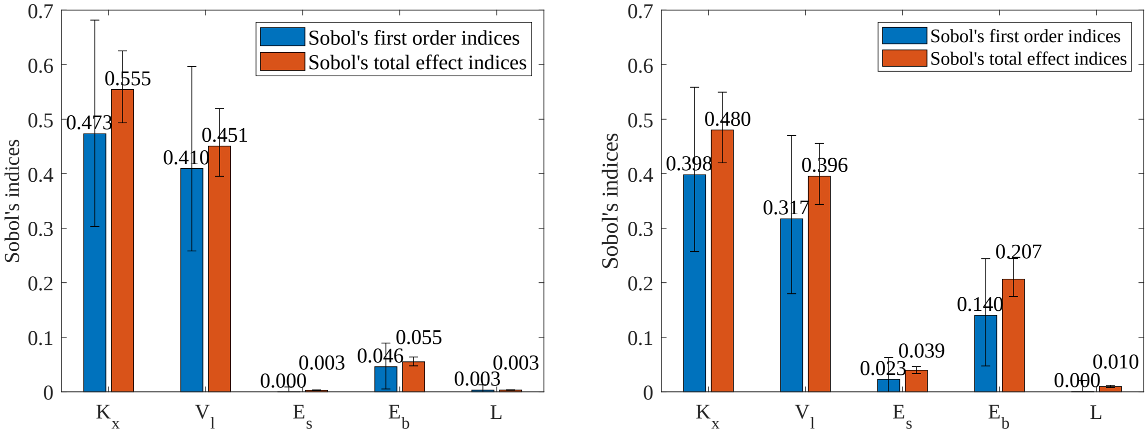

(a) Sensitivity analysis results of CS-1.

(b) Sensitivity analysis results of CS-2.

Figure 6.21: Case study 5 & 6: Sobol's sensitivity analysis results.

6.4 Case studies on the regional/community scale

6.4.1 Case study 7: Alaskan Way Viaduct Replacement program

The first regional scale base study is the Alaskan Way Viaduct replacement program, where a section of State Route 99 is replaced with a 2,830 m (1.756 mile) double-decker tunnel. The maximum depth of the tunnel is 65.5 m below the ground surface. The tunnel was constructed using a double shield EPBM with a 17.5 m (57.5 ft) diameter. The major geologic conditions along the tunnel are over-consolidated glacial and non-glacial pre-Vashon geologic units. The surface geologic conditions are mostly granular deposits, clay, silt, and fills [6]. A first stage assessment is conducted on all the buildings within 200 m of the tunnel axis. Fig. 6.22 is the total 319 buildings involved in the assessment, and Fig. 6.24 is the greenfield ground settlement contour if a constant $V_L = 1\%$ and $K = 0.5$ are assumed. The V_L is taken as 1% to ensure a conservative assessment, as suggested by Mair, Taylor, and Burland [120]. However, as discussed in Section 4.2.1, a 1% volume loss may not be necessarily conservative due to the large uncertainty in the ground movement control during tunnel excavation. To consider the spatial variability effect of the ground movements, the random field models for V_L and K developed in Section 4.2.1 is adopted. The mean value of V_L is taken as 0.5% and K is taken as 0.5. The covariance matrices of V_L and K at all building corner points are calculated, as shown in Fig. 6.23. The covariance matrices are expanded with the discrete Karhunen-Loève Expansion, and the first 99% eigenvalues are selected to generate realizations of the V_L and K random field samples. The number of eigenvalues adopted for V_L and K is 3,095 and 2,155, which correspond to 99.01% and 99.02% of total eigenvalues.

The `ImpactAsEDP` model is adopted to estimate building damage, where the building is considered a "failure" if the vertical displacement below the building is greater than 1 cm. The concept of "failure" is used to distinguish if a second-stage assessment is needed, and is not necessarily connected to physical building damage. Fig. 6.25 is the analysis using constant $V_L = 1\%$, and Fig. 6.26 is the probabilistic assessment results. In the deterministic assessment, 124 buildings are subject to non-negligible ground movements, and a second-stage assessment is needed. In the probabilistic assessment, 134 buildings need a second-stage assessment if 90% confidence is desired, and 157 buildings need a second-stage assessment if 95% confidence is desired. As expected, the probability assessment is slightly more conservative than the deterministic assessment approach because the possibility of $V_L > 1\%$ is considered. The building geographic data is downloaded from the open-source geographic database OpenStreetMap [16]. A parallel computation scheme in shared-memory personal workstations is also adopted, and the computation time for the probabilistic assessment is less than 5 min. Owing to the less effort of building surveying and the fast computation, the first-stage assessment approach may provide a practical tool at the early planning stage to select tunnel alignment alternatives.

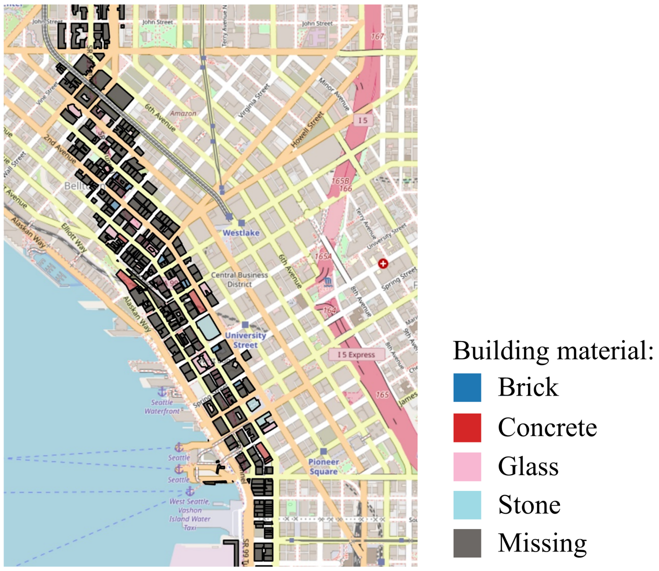

Figure 6.22: Case study 7: buildings assessed in the Alaskan Way Viaduct case study

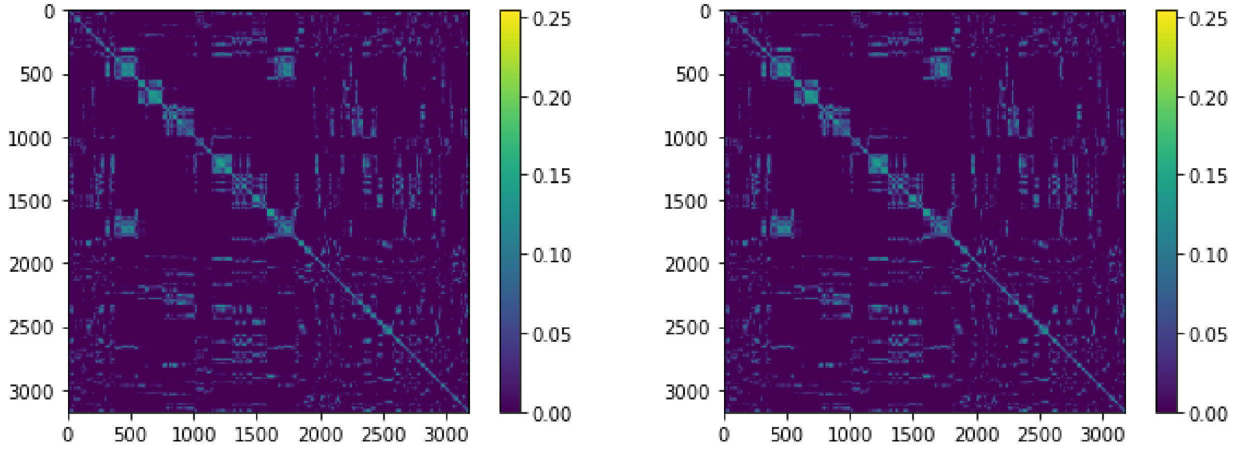

(a) Covariance matrix of V_L random field model in the AWV case study.

(b) Covariance matrix of K random field model in the AWV case study.

Figure 6.23: Case study 7: covariance matrix of ground movements in the Alaskan Way Viaduct case study.

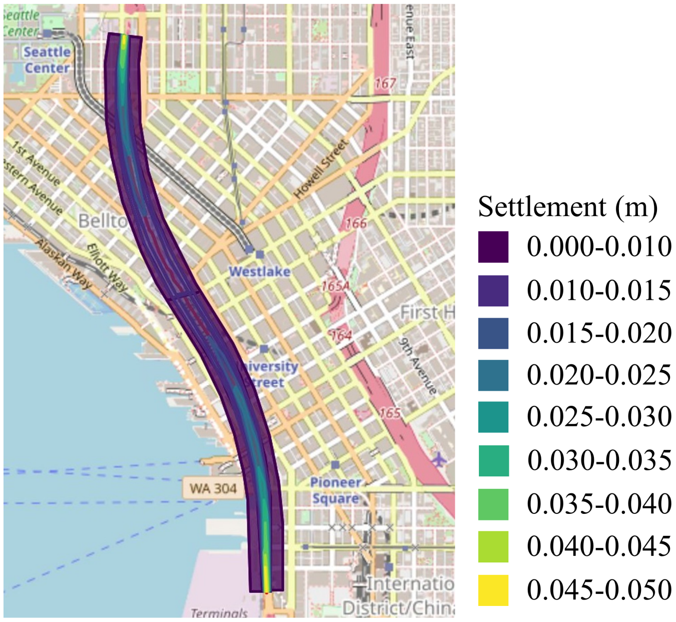

Figure 6.24: Case study 7: settlement contour used for deterministic assessment.

6.4.2 Case study 8: Infrastructure tunnel in Oslo, Norway

In this case study, the assessment of deep excavation-induced building damage in an infrastructure tunnel project in Oslo, Norway, is done on a community-level scale. The excavation depth is between 8.5 m and 11 m deep and is supported by steel props and concrete slabs. Sheet piles were first piled until the bedrock level, and the top concrete slab and steel props were then installed. Afterward, internal excavation was carried on, after which the bottom slab and internal vertical concrete walls were cast. The excavated soil was mostly clay, with an initial elastic modulus of approximately 50 MPa. To account for the stiffness reduction caused by very large soil strain induced by the excavation, a (17.9× beta(2,2)+1.06)×10^6 distribution, which corresponds to a 10 MPa mean and 40% coefficient of variance (CV), is used to model the uncertainty of the soil elastic modulus in the SSI model. The 40% CV is consistent with the suggestions given by Phoon and Kulhawy [151].

The analysis is done in two stages. In the first stage, the impact as EDP model is adopted, and the possible magnitude of ground settlements below all the buildings in the vicinity of the studied excavation is estimated. The random field models described in Section 4.2.1 are adopted to estimate the probability of non-negligible ground settlements under each building. The mean value of δ_{vm}/H_e is taken as 1%, which is estimated from the Norwegian Geotechnical Institute's database of similar excavation projects in Norway. The mean value of η is taken as 1.3, which is also

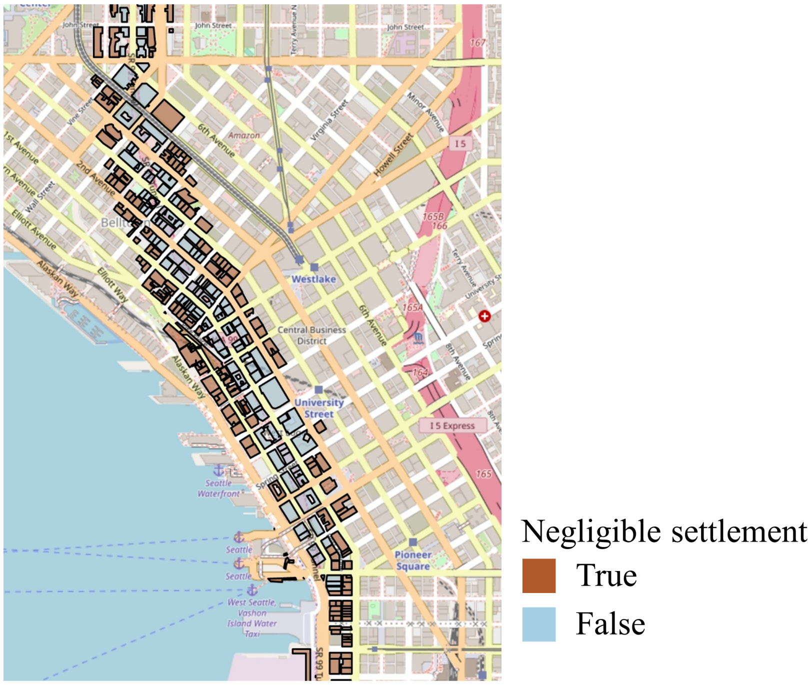

Figure 6.25: Case study 7: deterministic assessment results.

consistent with the case histories in Norway. Fig. 6.27 shows the studied area and the probability of non-negligible impact on each building. All the delineated buildings are considered vulnerable from the excavation and manually monitored with total stations over three years after the deep excavation. From the first-stage assessment result, it may be concluded that the conventional analysis approach is too conservative. With the effects of possibly underestimated ground movements considered with the random field ground movement models, the probability of non-negligible impact under most monitored buildings is small. As a result, the monitoring of a large portion of the buildings is not necessary, and significant monitoring cost could have been saved. This conclusion is confirmed by the monitoring result that most of the buildings experienced negligible settlements over the excavation period. The conclusion can also be confirmed by the ground motion measured with interferometric synthetic aperture radar (InSAR), as shown in Fig. 6.28. The dataset plotted in Fig. 6.28 is published by InSAR Norway, https://insar.ngu.no/, and is measured with Sentinel-1 with a ground resolution of approximately 5 x 20 m (5 m in East-West and 20 m in North-South direction). It is observed that the buildings classified as negligible impact experienced very small ground settlement. Ritter and Frauenfelder [161] presented InSAR datasets of the same area with higher spatial resolutions and the same results are observed. However, there are four buildings that may suffer from large ground movement impact and need to be assessed in a second stage. Fig. 6.29 is a plot of the ASRE3D models created for the four vulnerable buildings. The uncertainties

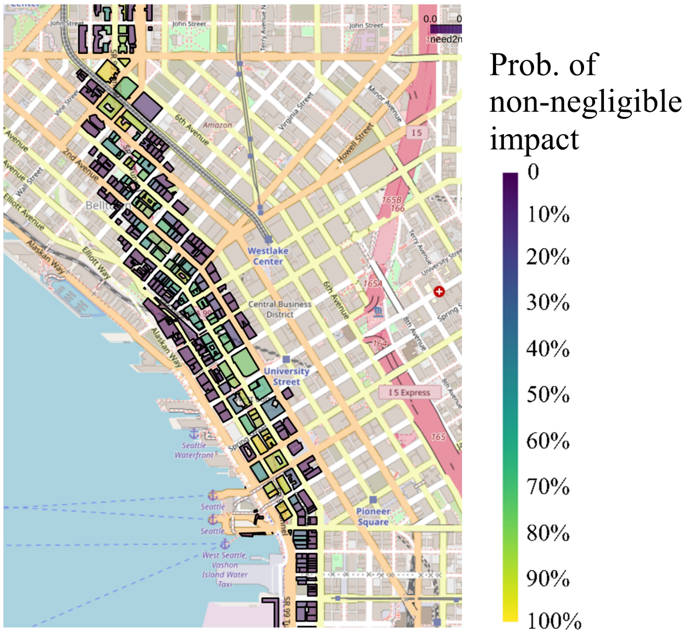

Figure 6.26: Case study 7: probabilistic assessment result in the Alaskan Way Viaduct case study.

considered in the second-stage assessment are the ground movements, soil stiffnesses, building stiffnesses, and building weights. The ground movements uncertainty model is the same with the first-stage assessment. The soil stiffnesses are modeled as a lognormal random field model with a exponential correlation function and scale of fluctuation equal to 10 m, which is the worst-case scenario in building differential settlement suggested by Ahmed and Soubra [1] and Stuedlein and Bong [180]. The studied buildings are hewn masonry buildings or solid brick buildings with nominal stiffnesses ranging from 1,200 MPa to 1,700 MPa, as suggested in the European Standard [176]. The buildings were built up to 200 years ago, and to account for degradation, reduction factors (RFs) with the distribution of 0.45 × beta (2,4)+0.55 are multiplied by the building stiffness values. The reduction factors are consistent with the strength reduction factor adopted in the ACI 530 building code for masonry structures [123], which suggested a small probability (10% in the proposed distribution) that the RFs are smaller than 0.6. The beta(2,4) distribution is adopted for RFs so that the distribution is skewed to the right, which ensures a conservative estimation of the building stiffnesses. To model the uncertainty in the estimation of building weight (L), the method suggested in [52] is adopted, where the mean of L was taken as 1.05 of the nominal design loads and a CV of 10% should be considered. The nominal design loads on the buildings were taken as the material self-weight plus 10 kPa per story, and a normal distribution is assumed for L. With the input uncertainties quantified for the studied buildings, 5,000 crude Monte Carlo simulations were conducted for each building to estimate the distribution of their characteristic strains ε_c. The crude

Monte Carlo method is adopted as a benchmark for the probabilistic approach. The computation is done on the HPC cluster SAVIO at UC Berkeley. 100 processes are deployed, and the computation time ranges from around 25 min (Bldg C) to around 3 hr 30 min (Bldg A), depending on the size of the buildings. The application of advanced Monte Carlo methods has been explored to shorten the computation time, as discussed in Section 4.4.

The probabilistic analysis is validated with building monitoring results. The vertical settlements of the buildings were measured manually with total stations. The monitoring was carried out between January 2016 and October 2022. The typical measurement interval is 2-3 weeks and the settlement is measured more frequently during the excavation construction period (roughly July 2018 and October 2018). Fig. 6.30 is a time series plot of the settlement of the studied buildings. It is observed that the studied buildings experienced a soil consolidation-induced settlement before and after the excavation construction period. Because this dissertation focuses on the effect of excavation-induced ground and building movements, the consolidation-induced settlements need to be subtracted from the total measured settlement. The consolidation rate before and after excavation is estimated with a linear regression (see dashed lines in Fig. 6.31), and the consolidation-induced settlement is estimated as the average consolidation rate times the excavation period. A more accurate estimation of consolidation-induced ground movements can be estimated with Terzaghi's One-Dimensional Consolidation Theory or 3D consolidation analyses, but the estimated consolidation is considered accurate enough in this case study, and more detailed consolidation analyses is out of the scope of this dissertation.

Fig. 6.32 - 6.35 are comparisons of the monitored building settlements versus the analysis of `ASRE3D` using the nominal ground movements, soil stiffnesses, building stiffnesses, and building weights. It is observed that despite the nominal values giving a reasonable prediction, the spatial variability of ground movements can not be captured with the current ground movement model discussed in Section 3.1.2. This again demonstrates the importance of the random field models and the modeling of the spatial variability in the proposed probabilistic analysis approach. Fig. 6.36 compares the ASRE3D calculated building settlements in the probabilistic Monte Carlo simulations and the monitored building settlements. It is observed that the Monte Carlo simulated values can cover the monitored value in a reasonable range, except at the far end in Bldg A. This discrepancy is believed to be caused by the error in total station monitoring and the calibration of consolidation-induced settlements. This is because the far end of bldg A is over 60 m away from excavation, and the greenfield ground movements induced by the excavation should be very close to zero. Moreover, bldg A is a relatively flexible 2-story masonry building, and the building stiffness may not modify the ground displacement at the far end significantly. Overall, it is concluded that the probabilistic analysis reasonably captured the uncertainty in the assessment of excavation-soil-structure interaction.

Similar to the other case studies, the probabilities of each damage state of each building can be calculated with Eq. 4.5b. Fig. 6.37a shows the damage state probabilities with confidence intervals. Besides the damage probabilities, it is observed that the maximum total ground movements (2nd norm of the ground movement vector) are strongly correlated to the characteristic strains in the buildings. As a result, the maximum total ground movements can be used as a predictor to estimate building damage probabilities. Fragility curves, which are defined as $\mathbf{P}[DS \geq DS_i|\delta_{gf,max}]$, can be estimated from the Monte Carlo simulations. Fig. 6.37b shows the fragility curves for Bldg B in this case study. With the fragility curves, a more practical probabilistic assessment approach can be defined, where the fragility curves are first produced in an offline stage when a tentative excavation design is developed. When an alternative design is proposed, new predictions of maximum ground movements will be estimated and the building damage probabilities can be quickly estimated from the fragility curves. The building damage probability estimate for alternative designs can be accomplished in real-time and is considered an online analysis. If the estimated maximum ground movements in the design alternatives is again a random variable, the conditional Monte Carlo method can be adopted to estimate the new building damage probabilities, as discussed in Section 4.6 of [110].

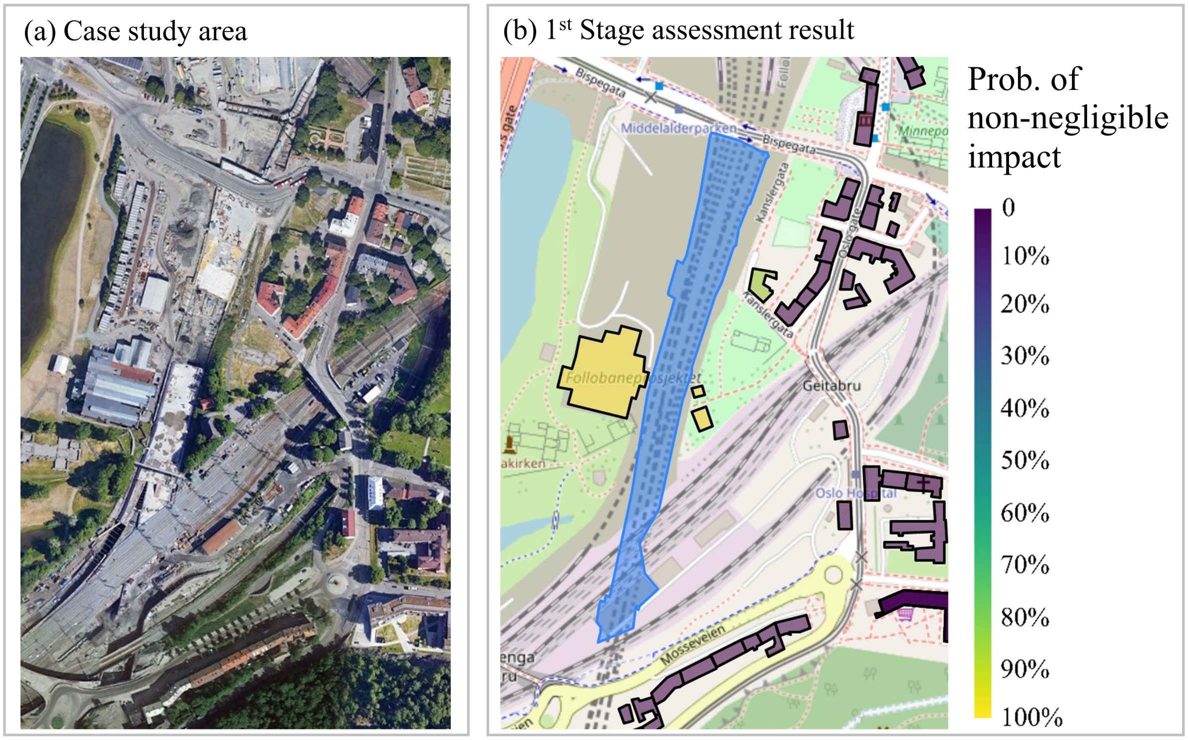
(a) Case study area

(b) 1st Stage assessment result

Figure 6.27: Case study 8: area of interest and the first stage assessment results

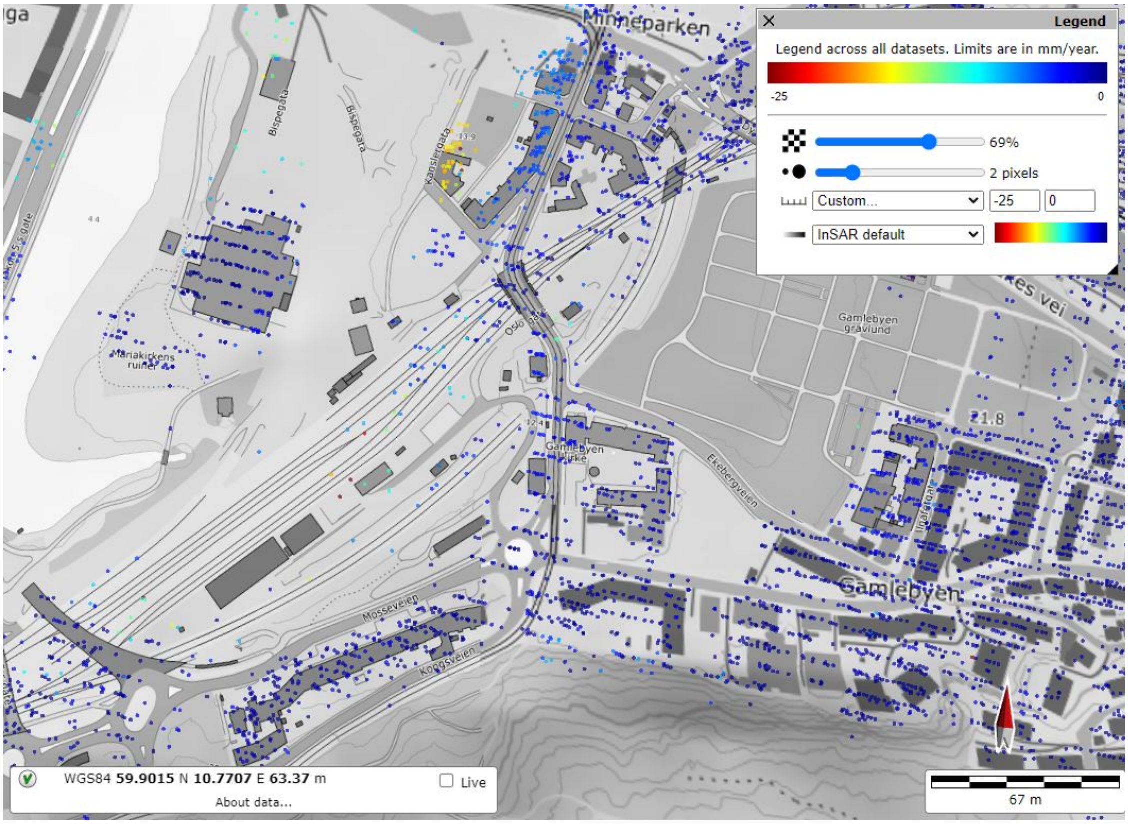

Legend across all datasets. Limits are in mm/year.

-25 0

69%

2 pixels

Custom... -25 0

InSAR default

WGS84 **59.9015** N **10.7707** E **63.37** m

Figure 6.28: Case study 8: settlement measured with InSAR (Published by InSAR Norway https://insar.ngu.no/)

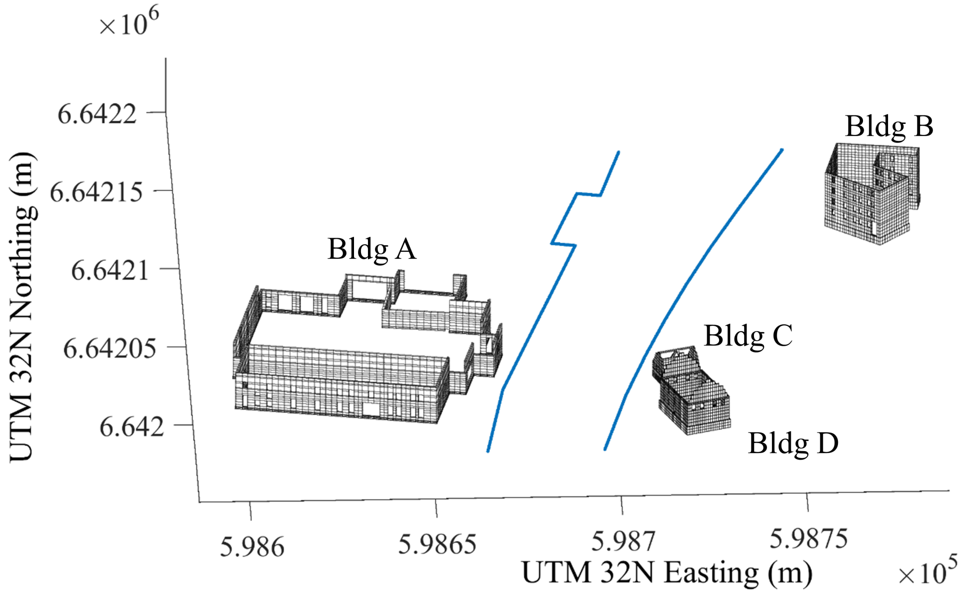

Figure 6.29: Case study 8: ASRE3D models of the second stage assessment

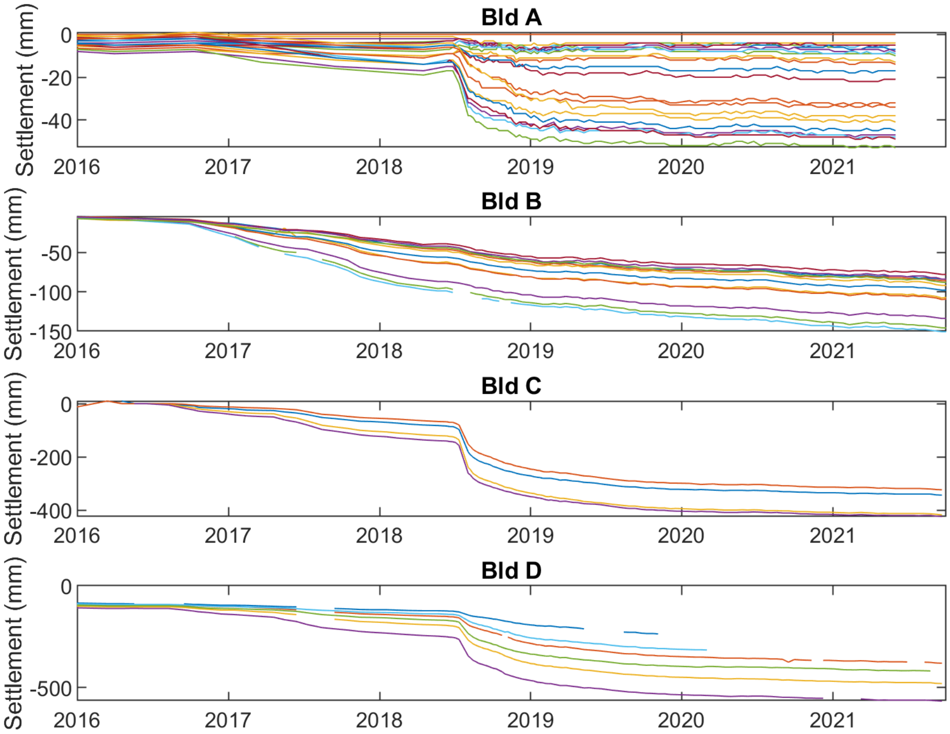

Figure 6.30: Case study 8: building settlements measured with total stations

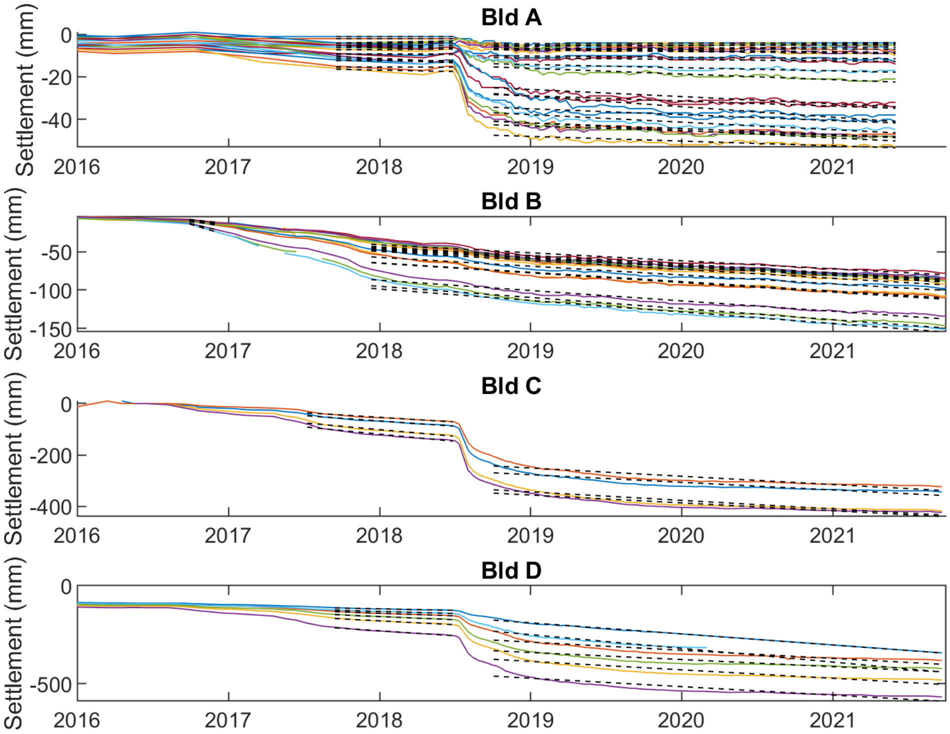

Figure 6.31: Case study 8: rate of consolidation induced ground movements

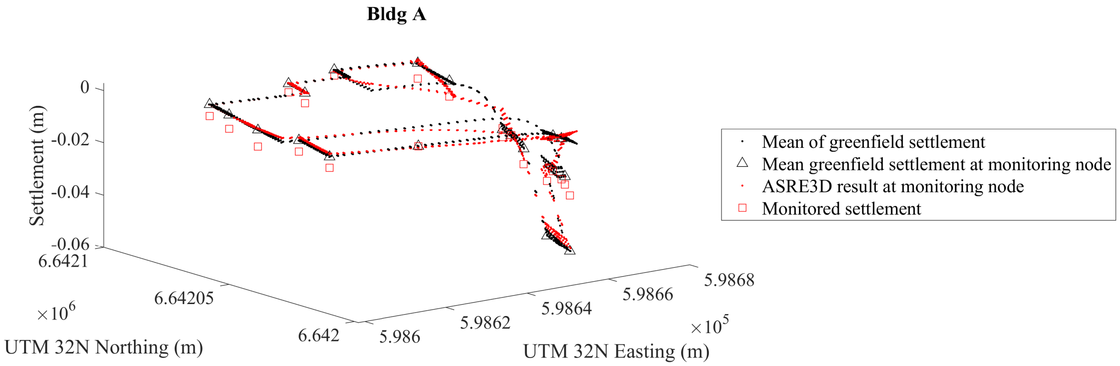

(a) Bldg A deterministic analysis result in 3D view.

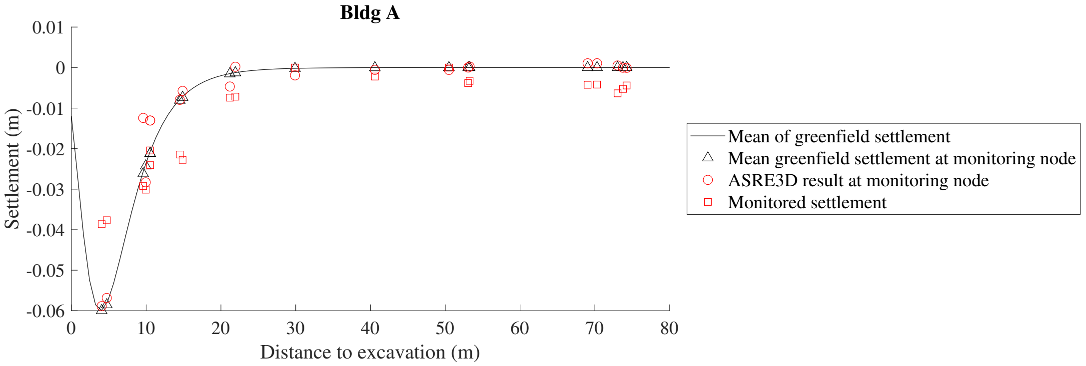

(b) Bldg A deterministic analysis result in 2D view.

Figure 6.32: Case study 8: deterministic analysis result of Bldg A and comparison to monitoring data.

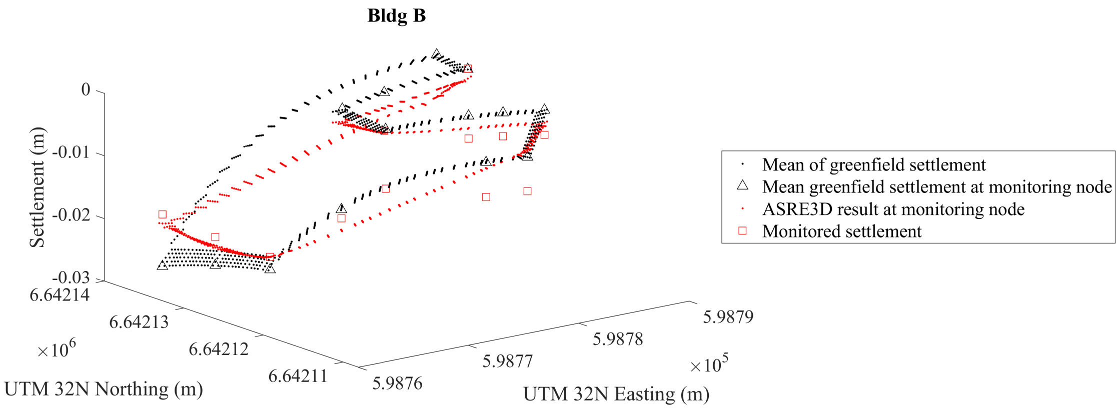

(a) Bldg B deterministic analysis result in 3D view.

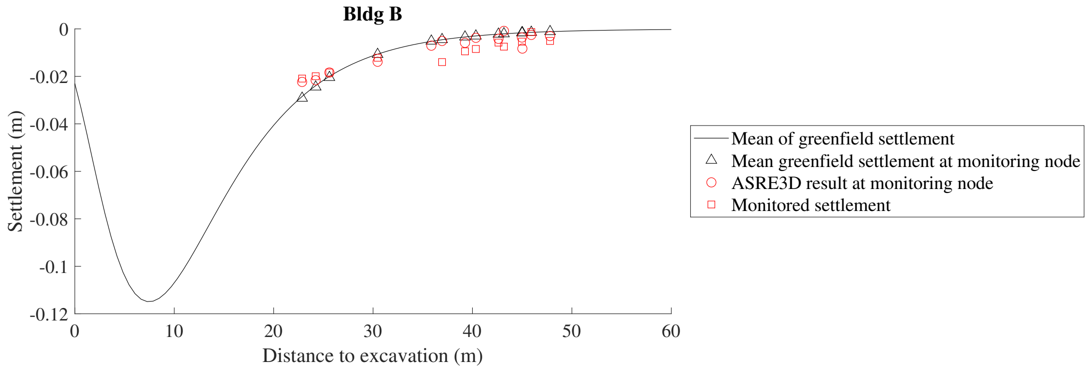

(b) Bldg B deterministic analysis result in 2D view.

Figure 6.33: Case study 8: deterministic analysis result of Bldg B and comparison to monitoring data.

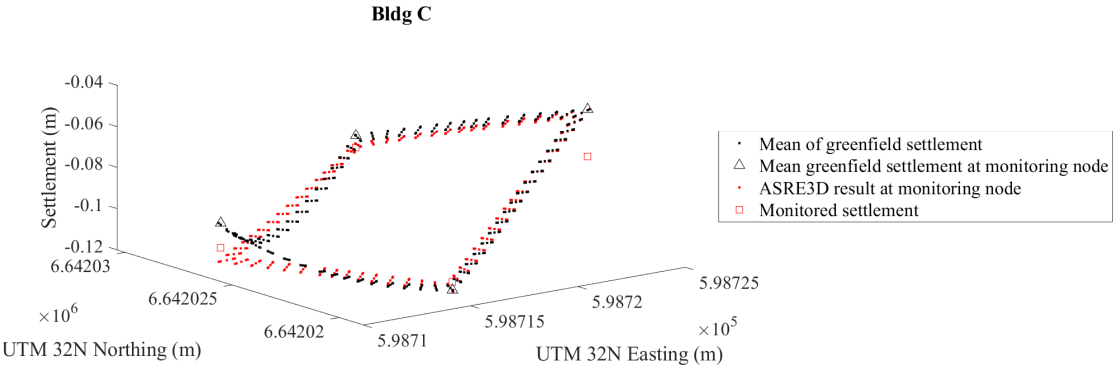

(a) Bldg C deterministic analysis result in 3D view.

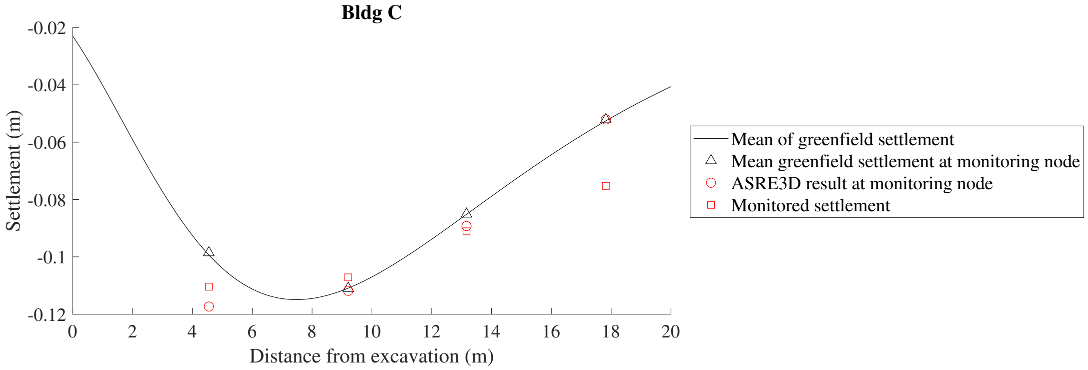

(b) Bldg C deterministic analysis result in 2D view.

Figure 6.34: Case study 8: deterministic analysis result of Bldg C and comparison to monitoring data.

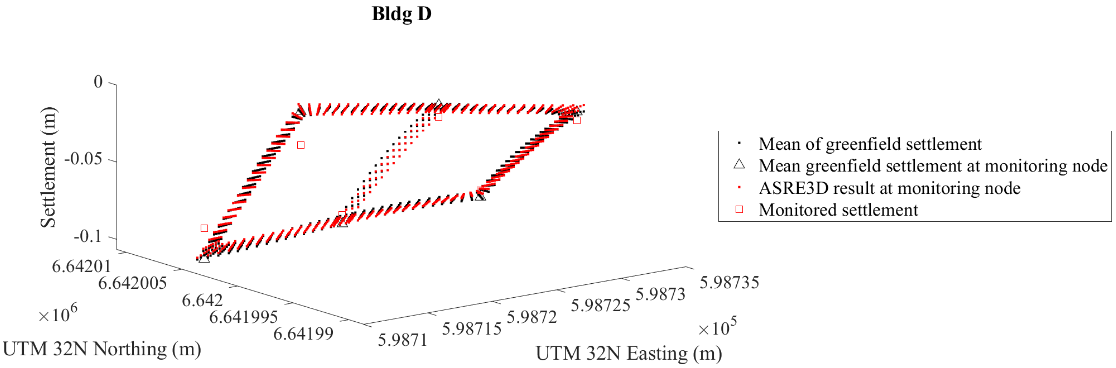

(a) Bldg D deterministic analysis result in 3D view.

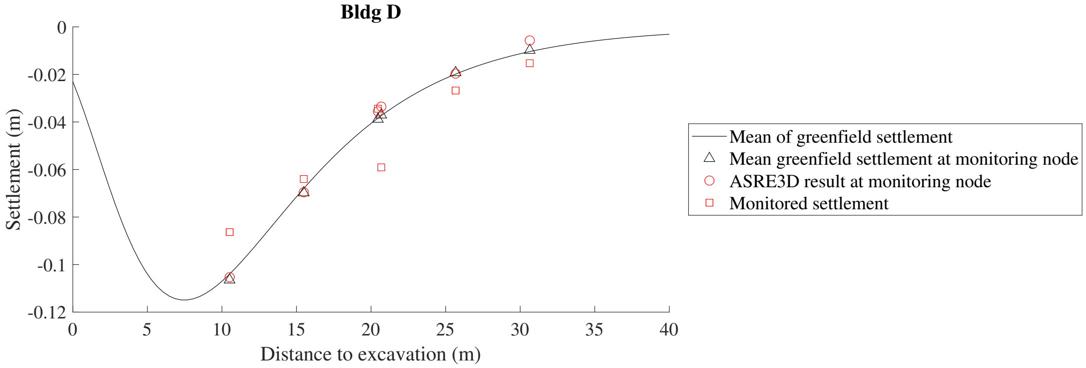

(b) Bldg D deterministic analysis result in 2D view.

Figure 6.35: Case study 8: deterministic analysis result of Bldg D and comparison to monitoring data.

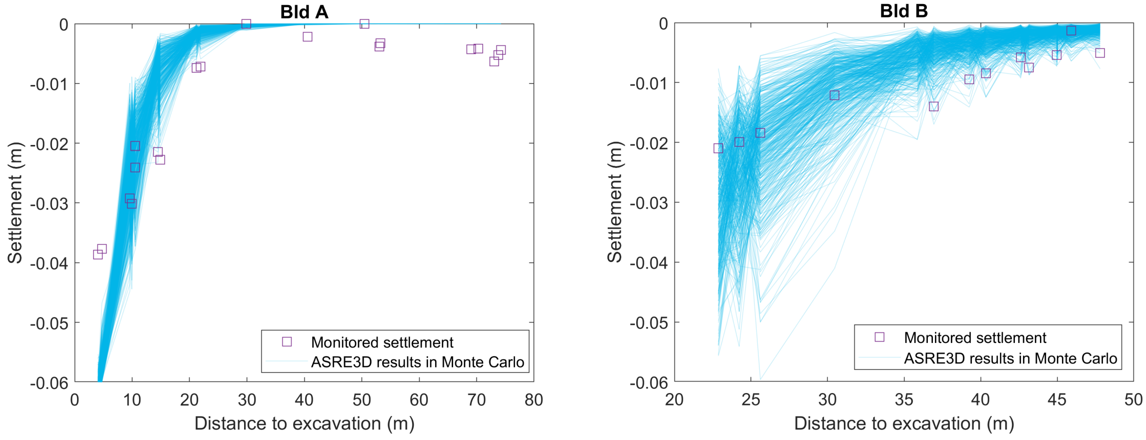

(a) Bldg A. (b) Bldg B.

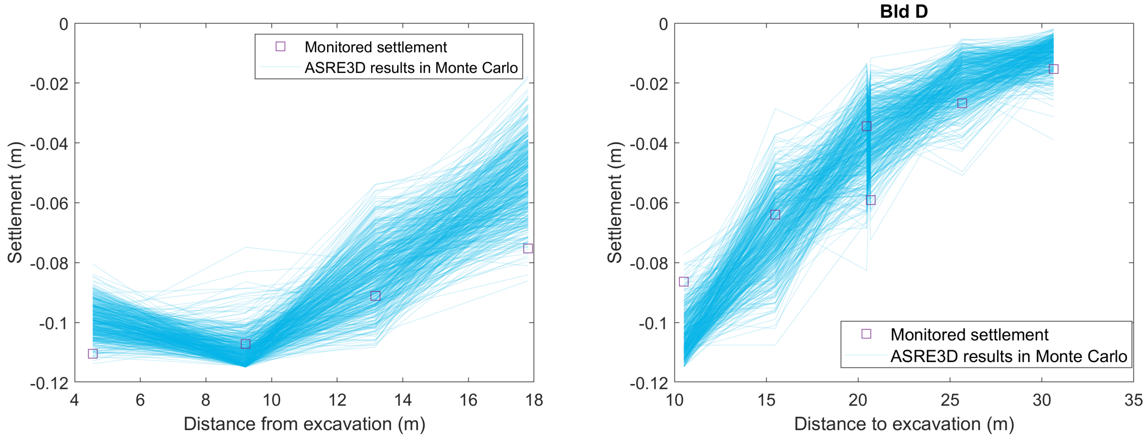

(c) Bldg C. (d) Bldg D.

Figure 6.36: Case study 8: Monte Carlo simulation results.

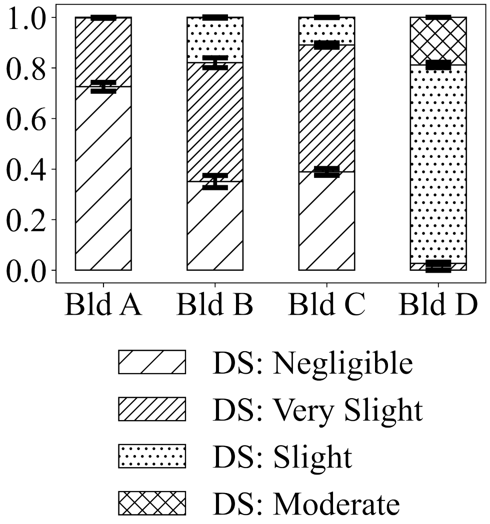

(a) Second stage assessment results.

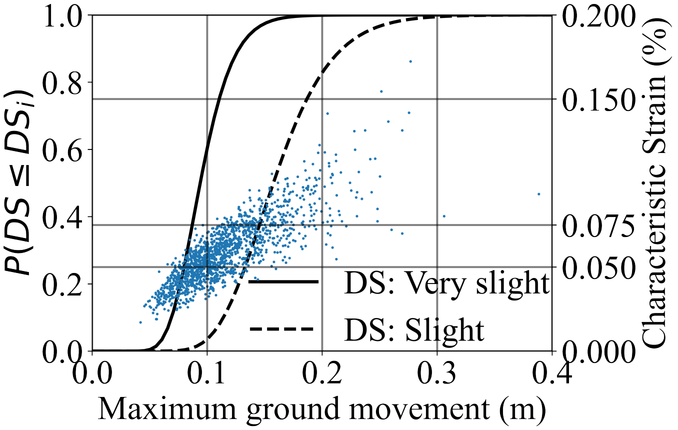

(b) Fragility curves of Bldg B.

Figure 6.37: Case study 8: probabilistic analysis results.

6.5 A parametric study of the uncertainty in tunneling-induced structural damage

The sensitivity study in the case studies revealed the most important source of uncertainty for multiple T&DE SSI scenarios. For example, comparing the first two case studies, it is observed that relatively stiff buildings that are multi-story and short in length compared to the settlement trough width, like case study 1, are more sensitive to the uncertainty of building properties, while relatively flexible buildings that are long and single-story, like case study 2, are more sensitive to the uncertainty of ground movements. However, the presented sensitivity studies can only describe the uncertainty attribution in the specific tunnel and building configurations in the case studies. To further understand the building damage sensitivity to uncertainty sources in various tunnel and SSI cases, a parametric study with 48 scenarios was conducted. The 2D Timoshenko beam model was adopted in the parametric study because (1) the Timoshenko beam model is similar to the most widely adopted equivalent beam model in the current early stage T&DE SSI assessment, and this parametric study may help to identify the most significant uncertainty sources in current engineering practice, and (2) as discussed in Section 4.5, the Sobol's sensitivity analysis is generally computationally expensive, and a parametric study using other structural analysis models may be prohibitively time-consuming for this dissertation. The details of the 48 studied scenarios are presented in Table 6.3. The effects of building length (B), building height (H), peak value of the E_b/G_b distribution, eccentricity (e/B) and the mean value of soil elastic modulus (E_s) are investigated. The tunnel depth and diameter are fixed as 20 m and 12 m. The stiffness of the buildings is assumed to be concentrated in facades; E_b = 3 GPa and a beam width of 0.5 m are assumed for the equivalent Timoshenko beam. The unit weight of the building is taken as 25 kN/m^3 and corresponding uniformly distributed loads are applied. The beam axis is assumed at the mid-height of the beams.

The Sobol's first order indices, total effect indices and Smirnov two sample tests are calculated for the 48 scenarios, and the results are shown in Figs. 6.38 to 6.40. The Sobol's indices and Smirnov test results are normalized by Eq. 6.1, where θ generically represents any of Sobol's first order indices, total effect indices or the Smirnov two-sample test, i corresponds to one of the six random variables and j stands for the j_{th} scenario. After normalization, the sum of θ in each scenario is 1, so that it is easier to compare the indices among scenarios.

In Figs. 6.38 and 6.39, both Sobol's first and total indices indicate that damage of longer buildings (B = 40 m) are more sensitive to V_L, while shorter buildings (B = 20 m) show more sensitivity to tunnel trough width (K). When the building is slender (i.e., long and low, e.g., B = 40 m and H = 5 m), almost all the uncertainty is contributed by V_L and K. This is because the building is flexible, and it deforms very similarly to the greenfield ground movement. For buildings with larger E_b/G_b, as shown by every even number bar in each subplot of Fig. 6.38 and 6.39, the shear modulus contributes more to the damage uncertainty, as expected, because of their shear dominated distortions. Interestingly, buildings located eccentrically to the tunnel have slightly smaller sensitivity to E_b and E_b/G_b than buildings concentrically above the tunnel, and the soil stiffness doesn't affect the damage sensitivity significantly.

Fig. 6.40 shows the Smirnov two-sample test results for the 48 scenarios. For four scenarios (15, 17, 39 and 41) involving stiff buildings (i.e., short in length and tall in height), most realizations fall in the nonbehavioral group, so the Smirnov two-sample test is not applicable due to lack of data in the behavioral group. However, it can still be observed that V_L plays a more important role in causing damage in more flexible buildings, while K has a similar effect in all scenarios. When E_b/G_b is large, G_b may be more responsible to building damage, while the effect of E_b is smaller. Different e/B and E_s make a small difference to the factor mapping results. It is worth noting that although the uncertainty from ground movement dominates the uncertainty of building damage in all scenarios, the building properties show a significant effect when distinguishing behavioral versus nonbehavioral damage, for most scenarios. This has implications for engineering design: estimation of building stiffness with higher accuracy may not reduce the overall uncertainty in damage assessment significantly, while increasing the building stiffness may be an effective method to mitigate structural damage.

$$\bar{\theta}_{ij} = \frac{\theta_{ij}}{\sum_{i=1}^{6} \theta_{ij}} \tag{6.1}$$

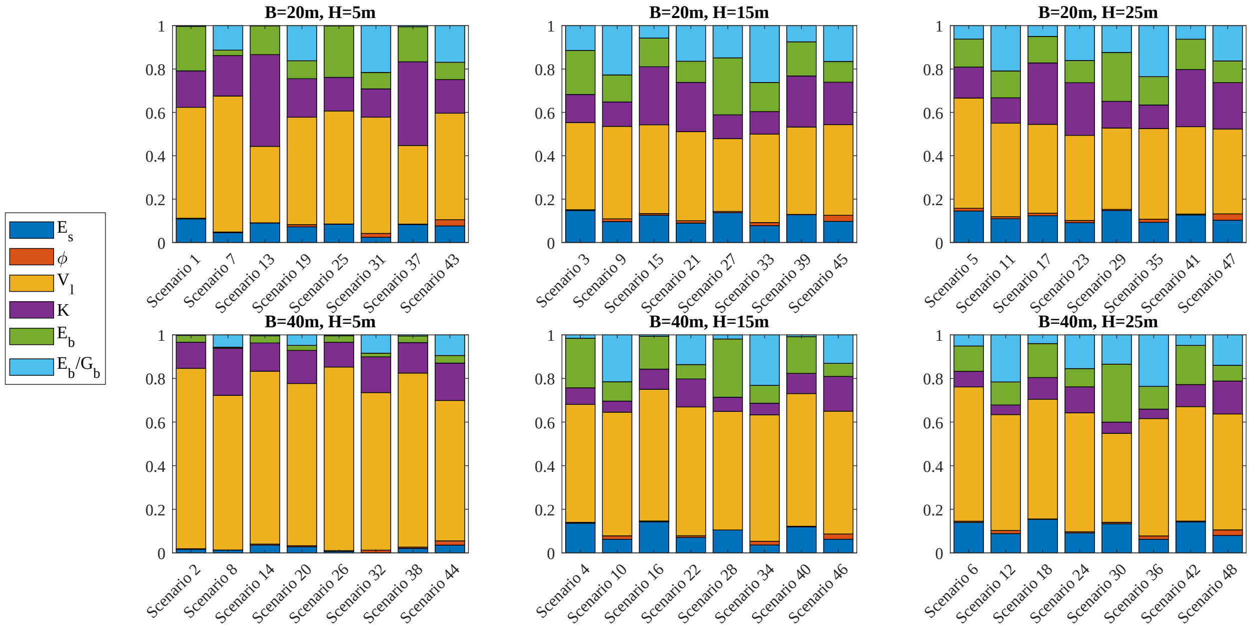

Figure 6.38: Parametric study on 48 hypothetical building-tunnel scenarios: Normalized Sobol's first order indices

Scenario	B (m)	H (m)	E_b/G_b	e/B	E_s (MPa)	Scenario	B (m)	H (m)	E_b/G_b	e/B	E_s (MPa)
1	20	5	2.6	0	50	25	20	5	2.6	0	100
2	40	5	2.6	0	50	26	40	5	2.6	0	100
3	20	15	2.6	0	50	27	20	15	2.6	0	100
4	40	15	2.6	0	50	28	40	15	2.6	0	100
5	20	25	2.6	0	50	29	20	25	2.6	0	100
6	40	25	2.6	0	50	30	40	25	2.6	0	100
7	20	5	12.5	0	50	31	20	5	12.5	0	100
8	40	5	12.5	0	50	32	40	5	12.5	0	100
9	20	15	12.5	0	50	33	20	15	12.5	0	100
10	40	15	12.5	0	50	34	40	15	12.5	0	100
11	20	25	12.5	0	50	35	20	25	12.5	0	100
12	40	25	12.5	0	50	36	40	25	12.5	0	100
13	20	5	2.6	0.5	50	37	20	5	2.6	0.5	100
14	40	5	2.6	0.5	50	38	40	5	2.6	0.5	100
15	20	15	2.6	0.5	50	39	20	15	2.6	0.5	100
16	40	15	2.6	0.5	50	40	40	15	2.6	0.5	100
17	20	25	2.6	0.5	50	41	20	25	2.6	0.5	100
18	40	25	2.6	0.5	50	42	40	25	2.6	0.5	100
19	20	5	12.5	0.5	50	43	20	5	12.5	0.5	100
30	40	5	12.5	0.5	50	44	40	5	12.5	0.5	100
21	20	15	12.5	0.5	50	45	20	15	12.5	0.5	100
22	40	15	12.5	0.5	50	46	40	15	12.5	0.5	100
23	20	25	12.5	0.5	50	47	20	25	12.5	0.5	100
24	40	25	12.5	0.5	50	48	40	25	12.5	0.5	100

Table 6.3: A parameter study of the uncertainty in tunneling induced structure damage

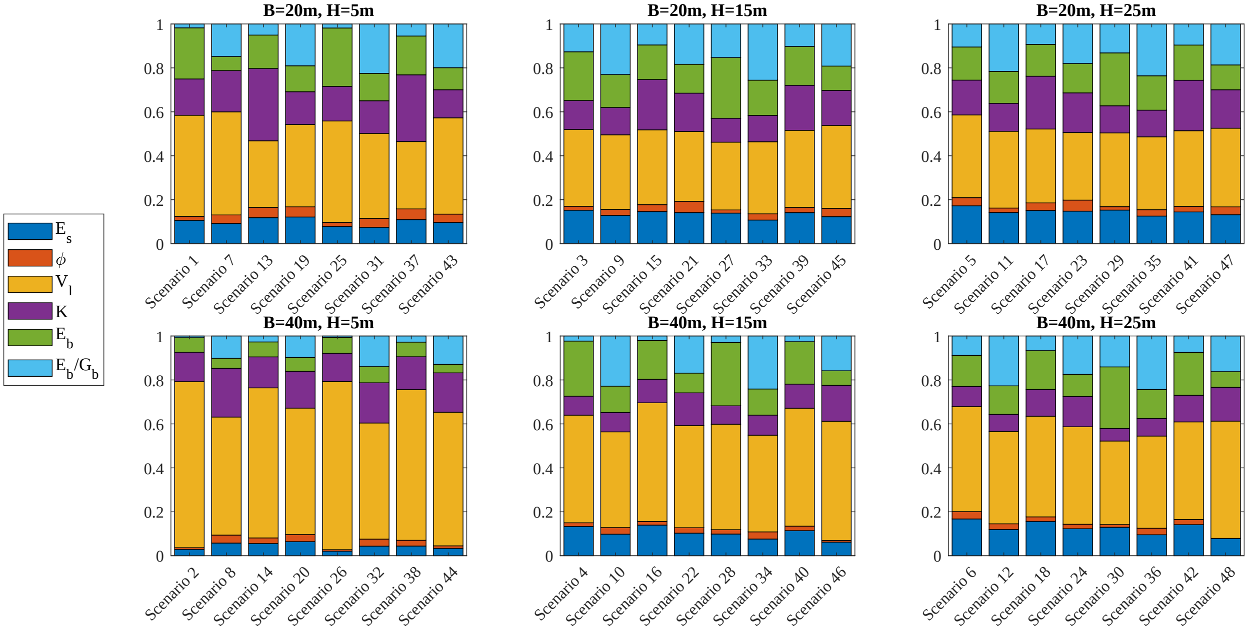

Figure 6.39: Parametric study on 48 hypothetical building-tunnel scenarios: Normalized Sobol's total effect indices

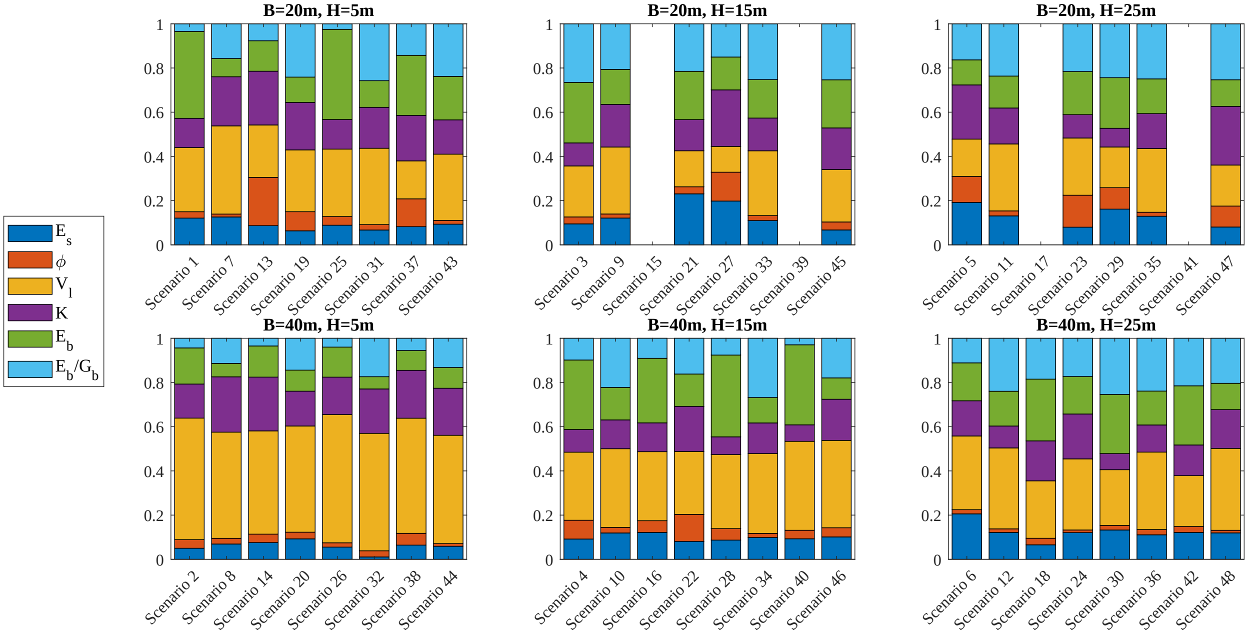

Figure 6.40: Parametric study on 48 hypothetical building-tunnel scenarios: Normalized Smirnov's two-sample tests

Chapter 7

Conclusions

The primary aim of this dissertation, as stated in Chapter 1, is to create a probabilistic performance-based engineering (PPBE) framework for the assessment of large-scale tunneling and deep excavation (T&DE)-induced building damage, and provide modeling methods and computational tools to support the framework's implementation. This objective was achieved by: 1) a modeling method to minimize the uncertainty in the early stage assessment of tunneling and deep excavation (T&DE)-induced building damage without significantly increasing the modeling effort, and 2) a probabilistic modeling and uncertainty quantification method and a tool to quantify the uncertainty in the T&DE-induced building damage assessment. The main findings, primary contributions, limitations, and some future research are summarized in this chapter.

7.1 Main findings

Soil-structure interaction mechanisms

Through the deterministic studies in this dissertation, it was found that the analysis results of the soil-structure interaction models are generally very different from the greenfield ground displacement, and could better capture the building responses than greenfield ground displacements, as shown by the comparison with monitoring data and some back analysis in multiple case studies. This confirmed that considering the soil-structure interaction effect is very important to obtain an accurate prediction of building behaviors in tunneling and deep excavations. Some influences of building characteristics on structural behavior were also confirmed: 1) the distance between the building and the tunnel/deep excavation has a significant influence on the building's deformation mode (e.g., sagging/hogging), 2) long-span and low-rising buildings are usually softer and behave more similarly to greenfield conditions than short-span and high-rising buildings, 3) 3D building layout, building openings, and building material properties may significantly influence the overall building stiffness, and the conventional equivalent beam models and relative stiffness methods may not characterize the SSI mechanisms very well.

After realizing the deficiency of the equivalent beam models and relative stiffness methods in characterizing the surface buildings, a 3D model (ASRE3D) that could model the 3D building layout, building openings, and potentially composite building materials was developed. Through the analysis of several case studies using the 3D model, a few soil-structure interaction mechanisms were discovered: 1) when the building is skewed from the tunnel axis in progressive tunnel excavation, the building façade walls may support each other and reduce overall building deformation, and as a result, analyzing the coupled walls will provide a more realistic result than analyzing each wall individually(note that some of this coupling effect is also discussed in [202]); 2) a 2D plane strain condition is usually assumed in the analysis of T&DE SSI, however, the out-of-plane differential ground displacement may introduce new building deformation modes and needs to be considered when predicting building responses.

Identified important sources of uncertainty in T&DE SSI

As summarized above, 3D building layout, building openings, and building material properties may introduce large uncertainty in T&DE SSI. Moreover, through the sensitivity analysis and parametric analysis, it is found that the uncertainty in ground displacement prediction usually introduces the most uncertainty in the assessment of low-rise buildings, which are usually vulnerable to tunneling and deep excavations, while the uncertainty in building stiffness might be of secondary importance. For relatively high-rise buildings, the modeling of building and soil stiffness may also introduce considerable uncertainty, and the uncertainty in building stiffness estimation generally causes larger effects on assessment results than the soil stiffness estimation in the current modeling method. The parametric study showed that relative sliding between building and soil occurs in most SSI scenarios, and building deformation is generally not sensitive to the soil-structure interface friction angle.

Advanced Monte-Carlo methods are powerful for uncertainty quantification in large tunneling and deep excavation projects

Building assessment in large T&DE projects often encounters high-dimensional uncertainty, especially when the spatial variability of ground movement and soil stiffness is considered. The current reliability analysis and surrogate-model-based UQ methods may not be applicable for such high-dimensional uncertainty forward propagation problems. However, Monte Carlo methods, whose convergence rates are usually independent of the uncertainty dimension, may be the most appropriate method for T&DE SSI analysis. Quasi-Monte Carlo is convenient to implement, provided that each model simulation is not too expensive, and may considerably improve the UQ efficiency. Multi-fidelity Monte Carlo can also be powerful in the staged assessment approach, and multi-fidelity models are readily available.

Besides advanced Monte Carlo methods, the computationally optimized implementation of ASRE reduced the computation time significantly compared with an implementation in Matlab. The parallel computation strategy and the application of high-performance computer clusters further reduced the computation time, which makes the Monte Carlo-based uncertainty quantification framework more practicable in engineering practice.

7.2 Contributions

A probabilistic performance-based engineering (PPBE) framework for T&DE-induced building damage assessment

The proposed PPBE borrows the workflow from earthquake engineering. Fig. 7.1 is a typical PPBE workflow in earthquake engineering, in which the first path is primarily developed from case history data, where the possible casualty and economic loss are estimated directly from earthquake intensity measures (IM) and building asset info. The second path in Fig. 7.1 models entire structures as single degree of freedom (SDOF) systems and computes engineering demand parameters with time history or response spectrum analyses. Corresponding damage measures are estimated from EDPs with fragility functions and decision variables can be estimated consequently. The third path in Fig. 7.1 involves full-scale modeling of the entire structure, and time history analysis is adopted to obtain component-level EDPs, which are then connected to the second path with fragility functions. Uncertainty quantification is incorporated in each path to address the random nature of earthquakes and the modeling uncertainties. The Hazus-MH model [170, 159, 127] provides a group of widely accepted vulnerability functions for earthquake and flood hazard, while detailed studies of fragility functions can be found in FEMA-P58 [128][129]. In practice, the first and second paths in Fig. 7.1 are usually applied to regional risk assessment, while the third path is applied to valuable and high-risk individual structures.

The proposed PPBE framework in T&DE SSI is formulated as shown in Fig. 7.2. The first path is similar to the traditional relative stiffness method reviewed in Section 2.1, but an uncertainty quantification in ground movements and building stiffness estimation is added to the relative stiffness method. In the second path in Fig. 7.2, soil-structure interaction models are created and EDPs (characteristic strain or drift ratio) are calculated. The probabilities of each damage category are then determined with the Monte-Carlo-based uncertainty propagation and the limiting strain method. The 2D elastic frame model and 3D solid models studied in this dissertation may be considered to be between the second and third path, where a relatively detailed structural analysis model is adopted and some component-level damage can be evaluated. However, this dissertation focused on the overall building damage category, and component-level EDPs were not analyzed individually. The development of consequence functions and decision variables requires much knowledge of social economy and public policy, and this work relies on future researchers to complete this final part of the PPBE framework.

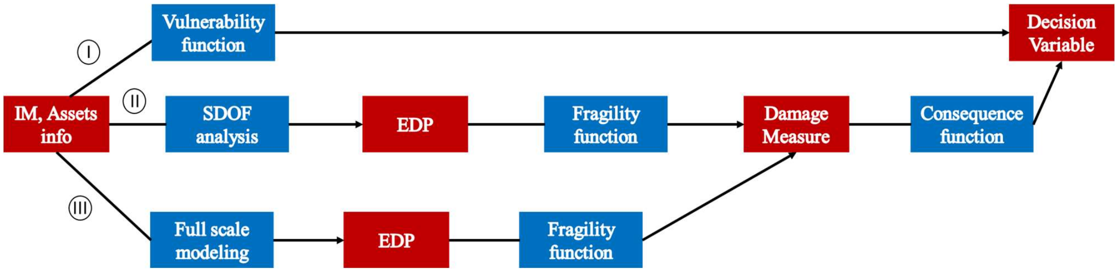

Figure 7.1: A typical Probabilistic Performance-Based Engineering (PPBE) workflow in earthquake engineering

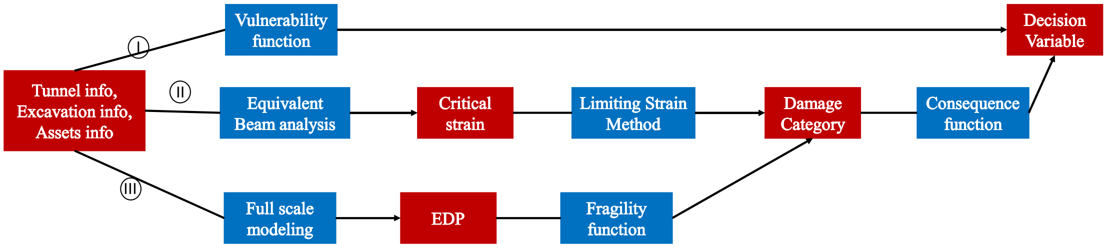

Figure 7.2: The proposed Probabilistic Performance-Based Engineering (PPBE) workflow in T&DE SSI

A hazard analysis approach and soil-structural analysis approaches for T&DE SSI

PPBE in earthquake engineering relies on probabilistic models to characterize the uncertainty in earthquake hazards, and the probabilistic models are usually derived from a combination of the analyses of geological information and seismic history information. Similarly, a probabilistic hazard analysis method for T&DE-induced ground movements is proposed (Section 4.2.1), in which the magnitude (mean) of ground movements can be estimated from empirical or numerical models of the T&DE system, and the variance or spatial variability can be estimated from case history data.

To realize the PPBE in large-scale assessment and to quantify the high-dimensional uncertainty, a balance between model accuracy and modeling effort needs to be pursued for the soil-structure analysis models. The soil-structure analysis models and computer implementations (e.g., Timoshenko beam and 3D finite element) that can be fit in the first and second paths of the proposed PPBE were provided in this dissertation.

A computational tool to facilitate the proposed PPBE

To facilitate the implementation of the proposed PPBE, a computational tool `UQ-TESSI` is developed. One of the largest obstacles in the application of PPBE is the heavy computation cost associated with the uncertainty forward propagation procedure. `UQ-TESSI` addresses this obstacle with optimized soil-structure analysis models, advanced Monte Carlo methods, and parallel high-performance computing. The civil engineering industry is gradually getting more exposed to high-performance computing through the rapidly growing cloud computing services, and `UQ-TESSI` may provide a practical tool for building damage assessment and decision-making in large T&DE projects.

Multiple case studies are presented to demonstrate the PPBE

Probabilistic assessment methods are proven helpful in seismic engineering, while relatively little probabilistic analysis is done in the area of T&DE SSI. The presented case studies demonstrate the benefits of the proposed PPBE: 1) The uncertainty of building damage assessment is formally quantified, and 2) the sources introducing the most uncertainties in the assessment are identified with global sensitivity analyses. The probabilistic measure of building damage may help to make monitoring, operation, and ground compensation decisions, and the sensitivity analyses can suggest the optimal way to reduce the uncertainty of the damage assessment results.

7.3 Limitations and future research

Some comments on the limitations of this dissertation and motivated future research are made in this section. These comments are grouped by limitations and research in deterministic soil-structure interaction modeling and in integrating monitoring data in the proposed PPBE framework.

Soil-structure interaction analysis

The soil-structure interaction analysis addressed in this dissertation adopted linear elastic constitutive models for soils and surface buildings. Although the effect of the model simplification may be quantified by the proposed probabilistic modeling approach and is usually deemed to be a secondary consideration in most T&DE-induced building damage assessments, the analysis uncertainty can be reduced if more realistic constitutive models are adopted. In future research, the heterogeneous nature of soil should be considered, and the nonlinear stress-strain behavior and yield criterion should be captured by the constitutive models. Moreover, excavation and soil-structure interaction may introduce redistribution of total stress and pore water pressure underground, and the short-term volumetric deformation in sands and long-term clay consolidation and creep need further research. Moreover, the linear elastic finite element model for surface buildings can not capture the building's behavior after crack initiation. Giardina et al. [78] showed that the continuum modeling of masonry using finite elements and proper elastoplastic constitutive models could be used to simulate damaged masonry behavior. Future structural models with more realistic material constitutive models could also enable the analysis of pre-existing damage in surface buildings.

Observational method and data integration

Underground construction has operated with significant uncertainty for a long time, and the observational method, which was first rigorously defined by Prof. Ralph Peck [147], has been used to address the uncertainty. The observational method can be briefly summarized as: 1) a preliminary design is made based on the most probable conditions, and contingency action plans are made based on the unfavorable conceivable deviations from the most probable conditions, (2) a monitoring plan is made for verifying that the structure behaves acceptably during construction, and (3) design modifications or contingency actions are put into operation if defined limits of acceptable behavior are exceeded. The long-standing observational method has highlighted the importance of incorporating instrument data in underground construction and design. In future research, a method to refine the ground movement hazard as the tunnel or deep excavation proceeds needs to be derived. Insights may be gained from the Kalman filter algorithm and control theories. Further, methods to optimize the instrumentation and data acquisition plan to minimize uncertainty and cost simultaneously requires more investigation.

Bibliography

[1] A. Ahmed and A. Soubra. “Probabilistic analysis at the serviceability limit state of two neighboring strip footings resting on a spatially random soil”. In: *Structural Safety* 49 (2014), pp. 2–9.

[2] D.E. Allen. “Limit states design—a probabilistic study”. In: *Canadian Journal of Civil Engineering* 2.1 (1975), pp. 36–49.

[3] M. Alpert and H. Raiffa. “A progress report on the training of probability assessors”. In: (1982).

[4] A. Amorosi, D. Boldini, G. De Felice, M. Malena, and M. Sebastianelli. “Tunnelling-induced deformation and damage on historical masonry structures”. In: *Géotechnique* 64.2 (2014), pp. 118–130.

[5] L. Anthony. “What’s wrong with risk matrices?” In: *Risk Analysis: An International Journal* 28.2 (2008), pp. 497–512.

[6] D. Apoji, Z. Ning, and K. Soga. “From Sensing to Machine Learning in Geoengineering”. In: *GeoStrata Magazine Archive* 26.6 (2022), pp. 44–51.

[7] ASCE and American Forest & Paper Association. *Standard for load and resistance factor design (LRFD) for engineered wood construction*. American Forest & Paper Association, 1996.

[8] D. Ashworth. “Ground surface movement behaviour influences from twin bored tunnels excavated within Longdon Clay”. MA thesis. The Old Schools, Trinity Ln, Cambridge CB2 1TN, United Kingdom: University of Cambridge, 2017.

[9] P.B. Attewell. “Predicting the dynamics of ground settlement and its derivatives caused by tunnelling in soil”. In: *Ground engineering* 15.8 (1982), pp. 13–22.

[10] Z.Z. Aye, D. Karki, and C. Schulz. “Ground movement prediction and building damage risk-assessment for the deep excavations and tunneling works in Bangkok subsoil”. In: *International Symposium on Underground Excavation and Tunnelling*. Vol. 281. Bangkok. 2006, p. 297.

[11] B.M. Ayyub and G.J. Klir. *Uncertainty modeling and analysis in engineering and the sciences*. CRC Press, 2006.

[12] G.B. Baecher and J.T. Christian. *Reliability and statistics in geotechnical engineering*. John Wiley & Sons, 2005.

[13] Z. Bai. "Krylov subspace techniques for reduced-order modeling of large-scale dynamical systems". In: *Applied numerical mathematics* 43.1-2 (2002), pp. 9–44.

[14] R. Bellman. "Adaptive control processes. A guided tour. Princeton, NJ, 1961. Princeton University Press." In: (1962).

[15] P. Benner, S. Gugercin, and K. Willcox. "A survey of projection-based model reduction methods for parametric dynamical systems". In: *SIAM review* 57.4 (2015), pp. 483–531.

[16] J. Bennett. *OpenStreetMap*. Packt Publishing Ltd, 2010.

[17] M. Berveiller, B. Sudret, and M. Lemaire. "Presentation of two methods for computing the response coefficients in stochastic finite element analysis". In: *Proc. 9th ASCE Specialty Conference on Probabilistic Mechanics and Structural Reliability, Albuquerque, USA*. 2004.

[18] BIA. "Technical notes 3A–brick masonry material properties". In: *Technical Notes on Brick Construction* 216 (1992).

[19] D. Boldini, N. Losacco, S. Bertolin, and A. Amorosi. "Finite Element modelling of tunnelling-induced displacements on framed structures". In: *Tunnelling and Underground Space Technology* 80 (2018), pp. 222–231.

[20] D. Boldini et al. "Tunneling-induced deformation of bare frame structures on sand: Numerical study of building deformations". In: *Journal of Geotechnical and Geoenvironmental Engineering* 147.11 (2021), p. 04021116.

[21] S.J. Boone. "Assessing risks of construction-induced building damage for large underground projects". In: *Probabilistic Applications in Geotechnical Engineering*. 2007, pp. 1–13.

[22] M.D. Boscardin and E.J. Cording. "Building response to excavation-induced settlement". In: *Journal of Geotechnical Engineering* 115.1 (1989), pp. 1–21.

[23] H.J. Burd, G.T. Houlsby, C.E. Augarde, and G. Liu. "Modelling tunnelling-induced settlement of masonry buildings". In: *Proceedings of the institution of civil engineers-geotechnical engineering* 143.1 (2000), pp. 17–29.

[24] H.J. Burd, W.N. Yiu, S. Acikgoz, and C.M. Martin. "Soil-foundation interaction model for the assessment of tunnelling-induced damage to masonry buildings". In: *Tunnelling and Underground Space Technology* 119 (2022), p. 104208.

[25] J.B. Burland. "Assessment of risk of damage to buildings due to tunnelling and excavatioins". In: *1st Int. Conf. on Earthquake Geotech. Engrg., IS-Tokyo'95*. 1995.

[26] J.B. Burland, B.B. Broms, and V.F.B. De Mello. "Behaviour of foundations and structures". In: (1978).

[27] J.B. Burland, R.J. Mair, and J.R. Standing. “Ground performance and building response due to tunnelling”. In: *Advances in geotechnical engineering: The Skempton conference: Proceedings of a three day conference on advances in geotechnical engineering, organised by the Institution of Civil Engineers and held at the Royal Geographical Society, London, UK, on 29–31 March 2004*. Thomas Telford Publishing. 2004, pp. 291–342.

[28] B. Cami, S. Javankhoshdel, K.K. Phoon, and J. Ching. “Scale of fluctuation for spatially varying soils: estimation methods and values”. In: *ASCE-ASME Journal of Risk and Uncertainty in Engineering Systems, Part A: Civil Engineering* 6.4 (2020), p. 03120002.

[29] C. Camós and C. Molins. “3D analytical prediction of building damage due to ground subsidence produced by tunneling”. In: *Tunnelling and Underground Space Technology* 50 (2015), pp. 424–437.

[30] C. Camós, C. Molins, and O. Arnau. “Case study of damage on masonry buildings produced by tunneling induced settlements”. In: *International Journal of Architectural Heritage* 8.4 (2014), pp. 602–625.

[31] C. Camós, O. Špačková, D. Straub, and C. Molins. “Probabilistic approach to assessing and monitoring settlements caused by tunneling”. In: *Tunnelling and Underground Space Technology* 51 (2016), pp. 313–325.

[32] P. Castaldo, M. Calvello, and B. Palazzo. “Probabilistic analysis of excavation-induced damages to existing structures”. In: *Computers and Geotechnics* 53 (2013), pp. 17–30.

[33] S. Choi, R. Grandhi, and R.A. Canfield. *Reliability-based structural design*. Springer Science & Business Media, 2006.

[34] C.A. Cornell. “A probability-based structural code”. In: *Journal Proceedings*. Vol. 66. 12. 1969, pp. 974–985.

[35] N. Cressie. *Statistics for spatial data*. John Wiley & Sons, 2015.

[36] K.D. Dalgic, M.A.N. Hendriks, and A. Ilki. “Building response to tunnelling-and excavation-induced ground movements: using transfer functions to review the limiting tensile strain method”. In: *Structure and Infrastructure Engineering* 14.6 (2018), pp. 766–779.

[37] R.A. Day and D.M. Potts. “Zero thickness interface elements—numerical stability and application”. In: *International Journal for numerical and analytical methods in geomechanics* 18.10 (1994), pp. 689–708.

[38] G.G. Deierlein et al. “A cloud-enabled application framework for simulating regional-scale impacts of natural hazards on the built environment”. In: *Frontiers in Built Environment* 6 (2020), p. 558706.

[39] M.J. DeJong, M.A.N. Hendriks, and J.G. Rots. “Sequentially linear analysis of fracture under non-proportional loading”. In: *Engineering Fracture Mechanics* 75.18 (2008), pp. 5042–5056.

[40] A. Der Kiureghian. *Structural and system reliability*. Cambridge University Press, 2022.

[41] A. Der Kiureghian, H. Lin, and S. Hwang. "Second-order reliability approximations". In: *Journal of Engineering mechanics* 113.8 (1987), pp. 1208–1225.

[42] A. Der Kiureghian and M.D. Stefano. "Efficient algorithm for second-order reliability analysis". In: *Journal of engineering mechanics* 117.12 (1991), pp. 2904–2923.

[43] P.S. Dimmock. "Tunnelling-induced ground and building movement on the Jubilee Line Extension". PhD thesis. University of Cambridge, 2003.

[44] P.S. Dimmock and R.J. Mair. "Effect of building stiffness on tunnelling-induced ground movement". In: *Tunnelling and Underground Space Technology* 23.4 (2008), pp. 438–450.

[45] N.A. Do, D. Dias, P. Oreste, and I. Djeran-Maigre. "Three-dimensional numerical simulation of a mechanized twin tunnels in soft ground". In: *Tunnelling and Underground Space Technology* 42 (2014), pp. 40–51.

[46] J.P. Doherty and D. Muir Wood. "An extended Mohr–Coulomb (EMC) model for predicting the settlement of shallow foundations on sand". In: *Géotechnique* 63.8 (2013), pp. 661–673.

[47] Y.P. Dong, H.J. Burd, and G.T. Houlsby. "Finite-element analysis of a deep excavation case history". In: *Géotechnique* 66.1 (2016), pp. 1–15.

[48] V. Dubourg, B. Sudret, and F. Deheeger. "Metamodel-based importance sampling for structural reliability analysis". In: *Probabilistic Engineering Mechanics* 33 (2013), pp. 47–57.

[49] B. Echard, N. Gayton, and M. Lemaire. "AK-MCS: an active learning reliability method combining Kriging and Monte Carlo simulation". In: *Structural Safety* 33.2 (2011), pp. 145–154.

[50] E. El Kahi, O. Deck, M. Khouri, R. Mehdizadeh, and P. Rahme. "Simplified probabilistic evaluation of the variability of soil-structure interaction parameters on the elastic transmission of ground movements". In: *Engineering Structures* 213 (2020), p. 110554.

[51] I. Elkayam and A. Klar. "Nonlinear elastoplastic formulation for tunneling effects on superstructures". In: *Canadian Geotechnical Journal* 56.7 (2019), pp. 956–969.

[52] B. Ellingwood. *Development of a probability based load criterion for American National Standard A58: Building code requirements for minimum design loads in buildings and other structures*. Vol. 13. US Department of Commerce, National Bureau of Standards, 1980.

[53] V. Fargnoli, C.G. Gragnano, D. Boldini, and A. Amorosi. "3D numerical modelling of soil–structure interaction during EPB tunnelling". In: *Géotechnique* 65.1 (2015), pp. 23–37.

[54] R.P. Farrell. "Tunnelling in sands and the response of buildings". PhD thesis. University of Cambridge, 2011.

[55] R.P. Farrell, R.J. Mair, A. Sciotti, A. Pigorini, and M. Ricci. "The response of buildings to tunnelling: a case study". In: *Geotechnical Aspects of Underground Construction in Soft Ground-Proceedings of the 7th International Symposium on Geotechnical Aspects of Underground Construction in Soft Ground*. 2012, pp. 877–885.

[56] FEMA. "Evaluation of earthquake damaged concrete and masonry wall buildings: Basic procedures manual". In: *FEMA 306: Prestandard and commentary for the seismic rehabilitation of buildings* (1998), p. 250.

[57] H.A. Fenton and D.V. Griffiths. *Risk assessment in geotechnical engineering*. Vol. 461. John Wiley & Sons New York, 2008.

[58] R.J. Finno and L.S. Bryson. "Response of building adjacent to stiff excavation support system in soft clay". In: *Journal of performance of constructed facilities* 16.1 (2002), pp. 10–20.

[59] R.J. Finno, F.T. Voss Jr, E. Rossow, and J.T. Blackburn. "Evaluating damage potential in buildings affected by excavations". In: *Journal of geotechnical and geoenvironmental engineering* 131.10 (2005), pp. 1199–1210.

[60] V.H. Franco, G. Gitirana, and A.P. de Assis. "Probabilistic assessment of tunneling-induced building damage". In: *Computers and Geotechnics* 113 (2019), p. 103097.

[61] Frank M., Stevan G., Adam Z., Zhong K., Wael E.,Pedro A. *NHERI-SimCenter/R2DTool*. Version 2.1.0. 2022. URL: `https://doi.org/10.5281/zenodo.6404528`.

[62] A. Franza, S. Acikgoz, and M.J. DeJong. "Timoshenko beam models for the coupled analysis of building response to tunnelling". In: *Tunnelling and Underground Space Technology* 96 (2020), p. 103160.

[63] A. Franza and M.J. DeJong. "Elastoplastic solutions to predict tunneling-induced load redistribution and deformation of surface structures". In: *Journal of Geotechnical and Geoenvironmental Engineering* 145.4 (2019), p. 04019007.

[64] A. Franza and A.M. Marshall. "Empirical and semi-analytical methods for evaluating tunnelling-induced ground movements in sands". In: *Tunnelling and Underground Space Technology* 88 (2019), pp. 47–62.

[65] A. Franza, S. Ritter, and M.J. DeJong. "Continuum solutions for tunnel–building interaction and a modified framework for deformation prediction". In: *Géotechnique* 70.2 (2020), pp. 108–122.

[66] J.N. Franzius. "Behaviour of buildings due to tunnel induced subsidence". PhD thesis. Imperial College London (University of London), 2004.

[67] J.N. Franzius and D.M. Potts. "Influence of mesh geometry on three-dimensional finite-element analysis of tunnel excavation". In: *International Journal of Geomechanics* 5.3 (2005), pp. 256–266.

[68] J.N. Franzius, D.M. Potts, and J.B. Burland. “The response of surface structures to tunnel construction”. In: *Proceedings of the Institution of Civil Engineers-Geotechnical Engineering* 159.1 (2006), pp. 3–17.

[69] J. Fu, J. Yang, H. Klapperich, and S. Wang. “Analytical prediction of ground movements due to a nonuniform deforming tunnel”. In: *International Journal of Geomechanics* 16.4 (2016), p. 04015089.

[70] C. Geuzaine and J.F. Remacle. “Gmsh: A 3-D finite element mesh generator with built-in pre-and post-processing facilities”. In: *International journal for numerical methods in engineering* 79.11 (2009), pp. 1309–1331.

[71] R. Ghanem. “The nonlinear Gaussian spectrum of log-normal stochastic processes and variables”. In: (1999).

[72] R.G. Ghanem and P.D. Spanos. *Stochastic finite elements: a spectral approach*. Courier Corporation, 2003.

[73] A. Ghobarah. “On drift limits associated with different damage levels”. In: *International workshop on performance-based seismic design*. Vol. 28. Dept. of Civil Engineering, McMaster University, June 28–July 1. 2004.

[74] G. Giardina, M.J. DeJong, B. Chalmers, B. Ormond, and R.J. Mair. “A comparison of current analytical methods for predicting soil-structure interaction due to tunnelling”. In: *Tunnelling and Underground Space Technology* 79 (2018), pp. 319–335.

[75] G. Giardina, M.J. DeJong, and R.J. Mair. “Interaction between surface structures and tunnelling in sand: centrifuge and computational modelling”. In: *Tunnelling and Underground Space Technology* 50 (2015), pp. 465–478.

[76] G. Giardina, M.A.N. Hendriks, and J.G. Rots. “Numerical analysis of tunnelling effects on masonry buildings: the influence of tunnel location on damage assessment”. In: *Advanced Materials Research*. Vol. 133. Trans Tech Publ. 2010, pp. 289–294.

[77] G. Giardina, N. Losacco, M.J. DeJong, G.M.B. Viggiani, and R.J. Mair. “Effect of soil models on the prediction of tunnelling-induced deformations of structures”. In: *Proceedings of the Institution of Civil Engineers-Geotechnical Engineering* 173.5 (2020), pp. 379–397.

[78] G. Giardina, A.V. Van de Graaf, M.A.N. Hendriks, J.G. Rots, and A. Marini. “Numerical analysis of a masonry façade subject to tunnelling-induced settlements”. In: *Engineering structures* 54 (2013), pp. 234–247.

[79] G. Giardina et al. “Experimental analysis of a masonry façade subject to tunnelling-induced settlement”. In: *Engineering Structures* 45 (2012), pp. 421–434.

[80] K.H. Goh. “Response of ground and buildings to deep excavations and tunnelling”. PhD thesis. University of Cambridge, 2011.

[81] K.H. Goh and R.J. Mair. “Building damage assessment for deep excavations in Singapore and the influence of building stiffness”. In: *Geotechnical Engineering* 42 (2011), pp. 1–12.

[82] C. Gonzalez and C. Sagaseta. “Patterns of soil deformations around tunnels. Application to the extension of Madrid Metro”. In: *Computers and Geotechnics* 28.6-7 (2001), pp. 445–468.

[83] R.J. Grant and R.N. Taylor. “Tunnelling-induced ground movements in clay”. In: *Proceedings of the Institution of Civil Engineers-Geotechnical Engineering* 143.1 (2000), pp. 43–55.

[84] T.K. Haji, A.M. Marshall, and A. Franza. “Mixed empirical-numerical method for investigating tunnelling effects on structures”. In: *Tunnelling and Underground Space Technology* 73 (2018), pp. 92–104.

[85] M.E. Harr. “Probabilistic estimates for multivariate analyses”. In: *Applied Mathematical Modelling* 13.5 (1989), pp. 313–318.

[86] Y.M.A. Hashash and A.J. Whittle. “Ground movement prediction for deep excavations in soft clay”. In: *Journal of geotechnical engineering* 122.6 (1996), pp. 474–486.

[87] Hazus-Mh. “Multi-hazard loss estimation methodology: Earthquake model”. In: *Department of Homeland Security, FEMA, Washington, DC* (2003), pp. 235–260.

[88] D.W. Hight and K.G. Higgins. “An approach to the prediction of ground movements in engineering practice: background and application”. In: *PRE-FAILURE DEFORMATION OF GEOMATERIALS. PROCEEDINGS OF THE INTERNATIONAL SYMPOSIUM, 12-14 SEPTEMBER 1994, SAPPORO, JAPAN. 2 VOLS.* 1995.

[89] D.A. Hills and D. Dini. “Characteristics of the process zone at sharp notch roots”. In: *International Journal of Solids and structures* 48.14-15 (2011), pp. 2177–2183.

[90] H.P. Hong. “An efficient point estimate method for probabilistic analysis”. In: *Reliability Engineering & System Safety* 59.3 (1998), pp. 261–267.

[91] H.P. Hong. “Point-estimate moment-based reliability analysis”. In: *Civil Engineering Systems* 13.4 (1996), pp. 281–294.

[92] G.T. Houlsby. “A model for the variable stiffness of undrained clay”. In: *Proc. Int. Symp. on Pre-Failure Deformation Characteristics of Soils, Turin, 26*. Vol. 1. Citeseer. 1999, pp. 443–450.

[93] E.C. Hsiao, M. Schuster, C.H. Juang, and G.T. Kung. “Reliability analysis and updating of excavation-induced ground settlement for building serviceability assessment”. In: *Journal of Geotechnical and Geoenvironmental Engineering* 134.10 (2008), pp. 1448–1458.

[94] P. Hsieh and C. Ou. “Shape of ground surface settlement profiles caused by excavation”. In: *Canadian geotechnical journal* 35.6 (1998), pp. 1004–1017.

[95] P.G. Hsieh, T.C. Kung, C.Y. Ou, and Y.G. Tang. "Deep excavation analysis with consideration of small strain modulus and its degradation behavior of clay". In: *Proc., 12th Asian Regional Conf. on Soil Mechanics and Geotechnical Engineering*. Vol. 1. World Scientific Publishing Singapore. 2003, pp. 785–788.

[96] Z. Hu and S. Mahadevan. "Probability models for data-driven global sensitivity analysis". In: *Reliability Engineering & System Safety* 187 (2019), pp. 40–57.

[97] T.J. Hughes. *The finite element method: linear static and dynamic finite element analysis*. Courier Corporation, 2012.

[98] M.B. Jaksa et al. "Towards reliable and effective site investigations". In: *Géotechnique* 55.2 (2005), pp. 109–121.

[99] R.J. Jardine, D.M. Potts, A.B. Fourie, and J.B. Burland. "Studies of the influence of non-linear stress–strain characteristics in soil–structure interaction". In: *Geotechnique* 36.3 (1986), pp. 377–396.

[100] S. Joe and F.Y. Kuo. "Constructing Sobol sequences with better two-dimensional projections". In: *SIAM Journal on Scientific Computing* 30.5 (2008), pp. 2635–2654.

[101] T. Kasper and G. Meschke. "A 3D finite element simulation model for TBM tunnelling in soft ground". In: *International journal for numerical and analytical methods in geomechanics* 28.14 (2004), pp. 1441–1460.

[102] Á. Kézdi and L. Réthàti. *Handbook of soil mechanics*. Vol. 1. Elsevier Amsterdam, 1974.

[103] A. Klar, T.E. Vorster, K. Soga, and R.J. Mair. "Elastoplastic solution for soil-pipe-tunnel interaction". In: *Journal of Geotechnical and Geoenvironmental Engineering* 133.7 (2007), pp. 782–792.

[104] C. Koch, A. Vonthron, and M. König. "A tunnel information modelling framework to support management, simulations and visualisations in mechanised tunnelling projects". In: *Automation in Construction* 83 (2017), pp. 78–90.

[105] G.T. Kung, C.H. Juang, E.C. Hsiao, and Y.M. Hashash. "Simplified model for wall deflection and ground-surface settlement caused by braced excavation in clays". In: *Journal of Geotechnical and Geoenvironmental Engineering* 133.6 (2007), pp. 731–747.

[106] P. L'Ecuyer. *Randomized quasi-Monte Carlo: An introduction for practitioners*. Springer, 2018.

[107] P. L'Ecuyer and C. Lemieux. "Recent advances in randomized quasi-Monte Carlo methods". In: *Modeling uncertainty: An examination of stochastic theory, methods, and applications* (2002), pp. 419–474.

[108] O.P. Le Maıtre, M.T. Reagan, H.N. Najm, R.G. Ghanem, and O.M. Knio. "A stochastic projection method for fluid flow: II. Random process". In: *Journal of computational Physics* 181.1 (2002), pp. 9–44.

[109] J. Lee and G.L. Fenves. “Plastic-damage model for cyclic loading of concrete structures”. In: *Journal of engineering mechanics* 124.8 (1998), pp. 892–900.

[110] C. Lemieux. *Monte carlo and quasi-monte carlo sampling*. Springer Science & Business Media, 2009.

[111] Y.F. Leung, A. Klar, and K. Soga. “Theoretical study on pile length optimization of pile groups and piled rafts”. In: *Journal of geotechnical and geoenvironmental engineering* 136.2 (2010), pp. 319–330.

[112] R.J. LeVeque. *Finite difference methods for ordinary and partial differential equations: steady-state and time-dependent problems*. SIAM, 2007.

[113] N. Loganathan and H.G. Poulos. “Analytical prediction for tunneling-induced ground movements in clays”. In: *Journal of Geotechnical and geoenvironmental engineering* 124.9 (1998), pp. 846–856.

[114] N. Losacco, A. Burghignoli, and L. Callisto. “Uncoupled evaluation of the structural damage induced by tunnelling”. In: *Géotechnique* 64.8 (2014), pp. 646–656.

[115] D.J. Lucia, P.S. Beran, and W.A. Silva. “Reduced-order modeling: new approaches for computational physics”. In: *Progress in aerospace sciences* 40.1-2 (2004), pp. 51–117.

[116] V. Macchiarulo et al. “Integrated InSAR monitoring and structural assessment of tunnelling-induced building deformations”. In: *Structural Control and Health Monitoring* 28.9 (2021), e2781.

[117] R.J. Mair. “Tunnelling and deep excavations: Ground movements and their effects”. In: *Proceedings of the 15th European conference on soil mechanics and geotechnical engineering–geotechnics of hard soils–weak rocks (part 4)*. IOS Press, Athens, Greece. 2013, pp. 39–70.

[118] R.J. Mair and R.N. Taylor. “Theme lecture: Bored tunnelling in the urban environment”. In: *Proceedings of the fourteenth international conference on soil mechanics and foundation engineering*. Rotterdam. 1997, pp. 2353–2385.

[119] R.J. Mair, R.N. Taylor, and A. Bracegirdle. “Subsurface settlement profiles above tunnels in clays”. In: *Geotechnique* 43.2 (1993), pp. 315–320.

[120] R.J. Mair, R.N. Taylor, and J.B. Burland. “Prediction of ground movements and assessment of risk of building damage due to bored tunnelling”. In: *Geotechnical aspects of underground construction in soft ground*. 1996, pp. 713–718.

[121] M. Maleki, H. Sereshteh, M. Mousivand, and M. Bayat. “An equivalent beam model for the analysis of tunnel-building interaction”. In: *Tunnelling and Underground Space Technology* 26.4 (2011), pp. 524–533.

[122] A. Marshall. “Tunnelling in sand and its effect on pipelines and piles”. PhD thesis. University of Cambridge, 2009.

[123] Reported by the Masonry Standards Joint Committee et al. “Building Code Requirements and Specification for Masonry Structures: Containing Building Code Requirements for Masonry Structures (TMS 402-08/ACI 530-08/ASCE 5-08, Specification for Masonry Structures (TMS 602-08/ACI 530.1-08/ASCE 6-08) and Companion Committees”. In: ASCE.

[124] H.G. Matthies and A. Keese. “Galerkin methods for linear and nonlinear elliptic stochastic partial differential equations”. In: *Computer methods in applied mechanics and engineering* 194.12-16 (2005), pp. 1295–1331.

[125] R.E. Melchers and A.T. Beck. *Structural reliability analysis and prediction*. John wiley & sons, 2018.

[126] G. Meschke, R. Breitenbücher, S. Freitag, M. König, and M. Thewes. *Interaction Modeling in Mechanized Tunneling*. Springer Nature, 2023.

[127] FEMA Multi-hazard Loss Estimation Methodology. “Earthquake Model-Technical Manual, Hazus-MH 2.1”. In: *Washington DC: Department of Homeland Security, Federal Emergency Management Agency, Mitigation Division* (2013).

[128] FEMA Multi-hazard Loss Estimation Methodology. “Seismic performance assessment of buildings volume 1—methodology, Technical report FEMA-P58”. In: *Washington DC: Department of Homeland Security, Federal Emergency Management Agency, Mitigation Division* (2012).

[129] FEMA Multi-hazard Loss Estimation Methodology. “Seismic performance assessment of buildings volume 2—implementation guide, Technical report FEMA-P58”. In: *Washington DC: Department of Homeland Security, Federal Emergency Management Agency, Mitigation Division* (2012).

[130] FEMA Multi-hazard Loss Estimation Methodology. “Seismic performance assessment of buildings volume 4—Methodology for Assessing Environmental Impacts, Technical report FEMA-P58”. In: *Washington DC: Department of Homeland Security, Federal Emergency Management Agency, Mitigation Division* (2012).

[131] A. Mirhabibi and A. Soroush. “Effects of surface buildings on twin tunnelling-induced ground settlements”. In: *Tunnelling and Underground Space Technology* 29 (2012), pp. 40–51.

[132] S. Miro, M. König, D. Hartmann, and T. Schanz. “A probabilistic analysis of subsoil parameters uncertainty impacts on tunnel-induced ground movements with a back-analysis study”. In: *Computers and Geotechnics* 68 (2015), pp. 38–53.

[133] G. Mollon, D. Dias, and A.H. Soubra. “Probabilistic analyses of tunneling-induced ground movements”. In: *Acta Geotechnica* 8.2 (2013), pp. 181–199.

[134] G. Mollon, D. Dias, and A.H. Soubra. "Probabilistic analysis of circular tunnels in homogeneous soil using response surface methodology". In: *Journal of geotechnical and geoenvironmental engineering* 135.9 (2009), pp. 1314–1325.

[135] K.P. Murphy. *Machine learning: a probabilistic perspective*. MIT press, 2012.

[136] C.W.W. Ng, G. Zheng, J. Ni, and C. Zhou. "Use of unsaturated small-strain soil stiffness to the design of wall deflection and ground movement adjacent to deep excavation". In: *Computers and Geotechnics* 119 (2020), p. 103375.

[137] H. Niederreiter. *Random number generation and quasi-Monte Carlo methods*. SIAM, 1992.

[138] T. Nilsen and T. Aven. "Models and model uncertainty in the context of risk analysis". In: *Reliability Engineering & System Safety* 79.3 (2003), pp. 309–317.

[139] J. Nossent, P. Elsen, and W. Bauwens. "Sobol'sensitivity analysis of a complex environmental model". In: *Environmental Modelling & Software* 26.12 (2011), pp. 1515–1525.

[140] M.P. O'Reilly and B.M. New. *Settlements above tunnels in the United Kingdom-their magnitude and prediction*. Tech. rep. 1982.

[141] M. Obel, M.A. Ahrens, and P. Mark. "Metamodel-Based Prediction of Structural Damages due to Tunneling-Induced Settlements". In: *ASCE-ASME Journal of Risk and Uncertainty in Engineering Systems, Part A: Civil Engineering* 6.4 (2020), p. 04020044.

[142] A.B. Owen. "Scrambled net variance for integrals of smooth functions". In: *The Annals of Statistics* 25.4 (1997), pp. 1541–1562.

[143] G. Pan, J. He, and R. Fang. "Automatic floor plan detection and recognition". In: *2017 2nd International Conference on Image, Vision and Computing (ICIVC)*. IEEE. 2017, pp. 201–205.

[144] K.H. Park. "Elastic solution for tunneling-induced ground movements in clays". In: *International Journal of Geomechanics* 4.4 (2004), pp. 310–318.

[145] D. Patsialis and A.A. Taflanidis. "Multi-fidelity Monte Carlo for seismic risk assessment applications". In: *Structural Safety* 93 (2021), p. 102129.

[146] E.J. Pebesma and C.G. Wesseling. "Gstat: a program for geostatistical modelling, prediction and simulation". In: *Computers & Geosciences* 24.1 (1998), pp. 17–31.

[147] R.B. Peck. "Advantages and limitations of the observational method in applied soil mechanics". In: *Geotechnique* 19.2 (1969), pp. 171–187.

[148] R.B. Peck. "Deep excavations and tunneling in soft ground". In: *Proc. 7th ICSMFE, 1969* (1969), pp. 225–290.

[149] B. Peherstorfer, P.S. Beran, and K.E. Willcox. "Multifidelity Monte Carlo estimation for large-scale uncertainty propagation". In: *2018 AIAA Non-Deterministic Approaches Conference*. 2018, p. 1660.

[150] B. Peherstorfer, K. Willcox, and M. Gunzburger. "Survey of multifidelity methods in uncertainty propagation, inference, and optimization". In: *Siam Review* 60.3 (2018), pp. 550–591.

[151] K.K. Phoon and F.H. Kulhawy. "Characterization of geotechnical variability". In: *Canadian geotechnical journal* 36.4 (1999), pp. 612–624.

[152] K.K. Phoon and F.H. Kulhawy. "Evaluation of geotechnical property variability". In: *Canadian Geotechnical Journal* 36.4 (1999), pp. 625–639.

[153] J.A. Pickhaver, H.J. Burd, and G.T. Houlsby. "An equivalent beam method to model masonry buildings in 3D finite element analysis". In: *Computers & structures* 88.19-20 (2010), pp. 1049–1063.

[154] F. Pinto and A.J. Whittle. "Discussion of "Elastic solution for tunneling-induced ground movements in clays" by KH Park". In: *International Journal of Geomechanics* 6.1 (2006), pp. 72–73.

[155] P.N. Pizarro, N. Hitschfeld, I. Sipiran, and J.M. Saavedra. "Automatic floor plan analysis and recognition". In: *Automation in Construction* 140 (2022), p. 104348.

[156] H.C. Plummer. *Brick and tile engineering*. Structural Clay Products Institute, 1962.

[157] D.M. Potts. "Behaviour of Lined and Unlined Tunnels in Sand." PhD thesis. University of Cambridge, 1976.

[158] D.M. Potts and T.I. Addenbrooke. "A structure's influence on tunnelling-induced ground movements." In: *Proceedings of the Institution of Civil Engineers-Geotechnical Engineering* 125.2 (1997), pp. 109–125.

[159] J.W.F. Remo and N. Pinter. "Hazus-MH earthquake modeling in the central USA". In: *Natural hazards* 63.2 (2012), pp. 1055–1081.

[160] S. Ritter. "Experiments in tunnel-soil-structure interaction". PhD thesis. University of Cambridge, 2018.

[161] S. Ritter and R. Frauenfelder. "InSAR monitoring data to assess building response to deep excavations". In: *IOP Conference Series: Earth and Environmental Science*. Vol. 710. 1. IOP Publishing. 2021, p. 012036.

[162] S. Ritter, G. Giardina, M.J. DeJong, and R.J. Mair. "Centrifuge modelling of building response to tunnel excavation". In: *International Journal of Physical Modelling in Geotechnics* 18.3 (2018), pp. 146–161.

[163] J. Roboski and R.J. Finno. "Distributions of ground movements parallel to deep excavations in clay". In: *Canadian geotechnical journal* 43.1 (2006), pp. 43–58.

[164] M. Rosenblatt. "Remarks on a multivariate transformation". In: *The annals of mathematical statistics* 23.3 (1952), pp. 470–472.

[165] E. Rosenblueth. "Point estimates for probability moments". In: *Proceedings of the National Academy of Sciences* 72.10 (1975), pp. 3812–3814.

[166] C. Sagaseta. "Analysis of undraind soil deformation due to ground loss". In: *Geotechnique* 37.3 (1987), pp. 301–320.

[167] A. Saltelli et al. *Global sensitivity analysis: the primer*. John Wiley & Sons, 2008.

[168] A. Saltelli et al. "Variance based sensitivity analysis of model output. Design and estimator for the total sensitivity index". In: *Computer physics communications* 181.2 (2010), pp. 259–270.

[169] C.A. Schenk and G.I. Schuëller. *Uncertainty assessment of large finite element systems*. Vol. 24. Springer Science & Business Media, 2005.

[170] P.J. Schneider and B.A. Schauer. "HAZUS—its development and its future". In: *Natural Hazards Review* 7.2 (2006), pp. 40–44.

[171] M. Schuster, G.T. Kung, C.H. Juang, and Y.M.A. Hashash. "Simplified model for evaluating damage potential of buildings adjacent to a braced excavation". In: *Journal of geotechnical and geoenvironmental engineering* 135.12 (2009), pp. 1823–1835.

[172] H.F. Schweiger, R. Thurner, and R. Pöttler. "Reliability analysis in geotechnics with deterministic finite elements—Theoretical concepts and practical application". In: *International Journal of Geomechanics* 1.4 (2001), pp. 389–413.

[173] M. Son and E.J. Cording. "Estimation of building damage due to excavation-induced ground movements". In: *Journal of geotechnical and geoenvironmental engineering* 131.2 (2005), pp. 162–177.

[174] M. Son and E.J. Cording. "Evaluation of building stiffness for building response analysis to excavation-induced ground movements". In: *Journal of geotechnical and geoenvironmental engineering* 133.8 (2007), pp. 995–1002.

[175] S.E. Stallebrass and R.N. Taylor. "The development and evaluation of a constitutive model for the prediction of ground movements in overconsolidated clay". In: *Géotechnique* 47.2 (1997), pp. 235–253.

[176] British Standard. "Eurocode 6—Design of masonry structures—". In: *British Standard Institution. London* 2005 (2005).

[177] G.P. Steck. "The Smirnov two sample tests as rank tests". In: *The Annals of Mathematical Statistics* 40.4 (1969), pp. 1449–1466.

[178] R.E. Stern, J. Song, and D.B. Work. "Accelerated Monte Carlo system reliability analysis through machine-learning-based surrogate models of network connectivity". In: *Reliability Engineering & System Safety* 164 (2017), pp. 1–9.

[179] O.E. Strack and A. Verruijt. “A complex variable solution for a deforming buoyant tunnel in a heavy elastic half-plane”. In: *International Journal for Numerical and Analytical Methods in Geomechanics* 26.12 (2002), pp. 1235–1252.

[180] A.W. Stuedlein and T. Bong. “Effect of spatial variability on static and liquefaction-induced differential settlements”. In: *Geo-Risk 2017*. 2017, pp. 31–51.

[181] C.A. Subasic and J.G. Borchelt. “Clay and shale brick material properties–a statistical report”. In: *The 6th North American Masonry Conference, Proceedings of the 6th North American Masonry Conference, The Masonry Society, Boulder, CO*. 1993.

[182] B. Sudret. “Global sensitivity analysis using polynomial chaos expansions”. In: *Reliability engineering & system safety* 93.7 (2008), pp. 964–979.

[183] S. Suwansawat and H.H. Einstein. “Artificial neural networks for predicting the maximum surface settlement caused by EPB shield tunneling”. In: *Tunnelling and underground space technology* 21.2 (2006), pp. 133–150.

[184] G. Swoboda and A. Abu-Krisha. “Three-dimensional numerical modelling for TBM tunnelling in consolidated clay”. In: *Tunnelling and Underground Space Technology* 14.3 (1999), pp. 327–333.

[185] S. Tarantola, D. Gatelli, and Y.A. Mara. “Random balance designs for the estimation of first order global sensitivity indices”. In: *Reliability Engineering & System Safety* 91.6 (2006), pp. 717–727.

[186] G.E. Torp-Petersen and M.G. Black. “Geotechnical investigation and assessment of potential building damage arising from ground movements: CrossRail”. In: *Proceedings of the Institution of Civil Engineers-Transport*. Vol. 147. 2. Thomas Telford Ltd. 2001, pp. 107–119.

[187] M. Uzielli, S. Lacasse, F. Nadim, K.K. Phoon, et al. “Soil variability analysis for geotechnical practice”. In: *Characterisation and engineering properties of natural soils* (2007), pp. 1653–1754.

[188] H. Vaziri, B. Simpson, J.W. Pappin, and L. Simpson. “Integrated forms of Mindlin’s equations”. In: *Géotechnique* 32.3 (1982), pp. 275–278.

[189] A. Verruijt. “A complex variable solution for a deforming circular tunnel in an elastic half-plane”. In: *International Journal for Numerical and Analytical Methods in Geomechanics* 21.2 (1997), pp. 77–89.

[190] A. Verruijt and J.R. Booker. “Surface settlements due to deformation of a tunnel in an elastic half plane”. In: *Geotechnique* 48.5 (1998), pp. 709–713.

[191] A. Verruijt and O.E. Strack. “Buoyancy of tunnels in soft soils”. In: *Géotechnique* 58.6 (2008), pp. 513–515.

[192] T.E. Vorster, A. Klar, K. Soga, and R.J. Mair. “Estimating the effects of tunneling on existing pipelines”. In: *Journal of Geotechnical and Geoenvironmental Engineering* 131.11 (2005), pp. 1399–1410.

[193] C. Wang et al. “Machine learning-based regional scale intelligent modeling of building information for natural hazard risk management”. In: *Automation in Construction* 122 (2021), p. 103474.

[194] Y. Wang and Z. Cao. “Probabilistic characterization of Young’s modulus of soil using equivalent samples”. In: *Engineering Geology* 159 (2013), pp. 106–118.

[195] Z. Wang and M. Broccardo. “A novel active learning-based Gaussian process metamodelling strategy for estimating the full probability distribution in forward UQ analysis”. In: *Structural Safety* 84 (2020), p. 101937.

[196] A.J. Whittle and Y.M.A. Hashash. “Soil modeling and prediction of deep excavation behavior”. In: *International symposium on pre-failure deformation characteristics of geomaterials*. 1994, pp. 589–594.

[197] A.J. Whittle, Y.M.A. Hashash, and R.V. Whitman. “Analysis of deep excavation in Boston”. In: *Journal of geotechnical engineering* 119.1 (1993), pp. 69–90.

[198] J. Wongsaroj et al. “Effect of TBM driving parameters on ground surface movements: Channel Tunnel Rail Link Contract 220”. In: *Geotechnical aspects of underground construction in soft ground* (2005), pp. 335–341.

[199] D. Xiu and G.E. Karniadakis. “The Wiener–Askey polynomial chaos for stochastic differential equations”. In: *SIAM journal on scientific computing* 24.2 (2002), pp. 619–644.

[200] J. Xu, A. Franza, A.M. Marshall, N. Losacco, and D. Boldini. “Tunnel–framed building interaction: comparison between raft and separate footing foundations”. In: *Géotechnique* 71.7 (2021), pp. 631–644.

[201] H. Yazdani, M. Khatibinia, S. Gharehbaghi, and K. Hatami. “Probabilistic performance-based optimum seismic design of RC structures considering soil–structure interaction effects”. In: *ASCE-ASME Journal of Risk and Uncertainty in Engineering Systems, Part A: Civil Engineering* 3.2 (2017), G4016004.

[202] W.N. Yiu, H.J. Burd, and C.M. Martin. “Finite-element modelling for the assessment of tunnel-induced damage to a masonry building”. In: *Géotechnique* 67.9 (2017), pp. 780–794.

[203] C. Yoo and D. Lee. “Deep excavation-induced ground surface movement characteristics–A numerical investigation”. In: *Computers and Geotechnics* 35.2 (2008), pp. 231–252.

[204] P.C. Young, G.M. Hornberger, and R.C. Spear. “Modeling badly defined systems: some further thoughts”. In: *Proceedings SIMSIG Conference, Canberra*. 1978, pp. 24–32.

[205] L. Zhang and A.M.Y. Ng. “Probabilistic limiting tolerable displacements for serviceability limit state design of foundations”. In: *Geotechnique* 55.2 (2005), pp. 151–161.

[206] W. Zhang et al. “State-of-the-art review of soft computing applications in underground excavations”. In: *Geoscience Frontiers* 11.4 (2020), pp. 1095–1106.

[207] Y. Zhang and A. Der Kiureghian. “Two improved algorithms for reliability analysis”. In: *Reliability and optimization of structural systems*. Springer, 1995, pp. 297–304.

[208] Z. Zhang, M. Huang, X. Xi, and X. Yang. “Complex variable solutions for soil and liner deformation due to tunneling in clays”. In: *International Journal of Geomechanics* 18.7 (2018), p. 04018074.

[209] Z. Zhang, C. Liu, X. Huang, C.Y. Kwok, and L. Teng. “Three-dimensional finite-element analysis on ground responses during twin-tunnel construction using the URUP method”. In: *Tunnelling and Underground Space Technology* 58 (2016), pp. 133–146.

[210] J. Zhao. “MasonMesh: A structured FEM mesh generator for masonry facade buildings (https://www.mathworks.com/matlabcentral/fileexchange/123345-masonmesh)”. In: *MATLAB Central File Exchange* (2023).

[211] J. Zhao and M.J. DeJong. “Application of Multi-Fidelity and Randomized Quasi-Monte Carlo Method in the Probabilistic Assessment of Excavation-Induced Building Damages”. In: *Proceedings of the 5th ECCOMAS Thematic Conference on Uncertainty Quantification in Computational Sciences and Engineering (UNCECOMP 2023)*. 2023.

[212] J. Zhao and M.J. DeJong. “Three-dimensional probabilistic assessment of tunneling induced structural damage using Monte-Carlo method and hybrid finite element model”. In: *Computers and Geotechnics* 154 (2023), p. 105122.

[213] J. Zhao, A. Franza, and M.J. DeJong. “Method for Probabilistic Assessment of Tunneling-Induced Damage to Surface Structures Considering Soil-Structure Interaction Effects”. In: *ASCE-ASME Journal of Risk and Uncertainty in Engineering Systems, Part A: Civil Engineering* 7.4 (2021), p. 04021055.

[214] J. Zhao, S. Ritter, and M.J. DeJong. “Early-stage assessment of structural damage caused by braced excavations: Uncertainty quantification and a probabilistic analysis approach”. In: *Tunnelling and Underground Space Technology* 125 (2022), p. 104499.

[215] A. Zsarnóczay and G.G. Deierlein. “PELICUN–A Computational Framework for Estimating Damage, Loss and Community Resilience”. In: *Proceedings, 17th World Conference on Earthquake Engineering,(Sendai: WCEE)*. 2020.